



**University of  
Nottingham**

UK | CHINA | MALAYSIA

# The Synthesis and Properties of Asymmetric Organic-Inorganic Hybrid Polyoxometalates

Elizabeth Hampson

School of Chemistry, University of Nottingham

A thesis submitted for the degree of Doctor of  
Philosophy

July 2021

## Acknowledgements

I would firstly like to thank my supervisor Dr. Graham Newton, for the opportunity to undertake this research and for all the support and encouragement that he has given throughout. Thank you for being excited about my research and keeping me inspired and motivated, and for always giving the time to offer me advice about anything.

I would also like to thank Dr. Jamie Cameron for his guidance throughout, and for his endless patience and willingness to help me with my research questions and with any of my worries. You and Graham have remained so supportive during the past year when we could only meet online, thank you both for always finding time for me.

I also thank Dr. Carmen Martin-Gandul for being an excellent teacher and guide in the lab. Your motivating energy in the lab is always missed!

Many thanks also go to Dr. Alex Kibler and Sharad Amin for all their helpful inputs across my projects and encouragement throughout, and thanks to Sharad for developing the synthesis of the  $C_n$  chain ligand.

I would like to thank Dr. Julie Watts for conducting the cryo-TEM experiments. Thank you for your willingness to run so many of our samples and for finding the time to fit them in when I was in a rush! I would also like to thank Dr. Stephen Davies for conducting the spectroelectrochemistry, Dr. Michael Fay for running the TEM experiments, and Ben Pointer-Gledhill for developing the mass spectroscopy technique for our group's compounds.

I must also thank the rest of the Newton group and wider NAMI group for their support. I could not have asked for a better research group to have done my PhD with- you are all such bright, encouraging people, and so willing to help anyone with anything.

Finally, I would like to thank Charlie for being my biggest support and for pushing me to keep going when I have so needed it. Thank you for always supporting me in everything I do and for being everything that you are.

# Table of Contents

|           |   |           |
|-----------|---|-----------|
| <b>1</b>  | <b>Introduction .....</b>   | <b>1</b>  |
| 1.1       | <b>Introduction to organic-inorganic hybrid polyoxometalates.....</b>   | <b>1</b>  |
| 1.1.1     | Brief introduction to polyoxometalates.....   | 1         |
| 1.1.1.1   | General POM structure and assembly.....   | 1         |
| 1.1.1.2   | The Wells-Dawson and Keggin structures .....  | 5         |
| 1.1.1.3   | Properties of POMs.....   | 9         |
| 1.1.2     | Organofunctionalisation of POMs.....  | 11        |
| 1.1.2.1   | Introduction to hybrid POMs.....  | 11        |
| 1.1.2.2   | Covalent organofunctionalisation strategies.....  | 13        |
| 1.1.2.2.1 | Organophosphonate hybrids - tuneable electronic structure ...   | 16        |
| 1.2       | <b>Functional hybrid POM systems .....</b>  | <b>18</b> |
| 1.2.1     | Combining properties with appended photoactive subunits.....  | 18        |
| 1.2.2     | Hybrid POM supramolecular assembly and immobilisation .....   | 22        |
| 1.2.2.1   | Metal-directed assembly of hybrid POMs.....   | 26        |
| 1.3       | <b>Asymmetric hybrid POMs- an emerging strategy for multifunctionality .</b>  | <b>30</b> |
| 1.3.1     | Current synthetic strategies for asymmetric functionalisation .....   | 31        |
| 1.3.1.1   | Purification from symmetric side-products.....  | 31        |
| 1.3.1.2   | Singly- organofunctionalised hybrid POMs .....  | 33        |
| 1.3.1.3   | Controlled postfunctionalisation of hybrid POMs.....  | 36        |
| 1.3.2     | Synergistic function in asymmetric hybrid POMs.....   | 37        |
| 1.3.3     | Assembly of asymmetric hybrid POMs .....  | 39        |
| 1.3.4     | New tuneable redox-active materials based on asymmetric hybrid POMs   | 41        |
| 2         | <b>Aims .....</b>   | <b>53</b> |
| 3         | <b>Design and synthesis of asymmetric hybrid POM (1) .....</b>  | <b>54</b> |
| 3.1       | <b>Preliminary asymmetric hybrid synthesis methodologies.....</b>   | <b>55</b> |
| 3.1.1     | Post-modification of symmetric hybrid POMs.....   | 55        |
| 3.1.2     | Purification from one pot reaction mixtures .....   | 58        |
| 3.2       | <b>Design of two distinct ligands, TPY and C<sub>18</sub> .....</b>   | <b>62</b> |
| 3.3       | <b>One-pot synthesis and purification of asymmetric hybrid POM [P<sub>2</sub>W<sub>17</sub>O<sub>57</sub>{(TPY)(C<sub>18</sub>)}] (1) .....</b>   | <b>66</b> |
| 3.4       | <b>Characterisation and properties of 1 .....</b>   | <b>68</b> |
| 3.5       | <b>Characterisation of symmetric hybrid POMs [P<sub>2</sub>W<sub>17</sub>O<sub>57</sub>{(TPY)<sub>2</sub>}] (2) and [P<sub>2</sub>W<sub>17</sub>O<sub>57</sub>{(C<sub>18</sub>)<sub>2</sub>}] (3) .....</b> | <b>75</b> |
| 3.5.1.1   | Characterisation of 2 .....   | 76        |
| 3.5.1.2   | Characterisation of 3 .....   | 79        |
| 3.5.1.3   | Self-assembling behaviour of 3 .....  | 83        |
| 3.6       | <b>Conclusions.....</b>   | <b>86</b> |

|            |   |            |
|------------|---|------------|
| <b>3.7</b> | <b>Experimental details .....</b>   | <b>87</b>  |
| 3.7.1      | Methods .....   | 87         |
| 3.7.2      | Syntheses .....   | 88         |
| 3.7.2.1    | $K_{10}[P_2W_{17}O_{61}] \{P_2W_{17}\}$ .....   | 88         |
| 3.7.2.2    | TPY .....   | 88         |
| 3.7.2.3    | $C_{18}$ .....  | 90         |
| 3.7.2.4    | $C_{16}$ & $C_{10}$ .....   | 92         |
| 3.7.2.5    | $[P_2W_{17}O_{57}\{(PPA)_2\}]$ , (SymPPA) .....                                       | 92         |
| 3.7.2.6    | $[P_2W_{17}O_{57}\{(TPY)(C_{10})\}]$ , (Asym $C_{10}$ ) .....                         | 93         |
| 3.7.2.7    | $[P_2W_{17}O_{57}\{(TPY)(C_{16})\}]$ (Asym $C_{16}$ ) .....                           | 95         |
| 3.7.2.8    | $[P_2W_{17}O_{57}\{(TPY)(C_{18})\}]$ , (1) .....                                      | 97         |
| 3.7.2.9    | $[P_2W_{17}O_{57}\{(TPY)_2\}]$ , (2) .....  | 98         |
| 3.7.2.10   | $[P_2W_{17}O_{57}\{(C_{18})_2\}]$ , (3) .....   | 99         |
| <b>3.8</b> | <b>References .....</b>   | <b>100</b> |
| <b>4</b>   | <b>Multifunctionality of asymmetric hybrid POM (1) .....</b>                          | <b>103</b> |
| 4.1        | Solvent-dependent self-assembly enabled by aliphatic ligand .....                     | 103        |
| 4.1.1      | Micelle characterisation .....  | 103        |
| 4.1.2      | Micelle electrochemistry .....  | 105        |
| 4.2        | Metal coordination at chelating ligand (Fe <sup>II</sup> ) .....                      | 108        |
| 4.2.1      | $[Fe(1)_2]$ dimer formation – (Fe-1) .....  | 109        |
| 4.2.1.1    | Preparation and characterisation of Fe-1 .....  | 109        |
| 4.2.1.2    | Assembly of Fe-1 .....  | 114        |
| 4.2.2      | Stoichiometric Fe <sup>2+</sup> -coordination .....                                   | 118        |
| 4.2.2.1    | UV-Vis titration experiments .....  | 118        |
| 4.2.2.2    | Preparation and characterisation of monomeric complex Fe-2 .....                      | 119        |
| 4.3        | Conclusions .....   | 124        |
| 4.4        | Experimental details .....  | 125        |
| 4.4.1      | Methods .....   | 125        |
| 4.4.2      | Syntheses .....   | 126        |
| 4.4.2.1    | $[Fe\{P_2W_{17}O_{57}(TPY)(C_{18})\}_2]$ (Fe-1) .....                                 | 126        |
| 4.4.2.2    | $[P_2W_{17}O_{57}\{(Fe-TPY)(C_{18})\}]$ (Fe-2) .....                                  | 128        |
| 4.5        | References .....  | 130        |
| <b>5</b>   | <b>Transition metal- functionalisation of asymmetric hybrid POMs</b>                  | <b>132</b> |
| 5.1        | Postfunctionalisation of an asymmetric hybrid POM by Pt <sup>II</sup> coordination    | 133        |
| 5.1.1      | Synthesis of $[P_2W_{17}O_{57}\{(Pt-TPY)(C_{18})\}]$ (Pt-1) .....                     | 134        |
| 5.1.2      | Characterisation of Pt-1 .....  | 135        |
| 5.1.3      | Solvent-dependent self-assembly of Pt-1 .....   | 142        |
| 5.2        | Preparation of a Ru <sup>II</sup> -functionalised asymmetric hybrid POM .....         | 147        |
| 5.2.1      | Synthesis of asymmetric hybrid POM $[P_2W_{17}O_{57}\{(Ru^{II}TPY)(C_{18})\}]$ (Ru-1) | 147        |
| 5.2.1.1    | Synthesis of RuTPY ligand .....   | 148        |

|            |   |            |
|------------|---|------------|
| 5.2.1.2    | One-pot synthesis and purification of Ru-1.....   | 149        |
| 5.2.2      | Characterisation of Ru-1 .....  | 151        |
| 5.2.3      | Multifunctionality of Ru-1.....   | 155        |
| 5.2.3.1    | Solvent-dependent self-assembly of Ru-1.....  | 155        |
| 5.2.3.2    | Photochemistry.....   | 159        |
| 5.2.3.2.1  | Photoluminescence .....   | 159        |
| 5.2.3.2.2  | Spectroelectrochemistry .....   | 161        |
| 5.2.3.2.3  | Photoreduction studies .....  | 163        |
| <b>5.3</b> | <b>Conclusions.....</b>   | <b>168</b> |
| <b>5.4</b> | <b>Experimental details .....</b>   | <b>169</b> |
| 5.4.1      | Methods .....   | 169        |
| 5.4.2      | Syntheses .....   | 171        |
| 5.4.2.1    | $[P_2W_{17}O_{57}\{(Pt^{II}-TPY)(C_{18})\}] - (Pt-1):$ .....  | 171        |
| 5.4.2.2    | Pt-PO(OEt) <sub>2</sub> TPY .....   | 172        |
| 5.4.2.3    | RuTPY .....   | 172        |
| 5.4.2.4    | $[P_2W_{17}O_{57}\{(RuTPY)(C_{18})\}] - (Ru-1)$ .....   | 174        |
| 5.4.2.5    | $[P_2W_{17}O_{57}\{(RuTPY)_2\}] - (Ru-2)$ .....   | 176        |
| <b>5.5</b> | <b>References.....</b>  | <b>177</b> |
| <b>6</b>   | <b>Surface-immobilisation of an asymmetric hybrid POM .....</b>   | <b>182</b> |
| <b>6.1</b> | <b>One-pot synthesis of asymmetric hybrid POM <math>[P_2W_{17}O_{57}\{(TPY)(C_{11}SH)\}]</math> (4)</b> | <b>184</b> |
| 6.1.1      | Characterisation of 4.....  | 187        |
| 6.1.2      | Self-assembly of 4 .....  | 189        |
| <b>6.2</b> | <b>Surface-immobilisation of 4 .....</b>  | <b>192</b> |
| 6.2.1      | Surface-confined electrochemistry of 4.....   | 192        |
| 6.2.2      | Surface modification of gold nanoparticles by 4 .....   | 196        |
| <b>6.3</b> | <b>Conclusion .....</b>   | <b>201</b> |
| <b>6.4</b> | <b>Experimental details .....</b>   | <b>202</b> |
| 6.4.1      | Methods .....   | 202        |
| 6.4.2      | Syntheses .....   | 203        |
| 6.4.2.1    | C <sub>11</sub> SH .....  | 203        |
| 6.4.2.2    | $[P_2W_{17}O_{57}\{(TPY)(C_{11}SH)\}]$ (4) .....  | 203        |
| 6.4.2.3    | 4-NPs.....  | 204        |
| <b>6.5</b> | <b>References.....</b>  | <b>205</b> |
| <b>7</b>   | <b>Summary and outlook .....</b>  | <b>208</b> |
| <b>7.1</b> | <b>Comparison of key data .....</b>   | <b>208</b> |
| <b>7.2</b> | <b>Final conclusions and outlook .....</b>  | <b>211</b> |

## Abbreviations

bpy – 2,2'-Bipyridine

calc – Calculated

CHN – Carbon, Hydrogen and Nitrogen (Elemental Analysis)

CV – Cyclic Voltammetry/Voltammogram

$D_h$  – Hydrodynamic diameter

DLS – Dynamic Light Scattering

DMA – Dimethylammonium

dmbpy – 4,4'-Dimethyl-2,2'-bipyridine

DMF – Dimethylformamide

DMSO – Dimethylsulfoxide

DPV – Differential Pulse Voltammetry/Voltammogram

ESI-MS – Electrospray Ionisation Mass Spectrometry

ICP-OES – Inductively Coupled Plasma- Optical Emission Spectrometry

HER – Hydrogen evolution reaction

IL – Intraligand

IR – Infra-red

IVCT – Intravalence charge transfer

LMCT – Ligand-to-metal charge transfer

MLCT – Metal-to-ligand charge transfer

MW – Molecular Weight

NMR – Nuclear Magnetic Resonance

obs – Observed

POM – Polyoxometalate

PPA – 3-Phosphonopropionic acid

RT – Room temperature

SAM – Self-assembled monolayer

TBA – Tetra-*n*-butylammonium

TEA – Triethylamine

TEM – Transmission Electron Microscopy

TGA – Thermogravimetric Analysis

TMSBr- Trimethylsilyl bromide

tpy – 2,2':6',2''-Terpyridine

TRIS – Tris(hydroxymethylmethane)  $(-(\text{OCH}_2)_3\text{C}-)$

UV-Vis – Ultraviolet-Visible

## Nomenclature, colour scheme

Synthesised hybrid POMs and free phosphonic acids are given in **bold**, e.g., **TPY**, **C<sub>18</sub>**, **1**, **Ru-1**

Organophosphonate ligand groups covalently attached in hybrid POM structures (RPO(O<sup>-</sup>)<sub>2</sub>) are given in *italics*, e.g., *TPY*, *C<sub>18</sub>*, *RuTPY*

Formulae for POM anions and POM hybrid anions are given in square brackets “[ ]”, and may not be assigned charge for simplicity as they are to be considered primarily in terms of the anionic molecular structure.

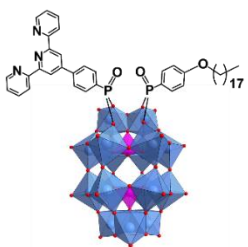
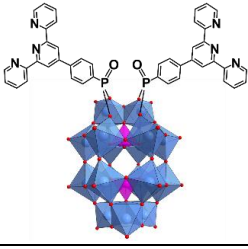
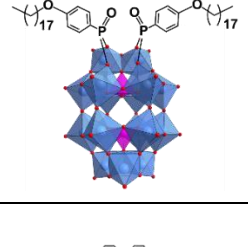
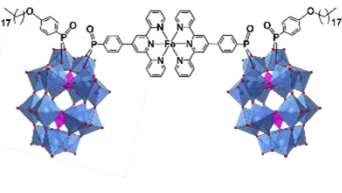
All POM and hybrid POM structures in figures and schemes are shown without their counter-cations or solvating molecules for simplicity.

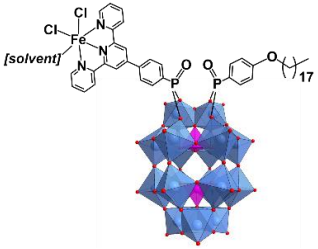
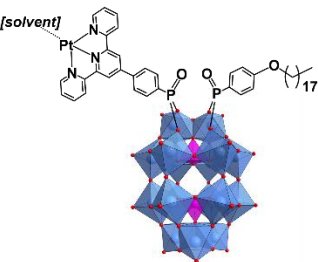
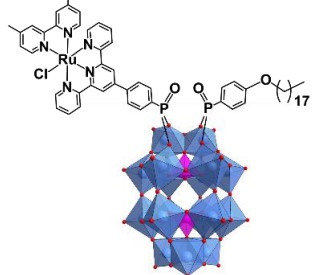
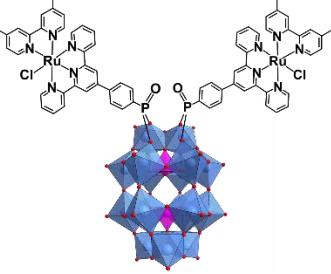
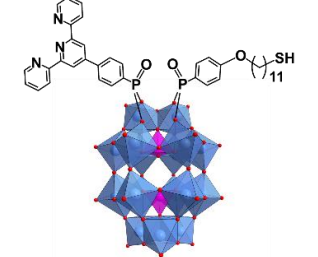
Unless specified, the general colour scheme for polyhedral representations of POM structures in this thesis is as follows. Most polyhedral representations in this work are of polyoxotungstate structures, in which: blue polyhedra = {WO<sub>6</sub>}; magenta polyhedra = {PO<sub>4</sub>}; red spheres = oxygen. Others: plum polyhedra = {MoO<sub>6</sub>}; yellow polyhedra = {MnO<sub>6</sub>}; orange polyhedra = {SiO<sub>4</sub>}; dark blue-grey polyhedra = {VO<sub>6</sub>}; grey spheres = carbon; magenta spheres = phosphorus.

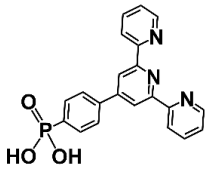
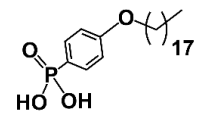
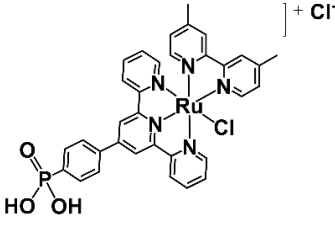
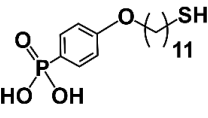


## List of compounds

The main compounds of focus (hybrid POMs and organophosphonate ligands) in this thesis are listed here, including their molecular structure, full molecular formula, and abbreviated/code names by which they are referred to in the text.

| <b>Hybrid POMs</b>                       |   |
|--|---|
| <b>Code name &amp; anionic structure</b> | Full molecular formula (with cations)<br><b>Shorthand formula using ligand code names</b>   |
| <b>1</b>                                 | <br>$\text{K}_4(\text{C}_2\text{H}_8\text{N})_2[\text{P}_2\text{W}_{17}\text{O}_{57}\{(\text{PO}_3\text{C}_{21}\text{H}_{14}\text{N}_3)(\text{PO}_4\text{C}_{24}\text{H}_{41})\}],$<br>$[\text{P}_2\text{W}_{17}\text{O}_{57}\{(\text{TPY})(\text{C}_{18})\}]$                              |
| <b>2</b>                                 | <br>$(\text{C}_2\text{H}_8\text{N})_6[\text{P}_2\text{W}_{17}\text{O}_{57}\{(\text{PO}_3\text{C}_{21}\text{H}_{14}\text{N}_3)_2\}],$<br>$[\text{P}_2\text{W}_{17}\text{O}_{57}\{(\text{TPY})_2\}]$   |
| <b>3</b>                                 | <br>$\text{K}_2(\text{C}_2\text{H}_8\text{N})_4[\text{P}_2\text{W}_{17}\text{O}_{57}\{(\text{PO}_4\text{C}_{24}\text{H}_{41})_2\}],$<br>$[\text{P}_2\text{W}_{17}\text{O}_{57}\{(\text{C}_{18})_2\}]$  |
| <b>Fe-1</b>                              | <br>$\text{K}_7(\text{C}_2\text{H}_8\text{N})_3$<br>$[\text{Fe}\{\text{P}_2\text{W}_{17}\text{O}_{57}(\text{PO}_3\text{C}_{21}\text{H}_{14}\text{N}_3)(\text{PO}_4\text{C}_{24}\text{H}_{41})\}_2],$<br>$[\text{Fe}\{\text{P}_2\text{W}_{17}\text{O}_{57}(\text{TPY})(\text{C}_{18})\}_2]$ |

|      |   |   |
|------|---|---|
| Fe-2 |    | $\text{K}_3(\text{C}_2\text{H}_8\text{N})_3$ $[\text{P}_2\text{W}_{17}\text{O}_{57}\{\text{FeCl}_2(\text{H}_2\text{O})(\text{PO}_3\text{C}_{21}\text{H}_{14}\text{N}_3)(\text{PO}_4\text{C}_{24}\text{H}_{41})\}],$ $[\text{P}_2\text{W}_{17}\text{O}_{57}(\text{Fe-TPY})(\text{C}_{18})]$                                    |
| Pt-1 |    | $\text{K}(\text{C}_2\text{H}_8\text{N})_3$ $[\text{P}_2\text{W}_{17}\text{O}_{57}\{(\text{PO}_3\text{C}_{21}\text{H}_{14}\text{N}_3\text{Pt}(\text{C}_3\text{H}_7\text{ON})(\text{PO}_4\text{C}_{24}\text{H}_{41}))\}].\text{C}_3\text{H}_7\text{ON},$ $[\text{P}_2\text{W}_{17}\text{O}_{57}(\text{Pt-TPY})(\text{C}_{18})]$ |
| Ru-1 |   | $\text{K}_2(\text{C}_2\text{H}_8\text{N})_3$ $[\text{P}_2\text{W}_{17}\text{O}_{57}\{(\text{PO}_3\text{C}_{21}\text{H}_{14}\text{N}_3\text{Ru}(\text{C}_{12}\text{H}_{12}\text{N}_2)\text{Cl})\}(\text{PO}_4\text{C}_{24}\text{H}_{41})]$ $[\text{P}_2\text{W}_{17}\text{O}_{57}(\text{RuTPY})(\text{C}_{18})]$               |
| Ru-2 |  | $\text{K}_4[\text{P}_2\text{W}_{17}\text{O}_{57}\{(\text{PO}_3\text{C}_{21}\text{H}_{14}\text{N}_3\text{Ru}(\text{C}_{12}\text{H}_{12}\text{N}_2)\text{Cl})_2\}]$ $[\text{P}_2\text{W}_{17}\text{O}_{57}(\text{RuTPY})_2]$  |
| 4    |  | $\text{K}_5(\text{C}_2\text{H}_8\text{N})[\text{P}_2\text{W}_{17}\text{O}_{57}\{(\text{PO}_3\text{C}_{21}\text{H}_{14}\text{N}_3)(\text{PO}_3\text{C}_{17}\text{H}_{26}\text{SH})\}]$ $[\text{P}_2\text{W}_{17}\text{O}_{57}(\text{TPY})(\text{C}_{11}\text{SH})]$  |

| Organophosphonate ligands |   |                                 |
|---------------------------|---|---------------------------------|
| Code name & structure     |   | Full molecular formula          |
| TPY                       |    | $C_{21}H_{16}N_3O_3P_1$         |
| C <sub>18</sub>           |    | $C_{24}H_{43}O_4P_1$            |
| RuTPY                     |   | $C_{33}H_{28}N_5O_3P_1Ru_1Cl_2$ |
| C <sub>11</sub> SH        |  | $C_{17}H_{29}O_4P_1S_1$         |

## Abstract

The development of accessible synthetic procedures in the preparation of multifunctional hybrid materials which allow fine control in the tuning of their structure and properties is an ongoing challenge. Access to asymmetrically organofunctionalised hybrid polyoxometalates (POMs) could lead to new molecular materials with multiple or modular functionality which can be tailored towards highly specific or advanced applications. Herein, an effective design strategy to the preparation of new asymmetric bi-functionalised hybrid polyoxometalates is presented and the characterisation of the structures and properties of the new multifunctional hybrid compounds is discussed.

A simple, inexpensive and high-yielding one-pot synthetic approach to the isolation of a new asymmetric hybrid POM based on the Wells–Dawson anion is presented in Chapter 3. The development of the synthetic methodology and the characterisation of the unique asymmetric structure of the hybrid molecule is described.

The unique multifunctionality of the modular system, derived from the redox-active Wells-Dawson polyanion and the two, distinct appended organophosphonate moieties with contrasting physical properties, is investigated in Chapter 4. The combined metal-coordinating and self-assembling functions are effectively demonstrated by the solvent-dependent self-assembly into redox-active supramolecular aggregates.

The incorporation of transition metal functionality into the asymmetric hybrid POM at the appended chelating group is explored in more detail in Chapter 5 in which two synthetic approaches are presented. First, a straightforward postfunctionalisation approach of metal coordination directly to the chelating ligand is demonstrated by the coordination of a platinum(II) ion. A modified one-pot synthesis is presented as a second approach, in which a ruthenium(II) polypyridyl complex is prepared as organophosphonate ligand that can be directly grafted to the cluster anion to isolate a new asymmetric hybrid derivative. The new Pt(II) and Ru(II) functionalised asymmetric hybrid POMs are shown to exhibit rich electro- and photo-chemical

properties, in addition to solvent-dependent self-assembly, and display promise in the development of new catalytically-active soft nanomaterials.

The final chapter explores the introduction of further complexity into the asymmetric hybrid POM structure through the addition of a terminal functionality which enables its covalent immobilisation. A new one-pot synthesis is presented to prepare an asymmetric hybrid POM which comprises a thiol-terminated aliphatic chain moiety, and the direct grafting of the hybrid POM onto the surfaces of gold materials is demonstrated through electrochemical studies on the redox-active self-assembled layer and the characterisation of composite gold nanoparticles.

This work ultimately provides an accessible modular approach that is promising for the creative design and development of new multifunctional POM-based hybrid molecules, supramolecular systems and soft-nanomaterials.

# 1 Introduction

## 1.1 Introduction to organic-inorganic hybrid polyoxometalates

First reported nearly 200 years ago,<sup>[1]</sup> polyoxometalates (POMs) now attract substantial attention in multidisciplinary areas of science, with applications in diverse fields including catalysis,<sup>[2]</sup> materials science<sup>[3]</sup> and medicine.<sup>[4-5]</sup> POMs are a class of discrete metal-oxo cluster anions, or polyoxoanions, constructed from early transition metals most commonly of group 5 and 6 in their higher oxidation states, particularly Mo(VI), W(VI), V(V).<sup>[6]</sup> Their vast structural diversity, excellent stability and versatile chemical and physical properties make them ideal building blocks for functional materials.<sup>[7-8]</sup>

### 1.1.1 Brief introduction to polyoxometalates

#### 1.1.1.1 General POM structure and assembly

As a large, structurally diverse class of compounds, polyoxoanions are often categorised broadly into several main subsets considering general structure and composition.<sup>[8]</sup> Isopolyoxoanions are comprised exclusively of a metal oxide framework, represented by the general formula  $[M_mO_y]^{n-}$ , where M is the metal atom. In heteropolyoxoanions,  $[X_xM_mO_y]^{n-}$ , one or more additional heteroanions,  $\{XO_y\}^{n-}$ , are incorporated in the metal oxide structure where X is often a main group element such as P, S or Si, and distinct structures are defined by the ratio of X/M.

The metal oxide framework is fundamentally built from  $\{MO_x\}$  coordination polyhedra, where x can be from 4 to 7, but is most commonly 6 in a pseudo-octahedral arrangement. Heteroanions which may be included can also exist in various coordination numbers, including 4 (tetrahedral) in the Wells-Dawson and Keggin structures, and 6 (octahedral) in the Anderson-Evans (or, "Anderson")

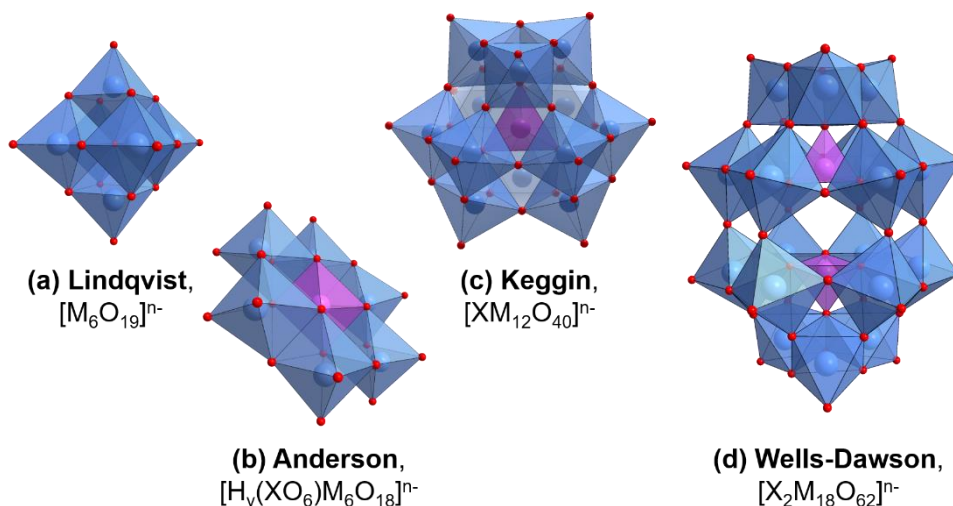


**Figure 1.** Polyhedral representations of some classical iso- and hetero- polyanion clusters: (a) Lindqvist  $[M_6O_{19}]^{n-}$  (typically  $M = W, V, Mo, Nb$ ); (b) Anderson  $[H_y(XO_6)M_6O_{18}]^{n-}$  (typically  $X = 1st\ row\ transition\ metal; M = W, V, Mo, y = 0-6, n = 2-8$ ); (c) Keggin  $[XM_{12}O_{40}]^{n-}$  (typically  $X = main\ group\ element, M = W, V, Mo, n = 3-5$ ); (d) Wells-Dawson  $[X_2M_{18}O_{62}]^{n-}$  (typically  $X = main\ group\ element, M = W, V, Mo, n = 4-8$ ). Colour code: blue polyhedra =  $\{MO_6\}$ ; magenta polyhedra =  $\{XO_4\}$ ; red spheres = oxygen. Counter-cations are omitted for clarity.

structure (Fig.1). Because POMs are anionic in nature, they are in combination with charge-balancing cations, and the complete structure is considered as collectively: the polyanion cluster, counterions, and solvating molecules of the hydration shell.

The discrete cluster formations of polyoxometalates are governed by a complex balance of coulombic forces involving the radii of atoms in the  $\{MO_x\}$  polyhedra and the polyhedral linkages. Suitably sized ionic radii and accessibility of empty d-orbitals in the transition metal centres are fundamental to the allowed high coordinate bonding to hard ligand oxygen atoms, including the formation of terminal metal-oxygen double bonds via  $d\pi-p\pi$  interactions. Fitting these requirements, the metal ions in polyoxoanions are most often early transition metals from groups V and VI in their highest oxidation state, possessing a  $d^0$  or  $d^1$  configuration.

## 1. Introduction

The oxo-ligands are positioned at the vertices of each polyhedral  $\{MO_x\}$  unit, bonded to the central addenda metal atom in either bridging or terminal modes (Fig.2a). POMs are generally formed via acid-mediated condensation reactions of these  $\{MO_x\}$  polyhedra, resulting in their polymerisation in which they connect by corner-, edge-, or very rarely, face- sharing modes through bridging M-O bonds (Fig.2b). Fundamentally, a strong *trans* influence of the unshared terminal M-O bonds restricts the total number of oxo-groups in each polyhedron that can be in a terminal position. In octahedral  $\{MO_6\}$  addenda commonly found in iso- and hetero-polyanions, one terminal oxo-ligand is most often observed but a maximum of two unshared oxygen atoms are known to be observed by “Lipscomb’s Principle”,<sup>[9]</sup> with the remaining bridging oxygen atoms shared with other addenda. The terminal M=O bonds at the cluster surface are significantly polarised towards the addenda atom, due to a displacement of the metal centre towards the terminal oxo-ligand. This is a result of the *trans*-effect weakening the M-O bond opposite and distorting the octahedron. (Fig.2a). Crucially, this results in a significant reduction in basicity at the polyoxoanion surface that limits polymerisation of the polyhedra by further protonation, confining

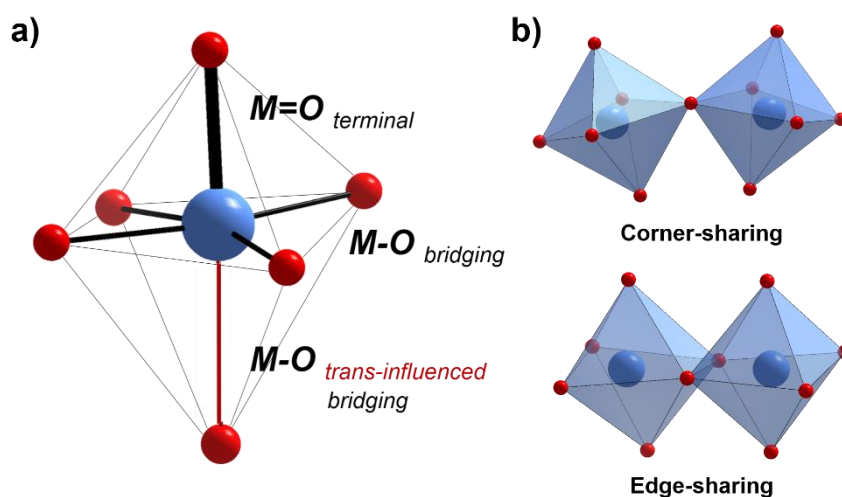


**Figure 2. a):** The most common type of addenda observed in POM structures- an  $\{MO_6\}$  octahedral unit, comprising one unshared terminal oxygen atom and five bridging oxygen atoms that are shared with other metal or hetero-atom addenda; **b)** The two common binding modes of  $\{MO_x\}$  polyhedra after condensation.



## 1. Introduction

---

the extent of condensation of the metal oxide framework, and is the explanation for their existence as molecular species.<sup>[6, 10]</sup>

POMs are generally prepared by self-assembly in a “one-pot” synthesis, involving acidification of an aqueous solution containing the metal oxo anions in the form of salt, such as  $\text{Na}_2\text{WO}_4$  or  $\text{NaHVO}_3$ . As the solution is acidified and the pH decreases, the metal oxide fragments increase in nuclearity and protonate to give oxide-hydroxide compounds, which then sequentially condense into intermediate building units, and finally, into the polyoxoanion structure (Fig.3).<sup>[6]</sup> In the case of heteropolyanion synthesis, a salt of the heteroanion is additionally added, such as a phosphate or silicate, which acts as a templating anion for which the metal oxide polyhedra condense around. The underlying self-assembly processes in POM cluster synthesis are highly complex, the mechanisms and considerable controlling factors of which remain of research interest.<sup>[11-13]</sup>

As well as the type of metal oxide anion, and heteroanion if included, numerous experimental parameters can be influential on the self-assembly and nature of the resulting POM, such as the relative concentrations (or stoichiometric ratio, M/X) of the included anions, pH, temperature, solvent, pressure and the presence of any

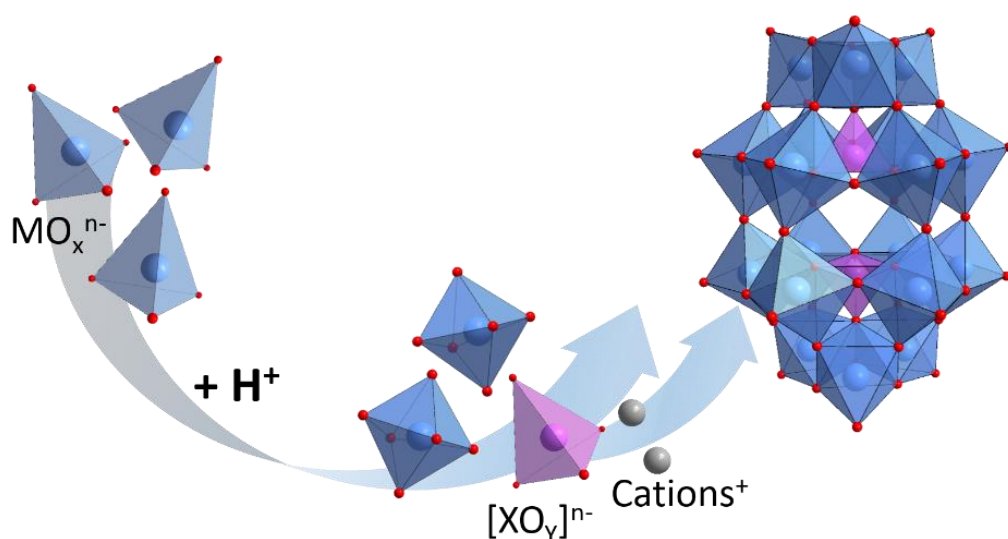


**Figure 3.** Schematic of the general POM self-assembly process by acid-mediated condensation of metal-oxo fragments. Colour code: blue polyhedra =  $\{\text{MO}_x\}^{n-}$ ; magenta polyhedra =  $\{\text{XO}_y\}^{n-}$ ; red spheres = oxygen; grey spheres =  $\{\text{cation}\}^+$ .

## 1. Introduction

---

ligands or reducing agents.<sup>[7, 14]</sup> Notably, the choice of counterion is important for controlling solubility and for successful crystallisation, and POMs are generally isolated in the solid state from solution by precipitation after the addition of such, most commonly of alkaline (usually Na<sup>+</sup> or K<sup>+</sup>), ammonium or organic tetraalkylammonium salts. Many studies have demonstrated that the role of the counterion is much more extensive, including influencing reactivity and assembling/aggregation behaviour.<sup>[15-16]</sup>

The high stability of POMs in solution is in view of their ability to retain their structural integrity by withstanding any transformation or degradation from it. However, the formal removal of one or more addenda metal-oxo units from POM clusters can be used to prepare “lacunary” POMs, a sub-class of defect-type structures, in which one or more cavities with unshared bridging oxygen atoms are left. The formation of lacunary species is typically through hydrolysis by pH decomposition, often by the treatment of a POM with a controlled quantity of base, but can also be achieved by one-pot reactions combining monomeric addenda and heteroanions under precise pH control.<sup>[17-18]</sup> Lacunary POM structures differ from complete POMs in charge, electronic properties, and reactivity, in addition to shape, and are often stable as isolated species. Importantly, the vacant site(s) open up opportunities for post-modification by metal ion binding or covalent grafting to organic or organometallic compounds, to prepare substituted structures and organic-inorganic hybrid POM complexes (see 1.1.2).<sup>[6, 19]</sup>

### 1.1.1.2 The Wells-Dawson and Keggin structures

The heteropolyanion clusters are particularly well-explored due to their inherently greater stability in comparison to isopolyanions. These clusters include the well-known Keggin  $[XM_{12}O_{40}]^{n-}$  and Wells-Dawson  $[X_2M_{18}O_{62}]^{n-}$  clusters, which are researched extensively for their redox properties and catalytic applications.<sup>[20]</sup> The phospho- molybdate and tungstate structures are the most typical compositions of both, the latter of which are the clusters of focus in the work in this thesis.

The Keggin is the best known and simplest structure of the heteropolyanions, first determined in 1933 by using the  $\alpha$ -phosphotungstate anion  $[PW_{12}O_{40}]^{3-}$  (Fig.4).<sup>[21]</sup> It

## 1. Introduction

is comprised of a central tetrahedral heteroanion,  $\{XO_4\}^-$ , that is surrounded by 12 octahedral  $\{MO_6\}$  polyhedra that are arranged in 4 units comprised of three grouped octahedra,  $\{M_3O_{13}\}$ . The Keggin structure can exist as five isomers,  $\alpha$ ,  $\beta$ ,  $\gamma$ ,  $\delta$  and  $\epsilon$ , due to the different orientations of the  $\{M_3O_{13}\}$  units possible by  $60^\circ$  rotations about three symmetry axes.<sup>[22]</sup>

First fully characterised almost 70 years ago,<sup>[23]</sup> the Wells-Dawson (or simply, "Dawson") cluster is closely related to the Keggin structure, as it can be seen as two fused tri-lacunary  $\{XM_9\}$  Keggin fragments (Fig.4). The structure comprises two internal heteroanion centres that are most often tetrahedral, each linked to one  $\{M_3O_{13}\}$  unit and to three dimetallic units which are formed from two condensed octahedra,  $\{M_2O_{10}\}$ . The trimetallic units form the two 'caps' of the Dawson cluster, located at the polar ends, whereas the dimetallic units form rings around each heteroanion to form the 'belt' of the cluster (Fig.5). Six terminal oxygen atoms are located on the polyhedra of the cap regions, and 12 are on those of the belt. Like the Keggin, the Dawson anion possesses symmetry elements that result in the occurrence of several structural isomers.<sup>[22]</sup> The  $\beta$ - and  $\gamma$ - isomers are derived from the most stable  $\alpha$ - isomer by the rotation of one or both  $\{M_3O_{13}\}$  caps respectively by  $60^\circ$  about

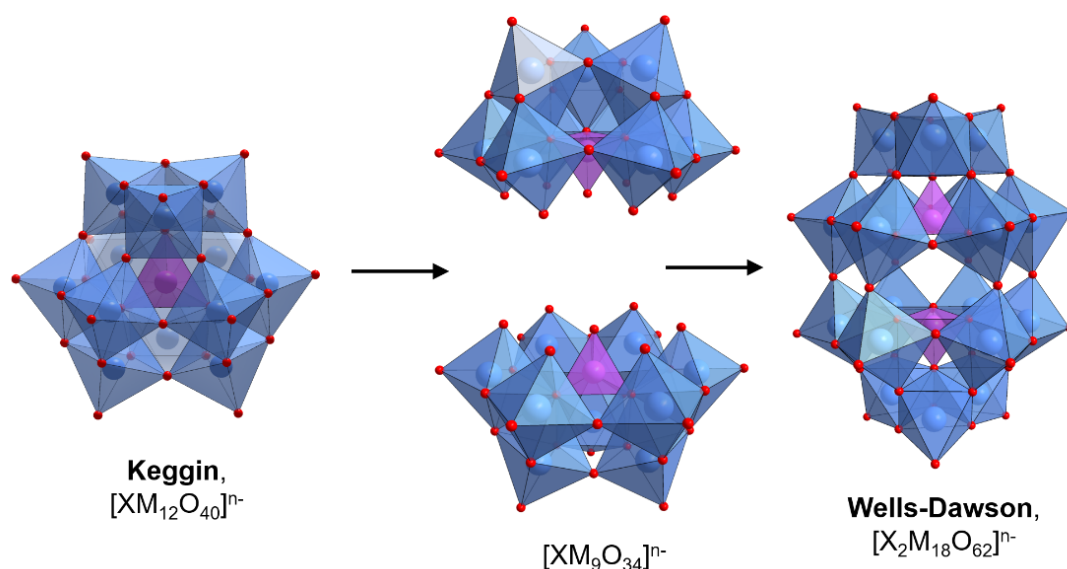


**Figure 4.** Polyhedral representation showing the relationship between the Keggin and Wells-Dawson structures.

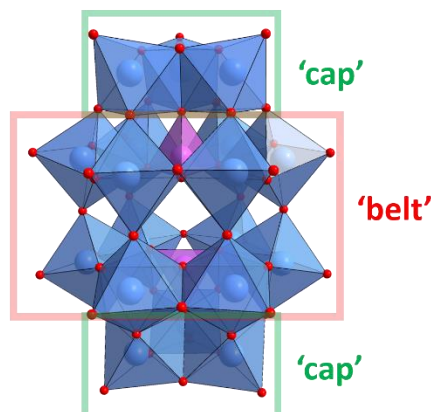


**Figure 5.** Polyhedral representation of the Dawson structure indicating the two types of polyhedral environment.

the  $C_3$  axis. From these, additional isomers,  $\alpha^*$ ,  $\beta^*$ , and  $\gamma^*$ , arise from the  $60^\circ$  rotation of one of the  $\{XW_9\}$  halves. However, only the  $\gamma^*$ - form has been experimentally observed.<sup>[24]</sup>

A large degree of variation is possible in the composition of the Keggin and Dawson heteropolyanion structures, in terms of the central heteroanion and addenda elements. The tungstate (VI), molybdate (VI) and vanadate (V) structures are the most widely studied, but many reported structures incorporate the metals as mixed addenda, or partially substitute addenda for other often metallic elements.<sup>[25-26]</sup> The main group heteroatoms P and Si are most common amongst others used such as S and As, and non-tetrahedral anions are also known in some non-classical structures.<sup>[7, 27]</sup>

The many lacunary structures of the Keggin and Dawson clusters form the largest and most well-studied group of lacunary polyanions,<sup>[6]</sup> due to their potential as platforms to prepare organic-inorganic hybrid compounds in a multitude of organofunctionalisations (see 1.1.2.2).<sup>[28]</sup> Mono-,  $\{XM_{11}\}$ , di-,  $\{XM_{10}\}$ , and tri-,  $\{XM_9\}$ , lacunary structures based on the Keggin cluster are known, most commonly derived from the P and Si templated cluster types, of which the tungstosilicates are generally more stable (Fig.6). The mono- and tri- lacunary structures can be accessible in several isomeric forms with respect to the isomer of the complete, or plenary, Keggin anion

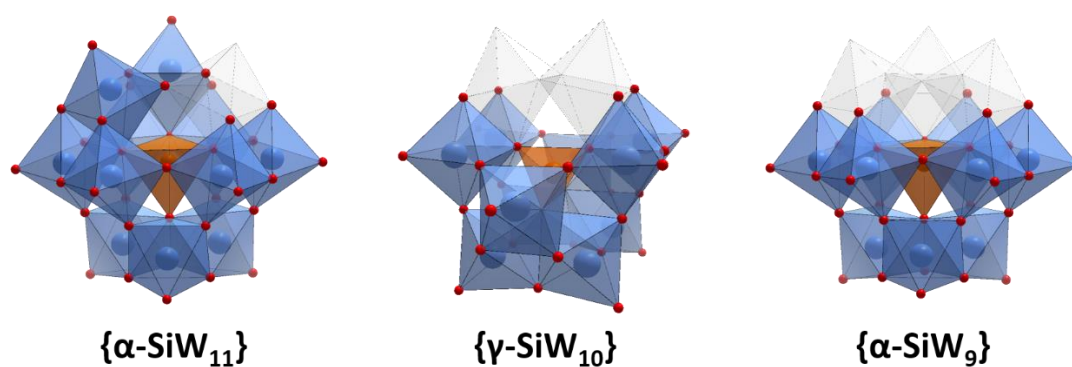


**Figure 6.** Polyhedral representations of selected isomers of mono-, di- and tri- lacunary structures based on the Si-templated Keggin anion.

they are structurally derived from, as well as in regard to the positions from which the addenda are removed. Di-lacunary  $\{W_{10}\}$  structures, although described for both phospho- and silico-tungstate Keggin anions, are much easier to prepare and isolate as stable species when derived from the Si analogue and exist in a single isomeric form ( $\gamma$ ).<sup>[29]</sup>

Fewer lacunary structures are accessible for the Dawson cluster with only the  $\alpha$ - $\{X_2W_{18}\}$  isomer capable of forming stable lacunary species, all of which are accessed

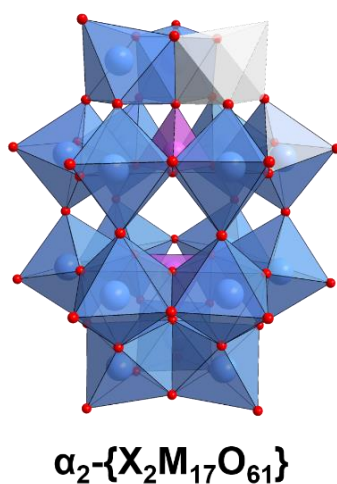


**Figure 7.** Polyhedral representation of one of the two isomers of the stable mono ( $\alpha$ )- lacunary Dawson structure.

## 1. Introduction

---

and isolated by base degradation of the complete structure.<sup>[30]</sup> The mono-lacunary structures are formed by the removal of a single metal, from either one of the two cap positions (Fig.7) or from one of the two belt positions, and can again possess positional isomerism. Additionally, less common tri-lacunary  $\{X_2M_{15}\}$  and hexa-lacunary  $\{X_2M_{12}\}$  structures can be formed by the removal of the three addenda of an entire  $\{M_3O_{13}\}$  cap or six addenda from a larger 'face' type unit  $\{M_6O_{14}\}$ , respectively.

### 1.1.1.3 Properties of POMs

The numerous properties and vast diversity in composition, structure, size and charge of POMs have attracted significant and continued interest in their applications in many fields. They can be considered as "soluble metal oxides", having often high solubility in a variety of polar solvent media due to their ability to form various interactions- hydrogen bonds, electrostatic, non-covalent and covalent.

The assembling behaviour of POMs as "building blocks" with uniform and tuneable architectures can be used in directing various nanostructures,<sup>[31-32]</sup> and in their incorporation into composite, polymer and film materials.<sup>[3, 33]</sup> Additionally, POMs may interact with biomolecules,<sup>[34-35]</sup> and in many studies have demonstrated to exhibit biological activity, finding emerging applications in drugs and biotechnology.<sup>[36-37]</sup>

Perhaps the most recognised and explored area of research and application of POMs is in catalysis,<sup>[2]</sup> for which the heteropolyacids, particularly those based on the Keggin and Dawson clusters, are the most widely used due to their acid-base properties and high redox activity. The Brønsted acidity of their protonated polyanions are used as strong acid catalysts in a broad range of reactions including esterification and hydrolysis.<sup>[38]</sup> Moreover, the electron-rich surface oxygen atoms on polyanions can act as basic sites, especially in highly charged lacunary structures, and can be used to attack electrophiles or abstract protons in many base-catalysed reactions.<sup>[39]</sup>

As there has been a growing interest in more recent years in the application of POMs in solving environmental issues,<sup>[40-41]</sup> they now draw substantial attention as catalysts in green energy generation, such as water oxidation and CO<sub>2</sub> reduction.<sup>[42]</sup> Key to these catalytic roles is the rich electrochemistry exhibited by many POMs. As they are

## 1. Introduction

---

comprised of a framework of highly, often fully ( $d^0$ ), oxidised transition metal ions, they have a unique capacity to store and transfer multiple electrons, and many can undergo rapid multi-electron redox processes whilst retaining structural stability, particularly the Dawson and Keggin clusters. As well as the redox-active metals in the POM framework, the electrochemistry of POMs is influenced by their charge density, geometry, and the nature of the counter-cations.

POMs are additionally well-known for their inherent photochemistry, which, coupled with their rich reversible redox chemistry renders them attractive photocatalysts.<sup>[43-44]</sup> They display characteristic strong absorption of UV light, mainly attributed to O  $\rightarrow$  M ligand-to-metal-charge transfer (LMCT) bands. On their photoexcitation, the promotion of an electron from a doubly occupied bonding orbital (the HOMO) of a terminal oxygen to an empty antibonding d-orbital (the LUMO) on the metal generates a radical centred on the oxo-ligand (Fig.8). This photo-excited species involves a short-lived triplet state that is more reactive both in oxidation and reduction in comparison to the ground state and is the basis of POM photocatalytic activity. Electron transfer (or proton-coupled electron transfer) from a suitable substrate can trap  $d^1$  electrons on the metal centres, forming the so-called “heteropoly blues”- mixed valence species marked by a distinctive blue colour due to a newly formed intervalence charge-transfer (IVCT) absorption band at around 700 nm.

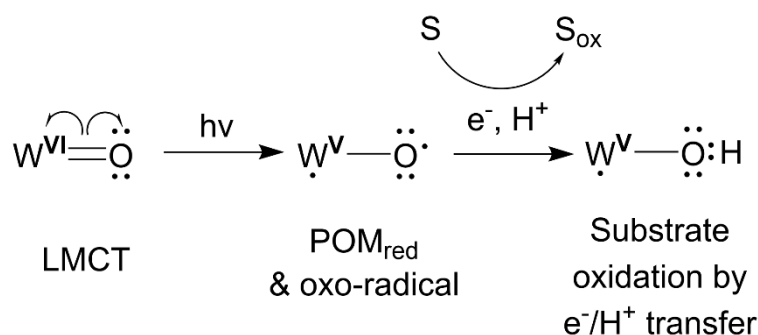


**Figure 8.** The photoreduction of a tungstate POM and the subsequent oxidation of a substrate.

### 1.1.2 Organofunctionalisation of POMs

The definition of a hybrid material is very broad, and they can be classified in terms of composition and interactions present between connected components, but is commonly considered to be a composite material comprised of two materials that are combined on a molecular scale, often one of which is organic in nature and the other inorganic.<sup>[45]</sup> Organic-inorganic hybrid chemistry attracts growing attention in the development of new functional materials in nanoscience and nanotechnology because of the potential in the combination of the physical and chemical properties of each constituent material.<sup>[46]</sup> Crucially, properties can be tailored in the designed structure and composition of each of the distinct organic and inorganic components and through their organisation or integration into a hybrid material. Specifically, the intrinsic properties of the molecular or nano building blocks can be enhanced in the resulting materials by synergistic effects, and additionally, new, and unusual properties and features can arise in the hybrid material that the individual components did not previously exhibit.

#### 1.1.2.1 Introduction to hybrid POMs

The rich inherent physical and chemical properties of POMs draw significant interest to them as highly versatile and functional inorganic components in hybrid systems. Importantly, exceptionally fine control is available at the molecular level during organic functionalisation of POM clusters, together with the immense structural diversity of POM clusters themselves, and so considerable opportunity to diversify and optimise them for a specific application is available. A brief overview of the synthetic strategies to combine organic moieties with POMs to prepare organic-inorganic hybrid POM compounds (or “hybrid POMs”), with a focus on covalent organofunctionalisation, is given here.

Fundamentally, the functionalisation of POMs is mainly via three approaches (Fig.9):

- 1) the substitution of addenda atoms in the vacant sites of lacunary POMs by transition metals, lanthanides or main-group elements;



## 1. Introduction

---

- 2) the non-covalent association of cationic inorganic or organic molecules and complexes with the POM; or
- 3) the covalent grafting of organic or organometallic species, either via substituted addenda atoms in the vacant sites of lacunary structures or to terminal oxygen atoms.

The latter two form the two classes of organic-inorganic hybrid POM, defined by the nature of the interaction between the POM and the associated components. Class I hybrids involve weak non-bonding interactions between components, such as electrostatic, van der Waals interactions, or hydrogen bonding. As such, the electrostatic association of common organic counter cations such as tetraalkyl ammoniums with POMs essentially comprises of a simple class I hybrid, but many studies have demonstrated much more complex cationic species in use, such as organometallic complexes, photosensitisers and ionic liquids.<sup>[47-49]</sup> However, these materials can be particularly sensitive to changes in solution (polarity, ionic strength, pH etc.), and the material properties are often largely determined by the cation and cannot be easily controlled through precise interactions.<sup>[50-51]</sup>

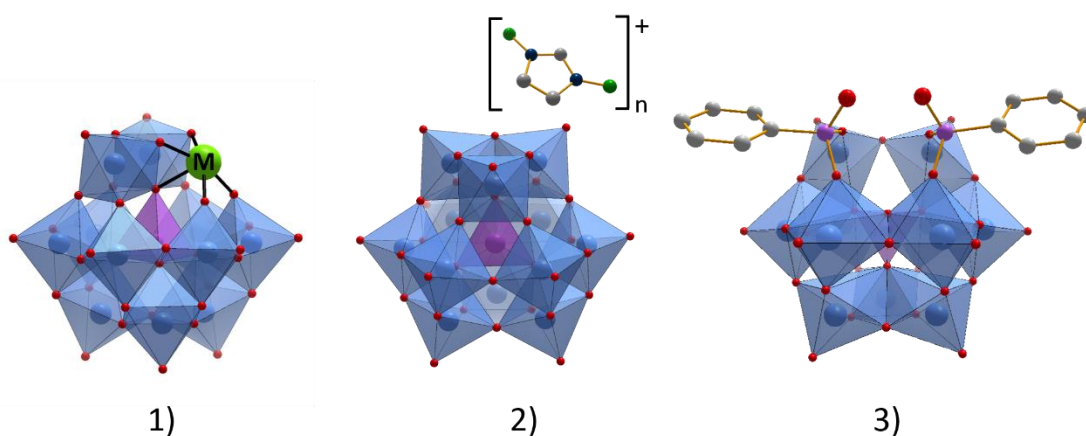


**Figure 9.** Polyhedral and ball and stick representations of the three types of functionalisation approaches to POMs.

## 1. Introduction

---

In class II hybrids, the organic components are linked with the POM via strong covalent bonds, and so although they are generally far more challenging to synthesise, they are much more robust than those of class I. Importantly, many properties can be fine-tuned through the covalent functionalisation, enabling a more effective design approach to functional materials. For the purposes of the work in this thesis, primary focus will be on class II organic-inorganic hybrid POMs.

### 1.1.2.2 Covalent organofunctionalisation strategies

Several extensive reviews on the broad scope of synthetic approaches to the covalent organofunctionalisation of POMs have been reported by Dolbecq,<sup>[19]</sup> Proust<sup>[52]</sup> and Parac-Vogt.<sup>[28]</sup> Organic ligands are often covalently attached to POMs in class II hybrids via the bonding of oxo-anions in the cluster, mainly in lacunary structures, to p-block elements such as N, Si, P, Ge and Sn, that are linked to the organic group. Alternatively, organic groups can be introduced via coordination to d- and f-block elements that are similarly incorporated into a vacancy or grafted to the cluster surface, but this type of covalent functionalisation will not be discussed further.

The organofunctionalisation of isopolyoxometalates is mainly via nitrogen-based bridging groups, bonded directly to metal addenda to replace oxo ligands. Organoimido groups are most common, but organo-azido, -hydrazido and -diazenido bridges are also well reported. Comparatively, the organic groups reported for the functionalisation of the heteropolyoxometalates, particularly the Keggin and Dawson clusters, are much more diverse. Herein, the common covalent organofunctionalisation modes of the heteropolyoxometalates are briefly overviewed.

One of the most largely used organic groups used in covalent functionalisation is alkoxides. The use of triols is by far the most common, particularly those based on tris(hydroxymethyl)alkanes. Although they have been used to functionalise a range of POM clusters, including mixed-addenda Dawson structures ( $[P_2W_{15}V_3O_{62}]^{9-}$ ),<sup>[53]</sup> they are most often attributed to the Anderson cluster, particularly polyoxomolybdates  $[XMo_6O_{18}\{(OCH_2)_3CR\}_2]^{n-}$  ( $X = Mn^{III}, Al^{III}, Cr^{III}, Fe^{III}, Co^{III}$ ).<sup>[54]</sup> Tris(hydroxymethyl)alkane Anderson hybrids are formed via a condensation or esterification of hydroxy or alkoxo

## 1. Introduction

groups with the bridging oxo ligands of the central octahedral heteroanion  $\{XO_6\}$  in the POM structure to form direct C-O-M bonds, typically forming a bifunctionalised structure by “capping” both faces of the cluster (Fig.10). The tris(hydroxymethyl)methane group  $-(OCH_2)_3C-$ , TRIS) has been used commonly as a postfunctionalisation platform when terminated by a reactive group that is available for reaction to build on the alkoxo ligand.<sup>[28]</sup>

The functionalisation of the Keggin and Dawson structures is mainly achieved via their lacunary species, particularly of the tungstate structures, as lacunary structures of molybdates and vanadates are uncommon. In these, one  $\{MO\}$  or several metal polyhedra units  $\{M_xO_{2x}\}$  have been formally removed from the cluster by pH-controlled degradation. The unshared oxygen atoms localised at the surface of the cavity, or “lacuna”, have increased nucleophilicity, and therefore are more reactive to electrophilic groups.

Organotin compounds are one such group that can be installed into the lacuna site(s), and organostannyl hybrids are some of the most extensively developed. Organotin

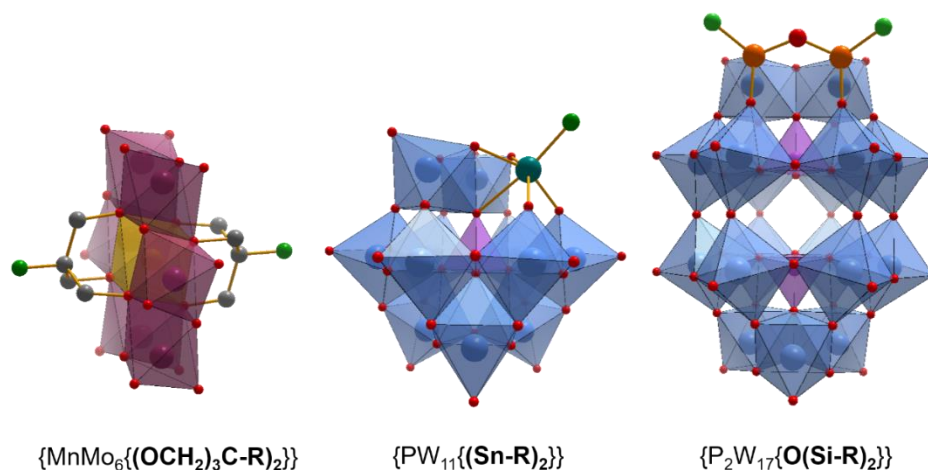


**Figure 10.** Polyhedral and ball and stick representations of hybrid heteropolyxometalates showing examples of three common organofunctionalisation strategies. Colour code: blue polyhedra =  $\{WO_6\}$ ; plum polyhedra =  $\{MoO_6\}$ ; magenta polyhedra =  $\{PO_4\}$ ; yellow polyhedra =  $\{MnO_6\}$ ; red spheres = oxygen; grey spheres = carbon; orange spheres = silicon; teal sphere = tin; green spheres = R group.

## 1. Introduction

---

trihalides are usually used as an electrophilic reagent, reacted commonly to install a single tin centre with one pendant R-group into a lacunary site via bonding to four lacuna oxo groups and one heteroanion oxo group (Fig.10).<sup>[55]</sup> Organogermanium functionalisation is very similar in nature, but much fewer examples are reported in comparison to the organotin analogues.<sup>[56]</sup>

Another commonly used organic group to modify lacunary Keggin and Dawson clusters are organosilicates, for which trichlorosilanes or trialkoxysilanes are used as reagents, in which Si-Cl or Si-OR bonds are hydrolysed. Many organosilyl hybrids have been reported using the mono-, di- and tri- lacunary structures of the Keggin POM, in which varying numbers of silicon centres can be incorporated,<sup>[57-58]</sup> whereas for the Dawson, only functionalised monolacunary structures have been reported. In such structures, two organosilyl groups are attached by the grafting of each silicon centre to one pair of the lacuna oxo-groups and they are linked via a siloxane bridge (-Si-O-Si-) across the vacant site (Fig.10).<sup>[59-60]</sup>

Last to mention are organophosphonate and organoarsenate derivatives, which have similarity in terms of reactivity and bonding mode, although very few examples of the latter are reported.<sup>[61]</sup> Unlike the organosilyl derivatives,<sup>[6]</sup> only two phosphonate groups have been reported to occupy vacant sites on a single cluster, whether in the mono-, di- or tri-lacunary structures of Keggin clusters and in mono-lacunary Dawson clusters (Fig.11).<sup>[61-64]</sup> As such, two organophosphonate ligands are introduced into a vacant site via the reaction of the pairs of nucleophilic oxoanions with phosphonic dichloride ( $\text{RPOCl}_2$ ) or phosphonic acid ( $\text{RPO(OH)}_2$ ) groups, and the latter requires additional stoichiometric acid as a catalyst for the condensation reaction. Reports of organophosphonate hybrids have accelerated in recent years due to interest in the strong electronic conjugation between the organic component and the POM cluster via the phosphonate linker,<sup>[65]</sup> which is discussed further below.

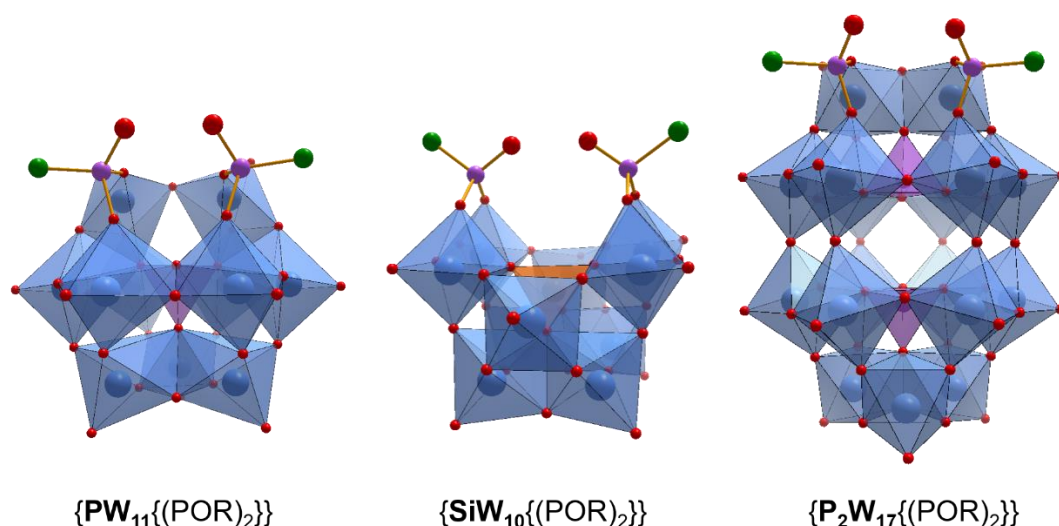


**Figure 11.** Polyhedral and ball and stick representations of organophosphonate hybrid Keggin and Dawson clusters. Colour code: blue polyhedra =  $\{\text{WO}_6\}$ ; magenta polyhedra =  $\{\text{PO}_4\}$ ; orange polyhedra =  $\{\text{SiO}_4\}$ ; red spheres = oxygen; magenta spheres = phosphorus; green spheres = R group.

#### 1.1.2.2.1 Organophosphonate hybrids - tuneable electronic structure

Functionalisation of the redox-rich Keggin and Dawson clusters by organophosphonate chemistry attracts particular attention because of the effective tuneability in the electronic properties of the hybrid system through the design of the organophosphonate group.

In the first electrochemical study on an organophosphonate functionalised Dawson by Boujtita *et al.*, it was shown that the first and second of the four reversible redox processes of the phenylphosphonate hybrid,  $[\text{P}_2\text{W}_{17}\text{O}_{57}\{(\text{PO}_3\text{C}_6\text{H}_5)_2\}]$ , were shifted positively relative to the “parent” Dawson  $[\text{P}_2\text{W}_{18}\text{O}_{62}]$  ( $\{\text{P}_2\text{W}_{18}\}$ ), and significantly more so than the phenylsiloxane analogue (in which the silyl group actually has an inverse effect on the redox potentials).<sup>[66]</sup> This indicated the strong inductive effects of the phosphonate group in a hybrid cluster, and many studies exploring functionalisation via phosphonate linkers have emerged since, including perylene and porphyrin moieties.<sup>[67-68]</sup>

## 1. Introduction

In thorough studies by Fujimoto and Cameron *et al.*, the frontier orbital energies of organophosphonate hybrid Dawson POMs were shown to be tuneable by the electron-withdrawing nature of the aryl organophosphonate ligand (Fig.12). Electron density in the HOMO and LUMO levels were shown to be delocalised across the POM and the ligand  $\pi^*$  orbitals, indicating inductive and resonance effects at play.<sup>[64]</sup> Redox potentials of the hybrids were positively shifted in relation to the parent cluster  $\{P_2W_{18}\}$ , due to the lowered LUMO and reduced HOMO-LUMO gap, and the photochemistry of the hybrids was also altered, with absorption bands shifting to tail in the visible region. The degree of these effects on the electrochemistry and photochemical reactivity of the hybrid POM was more so when the organophosphonate linkers had stronger electron-withdrawing effects (Fig.12).<sup>[69]</sup>

In more recent work, Cameron *et al.* explored the postfunctionalisation of a organophosphonate hybrid Dawson by the controlled addition of various transition metals, which coordinate at neighbouring P=O sites to form new dimeric hybrid POM complexes.<sup>[70]</sup> These interesting coordination properties of bis-organophosphonyl POM hybrids had been observed previously only in trilacunary Keggin derivatives.<sup>[61, 71]</sup> This metal-functionalisation demonstrated to further influence the Dawson

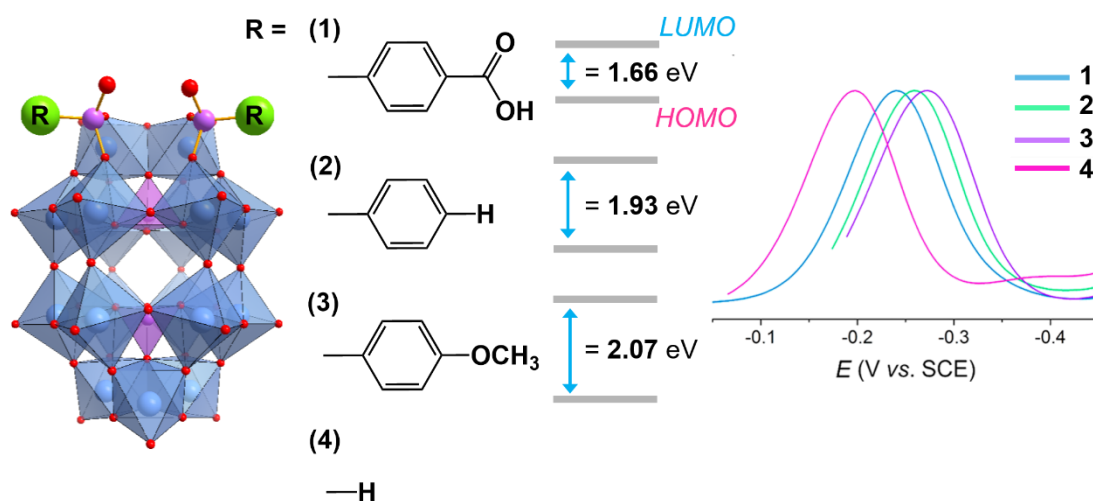


**Figure 12.** From left: Structural representation of organophosphonate hybrid POMs 1–4 showing the different substituent R-groups, the respective HOMO-LUMO energy gaps, and differential pulse voltammograms highlighting the first reduction wave of each species (current plotted on an arbitrary scale to aid comparison). Adapted from reference 69.

## 1. Introduction

---

cluster's electronic structure and photoactivity. Such new assemblies show potential for application in which the tuneable electrochemical and photochemical properties of the POM can be combined with the versatile design approaches available to hybrid POM and transition metal chemistry.

### 1.2 Functional hybrid POM systems

The intrinsic physical, chemical, and electronic properties of POMs can be tuned by the direct covalent attachment of organic functions, for which diverse organofunctionalisation strategies are available.<sup>[19]</sup> Furthermore, hybrid POMs can be suitable molecular platforms for postfunctionalisation, when bearing reactive sites on their organic appendages that allow further modification of the hybrid structure by covalent bonding to other organic molecules or by the coordination of metallic ion species. A variety of postfunctionalisation strategies, including amide and ester bond formations, metal-catalysed coupling reactions, and polymerisations, have been applied to multitudes of hybrid POMs in the literature, as recently summarised by Anyushin *et al.*,<sup>[28]</sup> demonstrating the complexity and immense extent of the opportunities that are available for POM functionalisation.

Accordingly, the covalent attachment of many functional molecular units, including organometallic complexes,<sup>[72]</sup> dyes<sup>[67, 73]</sup> and biomolecules,<sup>[74-75]</sup> to POMs has been achieved. Additionally, the combination of suitable organic groups with POMs has been used to configure them to undergo self-assembly, extended coordination, surface immobilisation, polymerisation and biological incorporation into new materials and devices.<sup>[52, 76]</sup> Covalent hybridisation, therefore, provides considerable opportunity for material properties at both the molecular and supramolecular levels to be controlled and tailored to the envisaged application, and a selection of notable reported examples of functional hybrid POM systems are highlighted herein.

#### 1.2.1 Combining properties with appended photoactive subunits

The controlled design of molecular photoactive systems can be used to develop highly active materials for photovoltaics, photocatalysis and solar energy conversion.<sup>[77-79]</sup>

## 1. Introduction

---

For the latter, multi-component systems are necessary that are capable of both visible light absorption and efficient multi-electronic processes, facilitated by charge accumulation on an appropriate reaction centre.<sup>[80]</sup> The combination of all required functions into one molecular photosensitiser–catalyst system is an effective approach, for which POMs are well-suited, particularly the Dawson and Keggin clusters with their rich photo- and redox- chemistry and ability to act as electron and proton reservoirs. As POMs characteristically show strong absorption centred in the UV region, their association with light-harvesting organic molecules or organometallic complexes is an effective strategy for achieving their visible-light sensitisation and optimising their photo-reactivity. Most reported photocatalytic POM-dye hybrid materials are non-covalent systems that typically combine a cationic photosensitiser (e.g.,  $[\text{Ru}(\text{bpy})_3]^{2+}$ ) with the POM anion via electrostatic interactions.<sup>[81]</sup> Although this synthetic approach is generally more straightforward, material properties are often largely dominated by the cation, and control of electronic structure across the hybrid can be limited.<sup>[50]</sup> The covalent grafting of photosensitising moieties has shown to be a more powerful approach, enabling better control of the orientation and interaction between the components which is important for achieving charge separation and efficient charge transfer between the functional subunits.<sup>[82]</sup>

Early studies on covalent POM-photosensitiser dyads were conducted by Odobel, Mayer and Harriman and co-workers, in which perylene-monoimide and zinc(II) tetraphenylporphyrin derivatives were covalently attached to Dawson POMs by the postfunctionalisation of organosilane and organophosphonate moieties via azide-alkyne ‘click’ chemistry (Fig.13a).<sup>[67, 83]</sup> Visible light irradiation was demonstrated to result in charge accumulation on the POM by charge transfer from the chromophores, but only single electron reduced species could be generated. Charge transfer dynamics also proved to be complex with the observation of competing through-space or intramolecular mechanisms, which highlighted the importance of the molecular design of such photoactive hybrid POMs in tailoring their charge transfer properties.

Photosensitive Ru(II)<sup>[84-85]</sup> and Re(I) polypyridyl complexes<sup>[86-87]</sup> have also been covalently linked to POMs in a few studies (Fig.13.b,c), and their photophysical



## 1. Introduction

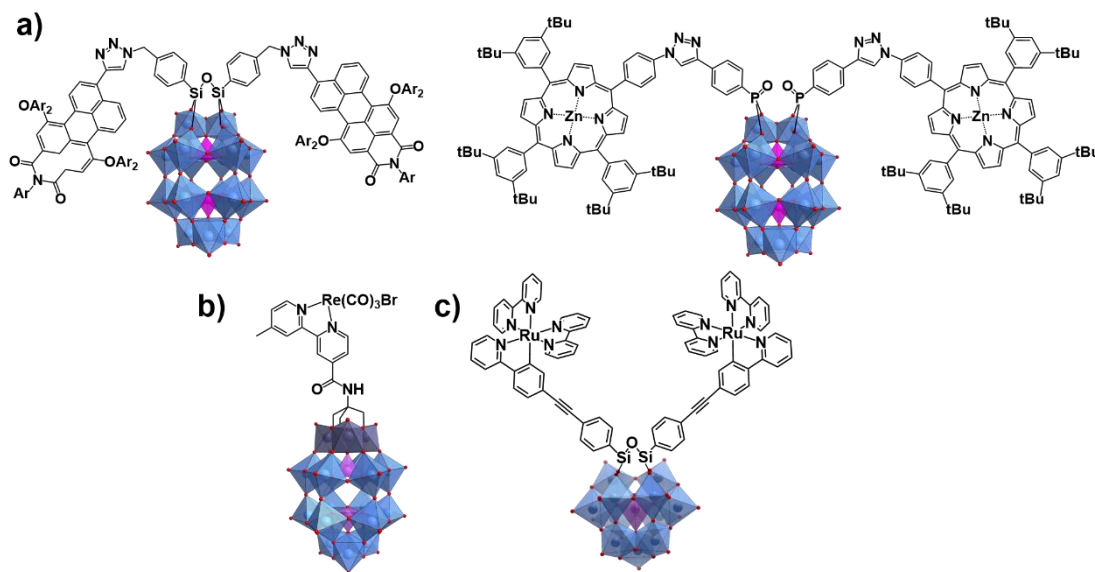


**Figure 13.** Selected examples of hybrid POMs covalently modified with photoactive functionalities: **a)** perylene-monoimide and Zn(II) tetraphenylporphyrin derivatives, reported by Odobel, Mayer and Harriman and co-workers.<sup>[67,83]</sup>; **b)** Re(I) complex, reported by Santoni *et al.*<sup>[87]</sup>; **c)** Ru(I) complexes, reported by Matt *et al.*<sup>[84]</sup>.

properties investigated. The development of such organometallic systems could be promising for photocatalytic applications, particularly in the reduction of CO<sub>2</sub>.<sup>[88]</sup>

Pioneering work on the design and application of covalent POM-photosensitiser systems as photocatalysts for the hydrogen-evolution reaction (HER) was carried out by Proust, Izzet, Artero and co-workers, in which cyclometalated Ir<sup>III</sup> complexes were attached to Keggin and Dawson POMs. Iodoaryl functionalised organotin and organosilyl hybrid POMs were used as platforms for postfunctionalisation, by which Sonogashira C-C cross-coupling reactions enabled the grafting of the Ir<sup>III</sup> complexes.<sup>[89-90]</sup> The Ir-POM hybrids displayed charge-separated states with lifetimes that were improved in relation to the isolated metal complex and amongst the longest reported

## 1. Introduction

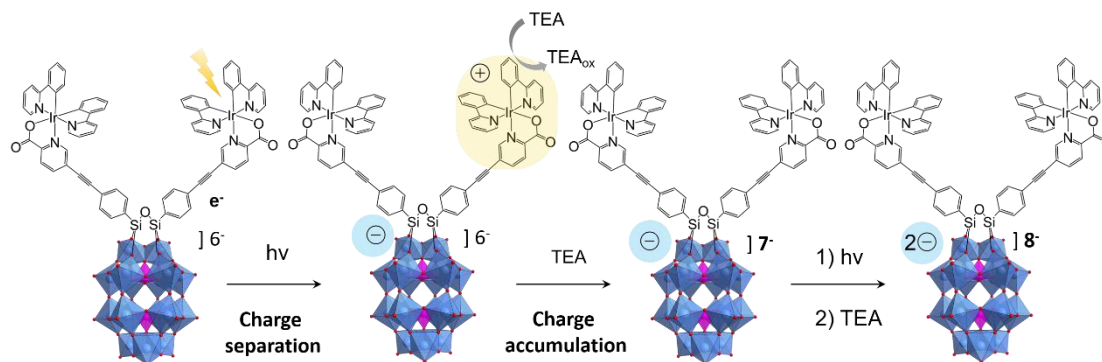


**Figure 14.** Multi-electron charge accumulation of an Ir-photosensitiser -functionalised hybrid Dawson reported by Proust, Izzet, Artero and co-workers. Adapted from reference 91.

for covalently bonded photosensitised POMs (on the order of ns to hundreds of ns), owing to the design of the heteroleptic Ir complex that provided directionality favourable in the nature of charge transfer. The Ir-organosilyl Dawson system was shown to be capable of efficient photoreduction and multi-electron charge accumulation under visible light irradiation in the presence of a sacrificial electron donor, triethylamine (TEA) (Fig.14). With an additional proton source, acetic acid, it performed modest photocatalytic hydrogen production with no degradation for more than a week, and with higher efficiency than the parent ionic multi-component system.<sup>[91]</sup> This work is hugely encouraging in the development of new covalent hybrid POMs capable of visible-light-driven multi-charge accumulation and sustainable photocatalytic hydrogen production.

More recently, cyclometalated Ir<sup>III</sup> chromophores were also linked to a series of TRIS hybrid Anderson-type clusters reported by Schönweiz *et al.*, prepared by the coordination of an Ir(III) complex to appended bipyridine moieties on the hybrids. They similarly demonstrated visible-light-driven HER catalytic activity that was significantly enhanced in comparison to the analogous non-covalent system.<sup>[92-93]</sup>

The covalent linking of POMs with various other organic dyes and photoactive units have been reported in the literature. Bonchio *et al.* reported the synthesis of a hybrid silicotungstate POM to which C<sub>60</sub>-fulleropyrrolidine units were covalently bonded via

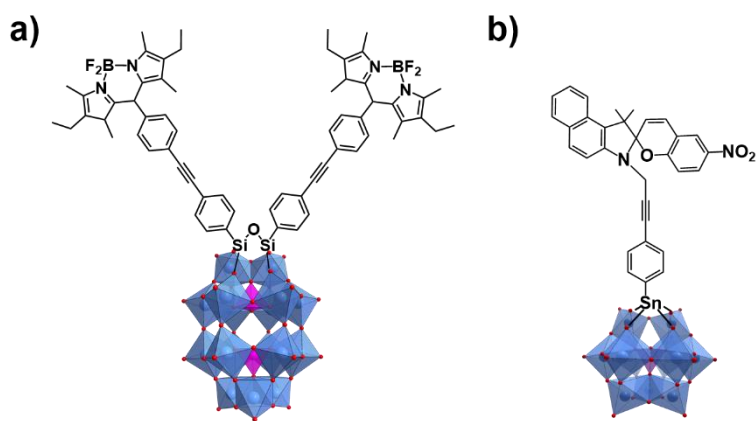


**Figure 15.** Hybrid POMs covalently attached to photoactive functionalities; a) bodipy, reported by Toupalas *et al.*<sup>[96]</sup> and; b) benzospiropyran, reported by Parrot *et al.*<sup>[97]</sup>

organosilane linkers. This hybrid system demonstrated to be an effective visible-light-driven heterogeneous catalyst for several organic substrate oxidations.<sup>[94]</sup>

The synthesis and photophysical properties of a series of bodipy (boron-dipyrromethene) functionalised Keggin and Dawson POMs (Fig.15a) have been reported in very recent studies by Izzet and Gibson and co-workers,<sup>[95-96]</sup> in which the first examples of charge-separated states on noble-metal free covalent POM-photosensitiser systems were demonstrated. The charge-separated states generated after rapid photoinduced charge transfer from the bodipy units to the POM displayed lifetimes that were notably not far from the earlier described Ir-systems (ranging from 1-10 ns).

Lastly, hybrid POMs incorporating photoswitchable molecular units, including spiropyrans (Fig.15b).<sup>[97-98]</sup> and azobenzenes,<sup>[99-100]</sup> have also been reported, that are interesting for the development of molecular optical switches and photoresponsive materials.

### 1.2.2 Hybrid POM supramolecular assembly and immobilisation

The design of multifunctional materials with well-defined nanostructured architectures is a challenging research issue in materials science and nanotechnology.<sup>[101-102]</sup> Classical bottom-up approaches use carefully designed primary building blocks, which are then hierarchically combined through self-

## 1. Introduction

---

assembly processes.<sup>[103]</sup> As structurally diverse nanosized compounds, POMs are attractive for the elaboration of functional materials by self-assembly, and covalent organofunctionalisation is highly effective in their preparation as molecular hybrid building blocks with well-defined structures and tuneable properties that can be transferred to the assembled material.

Hybrid POMs have drawn particular interest in recent years for the design of new “soft” nanomaterials with emergent properties. Organic groups covalently grafted to the POMs can transform them into amphiphilic hybrid systems, such as surfactants, with the cluster anion as the polar “head” group when grafted to hydrophobic aliphatic “tail” groups. The self-organisation of amphiphilic hybrid POMs in appropriate solvents into a variety of structures, including micelles, vesicles, reverse-vesicles and liquid crystalline phases, is well reported.<sup>[104]</sup>

As photo- and redox-active units, POMs are particularly attractive in the assembly of water-soluble surfactant hybrid materials for applications in catalysis, encapsulation and energy storage. Kastner *et al.* recently reported a surfactant organophosphonate Dawson hybrid with hydrophobic alkylthiol chain ligands,  $[P_2W_{17}O_{57}\{(PO_3C_6H_4O(CH_2)_{11}SH)_2\}]$  (Fig.16a), which displayed solvent-dependent self-assembly into micelles.<sup>[105]</sup> The supramolecular assemblies displayed high electrochemical stability and exhibited contrasting redox behaviour to their molecular units (Fig.16a).

The enhancement of electronic properties of such surfactant systems has been recently explored in a few studies by Klaiber and Polartz *et al.* Organosilyl groups comprising  $\pi$ -conjugated chain groups were linked to Keggin-type POMs to prepare double-tailed surfactants with both electronically conducting head and tail groups.<sup>[106-107]</sup> Assemblies formed from the surfactant hybrid in which the  $\pi$ -conjugated tail groups were terminated by anthraquinone residues (Fig.16b) displayed unique behaviour as a “micellar battery”.<sup>[107]</sup> Charge taken up by the POM head groups on electrochemical reduction could be transferred and effectively stored in the centre of

## 1. Introduction

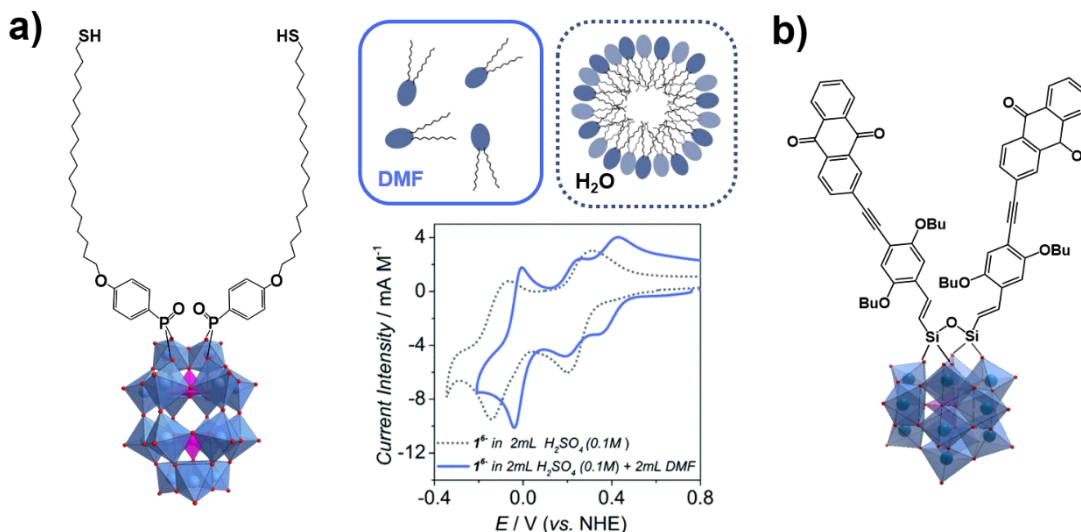


**Figure 16.** a) Structure and solvent-dependent self-assembly of surfactant hybrid Dawson reported by Kastner *et al.* Voltammetric data showing supramolecular behaviour in aqueous phase (grey dotted) and recovery of molecular behaviour (blue). Adapted from reference 105; b) Structure of an anthraquinone-functionalised hybrid Keggin surfactant reported by Klaiber *et al.*<sup>[107]</sup>

the micelles on the redox-active anthraquinone sites, and this was demonstrated to be reversible.

Zhou *et al.* recently reported the self-assembly of onion-like multi-walled vesicular structures by an amphiphilic hybrid Dawson-type POM to which C<sub>60</sub>-fulleropyrrolidine units were appended.<sup>[108]</sup> Alike Bonchio's molecular system mentioned above, the supramolecular assemblies were photoactive, generating singlet oxygen on irradiation which may be useful for catalysis as well as photodynamic therapies.

Photoactive groups in hybrid POM structures can also function by enabling the programmable assembly of the material. For example, the reversible light-driven *cis-trans* conformational change of appended azobenzene moieties in a hybrid Mn-Anderson cluster was demonstrated to enable morphological control in its self-assembled aggregates, between fibrous or spherical structures.<sup>[99]</sup> Tethered coumarin moieties in another hybrid Mn-Anderson POM were shown to dimerise on irradiation and result in photocrosslinking, enabling reversible light-driven polymerisation of the hybrid material.<sup>[109]</sup>

## 1. Introduction

---

Polymerisable units in organic groups covalently attached to hybrid POMs can also be used to incorporate POMs into functional architectures.<sup>[33]</sup> Photoactive films comprised of POM-porphyrin copolymers were reported by Ruhlmann, Lacôte, Hasenknopf and co-workers, prepared by the electropolymerisation of a zinc octaethylporphyrin with Anderson-type and Dawson-type POMs bearing dipyrindyl ligands.<sup>[110]</sup> The Anderson system was shown to be an effective heterogenous photocatalyst for the reduction of Ag<sup>I</sup> under visible light irradiation.<sup>[111]</sup> Catalytic polymeric materials incorporating POMs were also reported by Carraro *et al.*, in which hybrid Keggin-type POMs with terminal octenyl tails had been copolymerised with organic monomers in the porous structure, and were shown to provide reactive Lewis acidic sites in sulfide oxidation.<sup>[112]</sup>

Organofunctionalisation can also enable the covalent immobilisation of POM hybrids onto various substrates, which can be used to stabilise them and prepare new modified surfaces and composite materials.<sup>[113]</sup> The attachment of POMs to electrically active materials such as metals, graphene, semi-conductors and carbon nanotubes (CNTs), can be effective in their development towards application in electronic, photovoltaic and photo(electro)catalytic devices.<sup>[52, 113]</sup> Proust and co-workers have explored the covalent attachment of hybrid Keggin and Dawson POMs to gold and carbon electrode surfaces,<sup>[114]</sup> and in more recent years, silicon/silicon oxide and indium tin oxide (ITO) substrates, via various functionalities including diazonium and carboxylic acid groups.<sup>[115-116]</sup> Studies on the electronic transport properties in the POM-modified materials have highlighted that the molecular structure of the hybrid POMs and the nature of the anchoring function can have important implications for tuning the electronic properties and photoelectrochemical performances of the materials.<sup>[115-118]</sup>

The covalent linkage in a new composite composed of hybrid POMs and single-walled carbon nanotubes (SWCNTs) reported by Ji *et al.*, was shown to give access to a highly active anode material for lithium-ion batteries.<sup>[119]</sup> The composite material was prepared by amide bond formation between the TRIS moieties of a hybrid Mn-Anderson POM and carboxylate-functionalised SWCNTs, and it exhibited enhanced electrochemical performance compared with the pure SWCNTs or pure Anderson

## 1. Introduction

---

cluster due to improved conductivity facilitating faster electron transport and higher cycling stability.

In another example of a POM-based carbonaceous composite, the covalent combination of a hybrid Keggin silicotungstate via an isocyanate functionality with graphitic carbon nitride was shown to prepare a stable photocatalytic hybrid material. The POM demonstrated enhanced adsorption of O<sub>2</sub> in the composite, contributing to the material's efficient catalytic performance for H<sub>2</sub>O<sub>2</sub> production.<sup>[120]</sup>

### 1.2.2.1 Metal-directed assembly of hybrid POMs

The use of metal coordination chemistry in self-assembly is a powerful tool for the rational synthesis of discrete 0D to extended 3D assemblies.<sup>[121]</sup> A considerable number of metal-driven POM-based supramolecular structures have been reported in recent years, prepared by several general coordination approaches. POM anions can be reacted with either a mixture of transition metal salts and organic ligands or with pre-formed cationic organometallic complexes.<sup>[122-124]</sup> Additionally, transition-metal substituted POMs (TMSPOMs), a hetero-POM sub-class in which addenda metal atoms are substituted for transition metals via a lacunary species,<sup>[125]</sup> can be used in combination with organic ligands.<sup>[126]</sup> However, such preparations often use hydro- or solvo-thermal conditions, which can lead to unpredictable and complicated architectures.

The various synthetic approaches to the covalent linking of transition metal complexes with POMs have been described in a review by Santoni *et al.*<sup>[72]</sup> It is clear that the combination of organic and inorganic subunits and the methodology of their assembly is influential on the properties and architecture of the resulting multi-component hybrid material. The postfunctionalisation approach of metal coordination to chelating ligands on a pre-formed POM hybrid can enable great control in the assembly of POM supramolecular architectures, ranging from discrete nano-oligomers to coordination polymer frameworks and macroions, through fine-tuning the hybrid POM structure and selection of metal compound. The topology of the POM hybrid as a "ligand" and that of the metal linker are crucial parameters that determine the nature of the resulting metallosupramolecular assembly. For example,

## 1. Introduction

---

hybrid POMs that possess two chelating sites with a coordination vector close to  $180^\circ$  can behave as ditopic ligands, such as bis-capped Anderson POMs, forming linearly directed 1D coordination polymers, 2D layers and 3D frameworks.<sup>[127-128]</sup> In contrast, hybrid POMs with coordination vectors  $<180^\circ$  have been shown to assemble thermodynamically-favoured coordination oligomers. In the first example of a discrete oligomer, Santoni *et al.* isolated exclusively molecular triangles comprised of three POM anions and three metal linkers by reaction of a Lindqvist hybrid with terminating (3)-pyridyl groups (coordination vector of  $60^\circ$ ) with equimolar  $\text{Pd}^{\text{II}}$  ions.<sup>[129]</sup>

Izzet and co-workers have reported several similar metal-directed oligomers since, including a molecular triangle assembled by the coordination of  $\text{Pd}^{\text{II}}$  ( $[\text{PdCl}_2(\text{CH}_3\text{CN})_2]$ ) to (4)-pyridyl sites on an organosilyl hybrid Dawson,  $[\text{P}_2\text{W}_{17}\text{O}_{61}\{\text{O}(\text{Si}-\text{C}_6\text{H}_4\text{C}\equiv\text{C}-4\text{-Py})_2\}]$ (Fig.17).<sup>[130]</sup> The flexibility of the two pendant arms on each hybrid enable a distortion of the bite angle from the *ca.*  $90^\circ$  angle typically displayed in ditopic organosilyl hybrids, to result in a triangular formation that is entropically favoured over a tetramer/square. Following this, the Dawson hybrid was compared to a Keggin analogue, noting an important influence of cluster charge on the nature of the preferential metallocycles directed by metal coordination.<sup>[131]</sup> Whilst the more highly charged Dawson clusters resulted in only trimers/triangles, the Keggin analogue was observed in both trimer and tetramer/square formations (Fig.17).

The tailored design of hybrid POMs as “ligands” for metal coordination can also enable a bottom-up approach to the preparation of POM suprastructures, by hierarchical organisation from hybrid POM molecules to nanoscale metallomacrocycles and then to supramolecular structures. For example, Zhu *et al.* reported a mono-carboxylate functionalised hexamolybdate,  $[\text{Mo}_6\text{O}_{18}\equiv\text{NC}_6\text{H}_4-4\text{-COOH}]$ , which, on chelation to two  $\text{Cu}^{\text{II}}$  ions formed a paddle-wheel shaped tetrameric cluster which then demonstrated self-assembly as a building block into large blackberry-type structures.<sup>[132]</sup> The formation and size of the latter was shown to be tuneable to some extent by the polarity of the solvent mixture.



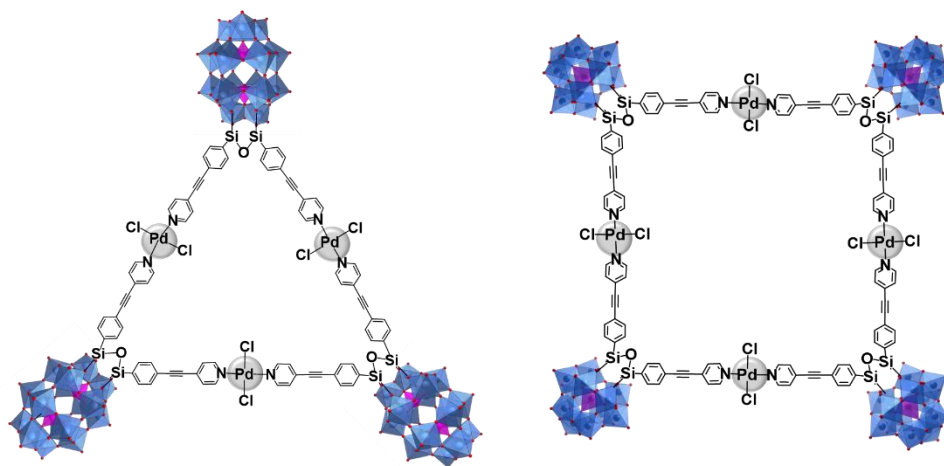


**Figure 17.** The metal-driven formation of molecular triangles and squares from ditopic pyridyl-terminated hybrid Dawson and Keggin clusters reported by Piot *et al.* Adapted from reference 131.

In a study returning to the earlier reported (bis)pyridyl organosilyl hybrid Keggin system, Izzet and co-workers demonstrated that by coordination of a Pd<sup>II</sup> linker with a 90° chelating angle, [Pd(en)(CH<sub>3</sub>CN)<sub>2</sub>], a cyclic oligomer comprised of just two POM linkers could be isolated.<sup>[133]</sup> Strikingly different and controllable hierarchical assembly was then observed with this dimeric hybrid POM building block, with its organisation into either branched “worms” or multi-layer vesicles depending on solvent composition (Fig.18).

Resembling their earlier reported molecular triangle,<sup>[130]</sup> Izzet and co-workers reported also trimers assembled from a bis(terpyridine) functionalised organosilyl hybrid Dawson on coordination with equimolar Fe<sup>II</sup>, which displayed reversible aggregation into dense supramolecular nanoparticles in polar solvents.<sup>[134]</sup> However, with cobalt coordination, two contrasting supramolecular aggregates were attainable with the hybrid POM depending on the preformed metallocycle and its subsequent organisation.<sup>[135]</sup> Dense particles alike those formed by the Fe<sup>II</sup> trimer assembled in acetonitrile, but on oxidation of the Co<sup>II</sup> metal linkers to Co<sup>III</sup>, the comparable aggregation gave worm-like structures comprised of stacked macrocycles, indicating

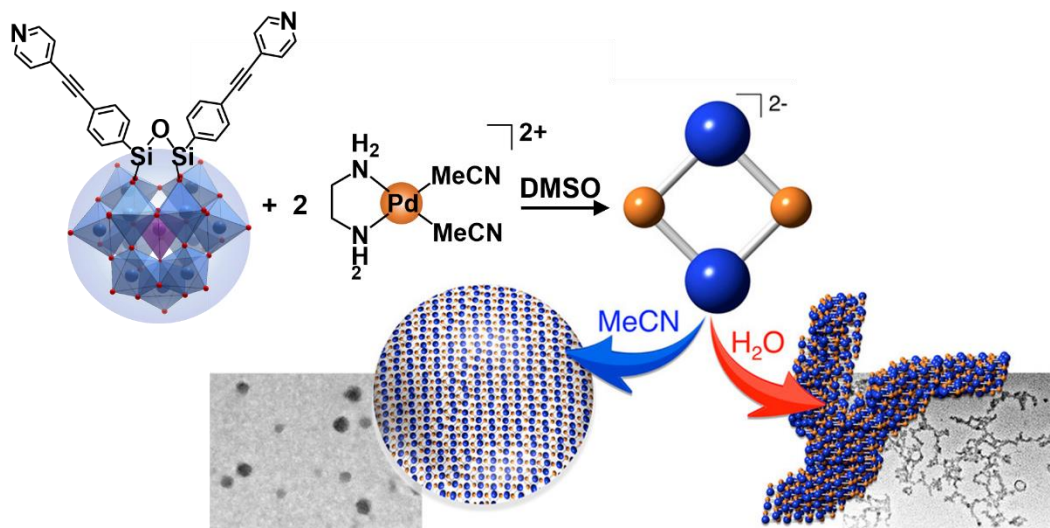


**Figure 18.** Formation of a metallomacrocyclic from  $\text{Pd}^{2+}$  coordination with a ditopic pyridyl-terminated hybrid Keggin reported by Salles *et al.*, and its hierarchical self-assembly into different nanostructures depending on solvent composition. Adapted from reference 133.

that electrostatic interactions and subsequent hierarchical organisation could be modified through redox state.

Remarkably switchable metal-driven self-assembly has been demonstrated by a unique ‘dumbbell’ hybrid POM reported by Yin *et al.*, comprised of two phosphovanadotungstate clusters covalently bridged by a bipyridine bis(tris-alkoxo) functionality (Fig.19).<sup>[136]</sup> By a reversible *trans-cis* transformation via metal chelation at the central bridging bipyridine unit, the dumbbell could be modified to a V-shaped amphiphile when in the *cis* conformation, which was capable of self-assembly into bi-layered vesicles. By the addition of a competitive ligand (EDTA) for the  $\text{Zn}^{2+}$  ions the vesicles could be disassembled into the molecular dumbbell building blocks.

The diverse organofunctionalisation strategies available in hybrid POM chemistry mean that, in theory, almost any organic functionality could be covalently grafted onto a POM with suitable synthetic control. The intrinsic properties of the POM cluster can be combined with the properties of the appended functional unit(s), and the covalent attachment is particularly effective for enabling the photochemical and electrochemical properties of the hybrid compound to be tuned for application.

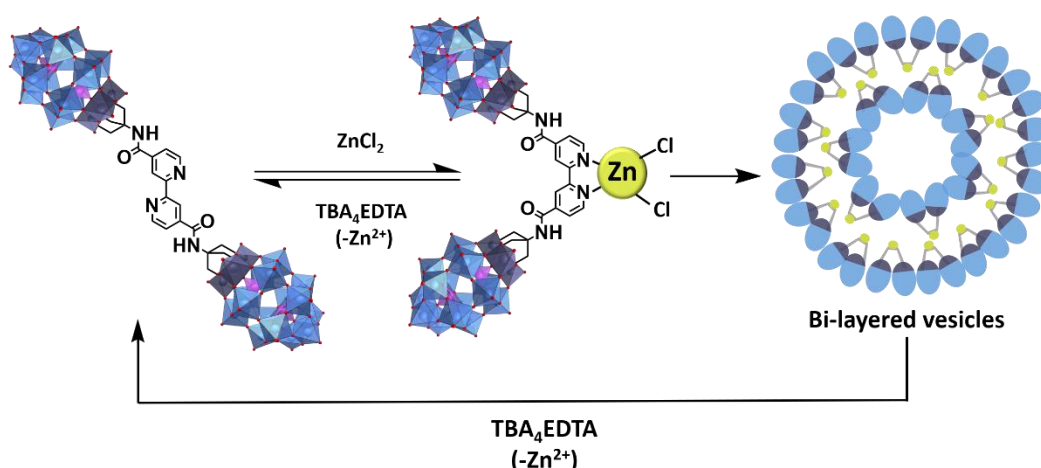


**Figure 19.** The reversible conformational transformation of a POM ‘dumbbell’,  $[\{P_2V_3W_{15}O_{59}(OCH_2)_3NHCO\}_2(C_5H_3N)_2]$  by metal complexation, and its consequent self-assembly into bi-layered vesicles. Adapted from references 28 and 136.

Moreover, the hybrid compound can be an attractive multi-component molecular ‘building block’ to be used in assembly or incorporation into more advanced supramolecular arrays, materials, and devices. Importantly, the design of covalently organofunctionalised POM hybrids with well-defined functionalities, anchoring modes and stoichiometry can be a powerful strategy in the preparation of multifunctional materials with fine-tuned properties and predictable and/or controllable architectures.

### 1.3 Asymmetric hybrid POMs- an emerging strategy for multifunctionality

The development of synthetic procedures for hybrid materials that allow optimal control in the introduction of multiple functionalities and tailoring of their properties is an ongoing challenge. Reported bi-functionalised hybrid POMs are predominantly symmetric systems, in which two identical organic groups are tethered to the inorganic core. The controlled addition of two different organic groups to create an asymmetric hybrid system allows another layer of complexity to be introduced into

## 1. Introduction

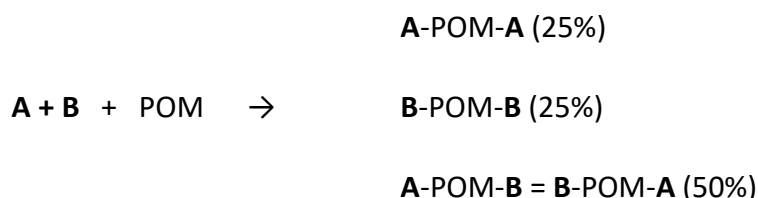
---

hybrid POM structures, and opens greater opportunities to achieve fine control over physicochemical properties and function, enhance synergistic effects between the various components and control self-assembling behaviours. This can enable the design of new molecular nanomaterials based on POMs which have multiple or modular functionality that tailor them towards highly specific or advanced applications. Owing to the significant challenge posed by their synthesis and purification, only a small number of asymmetrically functionalised hybrid POMs have been reported in recent years. The synthetic methodologies and notable properties and functionalities of some key examples are highlighted in this section.

### 1.3.1 Current synthetic strategies for asymmetric functionalisation

#### 1.3.1.1 Purification from symmetric side-products

An obvious approach to the synthesis of a bi-functionalised asymmetric hybrid POM is using stoichiometric amounts of each of the two organic linker groups (**A** and **B**) in a reaction with the POM centre and isolating the asymmetric product from the hybrid product mixture. A maximum yield of 50% can be expected for this product, assuming the reaction proceeds entirely statistically and to completion:



However, the differences in chemical structure of the organic linkers **A** and **B** may change the relative driving forces for their grafting onto the POM. The properties of the first of either **A** or **B** to graft, such as size, hydrophilicity, and inductive effects of functional groups could affect the reactivity of the second lacunary site towards a second **A** or **B**. In particular, the relative solubilities of the organic linkers **A** and **B** and their respective symmetric hybrid POMs in solvents may be quite different, and this can facilitate the separation of the three products in the mixture. This was the basis of slow fractional crystallisation used to isolate the first reported asymmetric hybrid

## 1. Introduction

POM,  $[\text{MnMo}_6\text{O}_{18}\{(\text{OCH}_2)_3\text{CNO}_2\}\{(\text{OCH}_2)_3\text{CNH}_2\}]$  (Fig.20a), synthesised in a one-pot reaction by Song *et al.* in which two distinct TRIS  $-(\text{OCH}_2)_3\text{C}-$  capping groups, terminated in amino and nitro groups, were reacted simultaneously with a Mn-Anderson cluster.<sup>[137]</sup> Precipitates crystallised from the mother liquor were collected every few hours by filtration and were analysed using electrospray ionisation mass spectrometry (ESI-MS). Isolation of the desired asymmetric product was achieved by recrystallisation of the specific batch identified as containing the corresponding molecular weight.

The significance of the unique asymmetric hybrid structure was then demonstrated by the group by its reaction with various aromatic aldehydes, resulting in a series of new asymmetric structures with imine moieties transformed from the terminating amine (Fig.20b). With the versatility in reactions to further expand and functionalise the organic moieties, this pioneering work signified the scope and control in molecular design that asymmetric hybrid structures can provide. However, batch analysis and slow crystallisation are time-consuming, highly involved processes, unlikely to work effectively for all POM hybrid mixtures and so it is beneficial to develop synthetic and purification strategies that are more widely applicable.

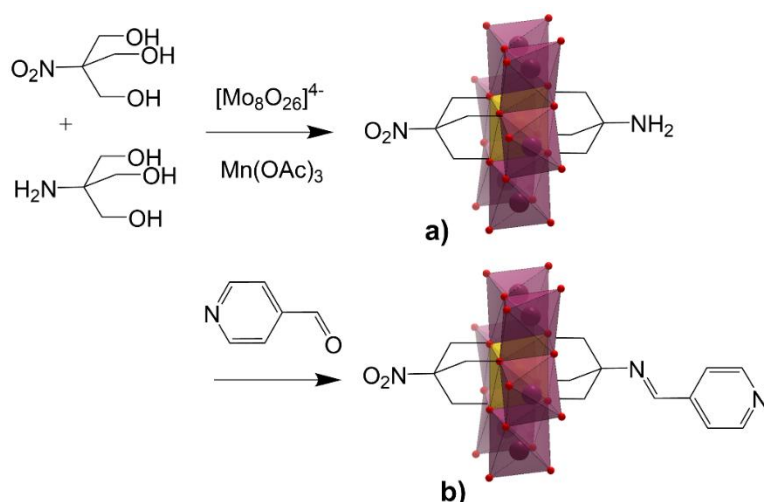


**Figure 20.** Synthetic schemes of asymmetric Anderson hybrids: **a)**  $[\text{MnMo}_6\text{O}_{18}\{(\text{OCH}_2)_3\text{CNO}_2\}\{(\text{OCH}_2)_3\text{CNH}_2\}]$ , via capping of an Mn-Anderson cluster and; **b)**  $[\text{MnMo}_6\text{O}_{18}\{(\text{OCH}_2)_3\text{CNO}_2\}\{(\text{OCH}_2)_3\text{CN}=\text{CH}(\text{C}_5\text{H}_4\text{N})\}]$ , after reaction of (a) with 4-pyridylcarboxylaldehyde. Adapted from reference 137.

## 1. Introduction

---

Silica or alumina column chromatography are alternative techniques, but are generally avoided in the purification of POM-based compounds due to their incompatible anionic nature risking strong adsorption, altering of cations and subsequently low yields.<sup>[138]</sup> However, it has been used successfully in a few cases,<sup>[139-140]</sup> including in the isolation of one asymmetric hybrid Anderson, prepared by the coupling of 3,5-bis(tetradecyloxy)benzoic acid to a symmetric TRIS-NH<sub>2</sub>/TRIS-NH<sub>2</sub> hybrid [MnMo<sub>6</sub>O<sub>18</sub>{(OCH<sub>2</sub>)<sub>3</sub>CNH<sub>2</sub>}<sub>2</sub>] precursor.<sup>[141]</sup> Interestingly, subsequent cation exchange was used to configure the molecule to be amphiphilic, enabling the formation of stable Langmuir-Blodgett films, and indicating potential in using asymmetric functionalisation in the tailored design of self-assembling materials.

A unique method of reverse-phase (RP)-HPLC for the purification of POM hybrid mixtures was developed by Yvon *et al.* designed to be adaptable for ideally a wide variety of POM and ligand combinations.<sup>[142]</sup> The method requires that the ligands and the respective symmetric and asymmetric POM hybrids differ significantly in affinity for RP media, with the asymmetric hybrid displaying an intermediate affinity to the symmetric forms. Several asymmetric Mn-Anderson hybrids were purified by this method from the mother liquors of one-pot reactions combining either: two distinct tris-alkoxy ligands with a Mn-Anderson cluster, or, in a postfunctionalisation reaction- a preformed TRIS-NH<sub>2</sub>/TRIS-NH<sub>2</sub> hybrid POM, [MnMo<sub>6</sub>O<sub>18</sub>{(OCH<sub>2</sub>)<sub>3</sub>CNH<sub>2</sub>}<sub>2</sub>], with two distinct anhydride and/or acyl chloride reagents.

### 1.3.1.2 Singly- organofunctionalised hybrid POMs

Isolated single-sided hybrid clusters have very recently drawn interest as platforms in the synthesis of asymmetrically bi-functionalised hybrid clusters. Wu *et al.* reported the first synthesis of a singly-TRIS-NH<sub>2</sub> functionalised Anderson-type POM, by esterification of pentaerythritol with the cluster [CrMo<sub>6</sub>O<sub>18</sub>(OH)<sub>6</sub>]<sup>3-</sup>,<sup>[143]</sup> showing potential in achieving asymmetric functionalisation in two steps without an initial doubly TRIS-modified POM and its subsequent postfunctionalisation and purification steps necessary. Unlike the Mn-Anderson cluster commonly selected for triol modification, the protonated structure of the Cr-Anderson-type cluster is not easily grafted to on both sides simultaneously. Replacement of three -OH groups located on

## 1. Introduction

the face of these clusters with the three from a TRIS-based ligand results in the increased stability of the other three hydroxy groups on the opposite face of the cluster, significantly reducing the reactivity towards a second ligand under the same conditions. Accordingly, the group used three singly triol-functionalised hybrid POMs as precursors in a following study, in reactions with a second different triol to afford a series of double-sided asymmetric derivatives,  $[[C_2H_5C(CH_2O)_3]MMo_6O_{18}\{(OCH_2)_3CNH_2\}]$  (M= Cr, Al, Mn). Notably, the ruling out of symmetric side-product formation allowed isolation in high purity and yields.<sup>[144]</sup> Interestingly, the high yields of asymmetric product were also shown to be obtainable via both possible orders of the two-step procedure from either single-sided hybrid precursor (Fig.21).

Fundamentally, almost all reported examples of asymmetric POM hybrids are based on the Anderson cluster, often reasoned by the authors to be due to the ease of preparation of versatile TRIS-based ligands. A notable exception is the elegant preparation of a series of organotin Dawson POM hybrids reported by Micoine *et al.*<sup>[145]</sup> In a unique synthetic approach, they reacted aromatic isocyanates (ArNCO) to organotin hybrid POMs,  $[P_2W_{17}O_{61}\{SnR\}]^{7-}$ , to yield a series of bi-functionalised

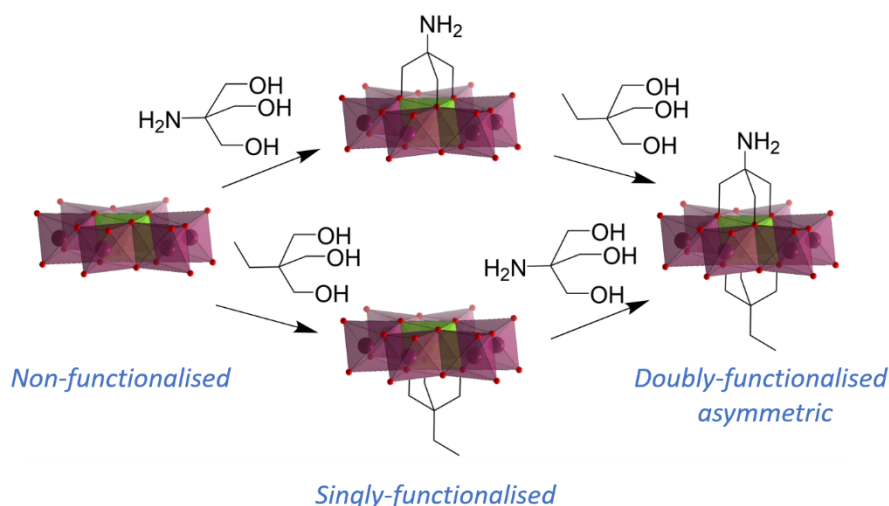


**Figure 21.** Synthetic scheme for the asymmetric hybrid Anderson-type POM  $[[C_2H_5C(CH_2O)_3]CrMo_6O_{18}\{(OCH_2)_3CNH_2\}]$ , showing both possible orders of the two-step procedure. Colour coding: plum polyhedra =  $\{MoO_6\}$ ; green polyhedra =  $\{CrO_6\}$ ; red spheres = oxygen. Adapted from reference 144.

## 1. Introduction

hybrids,  $[P_2W_{17}O_{61}\{(\text{SnR})(\text{CONHAr})\}]^{6-}$ , in which they showed that both the R and Ar organic moieties could be varied (Fig.22). They had previously noted that on incorporation of a low oxidation state metal centre into the lacunary site, the adjacent bridging oxo sites increase in nucleophilicity and in reactivity towards electrophilic reagents.<sup>[146]</sup> They then utilised this discovery of oxo-site activation to explore the introduction of a second, different organic moiety in order to prepare new asymmetrically-functionalised Dawson hybrids. The scope of the reaction was demonstrated by the grafting of a series of nine electrophilic aryl-isocyanates onto one organostannane modified Dawson (R= butyl), and phenyl-isocyanate onto two other derivatives (Fig.22b). Unfortunately, they found the doubly functionalised products were hydrolytically unstable, reverting to the Sn-hybrid starting materials shortly after handling in air. Nevertheless, this work demonstrates a sophisticated and promising approach for the preparation of new bi-functionalised Dawson POM hybrids with distinct organic moieties.

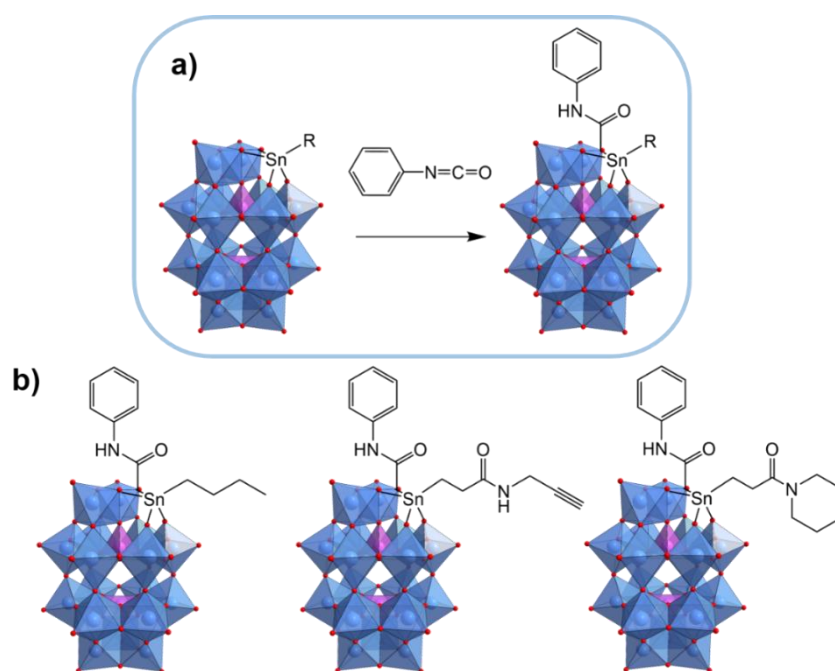


**Figure 22.** The general synthetic scheme for the reaction of aromatic isocyanates with the organotin hybrid,  $[P_2W_{17}O_{61}\{(\text{SnR})\}]$ ; **b)** three selected examples of the doubly-functionalised asymmetric hybrid POM products. Adapted from reference 145.



### 1.3.1.3 Controlled postfunctionalisation of hybrid POMs

The aforementioned RP-HPLC method developed by Yvon *et al.* was used to isolate a “universal” precursor hybrid, an Fmoc–TRIS/TRIS-NH<sub>2</sub> Mn–Anderson [MnMo<sub>6</sub>O<sub>18</sub>{(OCH<sub>2</sub>)<sub>3</sub>CNH-Fmoc}{(OCH<sub>2</sub>)<sub>3</sub>CNH<sub>2</sub>}] (Fmoc= 9-fluorenylmethyloxycarbonyl) (Fig.23a), which could then be used for postfunctionalisation at the TRIS-NH<sub>2</sub> amine.<sup>[142]</sup> The second amine could then be deprotected at the Fmoc group, allowing subsequent modification once more (Fig.23b). The “universal” precursor approach should allow the preparation of hybrid POMs which may not be easily separated from symmetric hybrid side-products due to similar hydrophobicity/hydrophilicity and poor retention on the stationary phase, as well as enable controlled stepwise reactions at both TRIS-based moieties. Indeed, the precursor was used in a later study by the group for the stepwise preparation of novel hybrid peptide chains.<sup>[147]</sup> Once attached to a preformed resin-supported amino

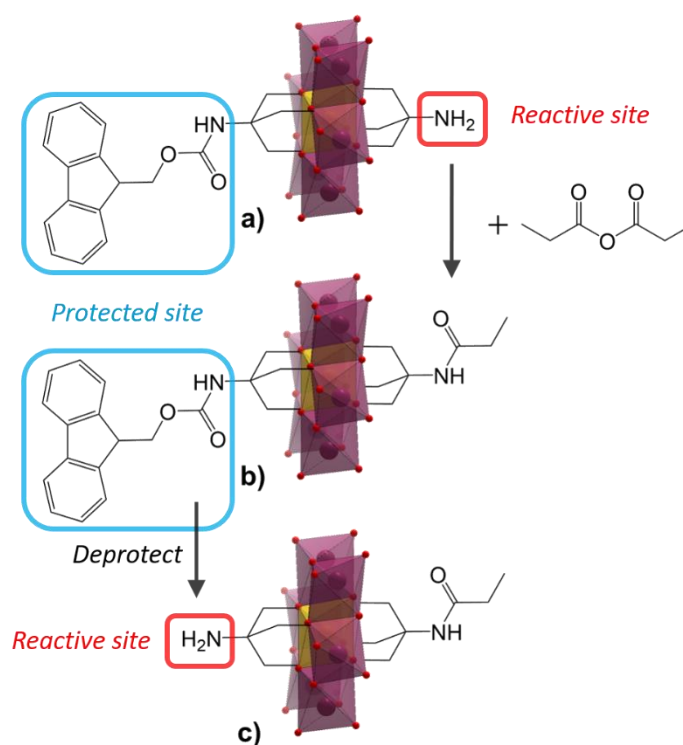


**Figure 23.** a) The “universal” precursor asymmetric POM, Fmoc–TRIS/TRIS-NH<sub>2</sub> Mn–Anderson [MnMo<sub>6</sub>O<sub>18</sub>{(OCH<sub>2</sub>)<sub>3</sub>CNH-Fmoc}{(OCH<sub>2</sub>)<sub>3</sub>CNH<sub>2</sub>}]; b) an asymmetric Fmoc–TRIS/TRIS-propylamine Mn–Anderson intermediate; c) an asymmetric TRIS-NH<sub>2</sub>/TRIS-propylamine Mn–Anderson synthesised by the postfunctionalisation of the “universal” precursor. Adapted from reference 142.

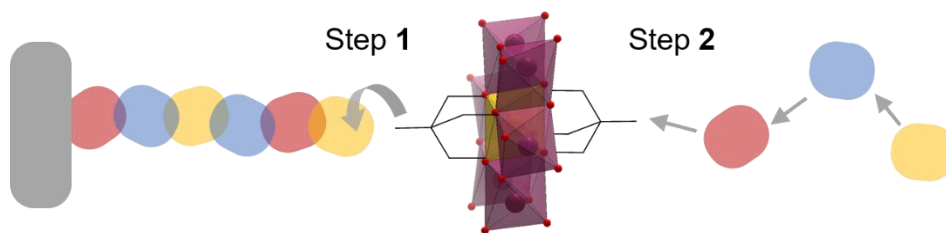


**Figure 24.** Schematic representation showing the stepwise attachment of amino-acids, shown as coloured blocks, in a peptide chain incorporating an Mn-Anderson cluster. Adapted from reference 147.

acid chain and after subsequent deprotection of the Fmoc group, amino acids could be attached one-by-one via peptide coupling reactions to the other side of the POM cluster (Fig.24), before release from the resin.

A similar strategy was used to controllably build POM hybrid oligomers sequentially, this time via Cu-catalysed alkyne-azide cycloadditions, or “click” reactions.<sup>[148]</sup> Asymmetric TRIS-NH<sub>2</sub>/TRIS-azide or TRIS-NH<sub>2</sub>/TRIS-alkyne POM synthons were initially prepared via postfunctionalisation of the “universal” precursor or isolated from one-pot reaction mixtures using RP-HPLC. They could then be “clicked” together as building blocks in a modular fashion, and the TRIS-NH<sub>2</sub> moieties at the oligomer ends could be activated selectively through coupling reactions to reintroduce terminal alkynes ready for the next “click” addition. By always using an asymmetric synthon, reactions can only occur one at a time and limit chain growth, whereas in the case of using symmetric synthons, uncontrolled polymerisation and polydisperse chains would result.

These studies further demonstrate the scope by which asymmetric structures can allow tailored design in the preparation of hybrid materials. By enabling step-wise postfunctionalisation at selected sites, the structure and composition of the hybrid material incorporating the POM hybrid(s) can be carefully designed and built.

### 1.3.2 Synergistic function in asymmetric hybrid POMs

There have been several reported asymmetric hybrid POM systems which display interesting functions that are enhanced in comparison to their individual components

## 1. Introduction

or symmetric hybrid POM analogues. Postfunctionalisation strategies have been utilised by Oms and Saad *et al.* to prepare unique photochromic compounds based on asymmetric spiropyran (SP)-functionalised hybrid clusters. A preformed symmetric TRIS-NH<sub>2</sub>/TRIS-NH<sub>2</sub> Mn-Anderson, [MnMo<sub>6</sub>O<sub>18</sub>{(OCH<sub>2</sub>)<sub>3</sub>CNH<sub>2</sub>}<sub>2</sub>], was coupled with <1 eq. of a carboxylic acid -terminated spiropyran, and the asymmetric TRIS-NH<sub>2</sub>/TRIS-SP hybrid product, [MnMo<sub>6</sub>O<sub>18</sub>{(OCH<sub>2</sub>)<sub>3</sub>CNH<sub>2</sub>}{(OCH<sub>2</sub>)<sub>3</sub>CNHC<sub>21</sub>H<sub>19</sub>N<sub>2</sub>O<sub>4</sub>}], was isolated by slow crystallisation.<sup>[98]</sup> The TRIS-NH<sub>2</sub>/TRIS-SP cluster exhibited solid-state photochromic properties under ambient conditions, with notable differences from in the symmetric TRIS-SP/TRIS-SP analogue.

The potential for elaboration of this compound by postfunctionalisation at the free amine site was then demonstrated by the coupling of a second functional moiety- an optically-active spironaphthoxazine (SN),<sup>[149]</sup> and a fluorescent boron-dipyrromethene (BODIPY).<sup>[73]</sup> Both asymmetric systems again exhibited differences to their symmetric analogues in their photochromic and/or fluorescent behaviour, indicating important synergistic effects between the two distinct moieties and the POM centres in the asymmetric structure. Most impressively, the BODIPY fluorescence in the TRIS-SP/TRIS-BODIPY (SP-POM-BODIPY) system was shown to be finely tuned through the activation of the photochromism of the SP moiety by UV or

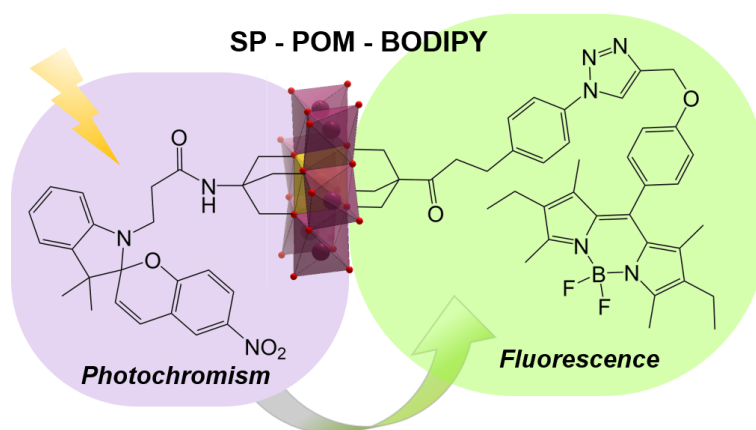


**Figure 25.** An asymmetric Anderson hybrid cluster functionalised with photochromic spiropyran (SP) and luminescent boron-dipyrromethene (BODIPY) moieties, which displays photoswitchable fluorescence. Adapted from reference 73.

## 1. Introduction

---

yellow light irradiation (Fig.25). The hybrid POM triad demonstrated to be an effective molecular switch, displaying excellent resistance to photofatigue relative to organic SP-BODIPY systems, with the photoswitchable fluorescence cycling efficiently twenty times. Boulmier *et al.* similarly postfunctionalised the TRIS-NH<sub>2</sub>/TRIS-SP asymmetric system to isolate a new tetrathiafulvalene (TTF) functionalised asymmetric Mn-Anderson cluster, TRIS-TTF/TRIS-SP, which displayed unusual optical properties uncommon to POM materials.<sup>[150]</sup>

These are fine examples of how the distinct components in an asymmetric hybrid POM structure can function synergistically and show great potential for their use in the design of advanced, switchable materials.

### 1.3.3 Assembly of asymmetric hybrid POMs

Organic moieties attached to POMs can be used to facilitate their assembly into various architectures, whether by rendering them amphiphilic, enabling polymerisation, or allowing covalent attachment to surfaces, to name a few.<sup>[28]</sup>

Song *et al.* further utilised their methodology of slow fractional crystallisation and ESI-MS to isolate the asymmetric cluster, [MnMo<sub>6</sub>O<sub>18</sub>{((OCH<sub>2</sub>)<sub>3</sub>CNH<sub>2</sub>)((OCH<sub>2</sub>)<sub>3</sub>CN=CH-(C<sub>16</sub>H<sub>9</sub>))}] in which one TRIS moiety is terminated in a pyrene.<sup>[151]</sup> The second TRIS-NH<sub>2</sub> moiety was used to bond to an alkylthiolate self-assembled monolayer (SAM) on a gold surface. In comparison to the other surface-grafted analogues, SAM-POM-TRIS-NH<sub>2</sub> or SAM-pyrene, the SAM-POM-TRIS-pyrene system showed highly selective adhesion to cells, indicating the superiority of a surface-patterned material that is based specifically on an asymmetric hybrid POM.

Following this work, a similar asymmetric hybrid POM was isolated by the same method, in which both distinct TRIS-based groups were now more elaborate- a pyrene and a C<sub>9</sub> alkyl chain, [MnMo<sub>6</sub>O<sub>18</sub>{(OCH<sub>2</sub>)<sub>3</sub>C-C<sub>9</sub>H<sub>17</sub>}{(OCH<sub>2</sub>)<sub>3</sub>CNH-CHC<sub>16</sub>H<sub>9</sub>}]<sup>[152]</sup> In a study comparing the self-assembled structures of the asymmetric system and two analogous symmetric systems, the combination of both aromatic and hydrophobic functionalities in the asymmetric structure resulted in unique fibril nanostructures with characteristics that reflected the nature of both ligands. These early studies show some of the first examples of controlled function and assembly enabled by an

## 1. Introduction

asymmetric hybrid structure and demonstrate the effectiveness of a modulated design approach towards the development of multifunctional materials.

Yang and Saad *et al.* postfunctionalised the earlier reported TRIS-NH<sub>2</sub>/TRIS-SP asymmetric hybrid POM in a later study to introduce a hydrophobic C<sub>16</sub> alkyl moiety, resulting in a hybrid system that demonstrated remarkable switchable self-assembly, [MnMo<sub>6</sub>O<sub>18</sub>{(OCH<sub>2</sub>)<sub>3</sub>CNHC<sub>21</sub>H<sub>19</sub>N<sub>2</sub>O<sub>4</sub>}{(OCH<sub>2</sub>)<sub>3</sub>CNHC<sub>16</sub>H<sub>28</sub>O}] (SP-POM-C<sub>16</sub>) (Fig.26).<sup>[153]</sup> Near-UV radiation was shown to cleave the C-O bond in the SP moiety and lead to its conversion into a zwitterionic merocyanine (MC) isomer, which could be reversed by visible light irradiation. Photoswitching between the hydrophobic SP and hydrophilic MC forms consequently enabled the reversible self-assembly of the amphiphilic MC-POM-C<sub>16</sub> system into vesicles in polar solvents (Fig.26). Furthermore, the type of vesicle and its size were shown to be solvent-dependent, with the formation of reverse-vesicles in non-polar solvents. The latter were found to be stable whether irradiated with UV or visible light, demonstrating that both light irradiation and

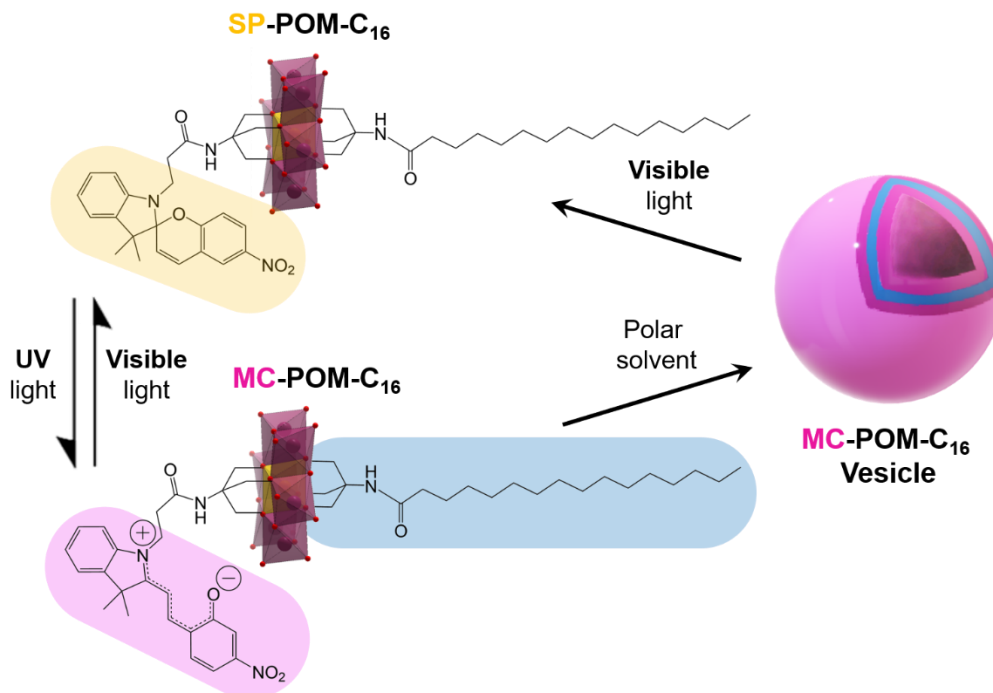


**Figure 26.** Schematic showing the reversible self-assembly of MC-POM-C<sub>16</sub> into vesicles in polar solvents by light-controlled conversion between the SP and MC forms. Adapted from reference 153.

## 1. Introduction

---

solvent polarity could be used to precisely tune the morphology of the assembled soft structures.

### 1.3.4 New tuneable redox-active materials based on asymmetric hybrid POMs

The asymmetric organofunctionalisation of POMs is evidently emerging as a sophisticated design strategy for the preparation of multifunctional hybrid systems. However, reported examples are few due to the ongoing synthetic challenges in their preparation, as high molecular weight, highly charged molecules. Many of the current strategies for synthesis and purification require demanding, expensive and time-consuming methods, such as chromatography or slow fractional crystallisation, followed by multiple synthetic steps in postfunctionalisation to obtain the desired asymmetric product. More accessible synthetic methodologies, ideally applicable for a variety of POM clusters and organic linker mixtures, are clearly necessary for the development of reliable design strategies for new multifunctional materials based on asymmetric hybrid POMs.

Reported examples of asymmetric hybrid POMs that exhibit complex functionalities are even fewer, but present great potential and inspiration in the design of materials with switchable function and morphologies and enhanced synergistic effects. Notably, examples remain limited substantially to the Anderson cluster type, which inherently displays limited photo- and redox-activity compared to many POMs. The electronic properties are typically dominated by the transition metal heteroatom or organic group in hybrid structures, and tuneability via structure design is limited due to poor conjugation across the triol functionalities.<sup>[65]</sup> Accordingly, the development of asymmetric functionalisation strategies targeting clusters such as the Dawson anion, with its capability for multi-electron redox processes and highly tuneable organic hybrid structures, are of particular value. This can provide new pathways for the isolation of more advanced multifunctional hybrid systems, with potentially novel applications as redox-, photo-, and catalytically active nanomaterials.

## References

- [1] J. Berzelius, *Poggendorff's Ann. Phys.*, 1826, **6**, 369-380.

## 1. Introduction

---

- [2] S.-S. Wang, G.-Y. Yang, Recent Advances in Polyoxometalate-Catalyzed Reactions, *Chem. Rev.*, 2015, **115**, 4893-4962.
- [3] Y.-F. Song, R. Tsunashima, Recent advances on polyoxometalate-based molecular and composite materials, *Chem. Soc. Rev.*, 2012, **41**, 7384-7402.
- [4] J. T. Rhule, C. L. Hill, D. A. Judd, R. F. Schinazi, Polyoxometalates in Medicine, *Chem. Rev.*, 1998, **98**, 327-358.
- [5] A. Bijelic, M. Aureliano, A. Rompel, The antibacterial activity of polyoxometalates: structures, antibiotic effects and future perspectives, *Chem. Commun.*, 2018, **54**, 1153-1169.
- [6] M.T. Pope, *Heteropoly and Isopoly Oxometalates*, Springer, New York, USA, **1983**.
- [7] D.-L. Long, E. Burkholder, L. Cronin, Polyoxometalate clusters, nanostructures and materials: From self assembly to designer materials and devices, *Chem. Soc. Rev.*, 2007, **36**, 105-121.
- [8] M. Hutin, M. H. Rosnes, D. L. Long, L. Cronin, in *Comprehensive Inorganic Chemistry II: From Elements to Applications, Vol. 2* (Eds.: J. Reedijk, K. Poeppelmeier), Elsevier, Oxford, **2013**, pp. 241-269.
- [9] W. N. Lipscomb, Paratungstate Ion, *Inorg. Chem.*, 1965, **4**, 132-134.
- [10] M. T. Pope, A. Müller, Polyoxometalate Chemistry: An Old Field with New Dimensions in Several Disciplines, *Angew. Chem. Int. Ed.*, 1991, **30**, 34-48.
- [11] H. N. Miras, D. L. Long, L. Cronin, in *Advances in Inorganic Chemistry, Vol. 69* (Eds.: R. van Eldik, L. Cronin), Academic Press, **2017**, pp. 1-28.
- [12] H. N. Miras, G. J. T. Cooper, D.-L. Long, H. Bögge, A. Müller, C. Streb, L. Cronin, Unveiling the Transient Template in the Self-Assembly of a Molecular Oxide Nanowheel, *Science*, 2010, **327**, 72-74.
- [13] Y. Wang, F. Li, N. Jiang, X. Liu, L. Xu, A "directed precursor self-assembly" strategy for the facile synthesis of heteropoly blues: crystal structures, formation mechanism and electron distribution, *Dalton Trans.*, 2019, **48**, 14347-14353.
- [14] H. N. Miras, J. Yan, D.-L. Long, L. Cronin, Engineering polyoxometalates with emergent properties, *Chem. Soc. Rev.*, 2012, **41**, 7403-7430.
- [15] A. Misra, K. Kozma, C. Streb, M. Nyman, Beyond Charge Balance: Counter-Cations in Polyoxometalate Chemistry, *Angew. Chem. Int. Ed.*, 2020, **59**, 596-612.
- [16] L. Dong, L. Zhuonan, S. Jie, L. Hui, Z. Baofang, Y. Panchao, Z. Z. Norm, R. J. E., T. Mesfin, H. C. L., L. Tianbo, Cation Translocation around Single Polyoxometalate–Organic Hybrid Cluster Regulated by Electrostatic and Cation– $\pi$  Interactions, *Angew. Chem. Int. Ed.*, 2017, **56**, 3294-3298.
- [17] R. Contant, in *Inorganic Syntheses, Vol. 27*, John Wiley & Sons, **1990**, pp. 71-135.
- [18] J. M. Cameron, J. Gao, D.-L. Long, L. Cronin, Self-assembly and structural transformations of high-nuclearity palladium-rich polyoxometalates, *Inorg. Chem. Front.*, 2014, **1**, 178-185.
- [19] A. Dolbecq, E. Dumas, C. R. Mayer, P. Mialane, Hybrid Organic–Inorganic Polyoxometalate Compounds: From Structural Diversity to Applications, *Chem. Rev.*, 2010, **110**, 6009-6048.

## 1. Introduction

---

- [20] A. Kondinski, T. N. Parac-Vogt, Keggin Structure, Quō Vādis?, *Front. Chem.*, 2018, **6**.
- [21] J. F. Keggin, Structure of the Molecule of 12-Phosphotungstic Acid, *Nature*, 1933, **131**, 908-909.
- [22] L. C. W. Baker, J. S. Figgis, New fundamental type of inorganic complex: hybrid between heteropoly and conventional coordination complexes. Possibilities for geometrical isomerisms in 11-, 12-, 17-, and 18-heteropoly derivatives, *J. Am. Chem. Soc.*, 1970, **92**, 3794-3797.
- [23] B. Dawson, The structure of the 9(18)-heteropoly anion in potassium 9(18)-tungstophosphate,  $K_6(P_2W_{18}O_{62}) \cdot 14H_2O$ , *Acta. Cryst.*, 1953, **6**, 113-126.
- [24] F.-Q. Zhang, W. Guan, L.-K. Yan, Y.-T. Zhang, M.-T. Xu, E. Hayfron-Benjamin, Z.-M. Su, On the Origin of the Relative Stability of Wells–Dawson Isomers: A DFT Study of  $\alpha$ -,  $\beta$ -,  $\gamma$ -,  $\alpha^*$ -,  $\beta^*$ -, and  $\gamma^*$ - $[(PO_4)_2W_{18}O_{54}]^{6-}$  Anions, *Inorg. Chem.*, 2011, **50**, 4967-4977.
- [25] L. E. Briand, G. T. Baronetti, H. J. Thomas, The state of the art on Wells–Dawson heteropoly-compounds: A review of their properties and applications, *Appl. Catal. A:Gen*, 2003, **256**, 37-50.
- [26] X. López, C. Bo, J. M. Poblet, Electronic Properties of Polyoxometalates: Electron and Proton Affinity of Mixed-Addenda Keggin and Wells–Dawson Anions, *J. Am. Chem. Soc.*, 2002, **124**, 12574-12582.
- [27] K. Nakajima, K. Eda, S. Himeno, Effect of the Central Oxoanion Size on the Voltammetric Properties of Keggin-Type  $[XW_{12}O_{40}]^{n-}$  ( $n = 2-6$ ) Complexes, *Inorg. Chem.*, 2010, **49**, 5212-5215.
- [28] A. V. Anyushin, A. Kondinski, T. N. Parac-Vogt, Hybrid polyoxometalates as post-functionalization platforms: from fundamentals to emerging applications, *Chem. Soc. Rev.*, 2020, **49**, 382-432.
- [29] J. Canny, A. Teze, R. Thouvenot, G. Herve, Disubstituted tungstosilicates. 1. Synthesis, stability, and structure of the lacunary precursor polyanion of a tungstosilicate  $\gamma$ - $SiW_{10}O_{36}^{8-}$ , *Inorg. Chem.*, 1986, **25**, 2114-2119.
- [30] R. Contant, W. G. Klemperer, O. Yaghi, in *Inorganic Syntheses, Vol. 27*, John Wiley & Sons, **1990**, pp. 104-111.
- [31] B. Li, W. Li, H. Li, L. Wu, Ionic Complexes of Metal Oxide Clusters for Versatile Self-Assemblies, *Acc. Chem. Res.*, 2017, **50**, 1391-1399.
- [32] Q. Liu, X. Wang, Polyoxometalate Clusters: Sub-nanometer Building Blocks for Construction of Advanced Materials, *Matter*, 2020, **2**, 816-841.
- [33] W. Qi, L. Wu, Polyoxometalate/polymer hybrid materials: fabrication and properties, *Polym. Int.*, 2009, **58**, 1217-1225.
- [34] P. Gao, Y. Wu, L. Wu, Co-assembly of polyoxometalates and peptides towards biological applications, *Soft Matter*, 2016, **12**, 8464-8479.
- [35] B. Zhang, M. Zhao, Y. Qi, R. Tian, B. B. Carter, H. Zou, C. Zhang, C. Wang, The Intrinsic Enzyme Activities of the Classic Polyoxometalates, *Sci. Rep.*, 2019, **9**, 14832.
- [36] N. Gao, H. Sun, K. Dong, J. Ren, T. Duan, C. Xu, X. Qu, Transition-metal-substituted polyoxometalate derivatives as functional anti-amyloid agents for Alzheimer's disease, *Nat. Commun.*, 2014, **5**, 3422.



## 1. Introduction

---

- [37] M. Inoue, T. Suzuki, Y. Fujita, M. Oda, N. Matsumoto, T. Yamase, Enhancement of antibacterial activity of  $\beta$ -lactam antibiotics by  $[P_2W_{18}O_{62}]^{6-}$ ,  $[SiMo_{12}O_{40}]^{4-}$ , and  $[PTi_2W_{10}O_{40}]^{7-}$  against methicillin-resistant and vancomycin-resistant *Staphylococcus aureus*, *J. Inorg. Biochem.*, 2006, **100**, 1225-1233.
- [38] M. N. Timofeeva, Acid catalysis by heteropoly acids, *Appl. Catal. A:Gen*, 2003, **256**, 19-35.
- [39] K. Kamata, K. Sugahara, Base Catalysis by Mono- and Polyoxometalates, *Catalysts*, 2017, **7**, 345.
- [40] S. Omwoma, C. T. Gore, Y. Ji, C. Hu, Y.-F. Song, Environmentally benign polyoxometalate materials, *Coord. Chem. Rev.*, 2015, **286**, 17-29.
- [41] Y. Zhang, J. Liu, S.-L. Li, Z.-M. Su, Y.-Q. Lan, Polyoxometalate-based materials for sustainable and clean energy conversion and storage, *EnergyChem*, 2019, **1**, 100021.
- [42] Y. Zhang, J. Liu, S.-L. Li, Z.-M. Su, Y.-Q. Lan, Polyoxometalate-based materials for sustainable and clean energy conversion and storage, *EnergyChem*, 2019, **1**, 100021.
- [43] E. Papaconstantinou, Photochemistry of polyoxometallates of molybdenum and tungsten and/or vanadium, *Chem. Soc. Rev.*, 1989, **18**, 1-31.
- [44] C. Streb, New trends in polyoxometalate photoredox chemistry: From photosensitisation to water oxidation catalysis, *Dalton Trans.*, 2012, **41**, 1651-1659.
- [45] G. Kickelbick, in *Hybrid Materials* (Ed.: G. Kickelbick), **2007**, pp. 1-48.
- [46] C. Sanchez, B. Julián, P. Belleville, M. Popall, Applications of hybrid organic-inorganic nanocomposites, *J. Mater. Chem.*, 2005, **15**, 3559-3592.
- [47] I. Hammami, F. Dhifallah, K. Ouari, M. S. Belkhiria, H. Nasri, A new assembly of a Wells-Dawson polyoxometalate-based iron(III) coordination complex hybrid: Synthesis, crystal structure, thermal and electrochemical properties, *Polyhedron*, 2019, **160**, 63-67.
- [48] D. Schaming, C. Costa-Coquelard, S. Sorgues, L. Ruhlmann, I. Lampre, Photocatalytic reduction of  $Ag_2SO_4$  by electrostatic complexes formed by tetracationic zinc porphyrins and tetracobalt Dawson-derived sandwich polyanion, *Appl. Catal. A:Gen*, 2010, **373**, 160-167.
- [49] Y. Martinetto, B. Pégot, C. Roch-Marchal, B. Cottyn-Boitte, S. Floquet, Designing Functional Polyoxometalate-Based Ionic Liquid Crystals and Ionic Liquids, *Eur. J. Inorg. Chem.*, 2020, **2020**, 228-247.
- [50] N. Fay, V. M. Hultgren, A. G. Wedd, T. E. Keyes, R. J. Forster, D. Leane, A. M. Bond, Sensitization of photo-reduction of the polyoxometalate anions  $[S_2M_{18}O_{62}]^{4-}$  (M = Mo, W) in the visible spectral region by the  $[Ru(bpy)_3]^{2+}$  cation, *Dalton Trans.*, 2006, 4218-4227.
- [51] B. Kirchoff, S. Rau, C. Streb, Detecting and Preventing the Formation of Photosensitizer-Catalyst Colloids in Homogeneous Light-Driven Water Oxidation, *Eur. J. Inorg. Chem.*, 2016, **2016**, 1425-1429.
- [52] A. Proust, B. Matt, R. Villanneau, G. Guillemot, P. Gouzerh, G. Izzet, Functionalization and post-functionalization: a step towards polyoxometalate-based materials, *Chem. Soc. Rev.*, 2012, **41**, 7605-7622.

## 1. Introduction

---

- [53] C. P. Pradeep, D.-L. Long, G. N. Newton, Y.-F. Song, L. Cronin, Supramolecular Metal Oxides: Programmed Hierarchical Assembly of a Protein-Sized 21 kDa  $[(C_{16}H_{36}N)_{19}\{H_2NC(CH_2O)_3P_2V_3W_{15}O_{59}\}_4]^{5-}$  Polyoxometalate Assembly, *Angew. Chem. Int. Ed.*, 2008, **47**, 4388-4391.
- [54] A. Blazevic, A. Rompel, The Anderson–Evans polyoxometalate: From inorganic building blocks via hybrid organic–inorganic structures to tomorrows “Bio-POM”, *Coord. Chem. Rev.*, 2016, **307**, 42-64.
- [55] S. Bareyt, S. Piligkos, B. Hasenknopf, P. Gouzerh, E. Lacôte, S. Thorimbert, M. Malacria, Efficient Preparation of Functionalized Hybrid Organic/Inorganic Wells–Dawson-type Polyoxotungstates, *J. Am. Chem. Soc.*, 2005, **127**, 6788-6794.
- [56] G. Sazani, M. T. Pope, Organotin and organogermanium linkers for simple, direct functionalization of polyoxotungstates, *Dalton Trans.*, 2004, **0**, 1989-1994.
- [57] C. R. Mayer, I. Fournier, R. Thouvenot, Bis- and Tetrakis(organosilyl) Decatungstosilicate,  $[\gamma\text{-SiW}_{10}\text{O}_{36}(\text{RSi})_2\text{O}]^{4-}$  and  $[\gamma\text{-SiW}_{10}\text{O}_{36}(\text{RSiO})_4]^{4-}$ : Synthesis and Structural Determination by Multinuclear NMR Spectroscopy and Matrix-Assisted Laser Desorption/Desorption Time-of-Flight Mass Spectrometry, *Chem. Eur. J.*, 2000, **6**, 105-110.
- [58] J. Niu, M. Li, J. Wang, Organosilyl derivatives of trivacant tungstophosphate of general formula  $\alpha\text{-A-}[\text{PW}_9\text{O}_{34}(\text{RSiO})_3(\text{RSi})]^{3-}$ : Synthesis and structure determination by X-ray crystallography, *J. Organomet. Chem.*, 2003, **675**, 84-90.
- [59] B. Matt, S. Renaudineau, L. M. Chamoreau, C. Afonso, G. Izzet, A. Proust, Hybrid Polyoxometalates: Keggin and Dawson Silyl Derivatives as Versatile Platforms, *J. Org. Chem.*, 2011, **76**, 3107-3112.
- [60] K. Nomiya, Y. Togashi, Y. Kasahara, S. Aoki, H. Seki, M. Noguchi, S. Yoshida, Synthesis and Structure of Dawson Polyoxometalate-Based, Multifunctional, Inorganic–Organic Hybrid Compounds: Organogermyl Complexes with One Terminal Functional Group and Organosilyl Analogues with Two Terminal Functional Groups, *Inorg. Chem.* 2011, **50**, 9606–9619
- [61] R. Villanneau, A. B. Djamâa, L.-M. Chamoreau, G. Gontard, A. Proust, Bisorganophosphonyl and -Organoarsenyl Derivatives of Heteropolytungstates as Hard Ligands for Early-Transition-Metal and Lanthanide Cations, *Eur. J. Inorg. Chem.*, 2013, **2013**, 1815-1820.
- [62] G. S. Kim, K. S. Hagen, C. L. Hill, Synthesis, structure, spectroscopic properties, and hydrolytic chemistry of organophosphonoyl polyoxotungstates of formula  $[\text{C}_6\text{H}_5\text{P}(\text{O})]_2\text{X}^{n+}\text{W}_{11}\text{O}_{39}^{(8-n)-}$  ( $\text{X}^{n+} = \text{P}^{5+}, \text{Si}^{4+}$ ), *Inorg. Chem.*, 1992, **31**, 5316-5324.
- [63] C. R. Mayer, P. Herson, R. Thouvenot, Organic–Inorganic Hybrids Based on Polyoxometalates. 5.1 Synthesis and Structural Characterization of Bis(organophosphoryl)decatungstosilicates  $[\gamma\text{-SiW}_{10}\text{O}_{36}((\text{RPO})_2)]^{4-}$ , *Inorg. Chem.*, 1999, **38**, 6152-6158.
- [64] J. M. Cameron, S. Fujimoto, K. Kastner, R.-J. Wei, D. Robinson, V. Sans, G. N. Newton, H. H. Oshio, Orbital Engineering: Photoactivation of an Organofunctionalized Polyoxotungstate, *Chem. Eur. J.*, 2017, **23**, 47-50.

## 1. Introduction

---

- [65] A. J. Kibler, G. N. Newton, Tuning the electronic structure of organic–inorganic hybrid polyoxometalates: The crucial role of the covalent linkage, *Polyhedron*, 2018, **154**, 1-20.
- [66] M. Boujtita, J. Boixel, E. Blart, C. R. Mayer, F. Odobel, Redox properties of hybrid Dawson type polyoxometalates disubstituted with organo-silyl or organo-phosphoryl moieties, *Polyhedron*, 2008, **27**, 688-692.
- [67] F. Odobel, M. Séverac, Y. Pellegrin, E. Blart, C. Fosse, C. Cannizzo, C. R. Mayer, K. J. Elliott, A. Harriman, Coupled Sensitizer–Catalyst Dyads: Electron-Transfer Reactions in a Perylene–Polyoxometalate Conjugate, *Chem. Eur. J.*, 2009, **15**, 3130-3138.
- [68] S.-X. Zhang, L. Liu, F.-B. Li, Z.-L. Du, Synthesis, characterization and photoelectric properties of Dawson-type polyoxometalate covalently linked to zinc(II) porphyrin, *Inorganica Chim. Acta*, 2016, **453**, 179-185.
- [69] S. Fujimoto, J. M. Cameron, R.-J. Wei, K. Kastner, D. Robinson, V. Sans, G. N. Newton, H. Oshio, A Simple Approach to the Visible-Light Photoactivation of Molecular Metal Oxides, *Inorg. Chem.*, 2017, **56**, 12169-12177.
- [70] J. M. Cameron, S. Fujimoto, R.-J. Wei, G. N. Newton, H. Oshio, Post-functionalization of a photoactive hybrid polyoxotungstate, *Dalton Trans.*, 2018, **47**, 10590-10594.
- [71] R. Villanneau, D. Racimor, E. Messner-Henning, H. Rousselière, S. Picart, R. Thouvenot, A. Proust, Insights into the Coordination Chemistry of Phosphonate Derivatives of Heteropolyoxotungstates, *Inorg. Chem.*, 2011, **50**, 1164-1166.
- [72] M.-P. Santoni, G. S. Hanan, B. Hasenknopf, Covalent multi-component systems of polyoxometalates and metal complexes: Toward multi-functional organic–inorganic hybrids in molecular and material sciences, *Coord. Chem. Rev.*, 2014, **281**, 64-85.
- [73] A. Saad, O. Oms, A. Dolbecq, C. Menet, R. Dessapt, H. Serier-Brault, E. Allard, K. Baczko, P. Mialane, A high fatigue resistant, photoswitchable fluorescent spiropyran-polyoxometalate-BODIPY single-molecule, *Chem. Commun.*, 2015, **51**, 16088-16091.
- [74] V. Tagliavini, C. Honisch, S. Serratì, A. Azzariti, M. Bonchio, P. Ruzza, M. Carraro, Enhancing the biological activity of polyoxometalate–peptide nano-fibrils by spacer design, *RSC Advances*, 2021, **11**, 4952-4957.
- [75] N. I. Gumerova, A. Blazevic, T. Fraile Caldera, A. Roller, G. Giester, A. Rempel, Synthesis and characterization of hybrid Anderson hexa-molybdoaluminates(III) functionalized with indometacin or cinnamic acid, *Acta. Cryst. C*, 2018, **74**, 1378-1383.
- [76] M. Stuckart, K. Y. Monakhov, Polyoxometalates as components of supramolecular assemblies, *Chem. Sci.*, 2019, **10**, 4364-4376.
- [77] Q. Yan, Z. Luo, K. Cai, Y. Ma, D. Zhao, Chemical designs of functional photoactive molecular assemblies, *Chem. Soc. Rev.*, 2014, **43**, 4199-4221.
- [78] D. L. Ashford, M. K. Gish, A. K. Vannucci, M. K. Brennaman, J. L. Templeton, J. M. Papanikolas, T. J. Meyer, Molecular Chromophore–Catalyst Assemblies for Solar Fuel Applications, *Chem. Rev.*, 2015, **115**, 13006-13049.
- [79] C. Dai, B. Liu, Conjugated polymers for visible-light-driven photocatalysis, *Energy Environ Sci*, 2020, **13**, 24-52.

## 1. Introduction

---

- [80] D. Gust, T. A. Moore, A. L. Moore, Solar Fuels via Artificial Photosynthesis, *Acc. Chem. Res.*, 2009, **42**, 1890-1898.
- [81] J. Xie, B. F. Abrahams, A. G. Wedd, Facile assembly of hybrid materials containing polyoxometalate cluster anions and organic dye cations: crystal structures and initial spectral characterization, *Chem. Commun.*, 2008, 576-578.
- [82] J. M. Cameron, D. J. Wales, G. N. Newton, Shining a light on the photo-sensitisation of organic–inorganic hybrid polyoxometalates, *Dalton Trans.*, 2018, **47**, 5120-5136.
- [83] A. Harriman, K. J. Elliott, M. A. H. Alamiry, L. L. Pleux, M. Séverac, Y. Pellegrin, E. Blart, C. Fosse, C. Cannizzo, C. R. Mayer, F. Odobel, Intramolecular Electron Transfer Reactions Observed for Dawson-Type Polyoxometalates Covalently Linked to Porphyrin Residues, *J. Phys. Chem. C*, 2009, **113**, 5834-5842.
- [84] B. Matt, C. Coudret, C. Viala, D. Jouvenot, F. Loiseau, G. Izzet, A. Proust, Elaboration of Covalently Linked Polyoxometalates with Ruthenium and Pyrene Chromophores and Characteriation of Their Photophysical Properties, *Inorg. Chem.*, 2011, **50**, 7761-7768.
- [85] K. Barthelmes, M. Sittig, A. Winter, U. S. Schubert, Molecular Dyads and Triads Based on Phenothiazine and  $\pi$ -Extended Tetrathiafulvalene Donors, Bis(terpyridine)ruthenium(II) Complexes, and Polyoxometalates, *Eur. J. Inorg. Chem.*, 2017, 3698-3706.
- [86] T. Auvray, M.-P. Santoni, B. Hasenknopf, G. S. Hanan, Covalent hybrids based on Re(i) tricarbonyl complexes and polypyridine-functionalized polyoxometalate: synthesis, characterization and electronic properties, *Dalton Trans.*, 2017, **46**, 10029-10036.
- [87] M.-P. Santoni, A. K. Pal, G. S. Hanan, M.-C. Tang, A. Furtos, B. Hasenknopf, A light-harvesting polyoxometalate-polypyridine hybrid induces electron transfer as its Re(i) complex, *Dalton Trans.*, 2014, **43**, 6990-6993.
- [88] J. Ettetdgui, Y. Diskin-Posner, L. Weiner, R. Neumann, Photoreduction of Carbon Dioxide to Carbon Monoxide with Hydrogen Catalyzed by a Rhenium(I) Phenanthroline–Polyoxometalate Hybrid Complex, *J. Am. Chem. Soc.*, 2011, **133**, 188-190.
- [89] G. Izzet, F. Volatron, A. Proust, Tailor–made Covalent Organic-Inorganic Polyoxometalate Hybrids: Versatile Platforms for the Elaboration of Functional Molecular Architectures, *The Chemical Record*, 2017, **17**, 250-266.
- [90] B. Matt, X. Xiang, A. L. Kaledin, N. Han, J. Moussa, H. Amouri, S. Alves, C. L. Hill, T. Lian, D. G. Musaev, G. Izzet, A. Proust, Long lived charge separation in iridium(iii)-photosensitized polyoxometalates: synthesis, photophysical and computational studies of organometallic-redox tunable oxide assemblies, *Chem. Sci.*, 2013, **4**, 1737-1745.
- [91] B. Matt, J. Fize, J. Moussa, H. Amouri, A. Pereira, V. Artero, G. Izzet, A. Proust, Charge Photo-Accumulation and Photocatalytic Hydrogen Evolution Under Visible Light at an Iridium(III)-Photosensitized Polyoxotungstate, *Energy Environ Sci*, 2013, **6**, 1504-1508.
- [92] S. Schönweiz, M. Heiland, M. Anjass, T. Jacob, S. Rau, C. Streb, Experimental and Theoretical Investigation of the Light-Driven Hydrogen Evolution by Polyoxometalate–Photosensitizer Dyads, *Chem. Eur. J.*, 2017, **23**, 15370-15376.

## 1. Introduction

---

- [93] S. Schönweiz, S. A. Rommel, J. Kübel, M. Micheel, B. Dietzek, S. Rau, C. Streb, Covalent Photosensitizer–Polyoxometalate–Catalyst Dyads for Visible-Light-Driven Hydrogen Evolution, *Chem. Eur. J.*, 2016, **22**, 12002-12005.
- [94] M. Bonchio, M. Carraro, G. Scorrano, A. Bagno, Photooxidation in Water by New Hybrid Molecular Photocatalysts Integrating an Organic Sensitizer with a Polyoxometalate Core, *Advanced Synthesis & Catalysis*, 2004, **346**, 648-654.
- [95] F. A. Black, A. Jacquart, G. Toupalas, S. Alves, A. Proust, I. P. Clark, E. A. Gibson, G. Izzet, Rapid photoinduced charge injection into covalent polyoxometalate–bodipy conjugates, *Chem. Sci.*, 2018, **9**, 5578-5584.
- [96] G. Toupalas, J. Karlsson, F. A. Black, A. Masip-Sánchez, X. López, Y. Ben M'Barek, S. Blanchard, A. Proust, S. Alves, P. Chabera, I. P. Clark, T. Pullerits, J. M. Poblet, E. A. Gibson, G. Izzet, Tuning Photoinduced Electron Transfer in POM-Bodipy Hybrids by Controlling the Environment: Experiment and Theory, *Angew. Chem. Int. Ed.*, 2020, **60**, 6518-6525.
- [97] A. Parrot, A. Bernard, A. Jacquart, S. A. Serapian, C. Bo, E. Derat, O. Oms, A. Dolbecq, A. Proust, R. Métivier, P. Mialane, G. Izzet, Photochromism and Dual-Color Fluorescence in a Polyoxometalate–Benzospiropyran Molecular Switch, *Angew. Chem. Int. Ed.*, 2017, **56**, 4872-4876.
- [98] O. Oms, K. Hakouk, R. Dessapt, P. Deniard, S. Jobic, A. Dolbecq, T. Palacin, L. Nadjo, B. Keita, J. Marrot, P. Mialane, Photo- and electrochromic properties of covalently connected symmetrical and unsymmetrical spiropyran-polyoxometalate dyads, *Chem. Commun.*, 2012, **48**, 12103-12105.
- [99] Y. Yan, H. Wang, B. Li, G. Hou, Z. Yin, L. Wu, V. W. W. Yam, Smart Self-Assemblies Based on a Surfactant-Encapsulated Photoresponsive Polyoxometalate Complex, *Angew. Chem. Int. Ed.*, 2010, **49**, 9233-9236.
- [100] J. Wang, C.-G. Lin, J. Zhang, J. Wei, Y.-F. Song, J. Guo, Polyoxometalate-based organic–inorganic hybrids for stabilization and optical switching of the liquid crystal blue phase, *J. Mater. Chem. C.*, 2015, **3**, 4179-4187.
- [101] G. M. Whitesides, J. K. Kriebel, B. T. Mayers, D. J. Lockwood, in *Nanoscale Assembly: Chemical Techniques, Vol. VIII* (Ed.: W. T. S. Huck), Springer (formerly Kluwer), Cambridge, UK, **2005**, pp. 217-239.
- [102] E. Busseron, Y. Ruff, E. Moulin, N. Giuseppone, Supramolecular self-assemblies as functional nanomaterials, *Nanoscale*, 2013, **5**, 7098-7140.
- [103] Y. Sun, C. Chen, P. J. Stang, Soft Materials with Diverse Suprastructures via the Self-Assembly of Metal–Organic Complexes, *Acc. Chem. Res.*, 2019, **52**, 802-817.
- [104] S. Landsmann, C. Lizandara-Pueyo, S. Polarz, A New Class of Surfactants with Multinuclear, Inorganic Head Groups, *J. Am. Chem. Soc.*, 2010, **132**, 5315-5321.
- [105] K. Kastner, A. J. Kibler, E. Karjalainen, J. A. Fernandes, V. Sans, G. N. Newton, Redox-active organic-inorganic hybrid polyoxometalate micelles, *J. Mater. Chem. A*, 2017, **5**, 11577-11581.
- [106] A. Klaiiber, S. Polarz, Passing Current through Electrically Conducting Lyotropic Liquid Crystals and Micelles Assembled from Hybrid Surfactants with  $\pi$ -Conjugated Tail and Polyoxometalate Head, *ACS Nano*, 2016, **10**, 10041-10048.

## 1. Introduction

---

- [107] A. Klaiber, T. Kollek, S. Cardinal, N. Hug, M. Drechsler, S. Polarz, Electron Transfer in Self-Assembled Micelles Built by Conductive Polyoxometalate-Surfactants Showing Battery-Like Behavior, *Adv. Mater. Interfaces*, 2018, **5**, 1701430.
- [108] S. Zhou, Y. Feng, M. Chen, Q. Li, B. Liu, J. Cao, X. Sun, H. Li, J. Hao, Robust onionlike structures with magnetic and photodynamic properties formed by a fullerene C60–POM hybrid, *Chem. Commun.*, 2016, **52**, 12171-12174.
- [109] U. Tong, W. Chen, C. Ritchie, X. Wang, Y.-F. Song, Reversible Light-Driven Polymerization of Polyoxometalate Tethered with Coumarin Molecules, *Chem. Eur. J.*, 2014, **20**, 1500-1504.
- [110] I. Azcarate, I. Ahmed, R. Farha, M. Goldmann, X. Wang, H. Xu, B. Hasenknopf, E. Lacôte, L. Ruhlmann, Synthesis and characterization of conjugated Dawson-type polyoxometalate–porphyrin copolymers, *Dalton Trans.*, 2013, **42**, 12688-12698.
- [111] D. Schaming, C. Allain, R. Farha, M. Goldmann, S. Lobstein, A. Giraudeau, B. Hasenknopf, L. Ruhlmann, Synthesis and Photocatalytic Properties of Mixed Polyoxometalate–Porphyrin Copolymers Obtained from Anderson-Type Polyoxomolybdates, *Langmuir*, 2010, **26**, 5101-5109.
- [112] M. Carraro, G. Fiorani, L. Mognon, F. Caneva, M. Gardan, C. Maccato, M. Bonchio, Hybrid Polyoxotungstates as Functional Comonomers in New Cross-Linked Catalytic Polymers for Sustainable Oxidation with Hydrogen Peroxide, *Chem. Eur. J.*, 2012, **18**, 13195-13202.
- [113] A. S. Cherevan, S. P. Nandan, I. Roger, R. Liu, C. Streb, D. Eder, Polyoxometalates on Functional Substrates: Concepts, Synergies, and Future Perspectives, *Adv. Sci.*, 2020, **7**, 1903511.
- [114] S. Gam Derouich, C. Rinfray, G. Izzet, J. Pinson, J.-J. Gallet, F. Kanoufi, A. Proust, C. Combellas, Control of the Grafting of Hybrid Polyoxometalates on Metal and Carbon Surfaces: Toward Submonolayers, *Langmuir*, 2014, **30**, 2287-2296.
- [115] M. Laurans, K. Trinh, K. Dalla Francesca, G. Izzet, S. Alves, E. Derat, V. Humblot, O. Pluchery, D. Vuillaume, S. Lenfant, F. Volatron, A. Proust, Covalent Grafting of Polyoxometalate Hybrids onto Flat Silicon/Silicon Oxide: Insights from POMs Layers on Oxides, *ACS Appl. Mater. Interfaces*, 2020, **12**, 48109-48123.
- [116] Y. Ben M'Barek, T. Rosser, J. Sum, S. Blanchard, F. Volatron, G. Izzet, R. Salles, J. Fize, M. Koepf, M. Chavarot-Kerlidou, V. Artero, A. Proust, Dye-Sensitized Photocathodes: Boosting Photoelectrochemical Performances with Polyoxometalate Electron Transfer Mediators, *ACS Applied Energy Materials*, 2020, **3**, 163-169.
- [117] F. Volatron, J.-M. Noël, C. Rinfray, P. Decorse, C. Combellas, F. Kanoufi, A. Proust, Electron transfer properties of a monolayer of hybrid polyoxometalates on silicon, *J. Mater. Chem. C.*, 2015, **3**, 6266-6275.
- [118] M. Laurans, K. Dalla Francesca, F. Volatron, G. Izzet, D. Guerin, D. Vuillaume, S. Lenfant, A. Proust, Molecular signature of polyoxometalates in electron transport of silicon-based molecular junctions, *Nanoscale*, 2018, **10**, 17156-17165.
- [119] Y. Ji, J. Hu, L. Huang, W. Chen, C. Streb, Y.-F. Song, Covalent Attachment of Anderson-Type Polyoxometalates to Single-Walled Carbon Nanotubes Gives Enhanced Performance Electrodes for Lithium Ion Batteries, *Chem. Eur. J.*, 2015, **21**, 6469-6474.

## 1. Introduction

---

- [120] S. Zhao, X. Zhao, S. Ouyang, Y. Zhu, Polyoxometalates covalently combined with graphitic carbon nitride for photocatalytic hydrogen peroxide production, *Catalysis Science & Technology*, 2018, **8**, 1686-1695.
- [121] R. Chakrabarty, P. S. Mukherjee, P. J. Stang, Supramolecular Coordination: Self-Assembly of Finite Two- and Three-Dimensional Ensembles, *Chem. Rev.*, 2011, **111**, 6810-6918.
- [122] H. Dong, Y. Yang, F. Zhao, W. Ji, B. Liu, H. Hu, Y. Wang, H. Huang, Y. Liu, Z. Kang, Coordination site induced controllable assembly of metal-organic units in polyoxometalate-based hybrids, *Inorg. Chem. Commun.*, 2014, **44**, 107-110.
- [123] Y.-Q. Jiao, C. Qin, H.-Y. Zang, W.-C. Chen, C.-G. Wang, T.-T. Zheng, K.-Z. Shao, Z.-M. Su, Assembly of organic-inorganic hybrid materials constructed from polyoxometalate and metal-1,2,4-triazole units: synthesis, structures, magnetic, electrochemical and photocatalytic properties, *CrystEngComm*, 2015, **17**, 2176-2189.
- [124] S. Farhadi, M. M. Amini, M. Dusek, M. Kucerakova, F. Mahmoudi, A new nanohybrid material constructed from Keggin-type polyoxometalate and Cd(II) semicarbazone Schiff base complex with excellent adsorption properties for the removal of cationic dye pollutants, *J. Mol. Struct.*, 2017, **1130**, 592-602.
- [125] X. Ma, H. Li, L. Chen, J. Zhao, The main progress over the past decade and future outlook on high-nuclear transition-metal substituted polyoxotungstates: from synthetic strategies, structural features to functional properties, *Dalton Trans.*, 2016, **45**, 4935-4960.
- [126] D. Li, P. Ma, J. Niu, J. Wang, Recent advances in transition-metal-containing Keggin-type polyoxometalate-based coordination polymers, *Coord. Chem. Rev.*, 2019, **392**, 49-80.
- [127] F.-J. Yazigi, C. Wilson, D.-L. Long, R. S. Forgan, Synthetic Considerations in the Self-Assembly of Coordination Polymers of Pyridine-Functionalized Hybrid Mn-Anderson Polyoxometalates, *Crystal Growth & Design*, 2017, **17**, 4739-4748.
- [128] J. W. Han, C. L. Hill, A Coordination Network That Catalyzes O<sub>2</sub>-Based Oxidations, *J. Am. Chem. Soc.*, 2007, **129**, 15094-15095.
- [129] M.-P. Santoni, A. K. Pal, G. S. Hanan, M.-C. Tang, K. Venne, A. Furtos, P. Ménard-Tremblay, C. Malveau, B. Hasenknopf, Coordination-driven self-assembly of polyoxometalates into discrete supramolecular triangles, *Chem. Commun.*, 2012, **48**, 200-202.
- [130] G. Izzet, A. Macdonell, C. Rinfrey, M. Piot, S. Renaudineau, E. Derat, B. Abécassis, C. Afonso, A. Proust, Metal-Directed Self-Assembly of a Polyoxometalate-Based Molecular Triangle: Using Powerful Analytical Tools to Probe the Chemical Structure of Complex Supramolecular Assemblies, *Chem. Eur. J.*, 2015, **21**, 19010-19015.
- [131] M. Piot, S. Hupin, H. Lavanant, C. Afonso, L. Bouteiller, A. Proust, G. Izzet, Charge Effect on the Formation of Polyoxometalate-Based Supramolecular Polygons Driven by Metal Coordination, *Inorg. Chem.*, 2017, **56**, 8490-8496.
- [132] Y. Zhu, P. Yin, F. Xiao, D. Li, E. Bitterlich, Z. Xiao, J. Zhang, J. Hao, T. Liu, Y. Wang, Y. Wei, Bottom-Up Construction of POM-Based Macrostructures: Coordination Assembled Paddle-Wheel Macroclusters and Their Vesicle-like Supramolecular Aggregation in Solution, *J. Am. Chem. Soc.*, 2013, **135**, 17155-17160.

## 1. Introduction

---

- [133] R. Salles, B. Abécassis, E. Derat, D. Brouri, A. Bernard, Q. Zhang, A. Proust, C. Desmarets, G. Izzet, Hierarchical Self-Assembly of Polyoxometalate-Based Organo Palladium(II) Metallomacrocycles via Electrostatic Interactions, *Inorg. Chem.*, 2020, **59**, 2458-2463.
- [134] G. Izzet, B. Abécassis, D. Brouri, M. Piot, B. Matt, S. A. Serapian, C. Bo, A. Proust, Hierarchical Self-Assembly of Polyoxometalate-Based Hybrids Driven by Metal Coordination and Electrostatic Interactions: From Discrete Supramolecular Species to Dense Monodisperse Nanoparticles, *J. Am. Chem. Soc.*, 2016, **138**, 5093-5099.
- [135] M. Piot, B. Abécassis, D. Brouri, C. Troufflard, A. Proust, G. Izzet, Control of the hierarchical self-assembly of polyoxometalate-based metallomacrocycles by redox trigger and solvent composition, *Proc. Nat. Acad. Sci.*, 2018, **115**, 8895-8900.
- [136] P. Yin, T. Li, R. S. Forgan, C. Lydon, X. Zuo, Z. N. Zheng, B. Lee, D. Long, L. Cronin, T. Liu, Exploring the Programmable Assembly of a Polyoxometalate–Organic Hybrid via Metal Ion Coordination, *J. Am. Chem. Soc.*, 2013, **135**, 13425-13432.
- [137] Y.-F. Song, D.-L. Long, S. E. Kelly, L. Cronin, Sorting the Assemblies of Unsymmetrically Covalently Functionalized Mn-Anderson Polyoxometalate Clusters with Mass Spectrometry, *Inorg. Chem.*, 2008, **47**, 9137-9139.
- [138] B. Liu, J. Yang, M. Yang, Y. Wang, N. Xia, Z. Zhang, P. Zheng, W. Wang, I. Lieberwirth, C. Kubel, Polyoxometalate cluster-contained hybrid gelator and hybrid organogel: a new concept of softening of polyoxometalate clusters, *Soft Matter*, 2011, **7**, 2317-2320.
- [139] V. Lahootun, C. Besson, R. Villanneau, F. Villain, L.-M. Chamoreau, K. Boubekur, S. Blanchard, R. Thouvenot, A. Proust, Synthesis and Characterization of the Keggin-Type Ruthenium-Nitrido Derivative  $[PW_{11}O_{39}\{RuN\}]^{4-}$  and Evidence of Its Electrophilic Reactivity, *J. Am. Chem. Soc.*, 2007, **129**, 7127-7135.
- [140] C. Dablemont, C. G. Hamaker, R. Thouvenot, Z. Sojka, M. Che, E. A. Maatta, A. Proust, Functionalization of Heteropolyanions—Osmium and Rhenium Nitrido Derivatives of Keggin- and Dawson-Type Polyoxotungstates: Synthesis, Characterization and Multinuclear ( $^{183}W$ ,  $^{15}N$ ) NMR, EPR, IR, and UV/Vis Fingerprints, *Chem. Eur. J.*, 2006, **12**, 9150-9160.
- [141] X.-L. Wang, Y.-L. Wang, W.-K. Miao, M.-B. Hu, J. Tang, W. Yu, Z.-Y. Hou, P. Zheng, W. Wang, Langmuir and Langmuir–Blodgett Films of Hybrid Amphiphiles with a Polyoxometalate Headgroup, *Langmuir*, 2013, **29**, 6537-6545.
- [142] C. Yvon, A. Macdonell, S. Buchwald, A. J. Surman, N. Follet, J. Alex, D.-L. Long, L. Cronin, A collection of robust methodologies for the preparation of asymmetric hybrid Mn-Anderson polyoxometalates for multifunctional materials, *Chem. Sci.*, 2013, **4**, 3810-3817.
- [143] P. Wu, P. Yin, J. Zhang, J. Hao, Z. Xiao, Y. Wei, Single-Side Organically Functionalized Anderson-Type Polyoxometalates, *Chem. Eur. J.*, 2011, **17**, 12002-12005.
- [144] J. Zhang, J. Luo, P. Wang, B. Ding, Y. Huang, Z. Zhao, J. Zhang, W. Yongge, Step-by-Step Strategy from Achiral Precursors to Polyoxometalates-Based Chiral Organic–Inorganic Hybrids, *Inorg. Chem.*, 2015, **54**, 2551-2559.
- [145] K. Micoine, M. Malacria, E. Lacôte, S. Thorimbert, B. Hasenknopf, Regioselective Double Organic Functionalization of Polyoxotungstates through Electrophilic Addition



## 1. Introduction

---

- of Aromatic Isocyanates to  $[P_2W_{17}O_{61}(SnR)]^{7-}$ , *Eur. J. Inorg. Chem.*, 2013, **2013**, 1737-1741.
- [146] C. Boglio, K. Micoine, É. Derat, R. Thouvenot, B. Hasenknopf, S. Thorimbert, E. Lacôte, M. Malacria, Regioselective Activation of Oxo Ligands in Functionalized Dawson Polyoxotungstates, *J. Am. Chem. Soc.*, 2008, **130**, 4553-4561.
- [147] C. Yvon, A. J. Surman, M. Hutin, J. Alex, B. O. Smith, D. L. Long, L. Cronin, Polyoxometalate Clusters Integrated into Peptide Chains and as Inorganic Amino Acids: Solution- and Solid-Phase Approaches, *Angew. Chem. Int. Ed.*, 2014, **53**, 3336-3341.
- [148] A. Macdonell, N. A. B. Johnson, A. J. Surman, L. Cronin, Configurable Nanosized Metal Oxide Oligomers via Precise "Click" Coupling Control of Hybrid Polyoxometalates, *J. Am. Chem. Soc.*, 2015, **137**, 5662-5665.
- [149] A. Saad, O. Oms, J. Marrot, A. Dolbecq, K. Hakouk, H. El Bekkachi, S. Jobic, P. Deniard, R. Dessapt, D. Garrot, K. Boukheddaden, R. Liu, G. Zhang, B. Keita, P. Mialane, Design and optical investigations of a spironaphthoxazine/polyoxometalate/spiropyran triad, *J. Mater. Chem. C.*, 2014, **2**, 4748-4758.
- [150] A. Boulmier, A. Vacher, D. Zang, S. Yang, A. Saad, J. Marrot, O. Oms, P. Mialane, I. Ledoux, L. Ruhlmann, D. Lorcy, A. Dolbecq, Anderson-Type Polyoxometalates Functionalized by Tetrathiafulvalene Groups: Synthesis, Electrochemical Studies, and NLO Properties, *Inorg. Chem.*, 2018, **57**, 3742-3752.
- [151] Y.-F. Song, N. McMillan, D.-L. Long, S. Kane, J. Malm, M. O. Riehle, C. P. Pradeep, N. Gadegaard, L. Cronin, Micropatterned Surfaces with Covalently Grafted Unsymmetrical Polyoxometalate-Hybrid Clusters Lead to Selective Cell Adhesion, *J. Am. Chem. Soc.*, 2009, **131**, 1340-1341.
- [152] M. H. Rosnes, C. Musumeci, C. P. Pradeep, J. S. Mathieson, D.-L. Long, Y.-F. Song, B. Pignataro, R. Cogdell, L. Cronin, Assembly of Modular Asymmetric Organic-Inorganic Polyoxometalate Hybrids into Anisotropic Nanostructures, *J. Am. Chem. Soc.*, 2010, **132**, 15490-15492.
- [153] Y. Chu, A. Saad, P. Yin, J. Wu, O. Oms, A. Dolbecq, P. Mialane, T. Liu, Light- and Solvent-Controlled Self-Assembly Behavior of Spiropyran-Polyoxometalate-Alkyl Hybrid Molecules, *Chem. Eur. J.*, 2016, **22**, 11756-11762.

## 2 Aims

The work presented in this thesis aimed to address the existing synthetic challenge in the preparation of asymmetrically functionalised organic–inorganic hybrid POMs to advance towards their development as multifunctional materials. Access to asymmetric hybrid structures specifically derived from the redox-active Wells-Dawson anion, for which stable asymmetric hybrid structures have not yet been reported, is of particularly high value as this could lead to the development of new multifunctional hybrid POM materials with electro-, photo- and redox- activity that is highly tuneable through their controlled molecular design.

This research aimed, firstly, to devise an effective and reliable synthetic approach to prepare asymmetrically organofunctionalised hybrid POMs based on the Wells-Dawson anion. A strategy was to be developed by which the covalent attachment of distinct organic components would ideally not only facilitate the isolation of the asymmetric hybrid POM, but also introduce multiple functions into the hybrid POM material.

Secondly, this work aimed to probe the functional characteristics of the asymmetric hybrid POMs by characterisation of their structures and their physical properties that are derived from the multiple components in the molecular structure.

This work also set out to gain insight into the design of asymmetric hybrid POMs as functional molecular ‘building blocks’, by probing their supramolecular assembly and exploring their functionalisation by metal-ion coordination and surface-immobilisation. This was with the key overall research aim to gain fundamental insights of the properties and structures of this new family of asymmetric hybrid POMs which can help to unlock new POM-based material applications.

### 3 Design and synthesis of asymmetric hybrid POM (1)

This chapter covers work published in the article: “Asymmetric Hybrid Polyoxometalates: A Platform for Multifunctional Redox-Active Nanomaterials”, E. Hampson, J. M. Cameron, S. Amin, J. Kyo, J. A. Watts, H. Oshio, G. N. Newton, *Angew. Chem. Int. Ed.* 2019, **58**, 18281-18285.

The development of asymmetric organofunctionalisation strategies for the redox-active Dawson anion will be valuable in the design of advanced multifunctional hybrid systems for new materials in a variety of applications. In this chapter, the synthesis of the unique asymmetric Dawson POM hybrid,  $K_4(C_2H_8N)_2[P_2W_{17}O_{57}\{(PO_3C_{21}H_{14}N_3)(PO_4C_{24}H_{41})\}]$  (**1**), will be presented, followed by its full characterisation.

The development and optimisation of the easily accessible and inexpensive one-pot synthetic procedure that has been devised for **1** will first be discussed. This involves initially an exploration of the post-modification of symmetrically organofunctionalised Keggin and Dawson hybrid POMs, through reactions of ligand terminal groups and a ligand cleavage methodology. Following on from this, the investigation of one-pot reactions of POM anions with distinct organophosphonate ligands will be discussed, leading on to the development of the finalised synthetic procedure for the preparation and isolation of **1**.

The characterisation of the unique structure of **1** is then discussed, including a study into its redox properties. Finally, the characterisation of the symmetric hybrid POMs that are side products in the preparation of **1** is also described. Their properties are explored and provide insight into the unique multifunctionality of the asymmetric hybrid **1**.

## 3.1 Preliminary asymmetric hybrid synthesis methodologies

### 3.1.1 Post-modification of symmetric hybrid POMs

The preparation of asymmetric hybrid POMs from the post-modification of symmetrically organo-functionalised hybrid POMs has been explored in a few studies as discussed in 1.3.1. The postfunctionalisation of symmetric hybrid POMs by the reaction of functional groups on the organic ligands has been a common approach. However, purification steps to remove unreacted and doubly-postfunctionalised symmetric hybrids are often unavoidable, at least initially, requiring slow crystallisation steps<sup>[1-2]</sup> or the use of protecting groups to allow controlled modification of the ligands.<sup>[3]</sup>

The use of stoichiometry in the postfunctionalisation of symmetric hybrid POMs was investigated briefly in this work. A Dawson hybrid POM,  $K_3(C_2H_8N)_3[P_2W_{17}O_{57}\{(PO_3C_2H_4COOH)_2\}]$ , (**Sym<sub>PPA</sub>**) was prepared using a simple, commercially available organophosphonate ligand with a terminal carboxylic acid group, 3-phosphonopropionic acid (PPA), that could be versatile in various postfunctionalisation reactions. The reaction of amines with carboxylic acid functionalised POM hybrids has been demonstrated in many instances in the literature.<sup>[4-6]</sup> Stoichiometric quantities of a primary amine compound were used in a condensation reaction with **Sym<sub>PPA</sub>** with the intention of forming an amide bond on just one of the two ligands. The reaction of one molar equivalent of 2,2-diphenylethylamine with **Sym<sub>PPA</sub>** using EEDQ ((2-ethoxy-1-ethoxycarbonyl-1,2-dihydroquinoline) as an amide coupling agent resulted in a POM hybrid mixture consisting of the desired singly coupled asymmetric product, but alongside doubly coupled product and uncoupled **Sym<sub>PPA</sub>** too, as revealed by <sup>31</sup>P NMR analysis (Fig.27). Attempts to then purify the mixture by solvent washes were not successful due to the similar solubilities of all three POM hybrids in all solvents used.

Attention was then brought to an approach along the lines of the elegant methodologies reported by Zhang *et al.* and Micoine *et al.*, in which singly-organofunctionalised Anderson and Dawson-type clusters respectively were

### 3. Design and synthesis of asymmetric hybrid POM (1)

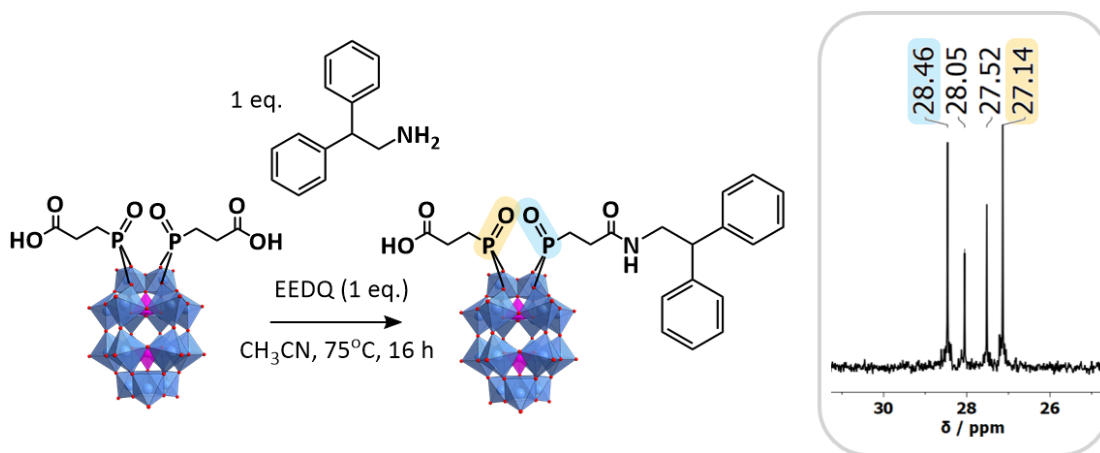


**Figure 27.** Left: amide coupling of carboxylic acid-terminated Dawson hybrid **Sym**<sub>PPA</sub> to prepare the desired asymmetric hybrid product; right: <sup>31</sup>P NMR in CD<sub>3</sub>CN of the hybrid POM product mixture showing the positive spectral region for simplicity and the signals for the asymmetric product highlighted. Signals for symmetric hybrids are at 27.52 (**Sym**<sub>PPA</sub>) and 28.05 ppm (doubly amide-coupled).

postfunctionalised with a second organic moiety in a two-step synthesis, avoiding the need for tenuous purification from symmetric side-products. A similar and particularly promising approach was found in the work published in a thesis by Laura M. Perkins.<sup>[7]</sup> She found that under certain basic conditions just one of the two covalently grafted ligands in symmetric organophosphonate decatungstosilicate hybrid POMs could be cleaved to leave a singly-functionalised hybrid. It was shown that this new hybrid could be isolated and then reacted in a subsequent step with a second, different organophosphonate to isolate asymmetric hybrid structures.

POMs are known to be base-sensitive, decomposing by hydrolysis by hydroxyl species (essentially, the reverse process of their assembly in acidic solution).<sup>[8]</sup> Base-degradation of hybrid POMs can result in the breaking of covalent bonds to grafted organic groups.<sup>[9]</sup> As the grafting of phosphonates onto POMs is also via acid hydrolysis, the degradation of organophosphonate hybrid POMs under basic conditions can be expected. The use of an organic base, benzylamine, was used by Perkins to remove various phosphonate groups, RPO, from [SiW<sub>10</sub>O<sub>36</sub>{(RPO)<sub>2</sub>}], where R=HOOC(CH<sub>2</sub>)<sub>n</sub> (n=1 or 2), H<sub>3</sub>CCOC<sub>6</sub>H<sub>4</sub>, CH<sub>2</sub>=CHCH<sub>2</sub>, CH<sub>2</sub>=CH or Et. A number of asymmetric silicotungstate hybrid POMs were then prepared from the singly-

### 3. Design and synthesis of asymmetric hybrid POM (1)

---

functionalisation hybrid POMs with the general formula,  $[\text{SiW}_{10}\text{O}_{36}\{(\text{R}_1\text{PO})(\text{R}_2\text{PO})\}]$ :  $\text{R}_1$  and  $\text{R}_2 = \text{H}_2\text{C}=\text{CH}$ ,  $\text{H}_2\text{C}=\text{CHCH}_2$ ,  $\text{HOOC}(\text{CH}_2)_n$  ( $n = 1$  or  $2$ ),  $\text{H}_3\text{CCOC}_6\text{H}_4$  or  $\text{H}_2\text{C}=\text{CHC}_6\text{H}_4$ .

To investigate this ligand cleavage approach, a phosphonopropionic acid-functionalised  $\{\text{SiW}_{10}\}$  cluster as used by Perkins was prepared. A slight excess of benzylamine, 3 equivalents (2 eq.s can be expected to be necessary for the cleavage of the two hydroxyl groups of one phosphonic acid), was stirred with the hybrid overnight and the isolated solid was characterised by  $^1\text{H}$  and  $^{31}\text{P}$  NMR. Propionic acid proton signals in the  $^1\text{H}$  NMR were promisingly shifted from in the starting material, and a single peak slightly downfield shifted by a few ppm was observed in the  $^{31}\text{P}$  NMR, indicative of a single new phosphorus environment, as observed in Perkins' work (Fig.28). However, on reaction with a second ligand, phenylphosphonic acid, signals corresponding to hybrid POMs symmetrically functionalised with both phosphonate ligands were observed in addition to the desired asymmetric product (Fig.28), suggesting both phosphonopropionic acid groups in some of the hybrid POM had been removed. The organic base likely assists the generation of hydroxyl species that hydrolyse the phosphonate groups, and despite the reaction being conducted under an inert dry atmosphere, as used by Perkins, traces of water must be sufficient for the base hydrolysis. Control in whether the available hydroxyls cleave just one or both of the phosphonates on a hybrid POM is likely to be very difficult with this method.

Reactions with the phosphonopropionic acid Dawson hybrid equivalent, **Sym<sub>PPA</sub>**, were attempted but were unsuccessful. Although transformation into a single new POM-based species was suggested by  $^{31}\text{P}$  NMR, only the symmetric hybrid starting material and free ligands were observed after reaction with a second ligand, phenylphosphonic acid, indicating unsuccessful cleavage. Finally, ligand cleavage with benzylamine was also attempted with a phenylphosphonate-functionalised  $\{\text{SiW}_{10}\}$  hybrid,  $\text{TBA}_3\text{H}[\text{SiW}_{10}\text{O}_{36}\{(\text{PhPO})_2\}]$ , under the same conditions. However, several new  $^{31}\text{P}$  signals were observed in the NMR suggestive of extensive decomposition, confirming the poor control in this method and it was not investigated further.

### 3. Design and synthesis of asymmetric hybrid POM (1)

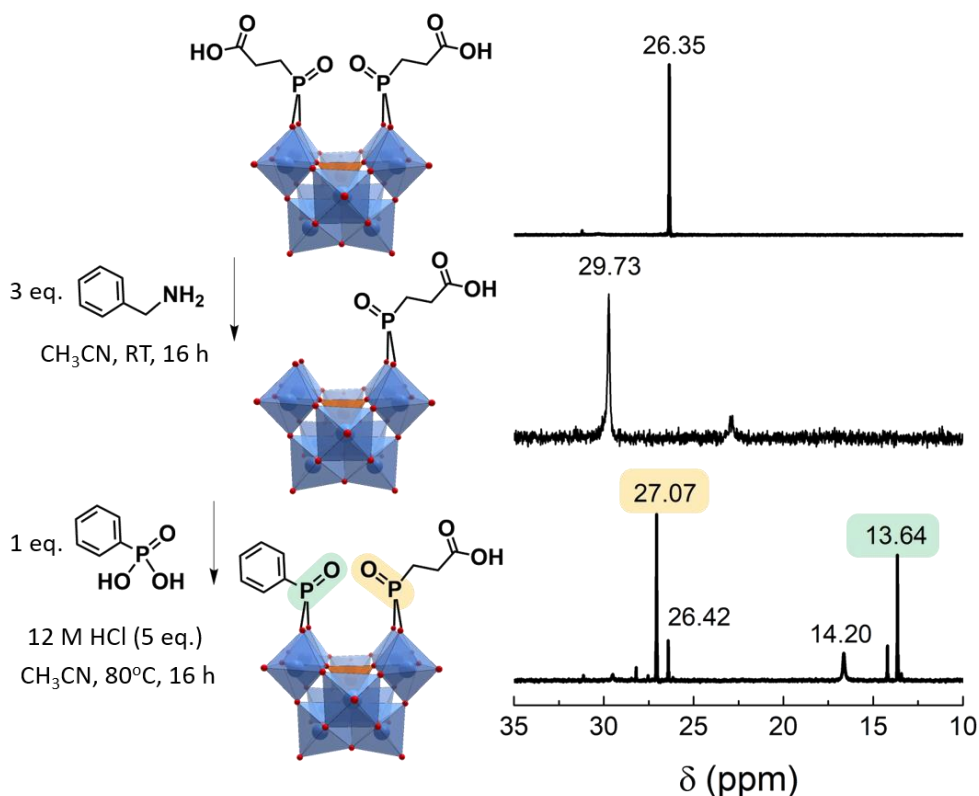


**Figure 28.** Left: Scheme for asymmetric hybrid synthesis via the partial base hydrolysis of a symmetric hybrid; right: stacked <sup>31</sup>P NMR spectra, top: symmetric PPA hybrid; middle: singly PPA- functionalised hybrid after hydrolysis; bottom: hybrid POM product mixture showing the signals for the desired asymmetric product highlighted, and signals for symmetric hybrid impurities at 14.20 (phenylphosphonic acid) and 26.42 (PPA) ppm.

#### 3.1.2 Purification from one pot reaction mixtures

A one-pot synthetic approach to asymmetric hybrid POM synthesis was then explored. The purification of the desired asymmetric hybrid POM from the symmetric hybrid POM side-products is the main challenge with this approach, as investigated by Cronin and co-workers in several studies.<sup>[3, 10]</sup> With the aim of isolating asymmetric hybrid products without the use of expensive or slow and complex purification techniques, such as reverse-phase HPLC and fractional crystallisation methods reported, solvent extraction steps to purify the asymmetric product were investigated. Different combinations of phosphonic acid ligands were used in

### 3. Design and synthesis of asymmetric hybrid POM (1)

reactions with POM anions to test the effectiveness of the solvent extraction approach.

The di-lacunary decatungstosilicate anion  $[\text{SiW}_{10}\text{O}_{36}]^{8-}$   $\{\text{SiW}_{10}\}$  and the mono-lacunary phosphotungstate anion  $[\text{P}_2\text{W}_{17}\text{O}_{61}]^{10-}$   $\{\text{P}_2\text{W}_{17}\}$  were again used for initial experimentation with this one-pot synthesis approach. The potassium salt of  $\{\text{SiW}_{10}\}$  was reacted with combinations of two phosphonic acid ligands. Three commercially available phosphonic acids were used: 3-phosphonopropionic acid, 2-aminoethylphosphonic acid and phenylphosphonic acid, in addition to a bulkier terpyridine-substituted phenylphosphonic acid, **TPY**, which was synthesised (described in 3.2) (Fig.29). Equimolar quantities of the anion and of each of the two ligands were reacted in an acid-catalysed condensation reaction. In a typical reaction, the starting materials were heated in DMA at 85°C overnight, using four molar equivalents of acid (12M HCl) and four molar equivalents of TBABr were additionally added to assist in the precipitation of the hybrids as TBA salts. On reaction completion, the crude hybrid mixtures were shown by  $^{31}\text{P}$  NMR analysis to consist of a mixture of the three hybrids expected- the asymmetric hybrid and two symmetric hybrid side-products.

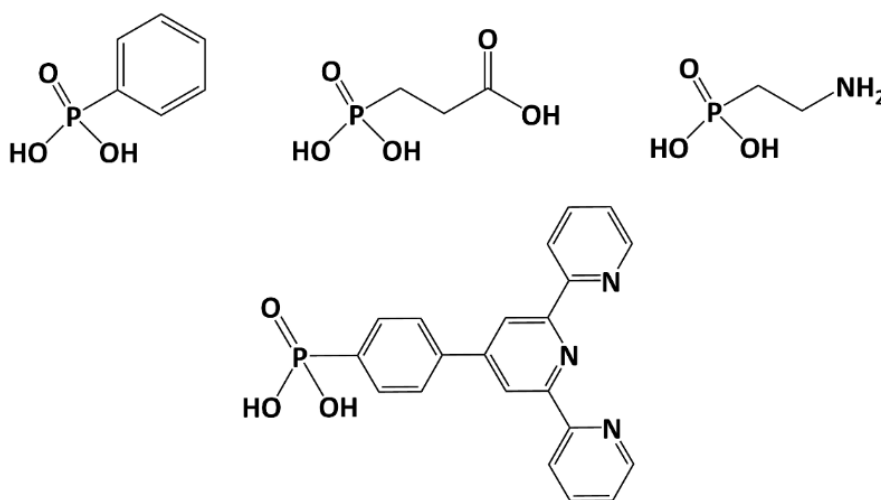


**Figure 29.** The phosphonic acids used, from top left: phenylphosphonic acid, 3-phosphonopropionic acid, 2-aminoethylphosphonic acid and **TPY**.



### 3. Design and synthesis of asymmetric hybrid POM (1)

---

Purification through solvent extractions was then explored for the crude hybrid mixtures, the results of which proved to be highly variable and poorly reproducible between reaction attempts for all ligand combinations. The symmetric and asymmetric hybrid products in all reactions unfortunately could not easily be separated by their exclusive dissolution in any solvent. The highest purity obtained in an asymmetric hybrid POM product was from a one-pot reaction of 3-phosphonopropionic acid and **TPY** with {SiW<sub>10</sub>}, the procedure of which is as follows. The crude hybrid mixture was isolated as a solid by precipitation with excess ether, which was then sonicated in a small volume of acetonitrile. On centrifugation of the suspension, a solid was collected that was shown by <sup>31</sup>P NMR to consist of the asymmetric product and symmetric *TPY* hybrid. The solid mixture was sonicated again in very small amounts of acetonitrile before centrifugation in attempts to dissolve just the asymmetric product which was expected to be more soluble. However, <sup>31</sup>P NMR revealed both the supernatant and solid to always remain a mixture of the two hybrids (Fig.30). In attempts to then isolate the asymmetric product from the acetonitrile supernatant obtained from the first centrifugation, the solvent was removed *in vacuo* and the obtained solid was then sonicated in acetone. After centrifugation, the insoluble solid was shown to consist of mostly the symmetric *TPY* hybrid with some asymmetric product, whilst the solid obtained from evaporation of the acetone was shown to be the asymmetric product, although in very small yield, in high purity. However, the reaction and work-up was repeated several times, conducting washes in acetonitrile and acetone similarly, but the asymmetric hybrid could not be isolated again without some symmetric *TPY* hybrid present. The similarity in solubility of the two hybrids is likely largely facilitated by the TBA cations, indicating the importance of the nature of the cations in determining the relative solubilities of hybrid POMs and the ease of their purification.

### 3. Design and synthesis of asymmetric hybrid POM (1)

The reaction and work-up procedures were then repeated using the Dawson POM anion  $\{P_2W_{17}\}$ , including both with the use of TBABr to prepare the hybrid products as TBA salts, as well as without- to isolate them as potassium salts. Unfortunately, most attempts at solvent extractions were unsuccessful with both, with isolated solid consisting of some amounts of two or all three hybrids throughout the process, and so reproducibility in the purification procedure could not be achieved. The solubility of the symmetric and asymmetric hybrid POM products in various solvents is still too similar using this ligand combination, indicating the need for the design and use of two more highly distinct ligands.

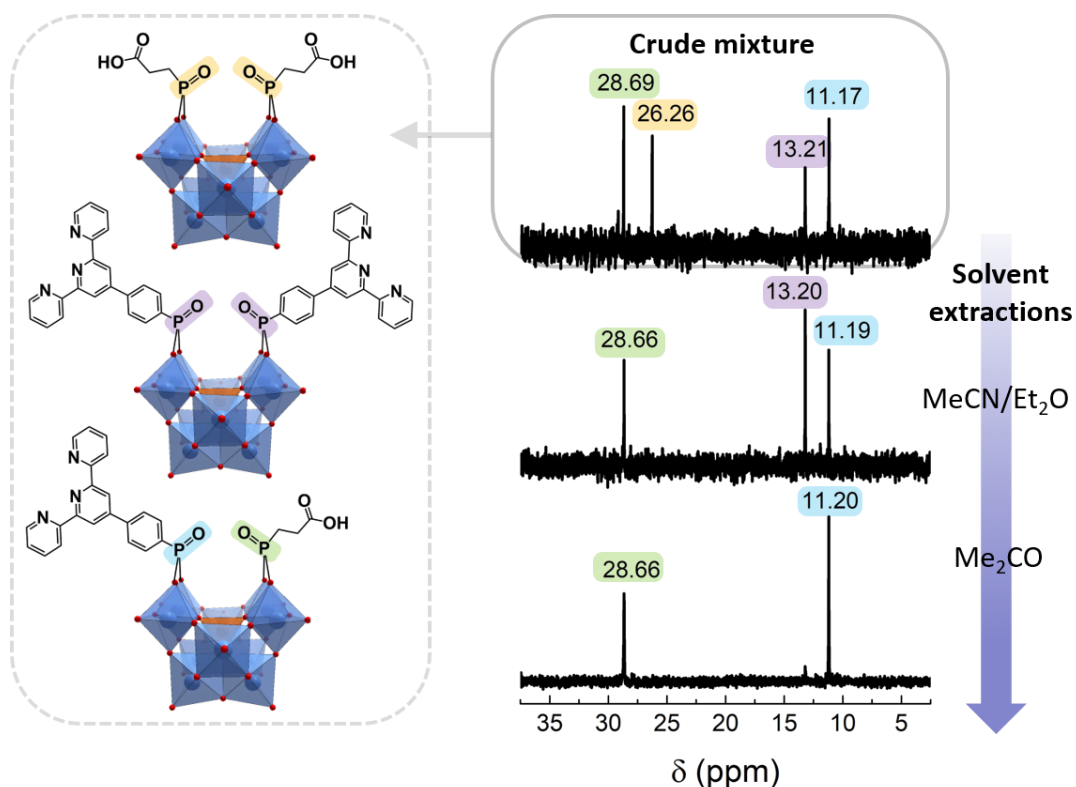


**Figure 30.** Left: The structures of the three hybrid POMs in the crude product mixture of the one-pot synthesis; Right: Stacked  $^{31}\text{P}$  NMR spectra in DMSO- $d_6$  of the reaction mixture following each purification step, top: crude mixture; middle: asymmetric product and symmetric *TPY*; bottom: purified asymmetric product.

### 3.2 Design of two distinct ligands, TPY and C<sub>18</sub>

With the aim to introduce two distinct, orthogonal functionalities via asymmetric functionalisation, two suitably different phosphonates were designed and synthesised. Due to the tuneability that aryl phosphonates can provide in the electronic structure of hybrid POMs because of their conjugation,<sup>[11]</sup> focus was drawn to aryl phosphonic acids and two were prepared accordingly: a terpyridine-based ligand, **TPY** (PO(OH)<sub>2</sub>C<sub>21</sub>H<sub>14</sub>N<sub>3</sub>), and an aliphatic chain group, **C<sub>n</sub>** (PO(OH)<sub>2</sub>C<sub>6</sub>H<sub>4</sub>C<sub>n</sub>H<sub>2n+1</sub>, n= 10, 16, 18)) (Fig.31). It was also hoped that the different nature of these two ligands would facilitate the one-pot synthetic approach by imparting sufficiently different solubilities in the hybrid products so that purification would be possible through successive solvent washes.

The terpyridine-based ligand, **TPY**, was prepared according to a 3-step procedure (Fig.32) starting with the Kröhnke condensation of 4-bromobenzaldehyde and 2-acetylpyridine to form the bromo-functionalised phenylterpyridine, BrTPY.<sup>[12]</sup> A phosphonate ester group was then introduced by a palladium-catalysed C-P coupling reaction using diethylphosphite to prepare PO(OEt)<sub>2</sub>TPY.<sup>[13]</sup> Lastly, hydrolysis of the phosphonate ester groups was performed using bromotrimethylsilane (TMSBr), leaving the desired phosphonic acid, **TPY**, after cleavage of the trimethylsilyl

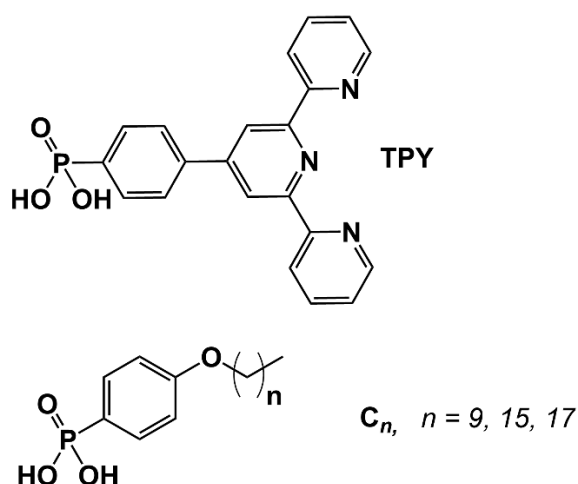


**Figure 31.** Structures of the synthesised phosphonic acid ligands, **TPY** and **C<sub>n</sub>**.

### 3. Design and synthesis of asymmetric hybrid POM (1)

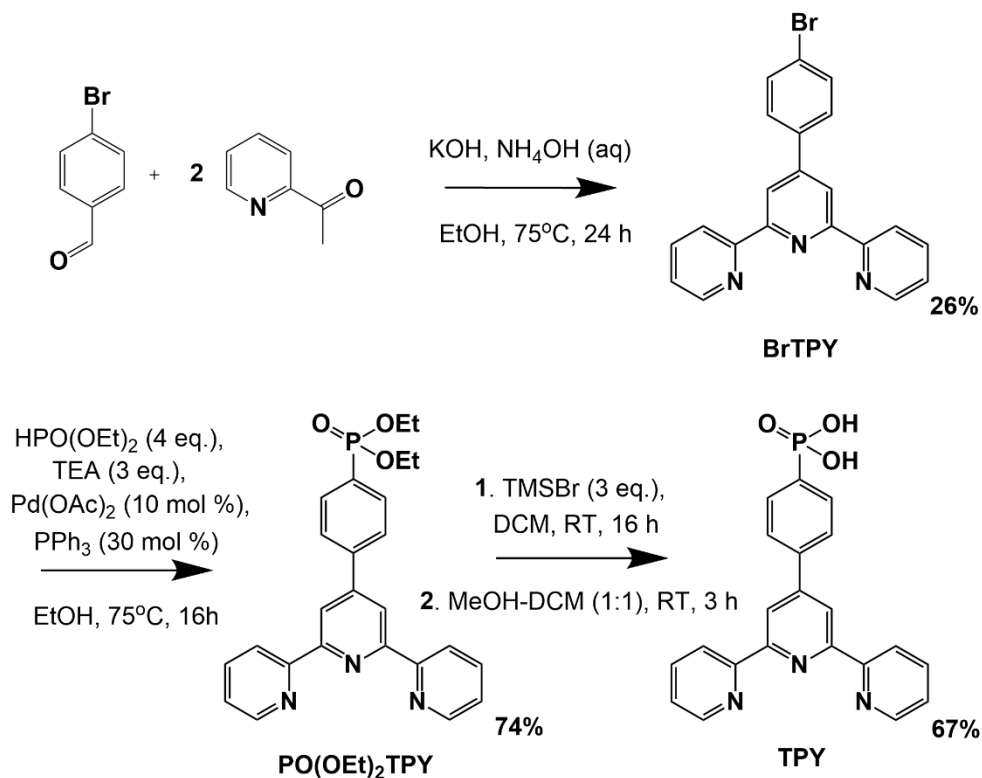


Figure 32. Synthesis of the TPY ligand.

protecting groups. The <sup>1</sup>H NMR of TPY confirmed successful hydrolysis with the disappearance of alkyl proton signals and presence of 14 aromatic protons (Fig.33), and a single P-containing species is observed in the <sup>31</sup>P NMR.

The aliphatic chain ligands, C<sub>10</sub>, C<sub>16</sub> and C<sub>18</sub> were prepared in similar 3-step synthetic procedures (Fig.34), which were optimised by another PhD student, Sharad Amin, in our research group and reported in a recent paper.<sup>[14]</sup> Only the synthesis of C<sub>18</sub> will be described here, as C<sub>10</sub> and C<sub>16</sub> samples were provided by Amin and were not reproduced. Bromophenol was first reacted with bromooctadecane to form the bromo aryl ether, Br-C<sub>18</sub>. This was then reacted with triethylphosphite in a C-P coupling catalysed by nickel (II) chloride under microwave conditions to give the phosphonate ester, PO(OEt)<sub>2</sub>-C<sub>18</sub>. Finally, the ester was hydrolysed via cleavage of trimethylsilyl groups using TMSBr similarly as for TPY. <sup>31</sup>P NMR confirmed the isolation of a single P-containing species and <sup>1</sup>H NMR confirmed the structure of C<sub>18</sub> containing

### 3. Design and synthesis of asymmetric hybrid POM (1)

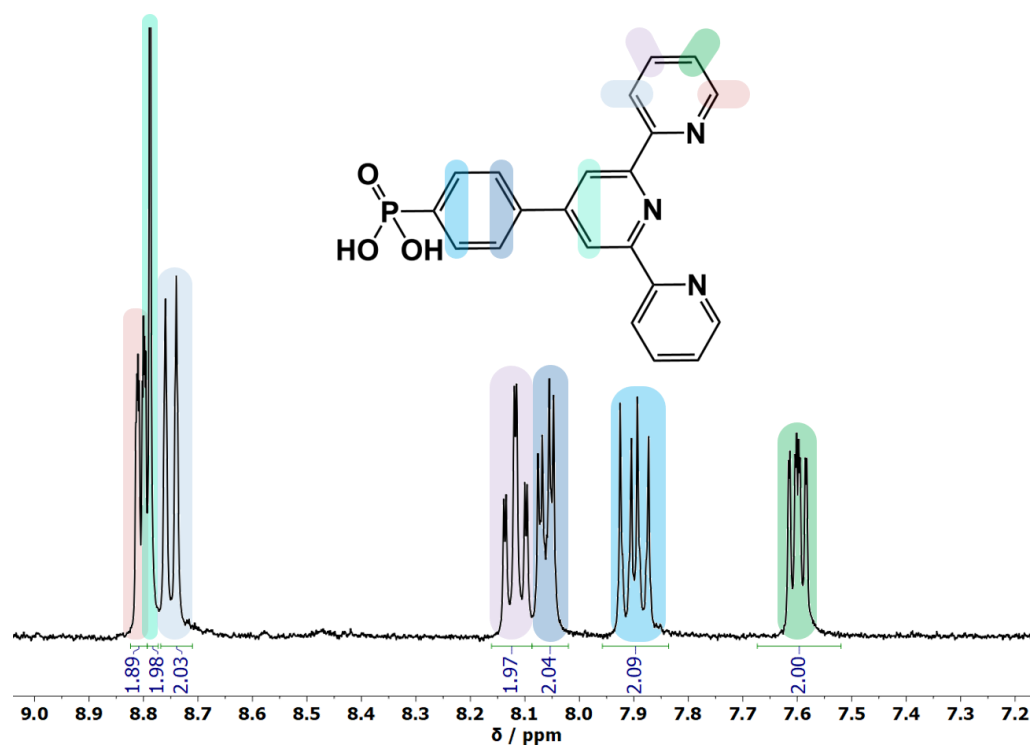


Figure 33.  $^1\text{H}$  NMR of the TPY ligand in  $\text{DMSO-d}_6$ .

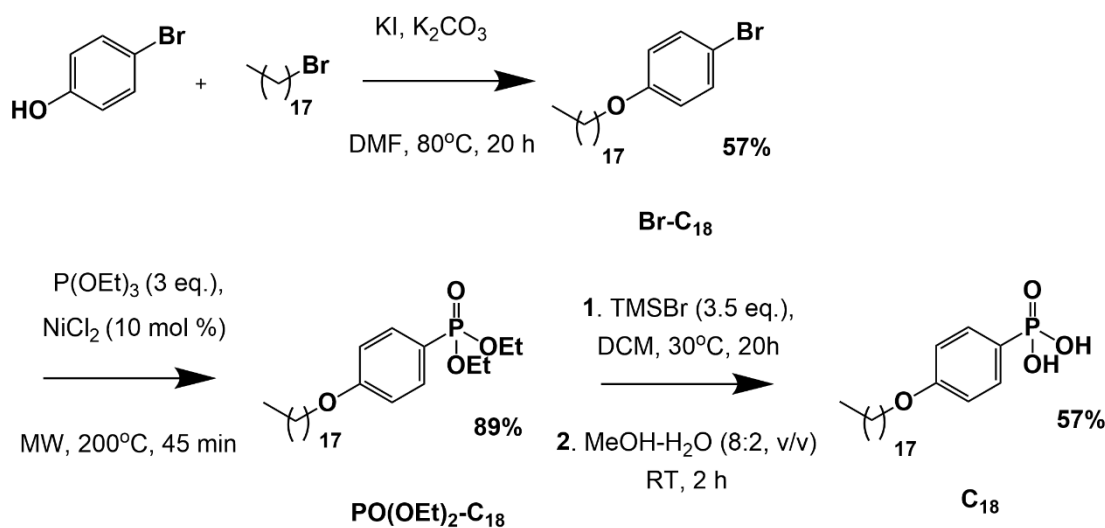
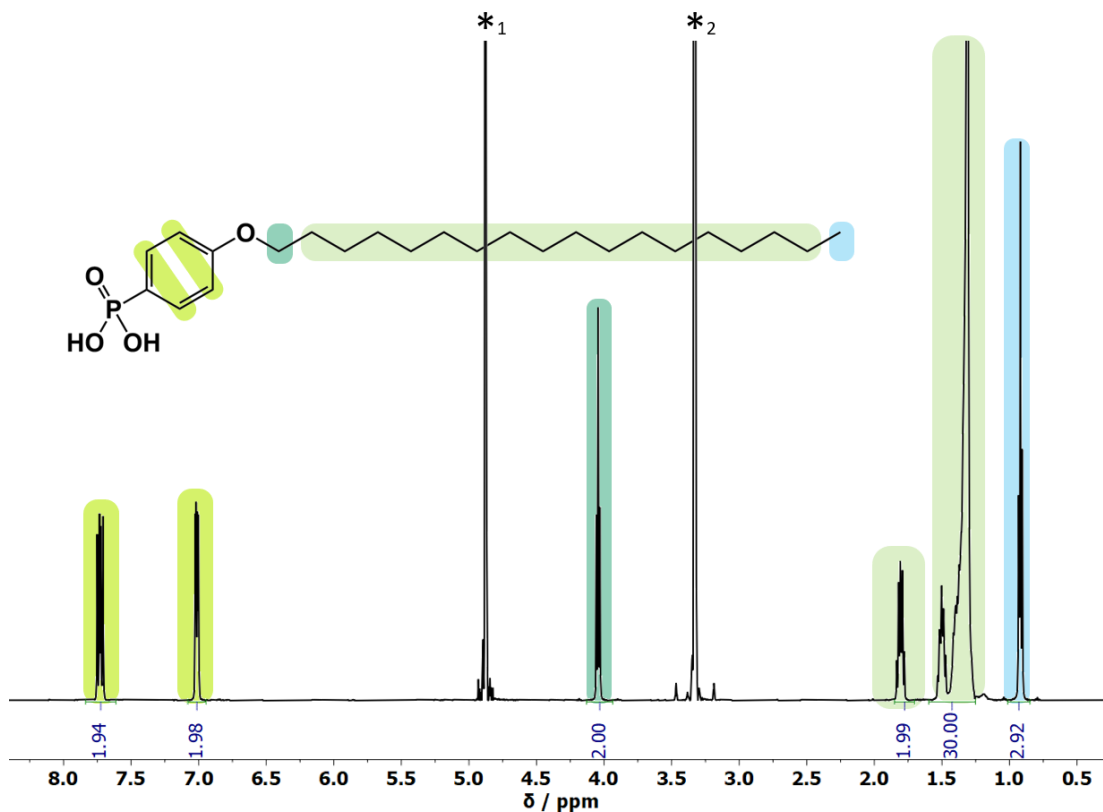


Figure 34. Synthesis of the  $\text{C}_{18}$  ligand.

4 aromatic protons and 37 alkyl protons (Fig.35). The structures of both phosphonic acids TPY and  $\text{C}_{18}$  were also further confirmed by ESI-MS and elemental (CHN) analysis.

### 3. Design and synthesis of asymmetric hybrid POM (1)



**Figure 35.**  $^1\text{H}$  NMR of  $\text{C}_{18}$  in methanol- $d_4$ . Black asterisks indicate solvent impurities: 1=  $\text{H}_2\text{O}$ , 2 = MeOH.

One pot reactions were then conducted with  $\{\text{P}_2\text{W}_{17}\}$  using the combination of the terpyridine-based ligand **TPY** with an aliphatic chain ligand  $\text{C}_n$ . Reactions were carried out in a 1:1 solvent mixture of DMF and acetonitrile and refluxed at  $85^\circ\text{C}$  in order to adequately solubilise both ligands.  $^{31}\text{P}$  NMR was again used to confirm successful covalent attachment of both phosphonates to result in a mixture of three hybrid POM products in the crude product mixture. The process of solvent extractions to isolate the asymmetric product was again experimented. This was hoped to be facilitated with the retention of the potassium cations of the  $\{\text{P}_2\text{W}_{17}\}$  anion by omitting the addition of an alkylammonium salt.

The initial product precipitated from the  $\text{CH}_3\text{CN}$ -DMF crude mixture using ether was analysed by  $^{31}\text{P}$  NMR. Notably, the signal for the symmetric  $\text{C}_n$  hybrid was often significantly reduced from that in the crude mixture while signals for the symmetric **TPY** and asymmetric products remained.  $^{31}\text{P}$  NMR of the solid residue after removing

### 3. Design and synthesis of asymmetric hybrid POM (1)

---

solvent from the supernatant *in vacuo* showed it to consist mostly of the symmetric  $C_n$  hybrid. The solubility of the symmetric  $C_n$  hybrids in a mostly ether-based solvent mixture is likely facilitated by the long alkyl chain ligands. The separation of the remaining mixture of hybrid POMs with consecutive extractions in acetonitrile and acetone, as used for the asymmetric {SiW<sub>10</sub>} discussed above, was then tested. Isolation of the asymmetric hybrids incorporating the two shorter chain ligands, **AsymC<sub>10</sub>** and **AsymC<sub>16</sub>**, in high purity was managed after sufficient cycles of solvent extractions (see experimental details in 3.7.2.6, 3.7.2.7). However, the purification was again poorly reproducible. The effectiveness of extraction steps as determined by <sup>31</sup>P NMR was found to vary between reaction batches, particularly in the separation of the symmetric  $C_n$  hybrid from the asymmetric hybrid, so high purity products could not be obtained consistently. Nevertheless, isolation of the asymmetric hybrid in which the longest chain ligand,  $C_{18}$ , was appended (**1**) was found to be significantly more straightforward, with greater consistency in the purification process. This is possibly due to an effect of the longer alkyl chain enhancing the solubility of the symmetric  $C_{18}$  hybrid in ether. A reliable synthesis and purification procedure for **1** could be developed, the details of which are discussed in the following section.

### 3.3 One-pot synthesis and purification of asymmetric hybrid POM [P<sub>2</sub>W<sub>17</sub>O<sub>57</sub>{(TPY)(C<sub>18</sub>)}] (1)

In a one-pot acid-catalysed condensation reaction, one molar equivalent each of the phosphonic acid ligands **TPY** and **C<sub>18</sub>**, were reacted with one molar equivalent of the potassium salt of the mono-lacunary Dawson-type anion [P<sub>2</sub>W<sub>17</sub>O<sub>61</sub>]<sup>10-</sup> in a 1:1 acidified solvent mixture of DMF and acetonitrile (Fig.36).

After reaction completion, <sup>31</sup>P NMR spectroscopy indicated the presence of three species in the crude product mixture, later fully characterised as the asymmetric hybrid, K<sub>4</sub>(C<sub>2</sub>H<sub>8</sub>N)<sub>2</sub>[P<sub>2</sub>W<sub>17</sub>O<sub>57</sub>{(PO<sub>3</sub>C<sub>21</sub>H<sub>14</sub>N<sub>3</sub>)(PO<sub>4</sub>C<sub>24</sub>H<sub>41</sub>)}] (**1**), the symmetric **TPY** hybrid, (C<sub>2</sub>H<sub>8</sub>N)<sub>6</sub>[P<sub>2</sub>W<sub>17</sub>O<sub>57</sub>{(PO<sub>3</sub>C<sub>21</sub>H<sub>14</sub>N<sub>3</sub>)<sub>2</sub>}] (**2**) (see 3.5), and symmetric  $C_{18}$  hybrid K<sub>2</sub>(C<sub>2</sub>H<sub>8</sub>N)<sub>4</sub>[P<sub>2</sub>W<sub>17</sub>O<sub>57</sub>{(PO<sub>4</sub>C<sub>24</sub>H<sub>41</sub>)<sub>2</sub>}] (**3**) (see 3.5). The signals for the covalently-bound

### 3. Design and synthesis of asymmetric hybrid POM (1)

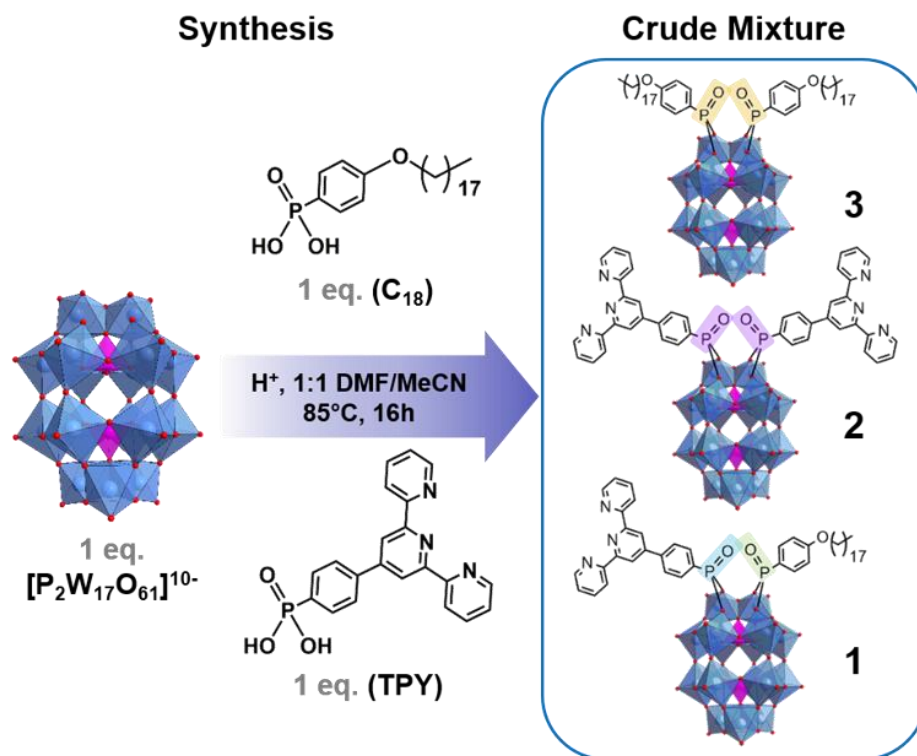


**Figure 36.** One pot synthesis of the asymmetric hybrid POM, **1**, and the crude product mixture also containing the symmetric hybrid POM side products, **2** and **3**.

ligands, *TPY* and *C<sub>18</sub>*, appear at 13.31 and 16.77 ppm respectively and the corresponding bound ligand peaks appear at 14.10 and 15.96 ppm for the respective symmetric structures, **2** and **3** (Fig.37). Three pairs of signals are also observed in the negative shift region assigned to the pairs of phosphorus centres in the POM core of each of the three hybrids.

Isolation of the desired asymmetric hybrid product, **1**, was achieved by a series of solvent extractions as follows. A large excess of ether was first added to the orange-yellow reaction mixture upon which the solution turned cloudy. On centrifugation, a mixture of orange-brown and green solid was collected and the yellow supernatant decanted. Removing the solvent from the supernatant leaves an orange-brown crystalline solid that by  $^{31}P$  NMR is identified as **3**. The remaining crude solid, a mixture of **2** and **1**, was re-dissolved in minimal acetonitrile, in which **2** is known to only be sparingly soluble and can be separated by centrifugation. Finally, an excess of



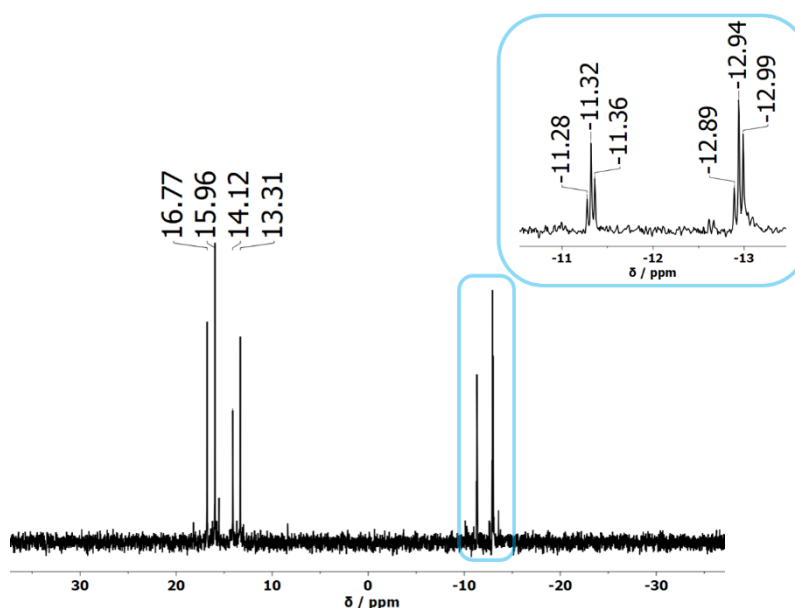


**Figure 37.**  $^{31}\text{P}$  NMR of the crude mixture of hybrid POM products in the synthesis of **1** in  $\text{DMSO-d}_6$ . Inset shows an expansion of the peaks in the negative spectral region.

ether was used to re-precipitate **1** from the acetonitrile, leaving any traces of **3** in solution. The process of dissolution in minimum acetonitrile to remove any insoluble **2**, followed by re-precipitating **1** from the supernatant with ether, is then repeated as necessary until no signals corresponding to **2** or **3** are visible by  $^{31}\text{P}$  or  $^1\text{H}$  NMR (Fig.38). The asymmetric hybrid **1** was synthesised in this way many times to prepare numerous batches and was found to be reliably isolated in good yield (typically 10-25 total yield %) and excellent purity (see full experimental details in 3.7.2.8).

### 3.4 Characterisation and properties of **1**

The composition and purity of **1** was confirmed by  $^1\text{H}$  NMR,  $^{31}\text{P}$  NMR, ESI-MS, elemental (CHN) analysis, thermogravimetric analysis (TGA) and Fourier-transform infrared spectroscopy (FT-IR).  $^1\text{H}$  NMR confirmed the presence of both the aliphatic  $\text{C}_{18}$  chain and the aromatic *TPY* group in a 1:1 stoichiometric ratio (Fig.39). Some of the aromatic proton signals for *TPY* in **1** appear shifted from those in the free *TPY*

### 3. Design and synthesis of asymmetric hybrid POM (1)

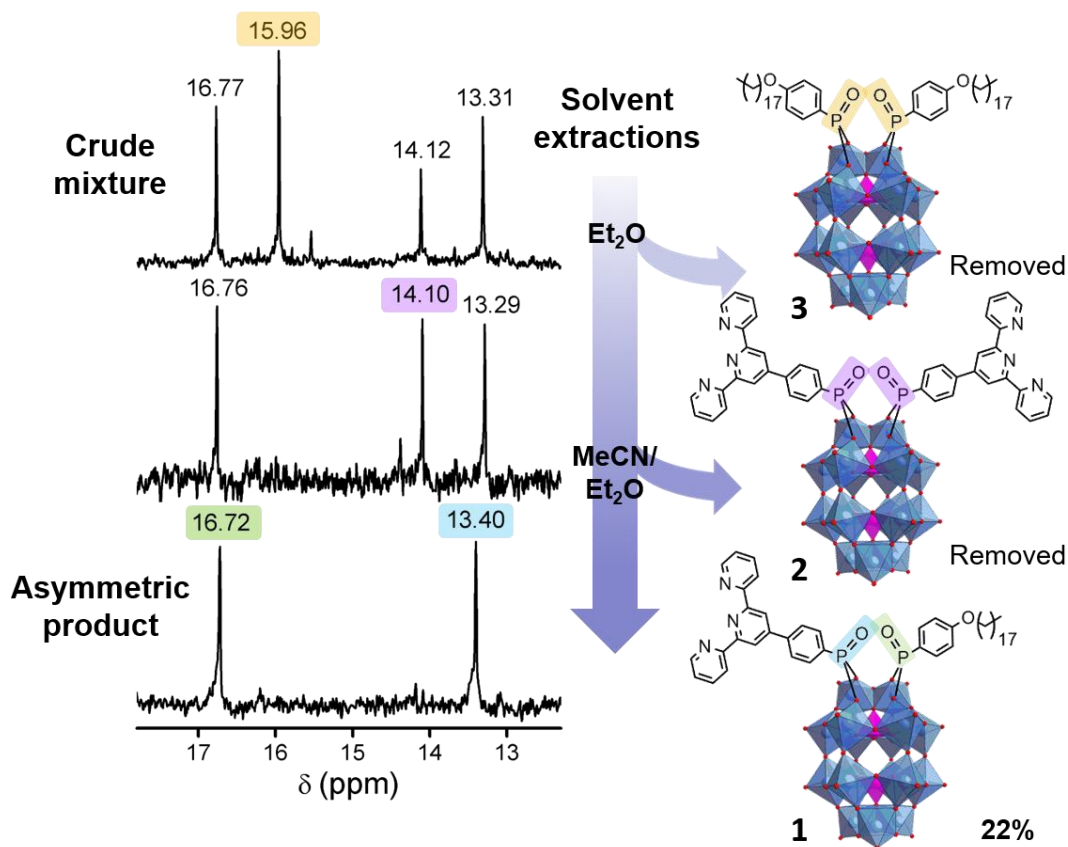


**Figure 38.** Illustration of the process of purification of asymmetric hybrid **1** from the crude mixture.  $^{31}\text{P}$  NMR of the reaction mixture in  $\text{DMSO-d}_6$  is shown on the left, taken after each purification step (top: crude; middle **1** + **2**; bottom: **1** only). Chemical shifts corresponding to each product are colour coded as shown (for simplicity only the positive chemical shift region for the organophosphonate  $^{31}\text{P}$  nuclei is presented).

ligand (Fig.40), indicating covalent grafting to the Dawson anion. Interestingly, slight shielding of the *TPY* phosphorus ( $\sim 0.8$  ppm) and deshielding of the *C*<sub>18</sub> phosphorus ( $\sim 0.7$  ppm) relative to their  $^{31}\text{P}$  chemical shifts in the respective symmetric hybrids, **2** and **3** (Fig.38), suggests a degree of electronic communication across the POM core of the asymmetric structure.<sup>[15]</sup> It should be noted that the asymmetric hybrid, **1**, (and any asymmetric organophosphonate  $\{\text{P}_2\text{W}_{17}\}$  hybrid, in theory) can be expected to exist as a racemic mixture of two enantiomers, but they do not appear to be distinguishable from the NMR spectra and their resolution is not investigated in this thesis.

### 3. Design and synthesis of asymmetric hybrid POM (1)

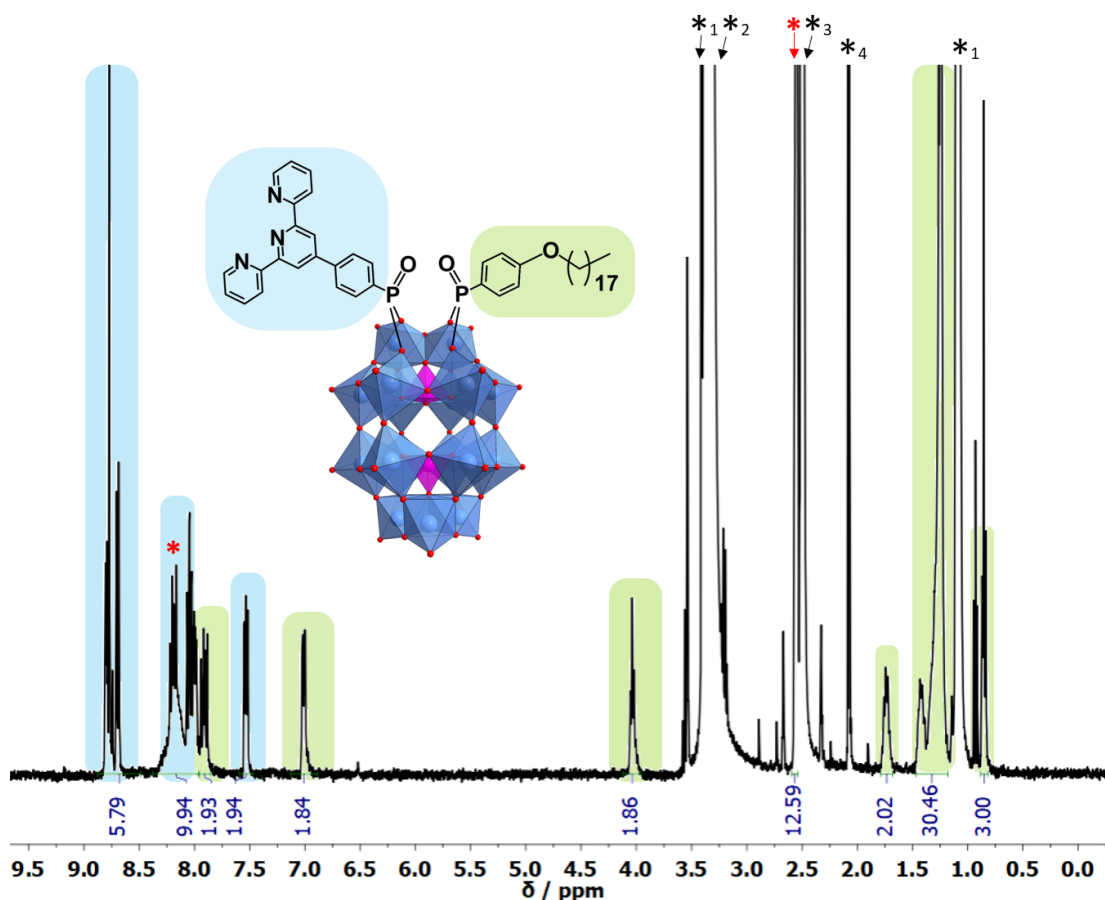


**Figure 39.**  $^1\text{H}$  NMR of **1** in  $\text{DMSO-d}_6$  showing the assignment of peaks to each ligand: green =  $\text{C}_{18}$ , blue =  $\text{TPY}$ . Red asterisks indicate DMA cation signals, and black asterisks indicate solvent impurities: 1= diethyl ether, 2=  $\text{H}_2\text{O}$ , 3=  $\text{DMSO}$ , 4=  $\text{CH}_3\text{CN}$ .

Dimethylammonium (DMA) cations are observed in the  $^1\text{H}$  NMR for **1** with peaks at 2.55 and 8.33-8.09 ppm which integrate to two cations (Fig.39). The formation of DMA cations has been observed after POM hybridisation reactions under similar conditions by our research group. It results from decomposition of the DMF which appears to be facilitated by the POM and proceeds particularly effectively at higher temperatures. As the base-assisted decarbonylation of DMF when heated is known, this is quite plausible.<sup>[16-17]</sup> TGA and CHN analysis assisted in further assignment of the two DMA cations.

The ESI mass spectrum of **1** showed two series of broad peak clusters from which assignments could be made to **1**, matching closely the calculated molecular weight of

### 3. Design and synthesis of asymmetric hybrid POM (1)

---

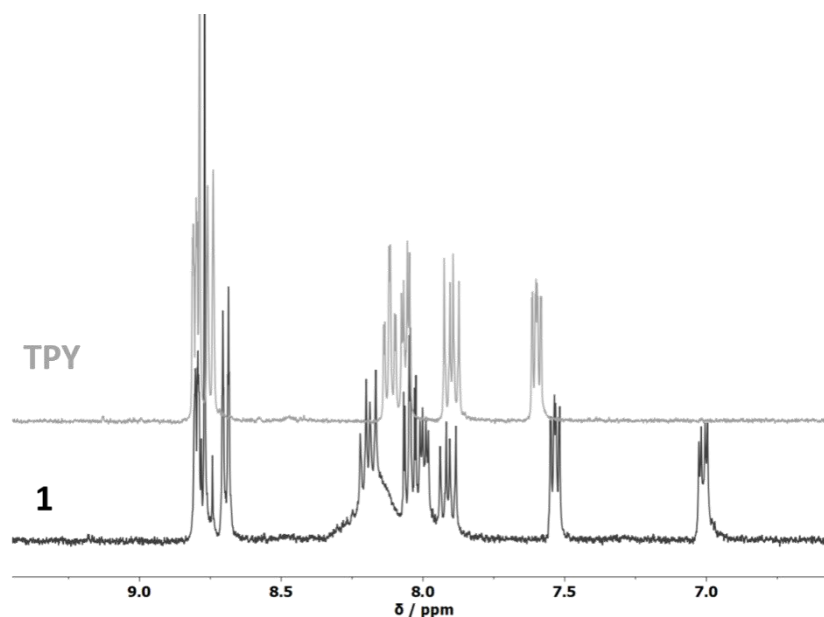


**Figure 40.** Overlaid <sup>1</sup>H NMR of **1** and **TPY** in DMSO-d<sub>6</sub>, showing the aromatic signal region.

the anion with the two distinct covalently grafted ligands. The  $m/z$  values to which assignments are made are those of the most central peak in the broad bell-shaped peak which arise from the various relatively abundant isotopes of tungsten. By looking at the peak-to-peak separation, the two peak series can be assigned to anionic species with 2- and 3- charges. The central  $m/z$  values could then be assigned to the POM hybrid anion with either 4 or 3 cations to total these charges, in varying combinations of proton and sodium cations (Fig.41, Table.1). Although the Dawson POM was prepared as a potassium salt, the observation of proton and sodium ions as counterions is not surprising as they can be commonly picked up in-source during ESI methods.<sup>[18]</sup> This free exchange of cations is especially common during analysis of POM clusters due to their inherent anionic nature.<sup>[19]</sup>

### 3. Design and synthesis of asymmetric hybrid POM (1)

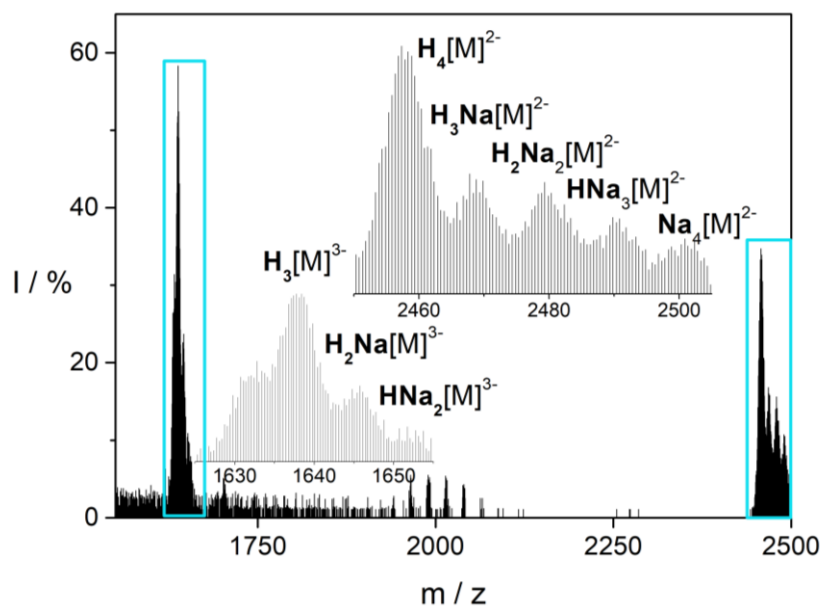


**Figure 41.** Negative mode ESI mass spectrum of **1** in acetonitrile. [M] =  $[P_2W_{17}O_{57}\{(PO_3C_{21}H_{14}N_3)(PO_4C_{24}H_{41})\}]$ .

| Assignment  | z  | m/z (obs.) | m/z (calc.) |
|---|----|------------|-------------|
| $H_3[P_2W_{17}O_{57}(PO_3C_{21}H_{14}N_3)(PO_4C_{24}H_{41})]$     | 3- | 1638.0753  | 1638.0672   |
| $H_2Na[P_2W_{17}O_{57}(PO_3C_{21}H_{14}N_3)(PO_4C_{24}H_{41})]$   | 3- | 1645.4042  | 1645.3945   |
| $HNa_2[P_2W_{17}O_{57}(PO_3C_{21}H_{14}N_3)(PO_4C_{24}H_{41})]$   | 3- | 1652.7300  | 1652.7219   |
| $H_4[P_2W_{17}O_{57}(PO_3C_{21}H_{14}N_3)(PO_4C_{24}H_{41})]$     | 2- | 2457.3475  | 2457.6050   |
| $H_3Na[P_2W_{17}O_{57}(PO_3C_{21}H_{14}N_3)(PO_4C_{24}H_{41})]$   | 2- | 2468.3490  | 2468.5960   |
| $H_2Na_2[P_2W_{17}O_{57}(PO_3C_{21}H_{14}N_3)(PO_4C_{24}H_{41})]$ | 2- | 2479.3527  | 2479.5870   |
| $HNa_3[P_2W_{17}O_{57}(PO_3C_{21}H_{14}N_3)(PO_4C_{24}H_{41})]$   | 2- | 2490.3401  | 2490.5780   |
| $Na_4[P_2W_{17}O_{57}(PO_3C_{21}H_{14}N_3)(PO_4C_{24}H_{41})]$    | 2- | 2501.3511  | 2501.5689   |

**Table 1.** Selected ESI-MS peak assignments for **1**.

IR spectroscopy also confirmed successful asymmetric organofunctionalisation in **1**, with the retained characteristic peaks of the lacunary Dawson cluster at low wavenumbers (including W-O-W, W=O and P-O vibrations from  $\sim 700$ - $1080\text{ cm}^{-1}$ ) as well as peaks characteristic of the ligands (Fig.42), including the C-H stretches attributed to the  $C_{18}$  alkyl chain observed at around  $2900\text{ cm}^{-1}$ . Peaks in **1** not observed in the spectrum of  $\{P_2W_{17}\}$  from *ca.*  $1100$  to  $1650\text{ cm}^{-1}$  can be attributed to bond

### 3. Design and synthesis of asymmetric hybrid POM (1)

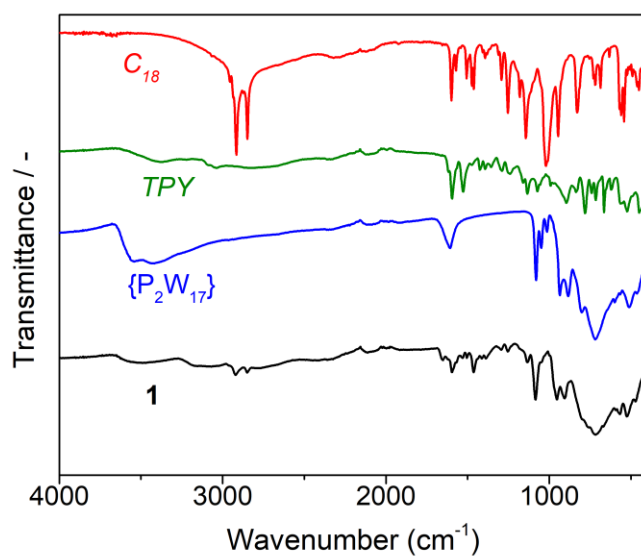


**Figure 42.** Stacked IR (ATR) spectra of asymmetric hybrid **1** (black line), lacunary Dawson K<sub>10</sub>-[P<sub>2</sub>W<sub>17</sub>O<sub>61</sub>]{P<sub>2</sub>W<sub>17</sub>} (blue line), and ligands TPY (green line) and C<sub>18</sub> (red line).

vibrations in both ligands and include those of phosphonate P=O stretch (1133 cm<sup>-1</sup>) and pyridine C=N and C=C stretches (1500-1595 cm<sup>-1</sup>). The signals in this complex region will also include C-C, C-H and C-O vibration modes and are difficult to resolve considering bands corresponding to vibrations of bonds in solvent and cation molecules associated with the cluster will also absorb in this region.

It should be noted that attempts were made to obtain crystals of **1** for single X-ray diffraction by slow evaporation and by vapour diffusion, using a range of solvents and solvent mixtures. Unfortunately, all were unsuccessful, likely due to the high flexibility of the long chain moiety on the C<sub>18</sub> ligand.

The UV-Visible (UV-Vis) absorption spectrum of **1** in DMF shows absorptions characteristic of the “parent” Dawson anion [P<sub>2</sub>W<sub>18</sub>O<sub>62</sub>]<sup>6-</sup>{P<sub>2</sub>W<sub>18</sub>}, with a broad ligand-to-metal charge-transfer (LMCT) O→W band centred at *ca.* 300 nm, as well as intraligand (IL) π-π\* absorption features of the grafted ligand TPY centred at *ca.* 280 and 320 nm (Fig.43).<sup>[20]</sup>

As the intrinsic redox chemistry of the Dawson anion core was expected to be retained in **1**, its electrochemistry was studied by cyclic voltammetry. A cyclic voltammogram

### 3. Design and synthesis of asymmetric hybrid POM (1)

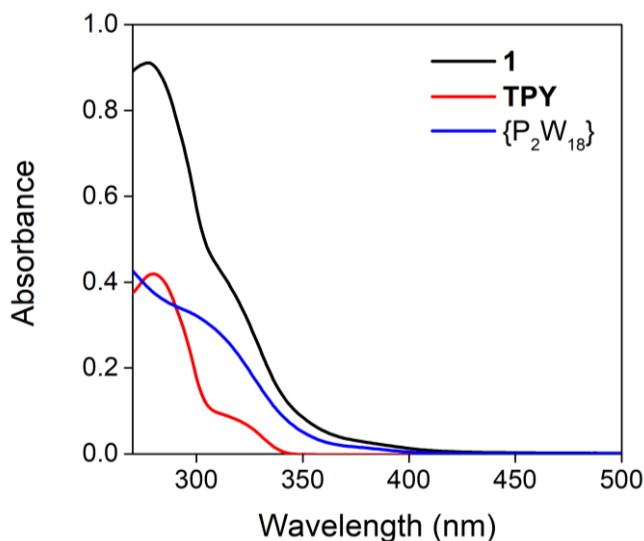


**Figure 43.** Overlaid UV-Vis absorbance spectra of asymmetric hybrid POM **1** (black line), **TPY** (red) and “parent” Dawson  $K_6[P_2W_{18}O_{62}] \{P_2W_{18}\}$  (blue) in DMF (all 10  $\mu$ M). An absorption spectrum of **C<sub>18</sub>** could not be obtained due to poor solubility.

(CV) of **1** in a DMF solution with 0.1 M TBAPF<sub>6</sub> as electrolyte revealed four distinct quasi-reversible redox processes in the potential range of  $-0.5$  to  $-2.0$  V vs. ferrocene/ferrocenium (Fc/Fc<sup>+</sup>) (Fig.44, Table.2). The first two redox processes, I and II, correspond to one electron  $W^{VI}/W^V$  processes ( $\Delta E_p = 62$  mV, 61 mV respectively). These are significantly positively shifted by *ca.* 450 mV relative to those in the “parent” Dawson anion  $\{P_2W_{18}\}$  in DMF, typical of organophosphonate hybrid POMs because of the electron-withdrawing nature of the organophosphonate linker group.<sup>[15]</sup> Furthermore,  $E_{1/2}$  potentials of **1** were found to be intermediate to those of the respective symmetric hybrids, **2** and **3** (Table.4,5). Redox processes in **2** more positively shifted by an average of 5 mV and those of **3** more negative by an average of 20 mV relative to the equivalent redox couples of **1**.

There appears to be a fifth redox process at around  $-2.1$  V, which could be attributed to a *TPY*-based reduction process, as terpyridine reductions are known to occur at highly negative potentials.<sup>[21]</sup> Potentiometric coulometry/bulk electrolysis measurements would be necessary to confirm definitively the number of electrons involved in each of the redox processes.

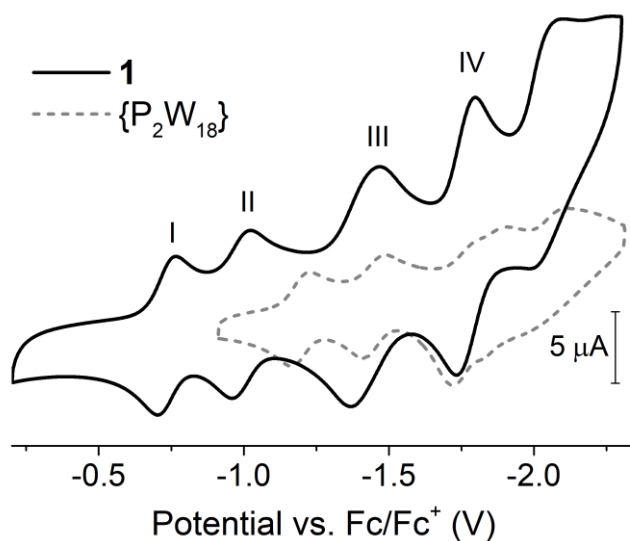


**Figure 44.** Overlaid cyclic voltammograms of **1** (0.5 mM) (black) and “parent” Dawson  $\{P_2W_{18}\}$  (0.5 mM) (grey dashed) in DMF, with 0.1M TBAPF<sub>6</sub> as electrolyte at a glassy carbon working electrode. Scan rate: 100 mVs<sup>-1</sup>.

| Redox potentials vs. Fc/Fc <sup>+</sup> (V) | I             | II            | III           | IV            |
|---|---------------|---------------|---------------|---------------|
| E <sub>red</sub>                            | -0.764        | -1.022        | -1.471        | -1.798        |
| E <sub>ox</sub>                             | -0.702        | -0.961        | -1.367        | -1.734        |
| E <sub>1/2</sub>                            | <b>-0.733</b> | <b>-0.992</b> | <b>-1.419</b> | <b>-1.766</b> |

**Table 2.** Redox potentials of **1** in DMF.

### 3.5 Characterisation of symmetric hybrid POMs

#### $[P_2W_{17}O_{57}\{(TPY)_2\}]$ (**2**) and $[P_2W_{17}O_{57}\{(C_{18})_2\}]$ (**3**)

The symmetric hybrids  $[P_2W_{17}O_{57}\{(TPY)_2\}]$  (**2**) and  $[P_2W_{17}O_{57}\{(C_{18})_2\}]$  (**3**) are side-products of the “one-pot” reaction to prepare the asymmetric hybrid **1**. Although they could be separated by solvent extractions during the purification process, they were synthesised separately to isolate them as pure compounds for characterisation, with



### 3. Design and synthesis of asymmetric hybrid POM (1)

the purpose of providing comparisons to **1** for a more thorough characterisation of its structure and properties.

#### 3.5.1.1 Characterisation of **2**

The reaction conditions and relative quantities in the synthesis of the symmetric hybrid POM with two *TPY* ligands, **2**, were as for **1** except 100% DMF was used as solvent and two molar equivalents of **TPY** were reacted with  $K_{10}[P_2W_{17}O_{61}]$  in an acid-catalysed reaction. The hybrid POM product was isolated from solution by precipitation with ether and was characterised once adequately dried.

The aromatic signals in the  $^1H$  NMR are slightly more shielded than those of the *TPY* ligand in **1**, indicating a deshielding effect of the  $C_{18}$  ligand on *TPY* in the asymmetric structure (Fig.45). A single peak in the positive region of the  $^{31}P$  spectrum at 14.20

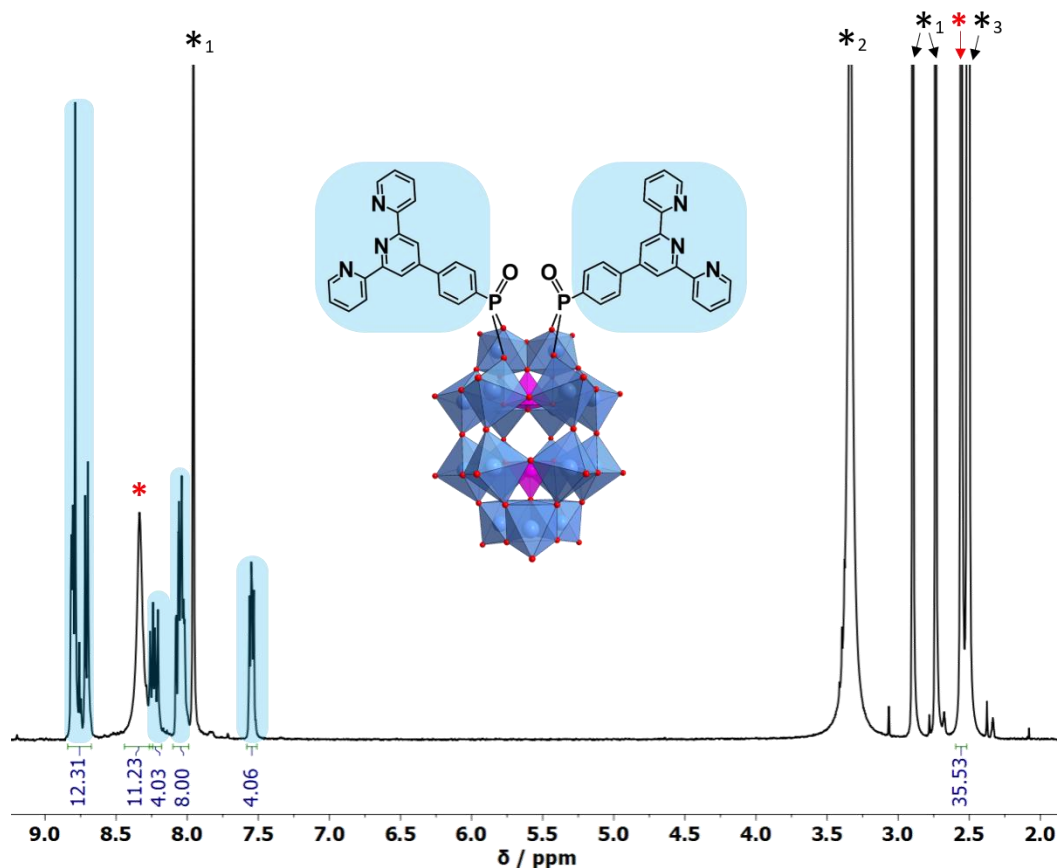


**Figure 45.**  $^1H$  NMR of **2** in  $DMSO-d_6$ . Red asterisks indicate DMA cation signals, and black asterisks indicate solvent impurities: 1= DMF, 2=  $H_2O$ , 3= DMSO.

### 3. Design and synthesis of asymmetric hybrid POM (1)

ppm indicates a single symmetrically organofunctionalised structure. All six cations associated with the POM hybrid were assigned as DMAs according to  $^1\text{H}$  NMR, CHN and TGA analysis.

Few peaks in the ESI mass spectrum of **2** could be assigned to the hybrid structure, but again corresponded to species with 2- and 3- charges which were identified as the POM hybrid anion with varying combinations of proton, sodium and potassium cations (Fig.46, Table.3).

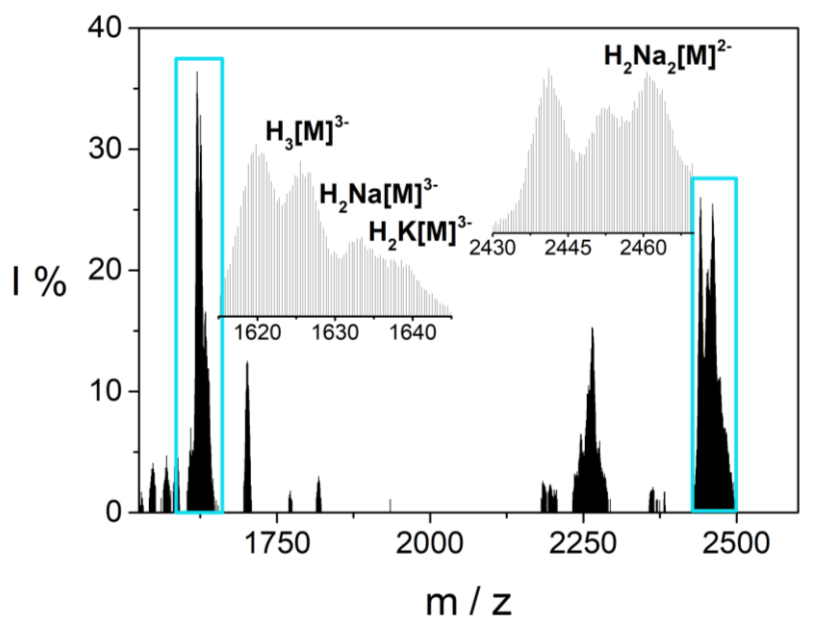


**Figure 46.** Negative mode ESI mass spectrum of **2** in acetonitrile.  $[\text{M}] = [\text{P}_2\text{W}_{17}\text{O}_{57}\{(\text{PO}_3\text{C}_{21}\text{H}_{14}\text{N}_3)_2\}]$ .

| Assignment   | z  | m/z (obs.) | m/z (calc.) |
|--|----|------------|-------------|
| $\text{H}_3[\text{P}_2\text{W}_{17}\text{O}_{57}\{(\text{PO}_3\text{C}_{21}\text{H}_{14}\text{N}_3)_2\}]$            | 3- | 1625.8502  | 1625.6432   |
| $\text{H}_2\text{Na}[\text{P}_2\text{W}_{17}\text{O}_{57}\{(\text{PO}_3\text{C}_{21}\text{H}_{14}\text{N}_3)_2\}]$   | 3- | 1632.8553  | 1632.9705   |
| $\text{H}_2\text{K}[\text{P}_2\text{W}_{17}\text{O}_{57}\{(\text{PO}_3\text{C}_{21}\text{H}_{14}\text{N}_3)_2\}]$    | 3- | 1638.1824  | 1638.2952   |
| $\text{H}_2\text{Na}_2[\text{P}_2\text{W}_{17}\text{O}_{57}\{(\text{PO}_3\text{C}_{21}\text{H}_{14}\text{N}_3)_2\}]$ | 2- | 2460.7279  | 2460.9510   |

**Table 3.** Selected ESI-MS peak assignments for **2**.

### 3. Design and synthesis of asymmetric hybrid POM (1)

---

The UV-Vis absorption spectrum of **2** is very similar to that of the **TPY** ligand, but with higher intensity bands due to the overlap of absorption bands of the Dawson anion core (Fig.43,47). In comparison to the asymmetric hybrid **1**, the highest energy IL  $\pi$ - $\pi^*$  band at 280 nm has a higher absorbance, which is as expected due to the presence of two *TPY* ligands per POM cluster.

The electrochemistry of **2** was studied by CV experiments in a DMF solution with 0.1M TBAPF<sub>6</sub> as electrolyte. As for **1**, four quasi-reversible redox processes in the potential range of -0.5 to -2.25 V vs. Fc/Fc<sup>+</sup> were observed (Fig.48, Table.4), very slightly positively shifted by *ca.* 5 mV from those in **1**. Interestingly, a fifth reduction process was observed during the first cycle, which appeared to merge with the fourth reduction process on successive cycles. This is likely a result of an irreversible terpyridine-based reduction observed at high potentials.<sup>[22]</sup>

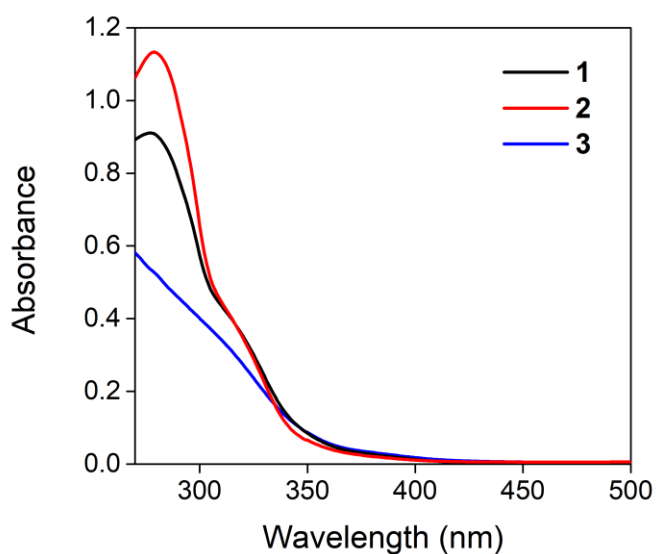


**Figure 47.** Overlaid UV-Vis absorption spectra of asymmetric hybrid POM **1** (black line) and symmetric hybrids **2** (red) and **3** (blue) in DMF (all 10  $\mu$ M).

### 3. Design and synthesis of asymmetric hybrid POM (1)

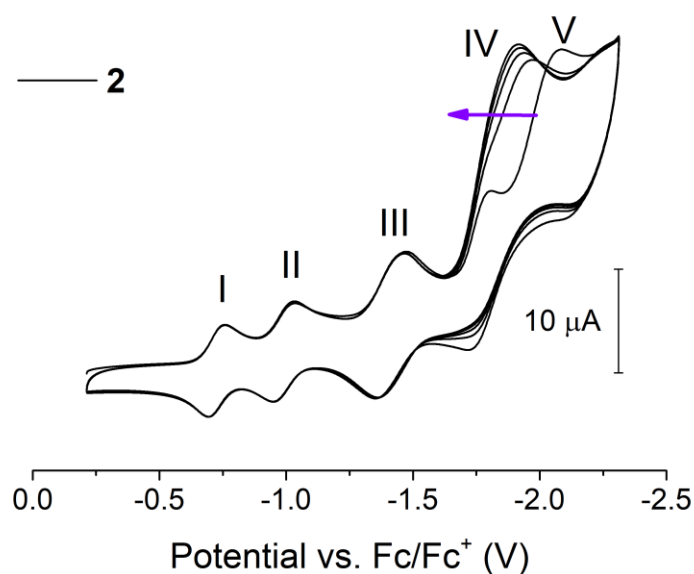


**Figure 48.** Cyclic voltammogram of **2** (0.5 mM) in DMF, with 0.1M TBAPF<sub>6</sub> as electrolyte at a glassy carbon working electrode. Cycles 1 to 5 at scan rate 100 mVs<sup>-1</sup>. Arrow showing direction of peak shift through progressive cycles as the reduction peaks of processes IV and V appear to merge.

| Redox potential vs. Fc/Fc <sup>+</sup> (V) | I             | II            | III           | IV            | V      |
|--|---------------|---------------|---------------|---------------|--------|
| E <sub>red</sub>                           | -0.762        | -1.031        | -1.462        | -1.803        | -2.057 |
| E <sub>ox</sub>                            | -0.694        | -0.950        | -1.354        | 1.722         | -      |
| E <sub>1/2</sub>                           | <b>-0.728</b> | <b>-0.991</b> | <b>-1.408</b> | <b>-1.763</b> | -      |

**Table 4.** Redox potentials of **2** in DMF (before the merging of the reductions peaks of processes IV & V).

#### 3.5.1.2 Characterisation of **3**

The reaction conditions and relative quantities in the synthesis of the symmetric hybrid POM with two C<sub>18</sub> ligands, **3**, were as for **1**, except two molar equivalents of C<sub>18</sub> were reacted with K<sub>10</sub>-[P<sub>2</sub>W<sub>17</sub>O<sub>61</sub>]. Although C<sub>18</sub> is soluble in CH<sub>3</sub>CN on heating, an acidified 50:50 DMF-CH<sub>3</sub>CN solvent mixture was still used to allow for the formation of the hybrid system with DMA cations for better comparison with **1** and **2**. The hybrid

### 3. Design and synthesis of asymmetric hybrid POM (1)

POM product was isolated from solution by removal of the solvent *in vacuo* and was characterised once adequately dried.

Alkyl and aromatic signals for the grafted  $C_{18}$  ligands were observed in the  $^1\text{H}$  NMR spectrum of **3** and a single peak in the positive region of the  $^{31}\text{P}$  spectrum at 16.04 ppm indicates a single symmetrically organofunctionalised structure (Fig.49). Four DMA cations associated with the POM hybrid were assigned according to  $^1\text{H}$  NMR, CHN and TGA analysis.

As for **1**, the ESI mass spectrum of **3** showed two series of broad peaks for species with 2- and 3- charges, which were similarly identified as the POM hybrid anion with varying combinations of proton and sodium cations (Fig.50, Table.5).

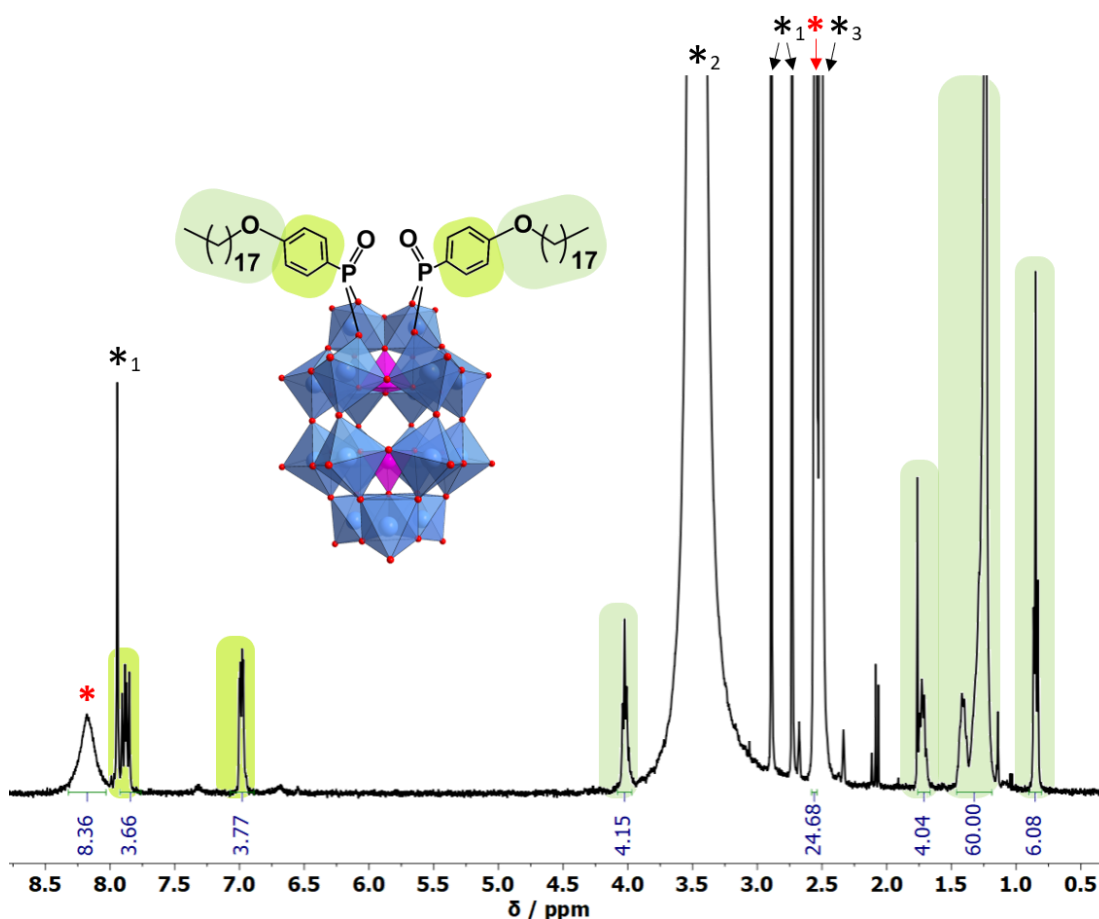


**Figure 49.**  $^1\text{H}$  NMR of **3** in  $\text{DMSO-d}_6$ . Red asterisks indicate DMA cation signals, and black asterisks indicate solvent impurities: 1= DMF, 2=  $\text{H}_2\text{O}$ , 3= DMSO.

### 3. Design and synthesis of asymmetric hybrid POM (1)

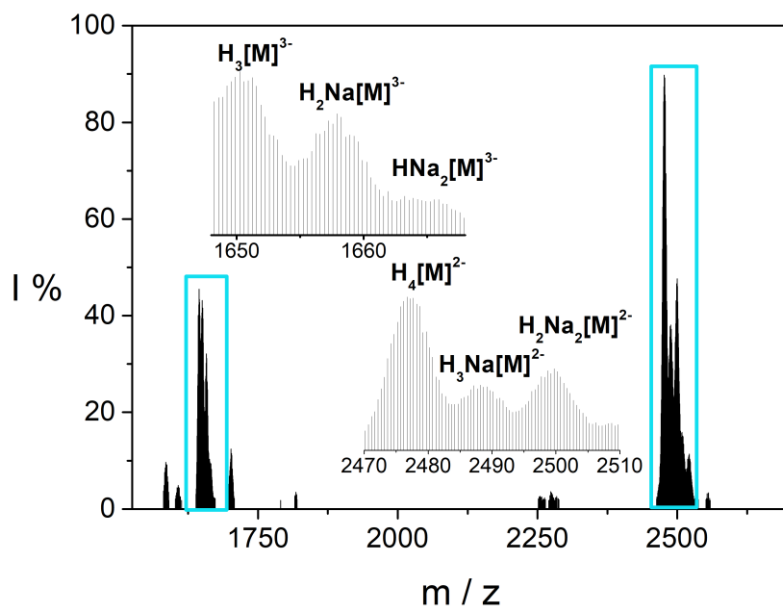


**Figure 50.** Negative mode ESI mass spectrum of **3** in acetonitrile. [M] =  $[P_2W_{17}O_{57}\{(PO_4C_{24}H_{41})_2\}]$ .

| Assignment   | z  | m/z (obs.) | m/z (calc.) |
|--|----|------------|-------------|
| $H_4[P_2W_{17}O_{57}\{(PO_4C_{24}H_{41})_2\}]$     | 2- | 2476.1823  | 2476.2036   |
| $H_3Na[P_2W_{17}O_{57}\{(PO_4C_{24}H_{41})_2\}]$   | 2- | 2487.1867  | 2487.1945   |
| $H_2Na_2[P_2W_{17}O_{57}\{(PO_4C_{24}H_{41})_2\}]$ | 2- | 2498.2286  | 2498.1855   |
| $H_3[P_2W_{17}O_{57}\{(PO_4C_{24}H_{41})_2\}]$     | 3- | 1650.5806  | 1650.4663   |
| $H_2Na[P_2W_{17}O_{57}\{(PO_4C_{24}H_{41})_2\}]$   | 3- | 1657.9094  | 1657.7936   |
| $HNa_2[P_2W_{17}O_{57}\{(PO_4C_{24}H_{41})_2\}]$   | 3- | 1665.2454  | 1665.1209   |

**Table 5.** Selected ESI-MS peak assignments for **3**.

The UV-Vis spectrum of **3** appears to consist predominantly of absorption features of the Dawson cluster core which can be expected due to the simple aromatic structure of the  $C_{18}$  ligand (Fig.47). The slight increase and tailing of absorbance in **3** to ca. 410 nm must be attributed to an effect of the attached  $C_{18}$  ligands and gives rise to the orange colour of the compound.

### 3. Design and synthesis of asymmetric hybrid POM (1)

The molecular redox chemistry of **3** was studied by CV experiments in a DMF solution with 0.1 M TBAPF<sub>6</sub> as electrolyte. As for **1**, four quasi-reversible redox processes in the potential range of -0.5 to -2.25 V vs. Fc/Fc<sup>+</sup> were observed (Fig.51, Table.6), slightly negatively shifted by *ca.* 20 mV from those in **1**. Notably, a possible fifth process appears to be visible just below -2.0 V, making the previous assignment of the similar process observed in **1** to a *TPY*-based redox process unclear. It is perhaps assignable to another POM-based process.

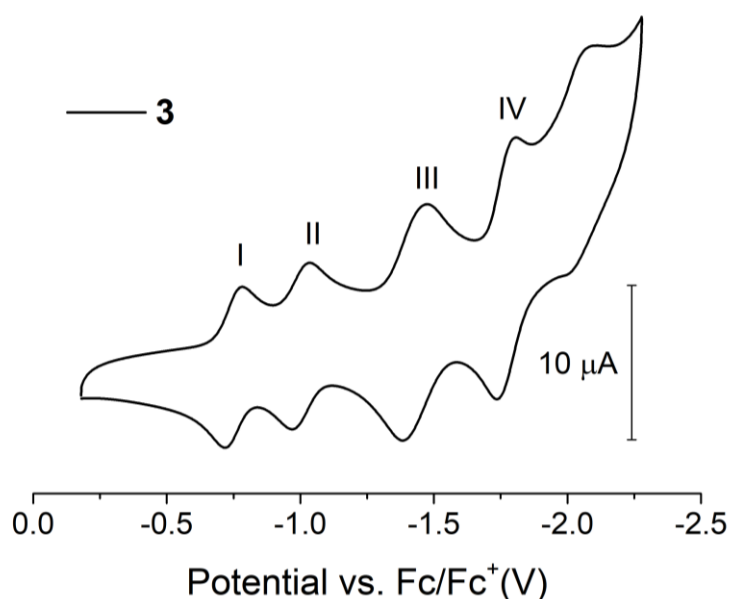


**Figure 51.** Cyclic voltammogram of **3** (0.5 mM) in DMF with 0.1M TBAPF<sub>6</sub> as electrolyte at a glassy carbon working electrode. Scan rate: 100 mVs<sup>-1</sup>.

| Redox potential vs. Fc/Fc <sup>+</sup> (V) | I             | II            | III           | IV            |
|--|---------------|---------------|---------------|---------------|
| E <sub>red</sub>                           | -0.787        | -1.040        | -1.480        | -1.806        |
| E <sub>ox</sub>                            | -0.720        | -0.976        | -1.403        | -1.766        |
| E <sub>1/2</sub>                           | <b>-0.754</b> | <b>-1.008</b> | <b>-1.442</b> | <b>-1.786</b> |

**Table 6.** Redox potentials of **3** in DMF.

### 3.5.1.3 Self-assembling behaviour of **3**

The aliphatic chain ligand  $C_{18}$  in **3** imparts an amphiphilic character on the hybrid POM, with the POM acting as a polar head-group. Therefore, self-assembling behaviour could be expected, as observed with similar amphiphilic covalent organofunctionalised hybrid systems<sup>[23]</sup> including those recently reported by our group.<sup>[14, 24]</sup> Due to the presence of DMA cations in **3**, it could not be dissolved in a 100%  $H_2O$  solution. A 9:1 (v/v)  $H_2O-CH_3CN$  mixture was found to facilitate self-assembly, by first dissolving the hybrid in  $CH_3CN$  and then to this water was added to prepare a 1.4 mM concentration solution. This concentration was used to allow direct comparison with amphiphilic POM systems previously reported by our group that were also prepared at a 1.4 mM concentration,<sup>[14, 24]</sup> and is in accordance with the upper limit of the range of Critical Micellar Concentrations observed for our symmetric  $C_{12}-C_{20}$  hybrid POM systems (0.75–1.4 mM).<sup>[14]</sup> Dynamic Light Scattering (DLS) studies on the solution confirmed the formation of nanoscale assemblies of low dispersity with a hydrodynamic diameter ( $D_h$ ) of approximately 5 nm (Fig.52). In

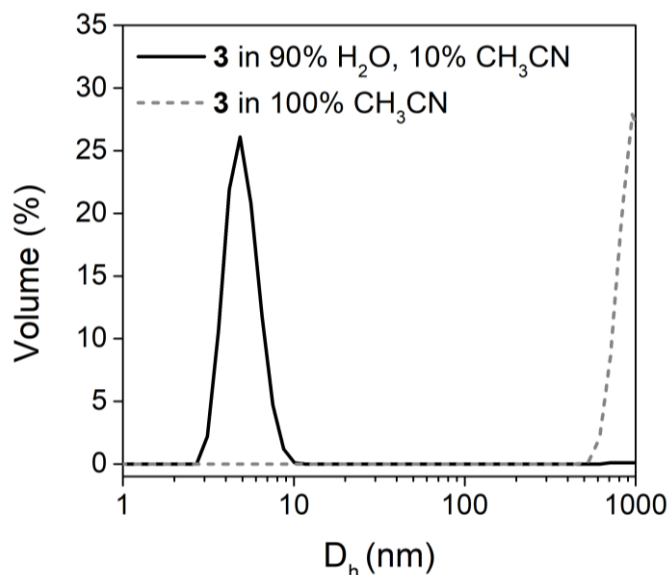


**Figure 52.** Particle-size distribution curves determined by DLS of **3** (1.4 mM) in a  $H_2O-CH_3CN$  (9:1 v/v) solution-  $D_h$  maxima at 4.8 nm (black), and in 100%  $CH_3CN$  (showing loss of the signal for the ca. 5 nm supramolecular assemblies observed in mixed  $H_2O-CH_3CN$  solution, grey, dashed).



### 3. Design and synthesis of asymmetric hybrid POM (1)

contrast, no signal was observed within that range in a 100% CH<sub>3</sub>CN solution indicating an absence of the assemblies (Fig.52).

Recently, research in our group showed that self-assembled micellar nanostructures formed from hybrid POM species exhibit different redox properties to their constituent molecular species. This is proposed to be due to intermolecular cooperativity or increased coulombic repulsion between neighbouring POM head groups in the supramolecular assembly.<sup>[14, 24]</sup> To study the redox behaviour in its supramolecular form, **3** was dissolved in a 0.1 M H<sub>2</sub>SO<sub>4</sub>-CH<sub>3</sub>CN (9:1, v/v) mixture to allow for spontaneous assembly into micellar species as described above. DLS measurements on an equivalent solution showed that small aggregates with a mean hydrodynamic diameter  $D_h$  of 7 nm are formed in this solvent mixture. Interestingly, a second signal corresponding to structures in the range of 15-100 nm was also observed, which was not seen in the H<sub>2</sub>O-CH<sub>3</sub>CN (9:1, v/v) mixture (Fig.53), indicating some influence of the ionic environment on further aggregation. CV experiments conducted on the solution showed just two redox processes were observed between

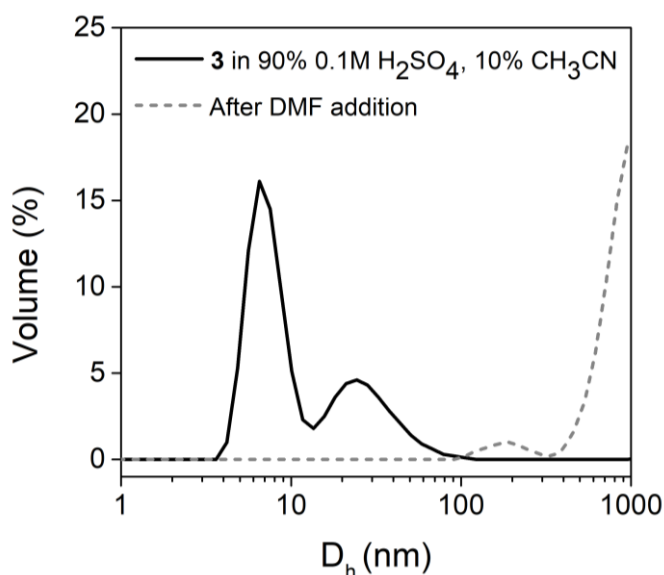


**Figure 53.** Particle-size distribution curve determined by DLS of **3** (1.4 mM) in 90% H<sub>2</sub>SO<sub>4</sub> (0.1M) 10% CH<sub>3</sub>CN matching the conditions used in the electrochemical analysis-  $D_h$  maxima at 6.5 nm and 24.4 nm (black), and after the addition of the same volume of DMF ( $c_{\text{new}} = 0.7$  mM) (grey dashed).

### 3. Design and synthesis of asymmetric hybrid POM (1)

+0.5 and -0.5V (vs. Ag/AgCl) in contrast to the three seen for **3** in pure DMF in the same range (Fig. 54). This is due to the first redox process negatively shifting, resulting in the first two 1-electron redox processes coalescing, as appears typical of micellar species of this type.<sup>[14, 24]</sup> On addition of the same volume of DMF to the electrolyte solution, the characteristic molecular redox behaviour was found to rapidly recover. Three distinct processes were observed just as in pure DMF solution and resembled the electrochemical signature of  $\{P_2W_{18}\}$  in the same range (Fig.54). DLS measurements on the same CV solution additionally confirmed the absence of the previously observed supramolecular assemblies (Fig 53).

With the hydrophobic  $C_{18}$  ligand in **1**, similar self-assembling behaviour in aqueous environments could be also expected in the asymmetric hybrid, but in the case of **1** both the POM cluster and *TPY* unit act as the polar head group of the amphiphilic structure. The in-depth investigation of the multifunctionality of **1**, including its self-

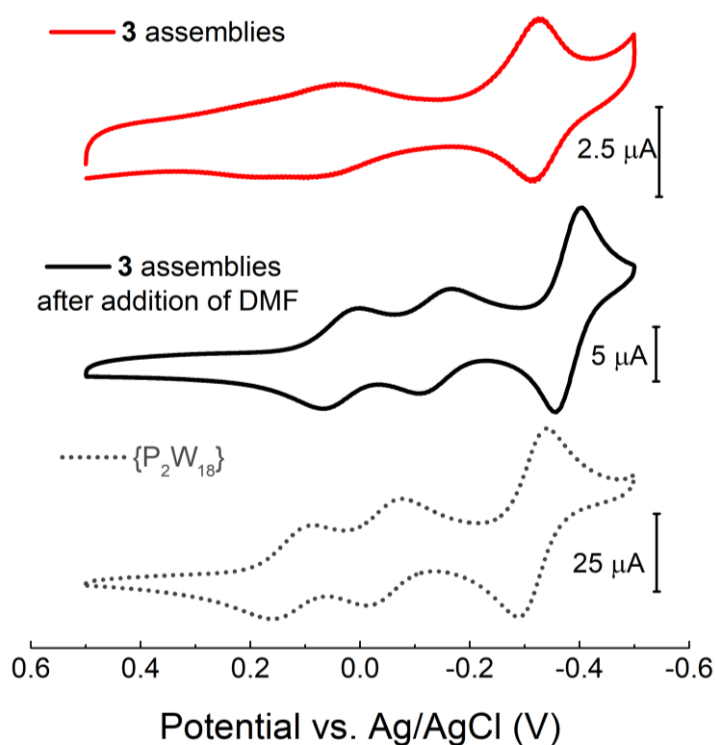


**Figure 54.** Comparison of the cyclic voltammograms of **3** (1.4 mM) in 90% 0.1M  $H_2SO_4$ , 10%  $CH_3CN$  before (red) and after (black) the addition of the same volume of DMF ( $c_{new} = 0.7$  mM), and of  $\{P_2W_{18}\}$  in 0.1M  $H_2SO_4$  (dotted). Scan rate:  $100\text{ mVs}^{-1}$ .

assembling behaviour and coordination to metal cations, will be discussed in the following two chapters of this thesis.

## 3.6 Conclusions

The synthesis of novel multifunctional hybrid materials based on molecular metal oxides has been investigated through the preparation and isolation of an asymmetric Wells-Dawson hybrid POM. Various synthetic routes were investigated including via the controlled hydrolysis and postfunctionalisation of symmetric hybrid POM starting materials. Clear limitations with these methodologies were encountered and focus was drawn to a one-pot synthesis approach in which the design and functionality of two different ligands, and the effectiveness of the purification of the symmetric and asymmetric hybrid products were explored. Attempts at the purification and isolation of an asymmetric hybrid POM product proved to be unpredictable and often unreproducible, but not with the combination of two sufficiently distinct ligands, **TPY** and **C<sub>18</sub>**. A markedly simple and inexpensive procedure in comparison to reported methodologies has been developed to successfully isolate the first stable asymmetric Wells-Dawson hybrid POM, utilising solvent extractions to purify the product from a one-pot reaction mixture.

The unique structure of the asymmetric Dawson hybrid, **1**, has been thoroughly characterised and its redox properties studied. It demonstrates capability to undergo multiple quasi-reversible redox processes that are retained from the “parent” Dawson cluster but also tuned by the nature of the appended organophosphonate groups. Investigation of the solvent-dependent self-assembling behaviour of the amphiphilic symmetric hybrid side-product, **3**, that is enabled by its two hydrophobic *C<sub>18</sub>* ligands, demonstrates potential for analogous behaviour in the asymmetric system. The additional chelating functionality in **1** offers extensive opportunity for postfunctionalisation by metal ion coordination, which can be uniquely combined with self-assembly in the asymmetric system.

This work ultimately provides a robust, modular and easily accessible strategy for the creative design and development of new multifunctional hybrid materials based on

### 3. Design and synthesis of asymmetric hybrid POM (1)

---

polyoxometalates, with a range of potentially novel applications as redox-, photo- and catalytically-active soft-nanomaterials. The multifunctionality of the new asymmetric hybrid system **1** enabled by the two distinct moieties,  $C_{18}$  and  $TPY$  will be investigated in the following two chapters of this thesis.

## 3.7 Experimental details

### 3.7.1 Methods

All microwave syntheses were carried out in a CEM Discover microwave reactor.

$^1\text{H}$  NMR,  $^{13}\text{C}$  NMR and  $^{31}\text{P}$  NMR spectra were obtained using Bruker Ascend™ 400MHz and 500MHz spectrometers.

Infra-red spectra were measured using a Bruker Alpha FTIR spectrometer with a platinum ATR module.

UV/Visible absorption spectroscopy was performed on a Cary 5000 UV/VIS NIR spectrophotometer.

Electrospray ionisation mass spectrometry (ESI-MS) was performed on Bruker MicroTOF and Impact II spectrometers operating in negative mode. The samples were prepared as acetonitrile solutions (ca.  $0.1 \text{ mg mL}^{-1}$ ) and introduced to the spectrometer via an autosampler which injected  $20 \mu\text{L}$  of the sample into a stream of 70:30 v/v MeOH/H<sub>2</sub>O. Data was analysed on the Bruker Compass Data Analysis software suite.

CHN microanalysis was carried out using an Exeter Analytical CE-440 Elemental Analyser.

Thermogravimetric analysis (TGA) was carried out using a TA Instruments Discovery TGA. Samples were heated from 25-1000°C under air at 10°C/min.

Dynamic Light Scattering (DLS) measurements were acquired using a Malvern Instrument Nano-ZS Zetasizer at room temperature.

### 3. Design and synthesis of asymmetric hybrid POM (1)

---

Electrochemical measurements were performed on a CHI600e (CH Instruments) workstation. Cyclic voltammetry (CV) experiments under non-aqueous conditions were performed using a three-electrode arrangement; working electrode (glassy carbon,  $d = 3\text{ mm}$ ), reference electrode (Ag wire) and a counter electrode (Pt wire). Experiments were performed in TBA.PF<sub>6</sub> (0.1 M) as the supporting electrolyte in dry DMF. All potentials with ferrocene as an internal standard are quoted relative to the  $E_{1/2}$  of the ferrocene/ferrocenium redox couple. Experiments under aqueous conditions were performed using a three-electrode arrangement; working electrode (glassy carbon,  $d = 3\text{ mm}$ ), reference electrode (Ag/AgCl) and a counter electrode (Pt wire). All solutions were purged with nitrogen for 10 mins and kept under a positive pressure of nitrogen for the duration of the experiment. All measurements were performed at a scan rate of  $100\text{ mVs}^{-1}$ .

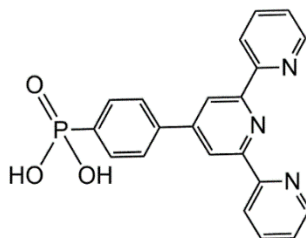
#### 3.7.2 Syntheses

All reagents and solvents obtained from commercial sources were used without further purification.

##### 3.7.2.1 $\text{K}_{10}[\text{P}_2\text{W}_{17}\text{O}_{61}] \{\text{P}_2\text{W}_{17}\}$

$\text{K}_{10}[\alpha_2\text{-P}_2\text{W}_{17}\text{O}_{61}]$  and its precursor,  $\text{K}_6[\alpha_2\text{-P}_2\text{W}_{18}\text{O}_{62}]$ , were synthesised according to procedures in literature.<sup>[25-26]</sup>

##### 3.7.2.2 TPY



Synthesis of BrPhTPY –  $\text{C}_{21}\text{H}_{14}\text{N}_3\text{Br}$

4-bromobenzaldehyde (5 g, 27.0 mmol), 2-acetylpyridine (6.06 mL, 54 mmol) and KOH (4.54 g, 81 mmol) were dissolved in ethanol (300 mL). Ammonium hydroxide solution (35 %, 62 mL) was added whilst stirring, and the mixture was heated at reflux ( $75\text{ }^\circ\text{C}$ )

### 3. Design and synthesis of asymmetric hybrid POM (1)

for 24h. The mixture was filtered and the collected precipitate was washed with ethanol and allowed to dry in air. The crude product was purified by re-precipitation from hot chloroform using cold ethanol, to yield BrPhTPY as a white powder. Further product was obtained via a second crop from the filtrate and these were combined and dried under vacuum (2.71 g, 26%).

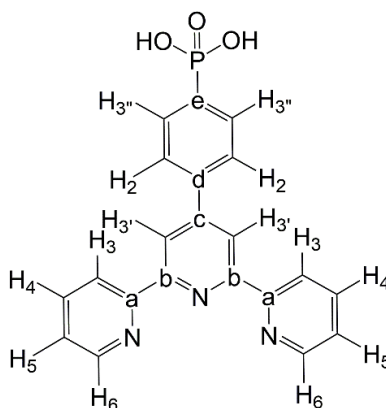
**<sup>1</sup>H NMR** (400.1 MHz, CDCl<sub>3</sub>): δ= 8.73 (ddd, *J*=4.8, 1.8, 0.9 Hz, 2H; Ar-H), 8.70 (s, br, 2H; Ar-H), 8.67 (dt, *J*=7.9, 1.1 Hz, 2H; Ar-H), 7.91-7.87 (td, *J*=7.5, 1.8, 6H; Ar-H), 7.79-7.77 (m, 2H; Ar-H), 7.65-7.63 (m, 2H; Ar-H), 7.38-7.35 (ddd, *J*=7.5, 4.8, 1.2 Hz, 2H; Ar-H) ppm; **MS (ESI)** *m/z* [*M*+H]<sup>+</sup> calc for [C<sub>21</sub>H<sub>14</sub>N<sub>3</sub>Br<sub>1</sub>+H]<sup>+</sup>: 390.0426, found: 390.0426.

#### Synthesis of PO(OEt)<sub>2</sub>PhTPY – C<sub>25</sub>H<sub>24</sub>N<sub>3</sub>PO<sub>3</sub>

Ethanol (80 mL), diethylphosphite (3.32 mL, 25.8 mmol) and triethylamine (2.69 mL, 19.3 mmol) were added to BrPhTPY (2.5 g, 6.4 mmol), Pd(OAc)<sub>2</sub> (145 mg, 0.65 mmol) and PPh<sub>3</sub> (507 mg, 1.9 mmol) under argon and the mixture was heated at reflux (75 °C) whilst stirring for 22h. The solution was allowed to cool to RT before filtering, and the solvent was removed in vacuo. The yellow precipitate was recrystallised from hot CH<sub>3</sub>CN twice to yield PO(OEt)<sub>2</sub>PhTPY as an off-white crystalline solid (2.16 g, 74%).

**<sup>1</sup>H NMR** (400.1 MHz, CDCl<sub>3</sub>) δ= 8.75 (s, br, 2H; Ar-H), 8.74-8.72 (ddd, *J*=4.8, 1.8, 0.9 Hz, 2H; Ar-H), 8.69-8.67 (dt, *J*=7.9, 1.1 Hz, 2H, Ar-H), 8.01-7.93 (m, 4H; Ar-H), 7.91-7.87 (td, *J*=7.7, 1.8 Hz, 2H; Ar-H), 7.35-7.38 (ddd, *J*=7.5, 4.8, 1.2 Hz, 2H; Ar-H), 4.24-4.08 (m, 4H; CH<sub>2</sub>), 1.35 (t, *J*=7.0 Hz, 6H; CH<sub>3</sub>) ppm; **<sup>31</sup>P NMR** (162 MHz, CDCl<sub>3</sub>) δ= 18.31 ppm; **MS (ESI)** *m/z* [*M*+H]<sup>+</sup> calc for [C<sub>25</sub>H<sub>24</sub>N<sub>3</sub>O<sub>3</sub>P<sub>1</sub>+H]<sup>+</sup>: 446.1628, found: 446.1624.

#### Synthesis of TPY, PO(OH)<sub>2</sub>PhTPY – C<sub>21</sub>H<sub>16</sub>N<sub>3</sub>PO<sub>3</sub>



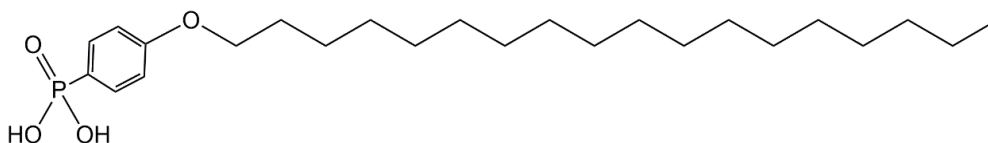
### 3. Design and synthesis of asymmetric hybrid POM (1)

PO(OEt)<sub>2</sub>PhTPY (2 g, 4.4 mmol) was dissolved in dry DCM (50 mL) and bromotrimethylsilane (1.8 mL, 13 mmol) was added under argon before the mixture was stirred at RT for 16 h. The solvent was removed in vacuo, before adding a methanol-DCM mixture (40 mL, 1:1 v/v), and the solution was stirred at RT for 3 h. The cloudy purple mixture was filtered to yield the crude product as a lilac powder. The crude was washed with hot CH<sub>3</sub>CN and then ether to give **TPY** as an off-white powder (1.15 g, 67%).

<sup>1</sup>H NMR (400.1 MHz, DMSO-d<sub>6</sub>): δ 8.80-8.79 (ddd, *J*=4.8, 1.8, 0.9 Hz, 2H; *H*<sub>6</sub>), 8.77 (s, br, 2H; *H*<sub>3'</sub>), 8.74-8.72 (dt, *J*=8.0, 1.1 Hz 2H; *H*<sub>3</sub>), 8.12-8.08 (td, *J*=7.7, 1.8 Hz, 2H; *H*<sub>4</sub>), 8.07-8.04 (m, 2H; *H*<sub>2</sub>), 7.92-7.87 (m, 2H; *H*<sub>3''</sub>), 7.60-7.57 (ddd, *J*=7.5, 4.8, 1.2 Hz, 2H; *H*<sub>5</sub>) ppm; <sup>13</sup>C NMR (100.6 MHz, DMSO-d<sub>6</sub>): δ 155.9 (s, C-b), 154.8 (C-a), 149.5 (C-6), 149.4 (C-e), 140.0 (C-c), 138.6 (C-4), 134.9 (C-d), 132.1/132.0 (C-2), 127.3/127.1 (C-3''), 125.3 (s, C-5), 121.8 (C-3), 118.8 (C-3') ppm; <sup>31</sup>P NMR (162 MHz, DMSO-d<sub>6</sub>): δ 11.95 ppm; **MS (ESI)** *m/z* [*M*+*H*]<sup>+</sup> calc for [C<sub>21</sub>H<sub>16</sub>N<sub>3</sub>O<sub>3</sub>P<sub>1</sub>+H]<sup>+</sup>: 390.1002, found: 390.1003; **IR (ATR)**: 665, 781, 894, 1071, 1133, 1241, 1288, 1393, 1424, 1527, 1595 cm<sup>-1</sup>; **Elemental Analysis** calc (%) for C<sub>21</sub>H<sub>16</sub>O<sub>3</sub>N<sub>3</sub>P<sub>1</sub>: C 64.78, H 4.14, N 10.79, found: C 60.35, H 4.01, N 9.95; **UV-Vis** (DMF): λ<sub>max</sub> (ε, mol<sup>-1</sup>Lcm<sup>-1</sup>)= 280 (41900), 320 (8750) nm.

#### 3.7.2.3 C<sub>18</sub>

C<sub>18</sub> was synthesised according to a procedure devised by Sharad Amin.<sup>[14]</sup>



#### Synthesis of BrPhOC<sub>18</sub> – C<sub>24</sub>H<sub>41</sub>BrO

1-Bromooctadecane (3.00g, 9.00 mmol) and 4-bromophenol (1.87 g, 10.8 mmol) were dissolved in DMF (40 mL). To this solution, KI (0.26 g, 1.57 mmol) and K<sub>2</sub>CO<sub>3</sub> (4.98 g, 36.0 mmol) were added, and the reaction mixture was heated (80°C) for 20 h. The reaction was then cooled to RT and the solvent was then removed *in vacuo*. The solid

### 3. Design and synthesis of asymmetric hybrid POM (1)

---

product was dissolved in diethyl ether (100 mL) and washed with 2M NaOH (2 x 100 mL), then brine (100 mL). The organic fraction was dried over MgSO<sub>4</sub> and the solvent was removed *in vacuo* to leave an orange oil. The crude product was then recrystallised from the minimal amount of hot ethanol to obtain **BrPhOC<sub>18</sub>** as a white solid (2.18 g, 57%).

**<sup>1</sup>H NMR** (400 MHz, CDCl<sub>3</sub>) δ= 7.38-7.32 (m, 2H; Ar-H), 6.79-6.74 (m, 2H; Ar-H), 3.91 (t, *J*=6.6 Hz, 2H; CH<sub>2</sub>), 1.80-1.71 (m, 2H; CH<sub>2</sub>), 1.48-1.23 (m, 30H; -CH<sub>2</sub>-), 0.88 (t, *J*= 6.7 Hz, 3H; CH<sub>3</sub>) ppm.

#### Synthesis of PO(OEt)<sub>2</sub>PhOC<sub>18</sub> – C<sub>28</sub>H<sub>51</sub>O<sub>4</sub>P

Triethylphosphite (2.42 mL, 14.1 mmol) and anhydrous NiCl<sub>2</sub> (0.061 g, 0.47 mmol) were added to a microwave vessel and stirred and purged with argon for 10 mins. Dried BrPhOC<sub>18</sub> (2.00 g, 4.70 mmol) was added to the black mixture which was briefly heated to dissolve and it was purged with argon for a further 10 mins. The vessel was then heated in the microwave at 190 °C for 45 mins. The reaction mixture was then cooled to RT and dissolved in ethyl acetate (80 mL). The solution was then filtered and centrifuged for 15 mins (8000 rpm). The black precipitate was filtered off and the solvent was evaporated *in vacuo* to leave a yellow oil. The crude product was then dissolved in hot acetonitrile (60 mL) and filtered to remove a pale yellow oily solid. The solvent was then removed from the filtrate *in vacuo* to yield **PO(OEt)<sub>2</sub>PhOC<sub>18</sub>** as an off-white waxy solid (2.03 g, 89%).

**<sup>1</sup>H NMR** (400 MHz, CDCl<sub>3</sub>) δ 7.75–7.65 (m, 2H; Ar-H), 6.97–6.89 (m, 2H; Ar-H), 4.19–4.01 (m, 6H; O-CH<sub>2</sub>), 1.83-1.75 (m, 2H; CH<sub>2</sub>), 1.49–1.20 (m, 30H; CH<sub>2</sub>), 0.87 (t, *J*=6.7 Hz, 3H; CH<sub>3</sub>) ppm; **<sup>31</sup>P NMR** (162 MHz, CDCl<sub>3</sub>) δ 19.90 ppm; **MS (ESI)** *m/z* [*M*+H]<sup>+</sup> calc for [C<sub>28</sub>H<sub>51</sub>O<sub>4</sub>P+H]<sup>+</sup>: 483.36, found: 483.36.

#### Synthesis of **C<sub>18</sub>**, PO(OH)<sub>2</sub>PhOC<sub>18</sub> – C<sub>24</sub>H<sub>43</sub>O<sub>4</sub>P

Dry **PO(OEt)<sub>2</sub>PhOC<sub>18</sub>** (2.03g, 4.21 mmol) was dissolved in dry DCM (20 mL) before bromotrimethylsilane (TMSBr) (1.94 mL, 14.7 mmol) was added under argon to form a pale yellow solution. The solution was then stirred for 20 h at RT. The solvent and excess TMSBr was removed *in vacuo* to yield a yellow oil. To the flask, methanol-water



### 3. Design and synthesis of asymmetric hybrid POM (1)

(80:20 v/v, 20 mL) was added and stirred for 3 h to form a white suspension. The mixture was then centrifuged and the solvent was decanted from the white precipitate. The solid was dried under vacuum to yield the crude as an off-white solid. The crude product was then washed with diethyl ether (2 x 25 mL), then stirred in hot acetonitrile (50 mL) and filtered. The solid was washed with ether again and left to dry in air to yield **C<sub>18</sub>** as a white powder (1.02 g, 57%).

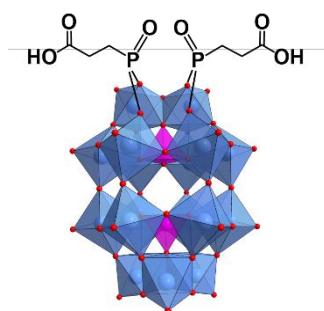
**<sup>1</sup>H NMR** (500 MHz, Methanol-*d*<sub>4</sub>) δ 7.74-7.69 (m, 2H; Ar-H), 7.02-6.96 (m, 2H; Ar-H), 4.02 (t, *J*=6.4 Hz, 2H; O-CH<sub>2</sub>), 1.82-1.74 (m, 2H; CH<sub>2</sub>), 1.52-1.24 (m, 30H; -CH<sub>2</sub>-), 0.90 (t, *J*=6.9 Hz, 3H; CH<sub>3</sub>) ppm; **<sup>31</sup>P NMR** (202 MHz, Methanol-*d*<sub>4</sub>) δ 17.28 ppm; **MS (ESI)** *m/z* [*M*-H]<sup>-</sup> calc for [C<sub>24</sub>H<sub>43</sub>O<sub>4</sub>P-H]<sup>-</sup>: 425.29, found: 425.29; **IR (ATR)**: 829 (s), 947 (vs), 1008 (br, vs), 1144 (vs), 1253 (s), 1292 (w), 1461 (m), 1474 (m), 1506 (w), 1527 (w), 1572 (w), 1599 (s), 2848 (vs), 2916 (vs) cm<sup>-1</sup>; **Elemental Analysis** calc (%) for C<sub>24</sub>H<sub>43</sub>O<sub>4</sub>P: C 67.58, H 10.16, N 0, found: C 67.61, H 10.63, N 0.04.

#### 3.7.2.4 **C<sub>16</sub> & C<sub>10</sub>**

**C<sub>16</sub>** and **C<sub>10</sub>** were provided by Sharad Amin, prepared by his procedures published in literature.<sup>[14]</sup>

#### 3.7.2.5 **[P<sub>2</sub>W<sub>17</sub>O<sub>57</sub>{(PPA)<sub>2</sub>}], (SymPPA)**

K<sub>3</sub>(C<sub>2</sub>H<sub>8</sub>N)<sub>3</sub>[P<sub>2</sub>W<sub>17</sub>O<sub>57</sub>{(PO<sub>3</sub>C<sub>2</sub>H<sub>4</sub>COOH)<sub>2</sub>}



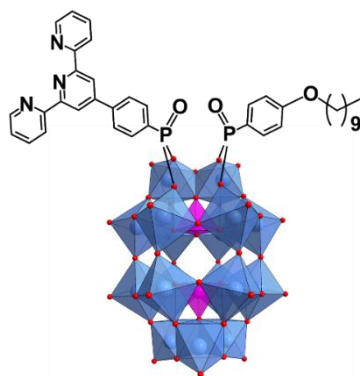
K<sub>10</sub>-[P<sub>2</sub>W<sub>17</sub>O<sub>61</sub>] (1.5 g, 0.33 mmol), 3-phosphonophosphonic acid (101 mg, 0.33 mmol) and KCl (0.49 g, 6.57 mmol) were suspended in DMF (30 mL). 12M HCl (275 μL, 3.3 mmol) was added dropwise to this whilst stirring, before the mixture was heated (85

### 3. Design and synthesis of asymmetric hybrid POM (1)

°C) overnight. The reaction mixture was allowed to cool before an excess of ether was added to precipitate a dark blue oily layer. The mixture was centrifuged and the supernatant was decanted from the oily layer. The dark blue oil was dissolved in the minimum volume of water and precipitated with the addition of an excess of dioxane. The mixture was centrifuged and the supernatant decanted to collect a pale blue solid. The solid was then dried under vacuum until it resembled a dry blue powder (0.67 g, 44 %).

$^1\text{H NMR}$  (DMSO- $d_6$ , 400.1 MHz)  $\delta$ = 12.19 (s, br, 2H, -COOH), 8.17 (s, br, 6H;  $\text{NH}_2(\text{CH}_3)_2^+$ ), 2.71-2.35 (m, 4H;  $\text{HOOC-CH}_2-$ ), 2.56 (s, br,  $J$ = 18H;  $\text{NH}_2(\text{CH}_3)_2^+$ ), 2.18-1.89 (m, 4H;  $\text{PO-CH}_2-$ ) ppm;  $^{31}\text{P NMR}$  (DMSO- $d_6$ , 162 MHz)  $\delta$ = 27.42, -11.45, -12.98 ppm; **IR (ATR)** 424 (s), 471 (s), 523 (vs), 720 (br, vs), 906 (s), 953 (s), 1085 (s), 1389 (w), 1412 (w), 1461 (m), 1611 (w), 1644 (m), 1721 (m, C=O), 2927 (w, C-H), 2968 (w, C-H), 2587-3250 (m, br, O-H)  $\text{cm}^{-1}$ ; **Elemental Analysis:** calc for  $\text{K}_3\text{P}_4\text{W}_{17}\text{O}_{67}\text{C}_{12}\text{H}_{34}\text{N}_3$ : C 3.09, H 0.74, N 0.90, found: C 4.36, H 0.93, N 1.05.

#### 3.7.2.6 $[\text{P}_2\text{W}_{17}\text{O}_{57}\{(\text{TPY})(\text{C}_{10})\}]$ , (Asym $\text{C}_{10}$ )



$\text{K}_{10}[\text{P}_2\text{W}_{17}\text{O}_{61}]$  (0.7 g, 0.154 mmol),  $\text{PO}(\text{OH})_2\text{PhTPY}$  (0.060 g, 0.154 mmol),  $\text{C}_{10}$  (0.066 g, 0.210 mmol), and  $\text{KCl}$  (0.23 g, 3.09 mmol) were suspended in  $\text{DMF-CH}_3\text{CN}$  (1:1 v/v) and stirred. 12M  $\text{HCl}$  (128  $\mu\text{L}$ , 1.54 mmol) was added dropwise to the solution whilst stirring, and the mixture was heated to 85°C for 16 h. The mixture was allowed to cool to RT before filtering and removing the solvent in vacuo. The solid was dissolved in the minimum volume of acetonitrile and centrifuged to remove a small amount of

### 3. Design and synthesis of asymmetric hybrid POM (1)

insoluble solid by decanting the supernatant. An excess of ether was added to the solvent to give a milky solution, which was centrifuged to give a dark orange precipitate in a yellow supernatant. The solvent was decanted and the process of sonicating the precipitate in ether, centrifuging and decanting was repeated until the solid resembled a free-flowing powder. The solid was then redissolved in the minimum volume of acetone and centrifuged to separate a small amount of insoluble solid. Finally, the solvent was decanted and then removed in vacuo to yield **AsymC<sub>10</sub>** as an orange crystalline solid (0.24 g, 31%).

<sup>1</sup>H NMR (DMSO-d<sub>6</sub> 400.1 MHz) δ= 8.97-8.86 (m, 6H; Ar-), 8.31 (ddd, *J*= 7.8, 6.7, 1.9 Hz, 2H; Ar-H), 8.26-8.17 (m, 2H), 8.26-8.07 (br, 4H; NH<sub>2</sub>(CH<sub>3</sub>)<sub>2</sub><sup>+</sup>), 8.14-8.07 (m, 2H; Ar-H), 7.95-7.86 (m, 2H; Ar-H) 7.78-7.72 (m, 2H; Ar-H), 7.01 (dd, *J*= 8.8, 3.4 Hz, 2H; Ar-H), 4.04 (t, *J*= 6.5 Hz, 2H; O-CH<sub>2</sub>), 2.55 (t, *J*= 5.6 Hz, 12H; NH<sub>2</sub>(CH<sub>3</sub>)<sub>2</sub><sup>+</sup>), 1.80-1.67 (m, 2H; CH<sub>2</sub>), 1.48-1.20 (m, 14H; -CH<sub>2</sub>-), 0.86 (t, 3H, CH<sub>3</sub>) ppm; <sup>31</sup>P NMR (DMSO-d<sub>6</sub>, 162 MHz) δ= 16.80, 13.26, -11.33, -12.95 ppm; **Elemental Analysis** calc (%) for K<sub>4</sub>P<sub>4</sub>W<sub>17</sub>O<sub>64</sub>C<sub>41</sub>H<sub>55</sub>N<sub>5</sub>: C 9.76, H 1.10, N 1.39, found: C 10.40, H 1.27, N 1.48.

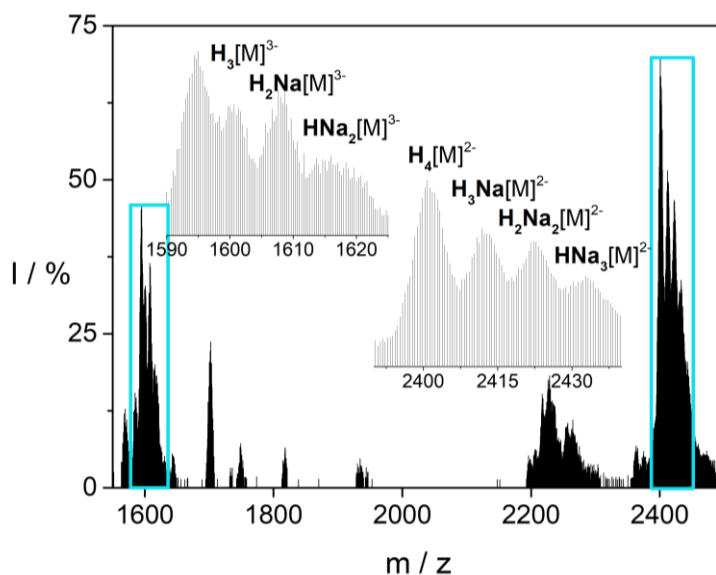


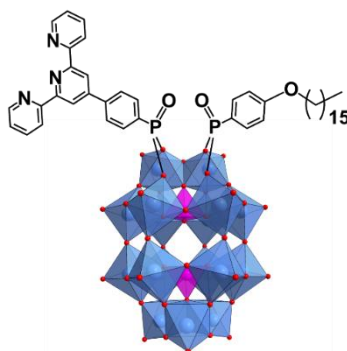
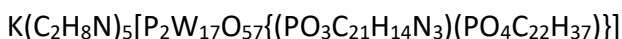
**Figure 55.** Negative mode ESI mass spectrum of **AsymC<sub>10</sub>** in acetonitrile. [M] =  $[P_2W_{17}O_{57}\{(PO_3C_{21}H_{14}N_3)(PO_4C_{16}H_{25})\}]^{6-}$ .

### 3. Design and synthesis of asymmetric hybrid POM (1)

| Assignment   | z  | m/z (obs.) | m/z (calc.) |
|--|----|------------|-------------|
| $\text{H}_3[\text{P}_2\text{W}_{17}\text{O}_{61}\{(\text{POC}_{21}\text{H}_{14}\text{N}_3)(\text{PO}_2\text{C}_{16}\text{H}_{25})\}]$            | 3- | 1600.6895  | 1600.6671   |
| $\text{H}_2\text{Na}[\text{P}_2\text{W}_{17}\text{O}_{61}\{(\text{POC}_{21}\text{H}_{14}\text{N}_3)(\text{PO}_2\text{C}_{16}\text{H}_{25})\}]$   | 3- | 1608.0137  | 1607.9944   |
| $\text{HNa}_2[\text{P}_2\text{W}_{17}\text{O}_{61}\{(\text{POC}_{21}\text{H}_{14}\text{N}_3)(\text{PO}_2\text{C}_{16}\text{H}_{25})\}]$          | 3- | 1615.3330  | 1615.3218   |
| $\text{H}_4[\text{P}_2\text{W}_{17}\text{O}_{61}\{(\text{POC}_{21}\text{H}_{14}\text{N}_3)(\text{PO}_2\text{C}_{16}\text{H}_{25})\}]$            | 2- | 2401.3161  | 2401.5046   |
| $\text{H}_3\text{Na}[\text{P}_2\text{W}_{17}\text{O}_{61}\{(\text{POC}_{21}\text{H}_{14}\text{N}_3)(\text{PO}_2\text{C}_{16}\text{H}_{25})\}]$   | 2- | 2412.2980  | 2412.4956   |
| $\text{H}_2\text{Na}_2[\text{P}_2\text{W}_{17}\text{O}_{61}\{(\text{POC}_{21}\text{H}_{14}\text{N}_3)(\text{PO}_2\text{C}_{16}\text{H}_{25})\}]$ | 2- | 2422.2891  | 2422.4866   |
| $\text{HNa}_3[\text{P}_2\text{W}_{17}\text{O}_{61}\{(\text{POC}_{21}\text{H}_{14}\text{N}_3)(\text{PO}_2\text{C}_{16}\text{H}_{25})\}]$          | 2- | 2433.7704  | 2434.4775   |

**Table 7.** Selected ESI-MS peak assignments for **AsymC10**.

#### 3.7.2.7 $[\text{P}_2\text{W}_{17}\text{O}_{57}\{(\text{TPY})(\text{C}_{16})\}]$ (**AsymC16**)



$\text{K}_{10}\text{-}[\text{P}_2\text{W}_{17}\text{O}_{61}]$  (1.43 g, 0.314 mmol),  $\text{PO}(\text{OH})_2\text{PhTPY}$  (0.125 g, 0.314 mmol),  $\text{C}_{16}$  (0.122g, 0.314 mmol), and KCl (0.47 g, 6.30 mmol) were suspended in DMF- $\text{CH}_3\text{CN}$  (30 mL, 1:1 v/v) and stirred. 12M HCl (262  $\mu\text{L}$ , 3.14 mmol) was added dropwise to the solution whilst stirring, and the mixture was heated (85°C) for 16 h. The mixture was allowed to cool to RT before filtering. An excess of ether was then added (~90 mL) to give a milky yellow-green solution, which was centrifuged to give a dark orange precipitate and yellow supernatant. The supernatant was decanted and the process of sonicating the precipitate in ether, centrifuging and decanting was repeated until the precipitate resembled a free-flowing powder. The solid was then dissolved in the minimum volume of acetonitrile (~5 mL) and centrifuged to separate an insoluble pale

### 3. Design and synthesis of asymmetric hybrid POM (1)

solid. The yellow supernatant was decanted and ether was added to it to precipitate a brown solid that was collected by centrifugation. The solid was redissolved in the minimum volume of acetone (~5 mL) and centrifuged to separate a small amount of insoluble blue solid. The solvent was decanted and removed in vacuo to leave an orange crystalline solid. The solid was then again redissolved in the minimum volume of acetonitrile, which was centrifuged to separate any insoluble solid before an excess of ether was added to the supernatant to cause precipitation. The precipitate was collected by centrifugation, sonicated in ether and dried in air with gentle heating to yield **AsymC<sub>16</sub>** as an orange-brown solid (0.156 g, 10%).

**<sup>1</sup>H NMR** (400.1 MHz, DMSO-*d*<sub>6</sub>) δ= 8.83-8.67 (m, 6H; Ar-H), 8.30-8.10 (br, 10H; NH<sub>2</sub>(CH<sub>3</sub>)<sub>2</sub><sup>+</sup>) 8.24-8.16 (m, br, 2H; Ar-H), 8.09-8.03 (m, 2H; Ar-H), 8.03-7.96 (m, 2H; Ar-H), 7.94-7.88 (m, 2H; Ar-H), 7.55 (ddd, *J*= 7.6, 4.6, 1.3 Hz, 2H; Ar-H), 7.01 (dd, *J*= 8.8, 3.4 Hz, 2H; Ar-H), 4.04 (t, *J*= 6.5 Hz, 2H; O-CH<sub>2</sub>), 2.55 (t, *J*= 5.4 Hz, 30H; NH<sub>2</sub>(CH<sub>3</sub>)<sub>2</sub><sup>+</sup>), 1.79-1.67 (m, 2H; CH<sub>2</sub>), 1.48-1.17 (m, 26H; -CH<sub>2</sub>-), 0.85 (t, 3H; CH<sub>3</sub>) ppm; **<sup>31</sup>P NMR** (162 MHz, DMSO-*d*<sub>6</sub>) δ= 16.75, 13.43, -11.33, -12.94 ppm; **Elemental Analysis** calc (%) for K<sub>1</sub>P<sub>4</sub>W<sub>17</sub>O<sub>64</sub>C<sub>53</sub>H<sub>91</sub>N<sub>8</sub>: C 12.35, H 1.78, N 2.17, found: C 12.00, H 1.65, N 1.94.

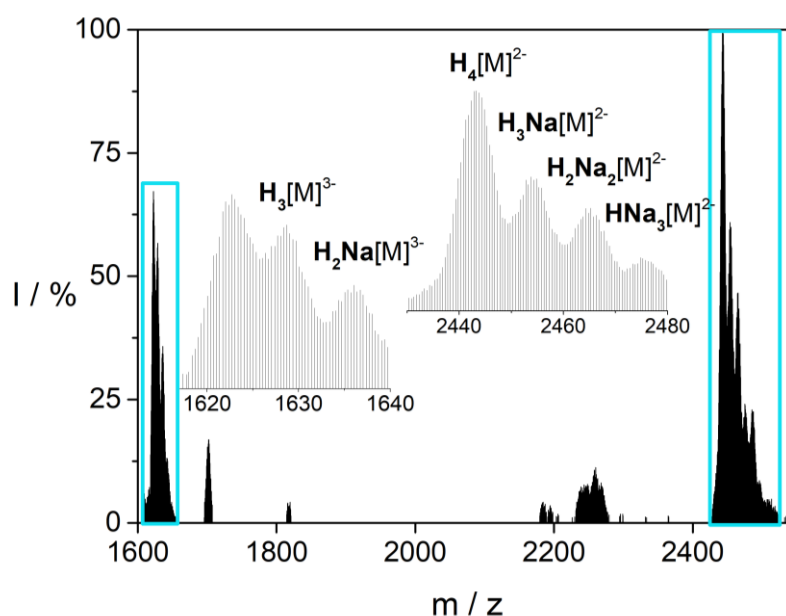


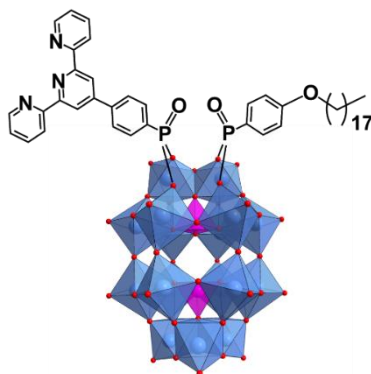
**Figure 56.** Negative mode ESI mass spectrum of **AsymC<sub>16</sub>** in acetonitrile. [M] = [P<sub>2</sub>W<sub>17</sub>O<sub>57</sub>{(PO<sub>3</sub>C<sub>21</sub>H<sub>14</sub>N<sub>3</sub>)(PO<sub>4</sub>C<sub>22</sub>H<sub>37</sub>)}]<sup>6-</sup>.

### 3. Design and synthesis of asymmetric hybrid POM (1)

| Assignment  | z  | m/z (obs.) | m/z (calc.) |
|---|----|------------|-------------|
| <b>H<sub>3</sub></b> [P <sub>2</sub> W <sub>17</sub> O <sub>61</sub> {(POC <sub>21</sub> H <sub>14</sub> N <sub>3</sub> )(PO <sub>2</sub> C <sub>22</sub> H <sub>37</sub> )}]               | 3- | 1628.7121  | 1628.6984   |
| <b>H<sub>2</sub>Na</b> [P <sub>2</sub> W <sub>17</sub> O <sub>61</sub> {(POC <sub>21</sub> H <sub>14</sub> N <sub>3</sub> )(PO <sub>2</sub> C <sub>22</sub> H <sub>37</sub> )}]             | 3- | 1626.0368  | 1636.0257   |
| <b>H<sub>4</sub></b> [P <sub>2</sub> W <sub>17</sub> O <sub>61</sub> {(POC <sub>21</sub> H <sub>14</sub> N <sub>3</sub> )(PO <sub>2</sub> C <sub>22</sub> H <sub>37</sub> )}]               | 2- | 2443.3250  | 2443.5516   |
| <b>H<sub>3</sub>Na</b> [P <sub>2</sub> W <sub>17</sub> O <sub>61</sub> {(POC <sub>21</sub> H <sub>14</sub> N <sub>3</sub> )(PO <sub>2</sub> C <sub>22</sub> H <sub>37</sub> )}]             | 2- | 2454.3106  | 2454.5425   |
| <b>H<sub>2</sub>Na<sub>2</sub></b> [P <sub>2</sub> W <sub>17</sub> O <sub>61</sub> {(POC <sub>21</sub> H <sub>14</sub> N <sub>3</sub> )(PO <sub>2</sub> C <sub>22</sub> H <sub>37</sub> )}] | 2- | 2465.3095  | 2465.5335   |
| <b>HN<sub>3</sub></b> [P <sub>2</sub> W <sub>17</sub> O <sub>61</sub> {(POC <sub>21</sub> H <sub>14</sub> N <sub>3</sub> )(PO <sub>2</sub> C <sub>22</sub> H <sub>37</sub> )}]              | 2- | 2475.7883  | 2476.5245   |

**Table 8.** Selected ESI-MS peak assignments for **AsymC<sub>16</sub>**.

#### 3.7.2.8 [P<sub>2</sub>W<sub>17</sub>O<sub>57</sub>{(TPY)(C<sub>18</sub>)}], (1)



K<sub>10</sub>-[P<sub>2</sub>W<sub>17</sub>O<sub>61</sub>] (1.6 g, 0.35 mmol), **TPY** (0.14 g, 0.35 mmol), **C<sub>18</sub>** (0.15g, 0.35 mmol), and KCl (0.52 g, 6.98 mmol) were suspended in DMF-CH<sub>3</sub>CN (50 mL, 1:1 v/v) and stirred. 12M HCl (290 μL, 3.5 mmol) was added dropwise to the solution whilst stirring, and the mixture was heated to 85°C for 16 h. The mixture was allowed to cool to RT before filtering. A large excess of ether was added (120 mL) to give a milky solution, which was centrifuged to give a dark orange-brown precipitate in a yellow supernatant. The solvent was decanted and the process of sonicating the precipitate in ether, centrifuging and decanting was repeated until the precipitate resembled a free-flowing green-brown powder. The solid was sonicated in acetonitrile (10-15 mL) and centrifuged to separate an insoluble pale green-blue solid. The yellow supernatant was decanted, and ether was added (25-30 mL) to it to precipitate a dark

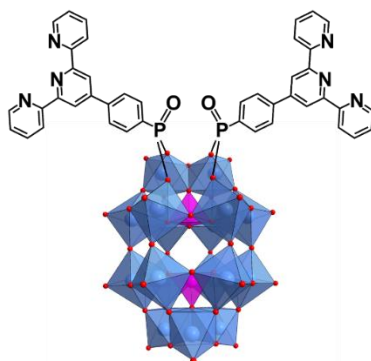
### 3. Design and synthesis of asymmetric hybrid POM (1)

orange-brown solid and leave a pale-yellow supernatant. The solid was collected by centrifugation, sonicated in ether and dried in air with gentle heating. The process of: re-dissolving in acetonitrile and centrifuging to remove any insoluble **2**, followed by re-precipitating **1** from the supernatant with ether, was repeated until no **2** or **3** was visible in the  $^{31}\text{P}$  and  $^1\text{H}$  NMR. The dry solid was finally dissolved in a minimum amount of acetone and centrifuged to separate any insoluble solid. The solvent was then removed in vacuo to yield **1** as a dark orange crystalline solid (390 mg, 22% (or 43%, assuming 50% is the max. recovery of asymmetric product statistically)).

$^1\text{H}$  NMR (400.1 MHz, DMSO- $d_6$ )  $\delta$ = 8.95-8.88 (m, 6H; Ar-H), 8.33-8.29 (td, 2H; Ar-H), 8.33-8.09 (br, 4H;  $\text{NH}_2(\text{CH}_3)_2^+$ ), 8.25-8.19 (m, 2H; Ar-H), 8.12-8.09 (m, 2H; Ar-H), 7.77-7.73 (m, 2H; Ar-H), 7.03-7.00 (dd, 2H; Ar-H), 4.04 (t, 2H; O- $\text{CH}_2$ ), 2.55 (t, 12H;  $\text{NH}_2(\text{CH}_3)_2^+$ ), 1.74 (q, 2H;  $\text{CH}_2$ ), 1.47-1.21 (m, 30H;  $-\text{CH}_2-$ ), 0.86 (t, 3H;  $\text{CH}_3$ ) ppm;  $^{31}\text{P}$  NMR (162 MHz, DMSO- $d_6$ )  $\delta$ = 16.72, 13.40, -11.32, -12.95 ppm; IR (ATR): 425 (s), 472 (s), 526 (s), 567 (s), 594 (s), 668 (s), 718 (br, vs, W-O-W), 800 (br, vs, W-O-W), 907 (s, W-O-W), 954 (s, W=O), 963 (s, W=O), 1084 (s, P-O), 1133 (w, P=O), 1253 (w), 1294 (w), 1387 (w), 1414 (w), 1463 (m), 1504 (w), 1531 (w), 1568-1595 (m), 1651 (w), 2850 (m, C-H), 2920 (m, C-H)  $\text{cm}^{-1}$ ; **Elemental Analysis** calc (%) for  $\text{K}_4\text{P}_4\text{W}_{17}\text{O}_{64}\text{C}_{49}\text{H}_{71}\text{N}_5$ : C 11.41, H 1.39, N 1.36, found: C 11.48, H 1.47, N 1.28; **TGA Analysis**: Weight change from (115.7 to 600.7°C) = 8.408 % = loss of 2  $\text{C}_2\text{H}_8\text{N}^+$  ( $\text{DMA}^+$ ) +  $\text{C}_{18}$  (cleaved at phosphonate linker unit) (calc= 8.673 %); **UV-Vis** (DMF):  $\lambda_{\text{max}}$  ( $\epsilon$ ,  $\text{mol}^{-1}\text{Lcm}^{-1}$ )= 277 (91,100), 315 (39,700) nm.

#### 3.7.2.9 $[\text{P}_2\text{W}_{17}\text{O}_{57}\{(\text{TPY})_2\}]$ , (**2**)

$(\text{C}_2\text{H}_8\text{N})_6[\text{P}_2\text{W}_{17}\text{O}_{57}\{(\text{PO}_3\text{C}_{21}\text{H}_{14}\text{N}_3)_2\}]\cdot\text{C}_3\text{H}_7\text{NO}$



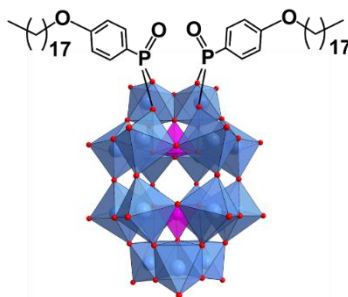
### 3. Design and synthesis of asymmetric hybrid POM (1)

$K_{10}[P_2W_{17}O_{61}]$  (2 g, 0.439 mmol),  $PO(OH)_2PhTPY$  (34 mg, 0.878 mmol) and KCl (0.66 g, 8.78 mmol) were suspended in DMF (20 mL). 12M HCl (370  $\mu$ L, 4.39 mmol) was added dropwise to this whilst stirring, before the mixture was heated (85 °C) for 16 h. An excess of ether was added to the filtrate to precipitate a dark blue-green oily layer. The mixture was centrifuged and then the solvent was decanted. The oil was redissolved in the minimum volume of DMF and precipitated again with ether. Then, the process of centrifugation, decanting and sonication with ether was repeated until it resembled a free-flowing powder. **2** was yielded as a green solid (1.9 g, 79%).

**$^1H$  NMR** (400.1 MHz, DMSO- $d_6$ ,)  $\delta$ = 8.81-8.79 (m, 4H; Ar-H), 8.78 (s, br, 4H; Ar-H), 8.71-8.68 (dt, 4H; Ar-H), 8.43-8.26 (br, 12H;  $NH_2(CH_3)_2^+$ ), 8.25-8.19 (m, 4H; Ar-H), 8.08-7.98 (m, 8H; Ar-H), 7.56-7.52 (ddd,  $J$ =7.5, 4.6, 4H; Ar-H) ppm; 2.56 (br, 36H;  $NH_2(CH_3)_2^+$ );  **$^{31}P$  NMR** (162 MHz, DMSO- $d_6$ ,)  $\delta$ = 14.20, -11.27, -12.90 ppm; **IR** (ATR): 426 (s), 523 (s), 575 (s), 668 (s), 718 (br, vs), 767 (br, vs), 909 (s), 950 (s), 1022 (w), 1084 (s), 1133 (w), 1259 (w), 1300 (w), 1387 (w), 1414 (w), 1463 (m), 1531 (w), 1568-1595 (m), 2766 (br, m), 2961 (br, m)  $cm^{-1}$ ; **Elemental Analysis**: calc (%) for  $P_4W_{17}O_{64}C_{57}H_{83}N_{13}$ : C 13.11, H 1.60, N 3.49, found: C 13.09, H 1.6, N 3.52; **TGA Analysis**: Step transition (170.31 to 380.3°C) wt loss = 6.481 % = loss of 6  $C_2H_8N^+$  ( $DMA^+$ ) + 1 DMF (calc= 6.655 %); **UV-Vis** (DMF):  $\lambda_{max}$  ( $\epsilon$ ,  $mol^{-1}Lcm^{-1}$ )= 280 (113,100), 315 (39,900) nm.

#### 3.7.2.10 $[P_2W_{17}O_{57}\{(C_{18})_2\}]$ , (**3**)

$K_2(C_2H_8N)_4[P_2W_{17}O_{57}\{(PO_4C_{24}H_{41})_2\}].3C_3H_7NO$



$K_{10}[P_2W_{17}O_{61}]$  (0.6 g, 0.132 mmol), **C<sub>18</sub>** (112 mg, 0.263 mmol), and KCl (0.2 g, 2.68 mmol) were suspended in DMF- $CH_3CN$  (50 mL, 1:1 v/v) and stirred. 12M HCl (110  $\mu$ L, 1.32 mmol) was added dropwise to the solution whilst stirring, and the mixture was heated (85°C) for 16 h. The mixture was allowed to cool to RT before filtering. The



### 3. Design and synthesis of asymmetric hybrid POM (1)

---

solvent was removed *in vacuo* and the sticky solid was then redissolved in acetone (~10 mL) before it was left in the fridge (4-5°C) overnight. The solution was then centrifuged and the yellow supernatant was decanted from any precipitate. The solvent was then removed *in vacuo* to yield **3** as a crystalline orange solid (0.51 g, 69%).

**<sup>1</sup>H NMR** (400.1 MHz, DMSO-d<sub>6</sub>,) δ= 8.33-8.03 (br, 8H; NH<sub>2</sub>(CH<sub>3</sub>)<sub>2</sub><sup>+</sup>), 7.87 (dd, *J*=13.6, 8.5 Hz, 4H; Ar-H), 6.98 (dd, *J*=8.8, 3.3 Hz, 4H; Ar-H), 4.02 (t, *J*=6.5 Hz, 4H; O-CH<sub>2</sub>-); 2.55 (br, 24H; NH<sub>2</sub>(CH<sub>3</sub>)<sub>2</sub><sup>+</sup>) 1.75-1.68 (m, 4H; -CH<sub>2</sub>-), 1.45-1.18 (m, 60H; -CH<sub>2</sub>-), 0.84 (t, *J*=6.9 Hz, 6H; -CH<sub>3</sub>) ppm; **<sup>31</sup>P NMR** (162 MHz, DMSO-d<sub>6</sub>,) δ= 16.04, -11.38, -13.01 ppm; **IR** (ATR): 422 (s), 471 (s), 523 (s), 566 (s), 716 (br, vs), 797 (br, vs), 906 (s), 955 (s), 1087 (s), 1136 (m), 1255 (w), 1292 (w), 1385 (w), 1412 (w), 1439 (w), 1463 (m), 1504 (m), 1595 (m), 1651 (s), 2850 (m), 2920 (m) cm<sup>-1</sup>; **Elemental Analysis**: calc (%) for K<sub>2</sub>P<sub>4</sub>W<sub>17</sub>O<sub>68</sub>C<sub>65</sub>H<sub>135</sub>N<sub>7</sub>: C 14.38, H 2.51, N 1.81, found: C 14.33, H 2.47, N 1.75; **TGA Analysis**: Step transition (120.7 to 307.4°C) wt loss = 7.891% = loss of 4C<sub>2</sub>H<sub>8</sub>N<sup>+</sup> (DMA<sup>+</sup>) + 3 DMF (calc = 7.433%), total weight loss from (113.5 to 1000°C) = 21.020 % = loss of 4C<sub>2</sub>H<sub>8</sub>N<sup>+</sup> (DMA<sup>+</sup>) + 3 DMF + 2C<sub>18</sub> (cleaved at phosphonate linker units (-PO)) (calc= 21.891 %); **UV-Vis** (DMF): λ<sub>max</sub> (ε, mol<sup>-1</sup>Lcm<sup>-1</sup>)= 320 (31,000) nm.

### 3.8 References

- [1] O. Oms, K. Hakouk, R. Dessapt, P. Deniard, S. Jobic, A. Dolbecq, T. Palacin, L. Nadjo, B. Keita, J. Marrot, P. Mialane, Photo- and electrochromic properties of covalently connected symmetrical and unsymmetrical spiropyran-polyoxometalate dyads, *Chem. Commun.*, 2012, **48**, 12103-12105.
- [2] Y.-F. Song, N. McMillan, D.-L. Long, S. Kane, J. Malm, M. O. Riehle, C. P. Pradeep, N. Gadegaard, L. Cronin, Micropatterned Surfaces with Covalently Grafted Unsymmetrical Polyoxometalate-Hybrid Clusters Lead to Selective Cell Adhesion, *J. Am. Chem. Soc.*, 2009, **131**, 1340-1341.
- [3] C. Yvon, A. Macdonell, S. Buchwald, A. J. Surman, N. Follet, J. Alex, D.-L. Long, L. Cronin, A collection of robust methodologies for the preparation of asymmetric hybrid Mn-Anderson polyoxometalates for multifunctional materials, *Chem. Sci.*, 2013, **4**, 3810-3817.
- [4] S. Bareyt, S. Piligkos, B. Hasenknopf, P. Gouzerh, E. Lacôte, S. Thorimbert, M. Malacria, Highly Efficient Peptide Bond Formation to Functionalized Wells-Dawson-Type Polyoxotungstates, *Angew. Chem. Int. Ed.*, 2003, **42**, 3404-3406.

### 3. Design and synthesis of asymmetric hybrid POM (1)

---

- [5] Z. Xiao, K. Chen, B. Wu, W. Li, P. Wu, Y. Wei, An Easy Way to Construct Polyoxovanadate-Based Organic–Inorganic Hybrids by Stepwise Functionalization, *Eur. J. Inorg. Chem.*, 2016, **2016**, 808-811.
- [6] O. Makrygenni, E. Secret, A. Michel, D. Brouri, V. Dupuis, A. Proust, J.-M. Siaugue, R. Villanneau, Heteropolytungstate-decorated core-shell magnetic nanoparticles: A covalent strategy for polyoxometalate-based hybrid nanomaterials, *J. Colloid Interface Sci.*, 2018, **514**, 49-58.
- [7] L. M. Perkins, *Organic-inorganic hybrid materials: new functionalised polyoxotungstates*, PhD thesis, University of Birmingham (University of Birmingham), **2009**.
- [8] N. I. Gumerova, A. Rompel, Polyoxometalates in solution: speciation under spotlight, *Chem. Soc. Rev.*, 2020, **49**, 7568-7601.
- [9] G. Izzet, M. Ménand, B. Matt, S. Renaudineau, L. M. Chamoreau, M. Sollogoub, A. Proust, Cyclodextrin-Induced Auto-Healing of Hybrid Polyoxometalates, *Angew. Chem. Int. Ed.*, 2012, **51**, 487-490.
- [10] Y.-F. Song, D.-L. Long, S. E. Kelly, L. Cronin, Sorting the Assemblies of Unsymmetrically Covalently Functionalized Mn-Anderson Polyoxometalate Clusters with Mass Spectrometry, *Inorg. Chem.*, 2008, **47**, 9137-9139.
- [11] S. Fujimoto, J. M. Cameron, R.-J. Wei, K. Kastner, D. Robinson, V. Sans, G. N. Newton, H. Oshio, A Simple Approach to the Visible-Light Photoactivation of Molecular Metal Oxides, *Inorg. Chem.*, 2017, **56**, 12169-12177.
- [12] D. Wu, T. Shao, J. Men, X. Chen, G. Gao, Superaromatic terpyridines based on corannulene responsive to metal ions, *Dalton Trans.*, 2014, **43**, 1753-1761.
- [13] A. Bessmertnykh, C. M. Douaihy, R. Guillard, Direct Synthesis of Amino-substituted Aromatic Phosphonates via Palladium-catalyzed Coupling of Aromatic Mono- and Dibromides with Diethyl Phosphite, *Chem. Lett.*, 2009, **38**, 738-739.
- [14] S. Amin, J. M. Cameron, J. A. Watts, D. A. Walsh, V. Sans, G. N. Newton, Effects of chain length on the size, stability, and electronic structure of redox-active organic–inorganic hybrid polyoxometalate micelles, *Mol. Syst. Des. Eng.*, 2019, **4**, 995-999.
- [15] A. J. Kibler, G. N. Newton, Tuning the electronic structure of organic–inorganic hybrid polyoxometalates: The crucial role of the covalent linkage, *Polyhedron*, 2018, **154**, 1-20.
- [16] A. Sharma, V. P. Mehta, E. Van der Eycken, A convenient microwave-assisted desulfitative dimethylamination of the 2(1H)-pyrazinone scaffold using N,N-dimethylformamide, *Tetrahedron*, 2008, **64**, 2605-2610.
- [17] Y. Wan, M. Alterman, M. Larhed, A. Hallberg, Dimethylformamide as a Carbon Monoxide Source in Fast Palladium-Catalyzed Aminocarbonylations of Aryl Bromides, *J. Org. Chem.*, 2002, **67**, 6232-6235.
- [18] A. Krueve, K. Kaupmees, J. Liigand, M. Oss, I. Leito, Sodium adduct formation efficiency in ESI source, *J. Mass Spectrom.*, 2013, **48**, 695-702.
- [19] Q. Jia, Y. Zhang, J. Cao, Characterization of polyoxometalates by electrospray ionization mass spectrometry, *Sci. China Chem.*, 2015, **58**, 1206-1210.

### 3. Design and synthesis of asymmetric hybrid POM (1)

---

- [20] T. Mutai, J.-D. Cheon, S. Arita, K. Araki, Phenyl-substituted 2,2':6',2''-terpyridine as a new series of fluorescent compounds—their photophysical properties and fluorescence tuning, *J. Chem. Soc., Perkin Trans. 2*, 2001, 1045-1050.
- [21] H. Ferreira, M. M. Conradie, J. Conradie, Electrochemical and electronic properties of a series of substituted polypyridine ligands and their Co(II) complexes, *Inorganica Chim. Acta*, 2019, **486**, 26-35.
- [22] C. Hamacher, N. Hurkes, A. Kaiser, A. Klein, A. Schüren, Electrochemistry and Spectroscopy of Organometallic Terpyridine Nickel Complexes, *Inorg. Chem.*, 2009, **48**, 9947-9951.
- [23] D. Li, P. Yin, T. Liu, Supramolecular architectures assembled from amphiphilic hybrid polyoxometalates, *Dalton Trans.*, 2012, **41**, 2853-2861.
- [24] K. Kastner, A. J. Kibler, E. Karjalainen, J. A. Fernandes, V. Sans, G. N. Newton, Redox-active organic-inorganic hybrid polyoxometalate micelles, *J. Mater. Chem. A*, 2017, **5**, 11577-11581.
- [25] R. Contant, W. G. Klemperer, O. Yaghi, in *Inorganic Syntheses, Vol. 27*, John Wiley & Sons, **1990**, p. 107.
- [26] C. R. Graham, R. G. Finke, The Classic Wells–Dawson Polyoxometalate,  $K_6[\alpha\text{-P}_2\text{W}_{18}\text{O}_{62}] \cdot 14\text{H}_2\text{O}$ . Answering an 88 Year-Old Question: What Is Its Preferred, Optimum Synthesis?, *Inorg. Chem.*, 2008, **47**, 3679-3686.

## 4 Multifunctionality of asymmetric hybrid POM (1)

Following the successful isolation and characterisation of the asymmetric hybrid Dawson **1**, the unique multifunctionality of the system derived from the redox-active POM core and two distinct appended groups in its asymmetric structure is explored in this chapter.

First, the self-assembling behaviour of **1** that is enabled by the aliphatic chain ligand,  $C_{18}$ , is examined, following the previously observed solvent-dependent self-assembly of the symmetric  $C_{18}$  hybrid POM, **3**.

In the second section, an investigation of transition metal coordination using Fe(II) at the chelation site on the second ligand, *TPY*, is discussed. The new supramolecular assemblies and Fe<sup>II</sup>-coordinated asymmetric hybrid POM complexes are characterised, and their properties are investigated.

### 4.1 Solvent-dependent self-assembly enabled by aliphatic ligand

#### 4.1.1 Micelle characterisation

Solvent-dependent self-assembly was enabled in **3** by the aliphatic chain ligand,  $C_{18}$ , which imparts amphiphilic character to the hybrid POM. In the amphiphilic structure of **1**, both the POM core and *TPY* group act as the polar head-group whereas the  $C_{18}$  ligand acts as the non-polar tail. **1** was first dissolved in CH<sub>3</sub>CN and then 9 equivalents of water were added to facilitate spontaneous self-assembly, resulting in a bubbly solution. As for the symmetric hybrid **3**, the inclusion of 10% CH<sub>3</sub>CN in the solvent mixture was necessary in order for complete dissolution, likely due to the DMA cations associated with the hybrid POM preventing complete solubility in water. DLS experiments on a 1.4 mM solution confirmed the formation of nanoscale assemblies of low dispersity with a hydrodynamic diameter ( $D_h$ ) of approximately 6 nm which are

#### 4. Multifunctionality of asymmetric hybrid POM (1)

not present in a 100% DMF solution (Fig.57a). In agreement with this, cryo-TEM analysis of a solution of **1** in a H<sub>2</sub>O-CH<sub>3</sub>CN (9:1 v/v, 1.4 mM) mixture deposited and frozen on a graphene-oxide and holey carbon-supported Cu grid showed spherical structures with diameters of 4-7 nm (Fig.58a,b). Additionally, <sup>1</sup>H and <sup>31</sup>P NMR experiments showed severe broadening/disappearance of peaks in a D<sub>2</sub>O-CD<sub>3</sub>CN (9:1 v/v) mixture, indicative of a reduced transverse (T<sub>2</sub>) relaxation time arising from the slow tumbling of nanostructures (Fig.57b).<sup>[1]</sup>

The nanoassemblies are proposed to be micellar in nature due to the expected orientation of the hydrophobic C<sub>18</sub> ligands inwards away from the aqueous solution (Fig.58c). Notably, some larger nanostructures can be observed that appear to be formed by the aggregation of multiple micelles, seen similarly in work recently reported by Amin *et al.*<sup>[2]</sup>

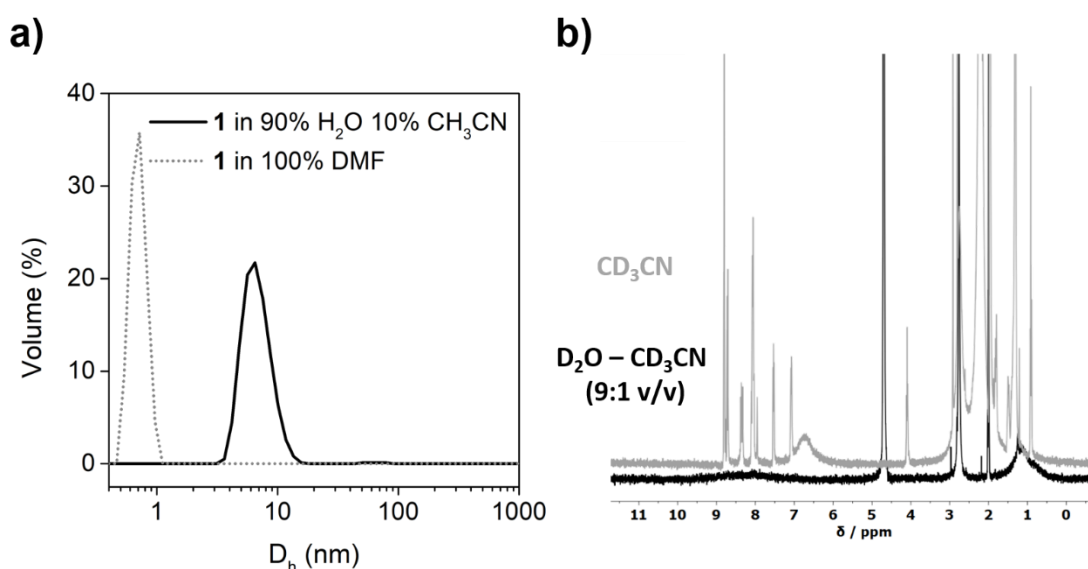


**Figure 57.** a) Particle-size distribution curves determined by DLS of: **1** (1.4 mM) in 90% H<sub>2</sub>O, 10% CH<sub>3</sub>CN- D<sub>h</sub> maxima at 6.5 nm (black), and **1** (1.4mM) in 100% DMF (grey dotted)- D<sub>h</sub> maxima at 0.7 nm (suggesting discrete molecular species only under these conditions); b) Overlaid <sup>1</sup>H NMR of **1** in D<sub>2</sub>O-CD<sub>3</sub>CN (9:1 v/v) (black) and in 100% CD<sub>3</sub>CN (grey).

#### 4. Multifunctionality of asymmetric hybrid POM (1)

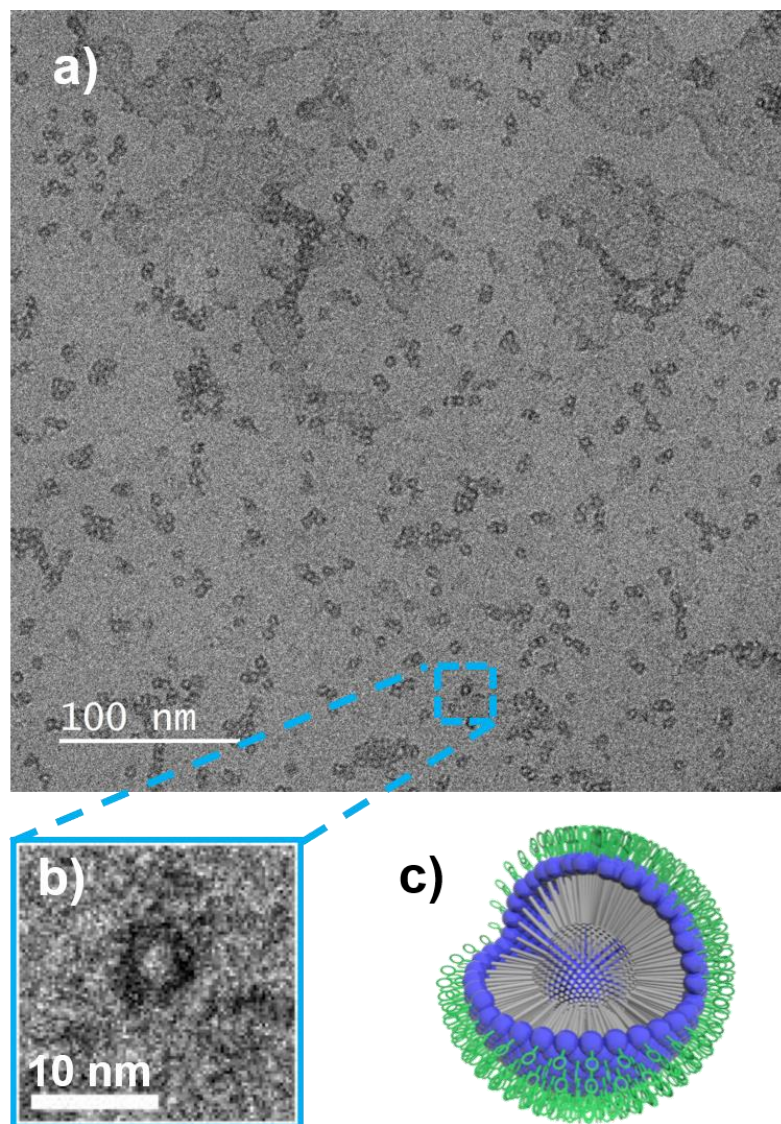


**Figure 58.** a) Cryo-TEM imaging of micellar assemblies of **1** formed in 1.4 mM water-acetonitrile (9:1 v/v) solution; b) expanded view of a single micelle; c) proposed structure of the micellar assemblies of **1**. Colour code: blue spheres =  $\{P_2W_{17}\}$  units, grey rods =  $C_{18}$  units, green rings =  $TPY$  units.

##### 4.1.2 Micelle electrochemistry

To investigate the electrochemistry of the micellar assemblies, **1** was dissolved in a suitable solvent mixture consisting of 90% aqueous electrolyte (0.1 M  $H_2SO_4$ ) and 10%  $CH_3CN$ , to prepare a 1.4 mM solution. DLS measurements on an equivalent solution showed that small aggregates with a mean hydrodynamic diameter  $D_h$  of 9 nm are formed in this solvent mixture (Fig.59). As observed for **3**, a second signal is seen

#### 4. Multifunctionality of asymmetric hybrid POM (1)

---

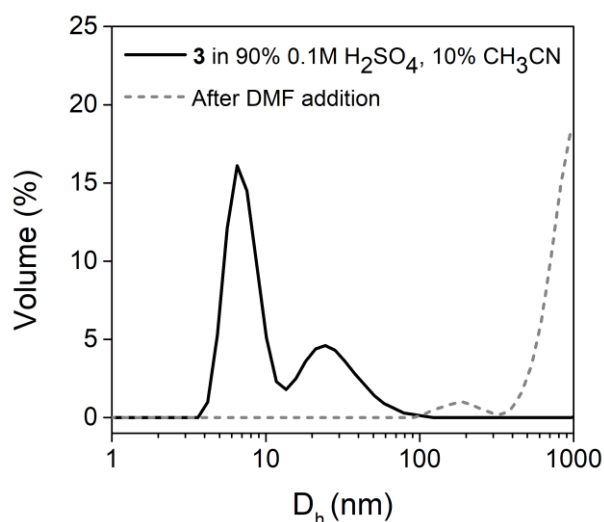


**Figure 59.** Particle-size distribution curve determined by DLS of: **1** (1.4 mM) in 90% H<sub>2</sub>SO<sub>4</sub> (0.1M), 10% CH<sub>3</sub>CN, D<sub>h</sub> maxima at 8.7 nm and 28.2 nm (black), and the solution of **1** after the addition of the same volume of DMF (c<sub>new</sub> = 0.7 mM).

corresponding to structures in the range of 20-100 nm which was not seen in the H<sub>2</sub>O-CH<sub>3</sub>CN (9:1, v/v) mixture, indicative of an effect of the acid on aggregation. As hydrophilic anions with high charge density, POMs exhibit a strong dependence on counterion and pH on self-assembly.<sup>[3]</sup> The larger sizes of particles formed by **1** observed in acidic solution could be due to the aggregation of micelles, or the formation of larger micelles, facilitated by the protonation of the polar POM head groups which would decrease their net charge and reduce repulsion between them. Similar observations were reported in studies by Yin *et al.*, in which the sizes of vesicles formed by a Dawson-type hybrid surfactant, H<sub>6</sub>[P<sub>2</sub>V<sub>3</sub>W<sub>15</sub>O<sub>59</sub>(OCH<sub>2</sub>)<sub>3</sub>CNHCOC<sub>15</sub>H<sub>31</sub>], were shown to decrease with the increase of pH, as deprotonation of the polar POM heads consequently increased the repulsive forces between them, resulting in larger curvature of the vesicle.<sup>[4]</sup>

#### 4. Multifunctionality of asymmetric hybrid POM (1)

Just two redox processes were observed between  $-0.5$  and  $0.5$  V (vs. Ag/AgCl) during CV experiments, in contrast to the three seen for the “parent” Dawson  $\{P_2W_{18}\}$  in the same range (Fig.60, Table.9). As observed for **3**, this is again due to the first redox process negatively shifting, resulting in the first two 1-electron redox processes coalescing.<sup>[5-6]</sup> The characteristic molecular redox behaviour was found to rapidly recover on addition of the same volume of DMF to the electrolyte solution and DLS experiments on the solution confirmed the disappearance of the 9 nm assemblies. Three distinct redox processes were observed in the potential range corresponding to two 1-electron waves and one 2-electron wave resembling the electrochemical

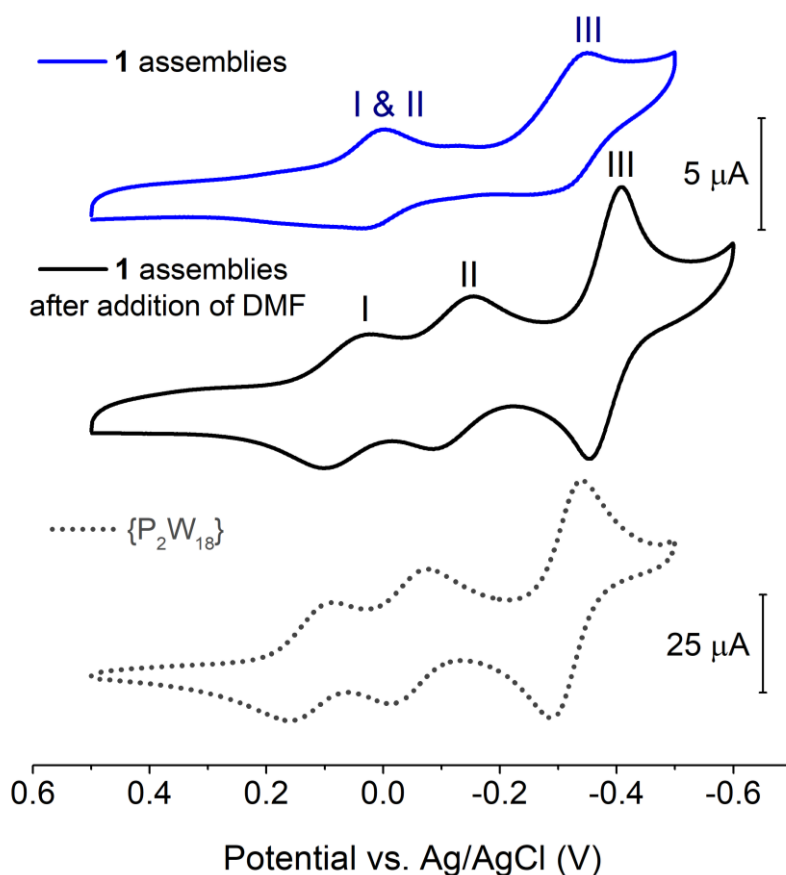


**Figure 60.** Comparison of the cyclic voltammograms of **1** (1.4 mM) in 90% 0.1M H<sub>2</sub>SO<sub>4</sub>, 10% CH<sub>3</sub>CN before (blue) and after the addition of the same volume of DMF ( $c_{\text{new}} = 0.7$  mM) (black) and of  $\{P_2W_{18}\}$  (1.4 mM) in 0.1M H<sub>2</sub>SO<sub>4</sub> (dotted). Scan rate: 100 mVs<sup>-1</sup>.



#### 4. Multifunctionality of asymmetric hybrid POM (1)

| Redox potentials vs. Ag/AgCl (V) | 1 assemblies  |               | After addition of DMF |               |               |
|----------------------------------|---------------|---------------|-----------------------|---------------|---------------|
|                                  | I & II        | III           | I                     | II            | III           |
| $E_{\text{red}}$                 | +0.012        | -0.332        | +0.034                | -0.148        | -0.410        |
| $E_{\text{ox}}$                  | +0.021        | -0.311        | +0.098                | -0.095        | -0.357        |
| $E_{1/2}$                        | <b>+0.017</b> | <b>-0.322</b> | <b>+0.066</b>         | <b>-0.122</b> | <b>-0.384</b> |

**Table 9.** Redox potentials of the assemblies of **1** in 90% 0.1M H<sub>2</sub>SO<sub>4</sub>, 10% CH<sub>3</sub>CN before and after the addition of the same volume of DMF.

signature of {P<sub>2</sub>W<sub>18</sub>} in the same potential range (Fig.60,Table.9). Furthermore, the peak currents were observed to increase after the addition of DMF despite the reduced solution concentration of **1**, which is as expected for a change from slow diffusing supramolecular assemblies to fast-diffusing molecular species. The positive shift in potential of the first redox process by 49 mV on the addition of DMF is unusual as a negative shift is expected on addition of a less polar solvent to an aqueous solvent mixture.<sup>[7]</sup> This has also been observed in previous work in our group on the electrochemistry of an amphiphilic symmetric hybrid POM, and implies that simple solvation effects are not at play here, but that there is an intrinsic difference between the electronic structure of the molecular and supramolecular hybrid POM states.<sup>[5]</sup>

#### 4.2 Metal coordination at chelating ligand (Fe<sup>II</sup>)

2,2':6',2''-Terpyridine (tpy) is a highly versatile tridentate chelating ligand with a strong coordination ability for the complexation of diverse transition metal ions. It has been used in the preparation of numerous organometallic complexes for a wide variety of catalytic applications, from organic transformations to artificial photosynthesis and CO<sub>2</sub> reduction.<sup>[8-10]</sup> Additionally, the linear directionality and stable connectivity in {tpy-M-tpy} complexes render terpyridine and its derivatives useful building block components in 2D and 3D metallosupramolecular structures for many material applications.<sup>[11-13]</sup>

#### 4. Multifunctionality of asymmetric hybrid POM (1)

Terpyridine moieties have been grafted to hybrid POMs by various linking modes,<sup>[14-15]</sup> and have been used in the construction of metal-directed hybrid POM assemblies from discrete metallomacrocycles to metallopolymers.<sup>[16-17]</sup> With this in mind, the *TPY* unit of **1** provides considerable opportunity for incorporating transition metal function into the hybrid POM and assembly into new architectures. In this section, the coordination of a metal ion in **1** is explored, and the characterisation and properties of the new asymmetric hybrid POM complexes are discussed.

##### 4.2.1 [Fe(1)<sub>2</sub>] dimer formation – (Fe-1)

###### 4.2.1.1 Preparation and characterisation of Fe-1

Terpyridine can be readily coordinated to various first-row transition metal ions under mild conditions,<sup>[18]</sup> and the post-functionalisation of **1** by metal-coordination at the *TPY* unit was investigated first with Fe(II). With a d<sup>6</sup> electron configuration, Fe(II) can form stable octahedral bis(*tpy*) complexes, and the hybrid POM was reacted with 0.5 molar equivalents of FeCl<sub>2</sub> to coordinate Fe<sup>2+</sup> ions at *TPY* sites with the intention to prepare such complexes (Fig.61). After stirring the reactants at RT overnight in acetonitrile, the product, K<sub>7</sub>(C<sub>2</sub>H<sub>8</sub>N)<sub>3</sub>[Fe{P<sub>2</sub>W<sub>17</sub>O<sub>57</sub>(PO<sub>3</sub>C<sub>21</sub>H<sub>14</sub>N<sub>3</sub>)(PO<sub>4</sub>C<sub>24</sub>H<sub>41</sub>)<sub>2</sub>}]<sub>2</sub> (**Fe-1**), was collected by removal of the solvent *in vacuo*.

The <sup>1</sup>H and <sup>31</sup>P NMR spectra of **Fe-1** confirmed the formation of a single new species. All aromatic *TPY* peaks in the <sup>1</sup>H NMR spectrum of **Fe-1** were shifted from in **1**,

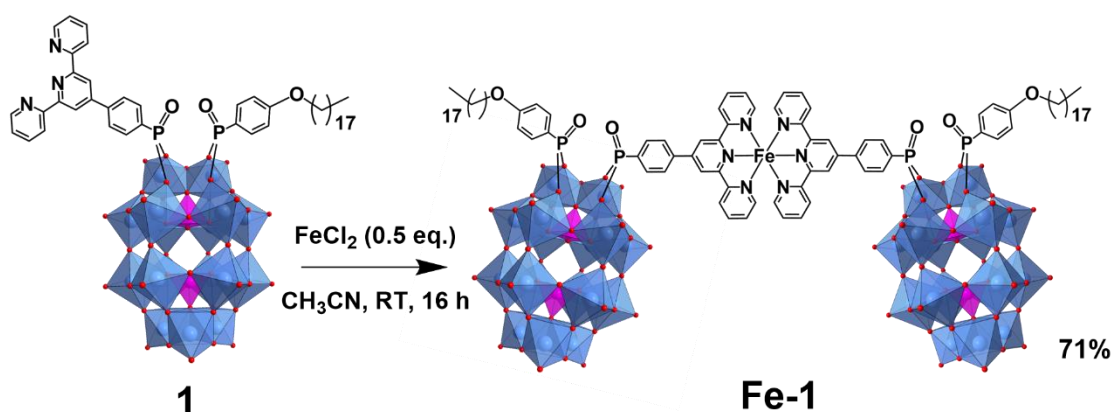


**Figure 61.** Coordination of Fe(II) to **1** to prepare the dimeric hybrid POM complex **Fe-1**.

#### 4. Multifunctionality of asymmetric hybrid POM (1)

suggesting successful coordination of Fe(II) (Fig.62,63a). Shifts were also observed for both ligand organophosphoryl signals in the  $^{31}\text{P}$  NMR spectrum of **Fe-1** from in **1**, which demonstrate a degree of electronic conjugation across the whole asymmetric system (Fig.63b). Phosphonate linkers have demonstrated to be particularly effective in facilitating electronic conjugation in hybrid structures through  $\pi$ -bonding between the appended organic groups and POM,<sup>[19]</sup> and the signal shifts observed confirm that there is appreciable  $\pi$ -conjugation between the chelating site on *TPY* and the  $\text{C}_{18}$  phosphonate linker, across the POM core.

ESI-MS confirmed the formation of a POM-Fe<sup>II</sup>-POM dimeric structure with the expected 10- charge, considering the 2+ charge of the bridging *TPY*-Fe<sup>II</sup>-*TPY* complex that reduces the overall 12- charge of two combined hybrid POMs. Peaks

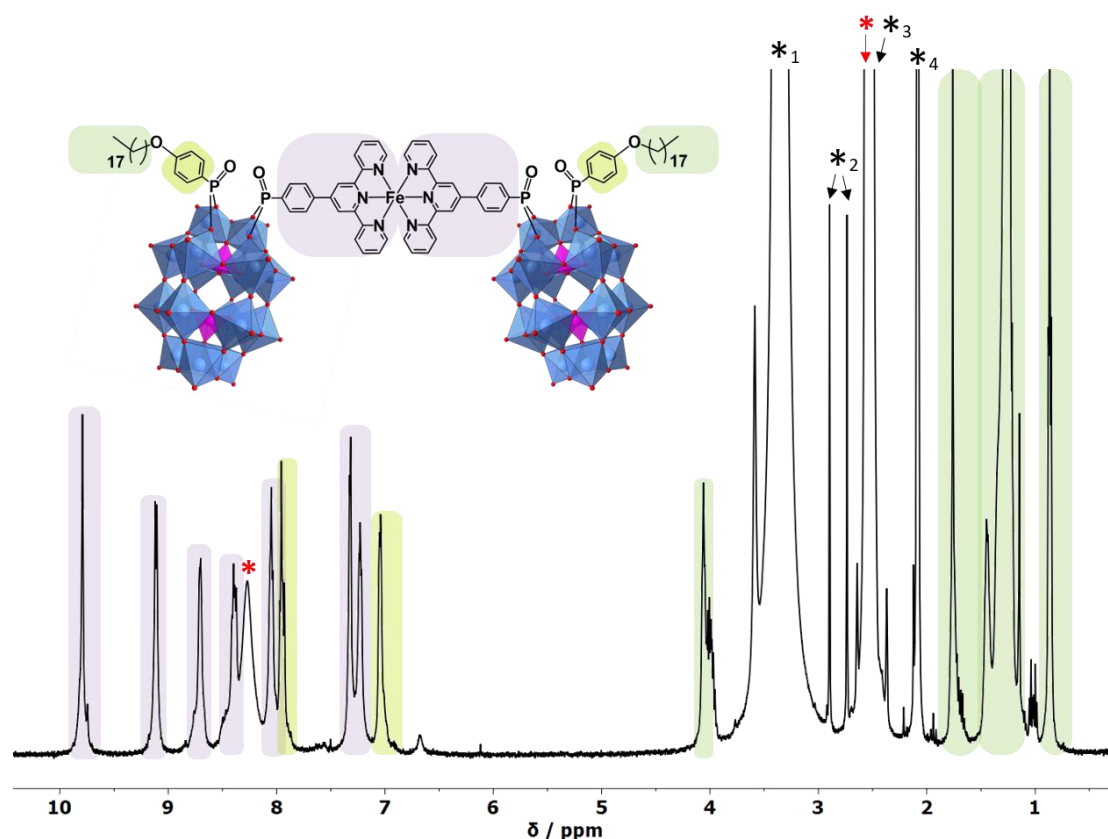


**Figure 62.**  $^1\text{H}$  NMR of **1** in  $\text{DMSO-}d_6$  showing the assignment of peaks to each ligand: green =  $\text{C}_{18}$ , purple =  $\text{TPY(Fe}^{II})$ . Red asterisks indicate DMA cation signals, and black asterisks indicate solvent impurities: 1=  $\text{H}_2\text{O}$ , 2=  $\text{DMF}$ , 3=  $\text{DMSO}$ , 4=  $\text{CH}_3\text{CN}$ .

#### 4. Multifunctionality of asymmetric hybrid POM (1)

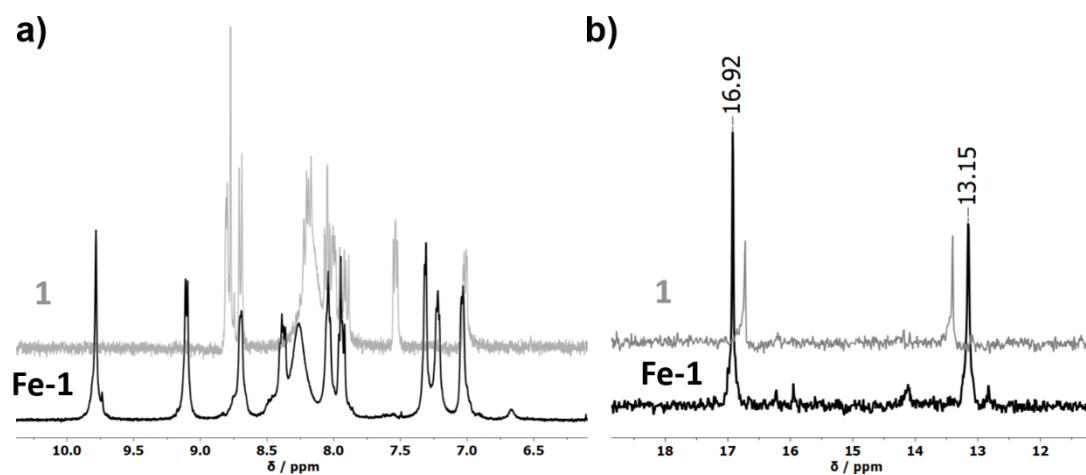


**Figure 63.** Overlaid a)  $^1\text{H}$  NMR spectra (focused on the aromatic proton signal region) and b)  $^{31}\text{P}$  NMR spectra of Fe-1 (black) and 1 (grey) in  $\text{DMSO-d}_6$ . Only the positive chemical shift region for the organophosphonate  $^{31}\text{P}$  nuclei is presented here for simplicity.

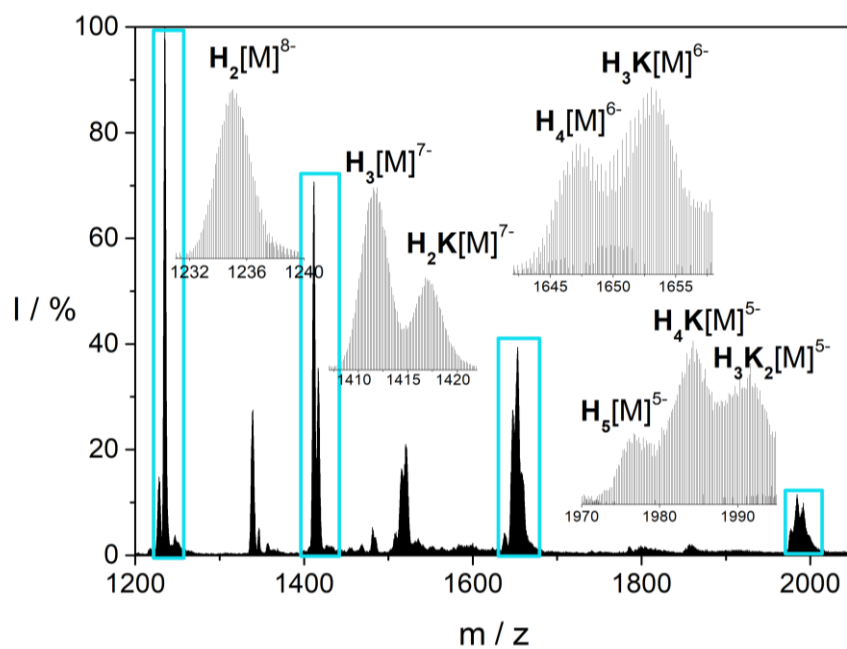


**Figure 64.** Negative mode ESI mass spectrum of Fe-1 in acetonitrile.  $[\text{M}] = [\text{Fe}\{\text{P}_2\text{W}_{17}\text{O}_{57}(\text{PO}_3\text{C}_{21}\text{H}_{14}\text{N}_3)(\text{PO}_4\text{C}_{24}\text{H}_{41})_2\}]^{10-}$ .

corresponding to ions carrying 5-, 6-, 7- and 8- charges were observed as either proton or mixed proton/potassium salts (Fig.64, Table 10).

#### 4. Multifunctionality of asymmetric hybrid POM (1)

| Assignment  | z  | m/z (obs.) | m/z (calc.) |
|---|----|------------|-------------|
| $\text{H}_2[\text{Fe}\{\text{P}_2\text{W}_{17}\text{O}_{57}(\text{PO}_3\text{C}_{21}\text{H}_{14}\text{N}_3)(\text{PO}_4\text{C}_{24}\text{H}_{41})\}_2]$           | 8- | 1235.0435  | 1235.0383   |
| $\text{H}_2[\text{Fe}\{\text{P}_2\text{W}_{17}\text{O}_{57}(\text{PO}_3\text{C}_{21}\text{H}_{14}\text{N}_3)(\text{PO}_4\text{C}_{24}\text{H}_{41})\}_2]$           | 7- | 1411.6222  | 1411.6164   |
| $\text{H}_2\text{K}[\text{Fe}\{\text{P}_2\text{W}_{17}\text{O}_{57}(\text{PO}_3\text{C}_{21}\text{H}_{14}\text{N}_3)(\text{PO}_4\text{C}_{24}\text{H}_{41})\}_2]$   | 7- | 1417.0442  | 1417.0386   |
| $\text{H}_4[\text{Fe}\{\text{P}_2\text{W}_{17}\text{O}_{57}(\text{PO}_3\text{C}_{21}\text{H}_{14}\text{N}_3)(\text{PO}_4\text{C}_{24}\text{H}_{41})\}_2]$           | 6- | 1647.0585  | 1647.0539   |
| $\text{H}_3\text{K}[\text{Fe}\{\text{P}_2\text{W}_{17}\text{O}_{57}(\text{PO}_3\text{C}_{21}\text{H}_{14}\text{N}_3)(\text{PO}_4\text{C}_{24}\text{H}_{41})\}_2]$   | 6- | 1653.3864  | 1653.3798   |
| $\text{H}_5[\text{Fe}\{\text{P}_2\text{W}_{17}\text{O}_{57}(\text{PO}_3\text{C}_{21}\text{H}_{14}\text{N}_3)(\text{PO}_4\text{C}_{24}\text{H}_{41})\}_2]$           | 5- | 1976.6718  | 1976.6663   |
| $\text{H}_4\text{K}[\text{Fe}\{\text{P}_2\text{W}_{17}\text{O}_{57}(\text{PO}_3\text{C}_{21}\text{H}_{14}\text{N}_3)(\text{PO}_4\text{C}_{24}\text{H}_{41})\}_2]$   | 5- | 1984.2644  | 1984.2574   |
| $\text{H}_3\text{K}_2[\text{Fe}\{\text{P}_2\text{W}_{17}\text{O}_{57}(\text{PO}_3\text{C}_{21}\text{H}_{14}\text{N}_3)(\text{PO}_4\text{C}_{24}\text{H}_{41})\}_2]$ | 5- | 1991.8572  | 1991.8485   |

**Table 10.** Selected ESI-MS peak assignments for **Fe-1**.

As the purification of **Fe-1** involved washes with only ether, the two chloride ions introduced for every  $\text{Fe}^{2+}$  ion in the synthesis were considered in the molecular formula as DMACl salts to account for the overall charge, which was supported by CHN and TGA analysis.

The dark purple colour of the product is characteristic of a low spin  $d^6 \text{Fe}^{2+}$  centre, and UV-Vis absorption spectroscopy confirmed the presence of a metal-to-ligand-charge-transfer (MLCT) band at 576 nm assigned to the  $d-\pi^*$  transition of the  $\text{Fe}^{2+}$ -TPY complex (Fig.65). In the UV region, ligand-centred (LC) bands corresponding to  $\pi-\pi^*$  transitions of the chelating TPY ligand are also evident.<sup>[20]</sup>

CV studies in DMF revealed a quasi-reversible  $\text{Fe}^{2+/3+}$  redox couple ( $E_{1/2} = 0.543$  V vs.  $\text{Fc}/\text{Fc}^+$ ) alongside the four quasi-reversible POM-centred processes (Fig.66). The  $E_{1/2}$  values of the POM redox processes are only slightly shifted negatively in potential from those of **1** when un-coordinated, indicating a very weak influence of the  $\text{Fe}^{\text{II}}$  centre on the reducibility of the POM clusters of **Fe-1** (Table.6,11).

#### 4. Multifunctionality of asymmetric hybrid POM (1)

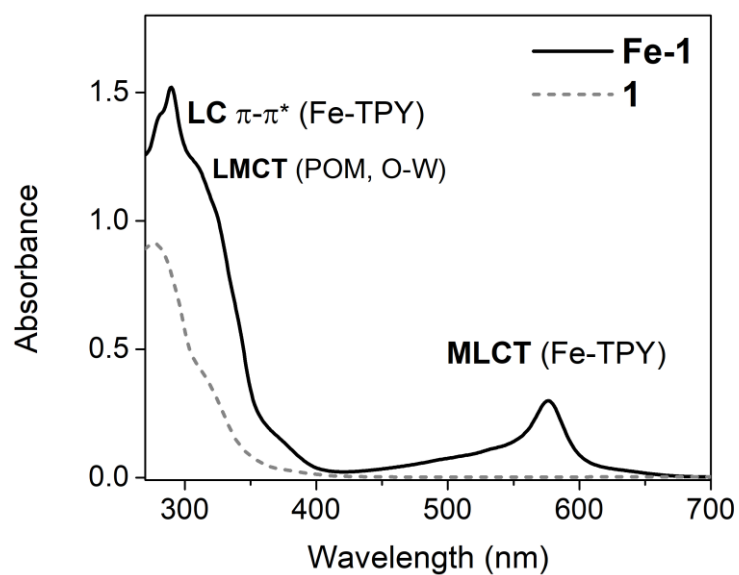


**Figure 65.** Overlaid UV-Vis absorption spectra of Fe-1 (black) and **1** (grey dashed) in DMF (both 10  $\mu$ M).

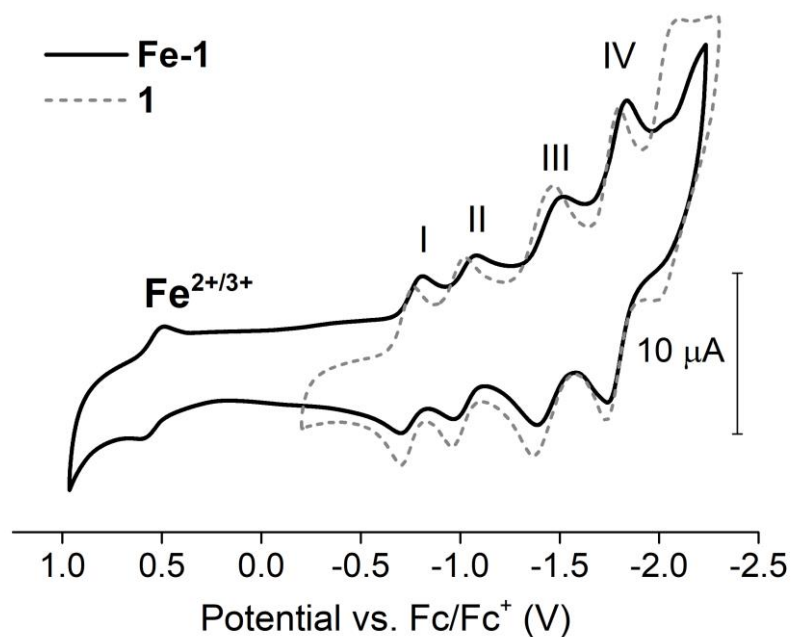


**Figure 66.** Cyclic voltammograms of Fe-1 (0.25 mM) (black) and **1** (0.5 mM) (grey dashed) in DMF, with 0.1M TBAPF<sub>6</sub> as electrolyte. Scan rate: 100 mVs<sup>-1</sup>.

#### 4. Multifunctionality of asymmetric hybrid POM (1)

| Redox potentials vs. Fc/Fc <sup>+</sup> (V) | Fe <sup>2+/3+</sup> | I             | II            | III           | IV            |
|---|---------------------|---------------|---------------|---------------|---------------|
| E <sub>red</sub>                            | +0.485              | -0.811        | -1.081        | -1.515        | -1.839        |
| E <sub>ox</sub>                             | +0.601              | -0.702        | -0.966        | -1.387        | -1.737        |
| E <sub>1/2</sub>                            | <b>+0.543</b>       | <b>-0.757</b> | <b>-1.024</b> | <b>-1.451</b> | <b>-1.788</b> |

**Table 11.** Redox potentials of **Fe-1** in DMF.

##### 4.2.1.2 Assembly of Fe-1

The combination of metal-coordination and self-assembly of **1** was then investigated by dissolving **Fe-1** in a H<sub>2</sub>O-CH<sub>3</sub>CN (9:1 v/v) mixture at RT to facilitate spontaneous self-assembly. DLS studies on a 0.7 mM solution indicated the formation of nanoscale aggregates (Fig.67) with D<sub>h</sub> of approximately 4 nm, and NMR studies again showed the disappearance of the peaks in a D<sub>2</sub>O-CD<sub>3</sub>CN (9:1 v/v) solution. Cryo-TEM analysis confirmed the presence of nano-assemblies, but unlike the corresponding studies on **1**, the aggregates were of variable shape and were not hollow (Fig.68). This is

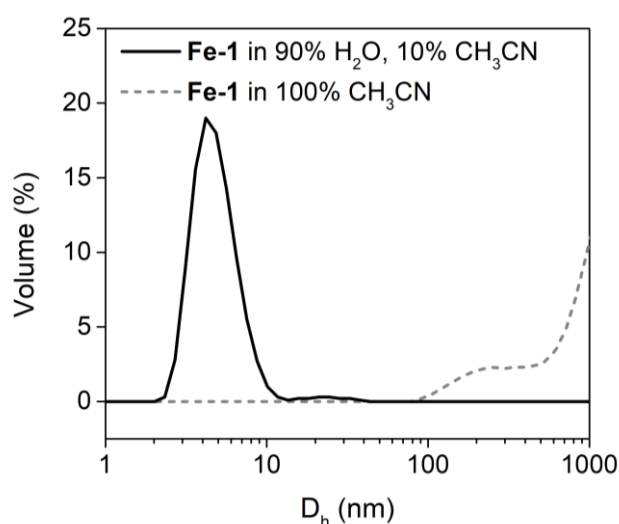


**Figure 67.** Particle-size distribution curves determined by DLS of **Fe-1** (0.7mM) in 90% H<sub>2</sub>O, 10% CH<sub>3</sub>CN- D<sub>h</sub> maxima at 4.2 nm (black) and in 100% CH<sub>3</sub>CN (0.7 mM) (grey dashed).

#### 4. Multifunctionality of asymmetric hybrid POM (1)

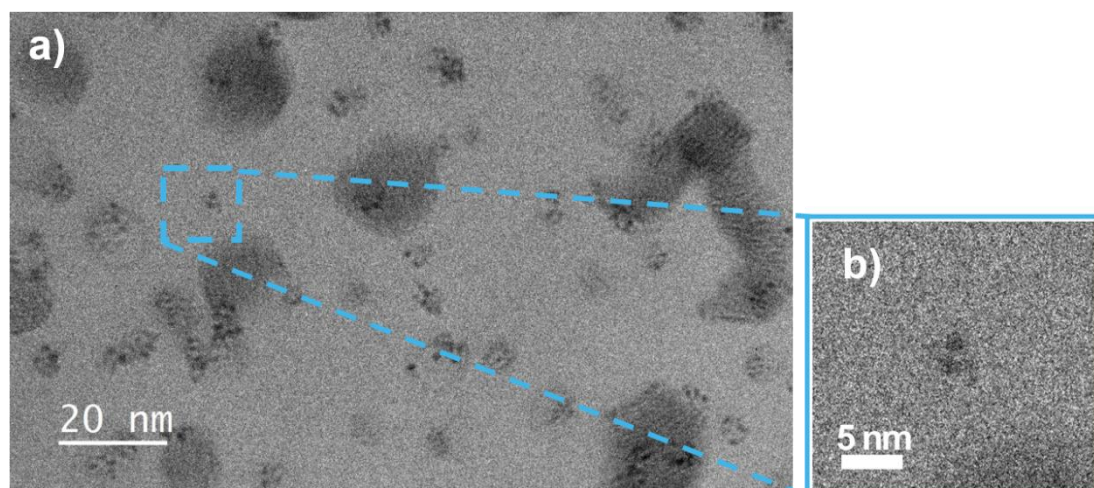


**Figure 68.** a) Cryo-TEM image of the aggregates of **Fe-1** formed in a 0.7 mM water-acetonitrile (9:1 v/v) solution; b) expanded view of a single dimeric POM structure.

reasonable given that **Fe-1** lacks the head-tail structure of **1** and is therefore unlikely to form typical micellar assemblies. It is also apparent that many of the POMs (dark spots on the micrograph) appear in 'pairs' (Fig.68b), consistent with the expected molecular structure of **Fe-1**, in which the two POM clusters in the dimer should be separated by approximately 2 nm. The aggregates appear to resemble somewhat those recently reported by Izzet *et al.*, who demonstrated the solvent-dependent aggregation of metal-directed oligomers comprised of symmetric terpyridine-functionalised POMs, although the nanoaggregates they reported were comparatively much more dense.<sup>[21]</sup>

As with **1**, the assemblies of **Fe-1** exhibited contrasting electrochemical behaviour to the molecular state in a 0.1 M H<sub>2</sub>SO<sub>4</sub>-DMF (9:1, v/v) solution, with just two POM redox processes observed from 0.5 to -0.5 V (vs. Ag/AgCl) (Fig.69a). Interestingly, the Fe<sup>2+/3+</sup> redox process appeared to have become indiscernible. The molecular redox behaviour was again recoverable upon addition of DMF, including the return of the reversible Fe<sup>2+/3+</sup> redox process. To further confirm this, differential pulse voltammetry (DPV) was performed on the solution, a voltammetric technique in which higher sensitivities can be achieved as background charging currents can be minimised. Clearly, no peak is observed at positive potentials in the 90% aqueous



#### 4. Multifunctionality of asymmetric hybrid POM (1)

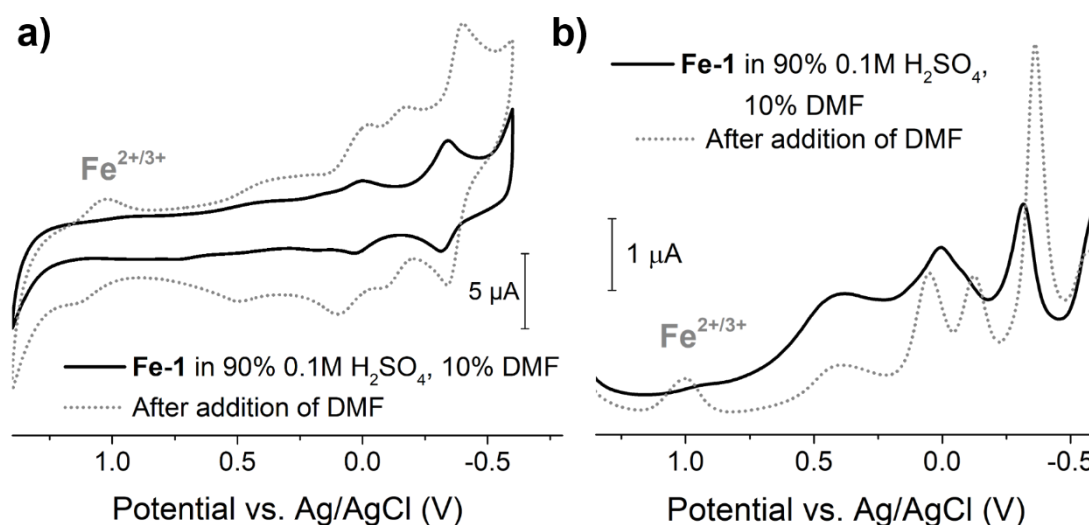


**Figure 69.** a) Overlaid cyclic voltammograms and b) overlaid differential pulse voltammograms of **Fe-1** (0.7 mM) in 90% H<sub>2</sub>SO<sub>4</sub> (0.1 M), 10% DMF (black) and after the addition of the same volume of DMF ( $C_{\text{new}} = 0.35$  mM) (grey dotted). Scan rate: 100 mVs<sup>-1</sup>.

solution for the Fe<sup>2+/3+</sup> process, but upon the addition of the same volume of DMF to the CV solution one becomes visible (Fig.69b). As observed for **1**, the currents were seen to increase after the addition of DMF due to the change from slow diffusing supramolecular aggregates to fast-diffusing molecular species. The more significant change in current of the Fe<sup>2+/3+</sup> process could be suggestive of a hindrance of the Fe(II) complex in **Fe-1** from the electrode when aggregated.

The gradual addition of FeCl<sub>2</sub> to a solution of micelles of **1** was also carried out to investigate the coordination of Fe<sup>2+</sup> to the POMs once already assembled into micelles. DLS measurements were taken of a solution of **1** (1.4 mM) in a H<sub>2</sub>O-DMF (9:1 v/v) mixture after increasing molar equivalents of FeCl<sub>2</sub> from 0.1 to 5 were added (as a 0.05 M solution in H<sub>2</sub>O-DMF (9:1 v/v)) to the micelle solution. Measurements were taken after an hour of stirring for each addition. It could be expected that, with the assumed outward-facing orientation of *TPY* units from the micelles, the coordination of Fe<sup>2+</sup> ions could result in micelle aggregation through the formation of dimeric complexes like that of **Fe-1** between pairs of **1** from neighbouring micelles. Despite an immediate change in colour from yellow to purple on the first addition, indicative of

#### 4. Multifunctionality of asymmetric hybrid POM (1)

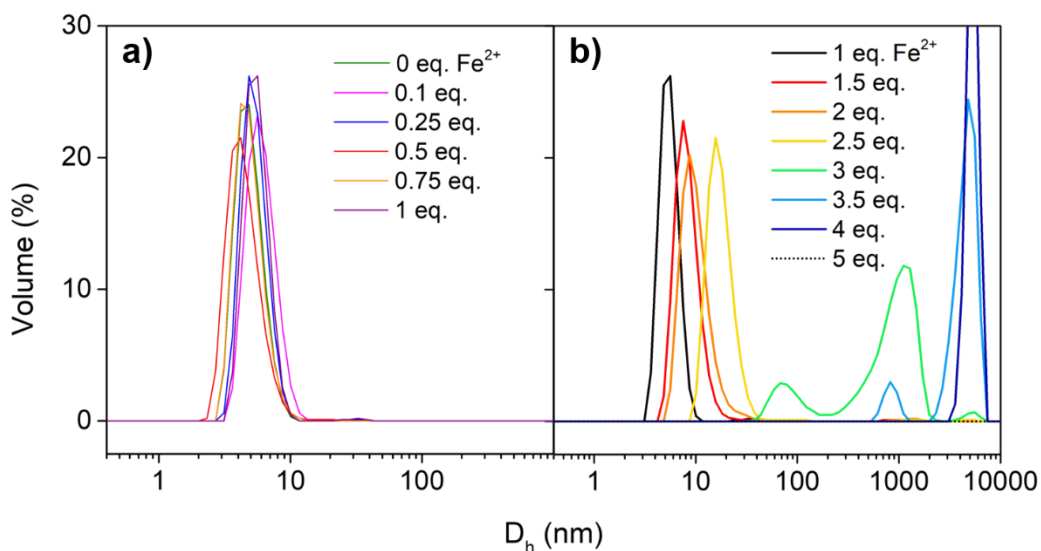


**Figure 70.** Particle-size distribution curves determined by DLS of a solution of **1** (1.4 mM) in 90% H<sub>2</sub>O, 10% DMF after the stepwise addition of: **a)** 0 to 1 molar eq. of FeCl<sub>2</sub>; **b)** 1 to 5 molar eq. of FeCl<sub>2</sub>.

Fe<sup>2+</sup>-TPY coordination, no significant increase in assembly size was observed after a total of 1 equivalent was added (Fig.70a). Micelles are perhaps unable to come into close contact to allow the coordination of Fe<sup>2+</sup> to two TPY groups across micelles due to strong repulsive electrostatic charges between the negatively charged micelle surfaces, so only monomeric POM(TPY-Fe<sup>2+</sup>)-type structures are formed. Alternatively, Fe<sup>2+</sup> ions may also be coordinating to free molecules of **1** that may be present in solution. Once the concentration of Fe<sup>2+</sup> ions was increased beyond 2 equivalents, however, rapid increases in D<sub>h</sub> were observed and aggregates of sizes beyond the detection limit of the instrument (>10,000 nm) were observed by 3.5 equivalents (Fig.70b). It is possible that the high concentration of cationic iron species shields the negative charge of the micelles through electrostatic association more effectively than that of the interaction in the POM(TPY-Fe<sup>2+</sup>) species, resulting in stronger/less dynamic aggregation.

As a control, the gradual addition of Fe<sup>2+</sup> was repeated for a solution of **3** micelles (1.4 mM, H<sub>2</sub>O-DMF (9:1 v/v)), in which metal chelation is not possible. An immediate green colour change was observed, indicative of iron aqua complex ions ([Fe(H<sub>2</sub>O)<sub>6</sub>]<sup>2+</sup>). Again, no increase in assembly size was observed by DLS after 1 molar equivalent of

#### 4. Multifunctionality of asymmetric hybrid POM (**1**)

$\text{Fe}^{2+}$  ions was added (Fig.77). An increase in  $D_h$  was then observed as equivalents were increased up to 5, although slower than in **1**, suggesting that the additional presence of  $\text{Fe}^{2+}$ -TPY moieties in **1** accelerates somewhat the electrostatic aggregation of micelles.

#### 4.2.2 Stoichiometric $\text{Fe}^{2+}$ -coordination

##### 4.2.2.1 UV-Vis titration experiments

The coordination of  $\text{Fe}^{2+}$  to **1** was also investigated by UV-Vis titrations, by measuring the change in absorbance of the Fe-TPY MLCT band at 577 nm with increasing concentrations of  $\text{FeCl}_2$ . UV-Vis titrations were performed by adding a solution of  $\text{FeCl}_2$  (20 mM in dry DMF) to a solution of **1** (2.5 mL, 2 mM in dry DMF) under argon in steps of 0.1 molar equivalents (50  $\mu\text{L}$ ) up to 1 molar equivalent. The mixture was left stirring at RT for 24 h before each spectrum was taken, using an aliquot (50  $\mu\text{L}$ ) that was diluted to prepare a 20  $\mu\text{M}$  solution (5 mL). The absorbance was found to increase approximately linearly with  $[\text{FeCl}_2]$  up to *ca.* 0.7 molar equivalents, before it started to slow and plateau at 1 (Fig.71a,b). This can be somewhat expected

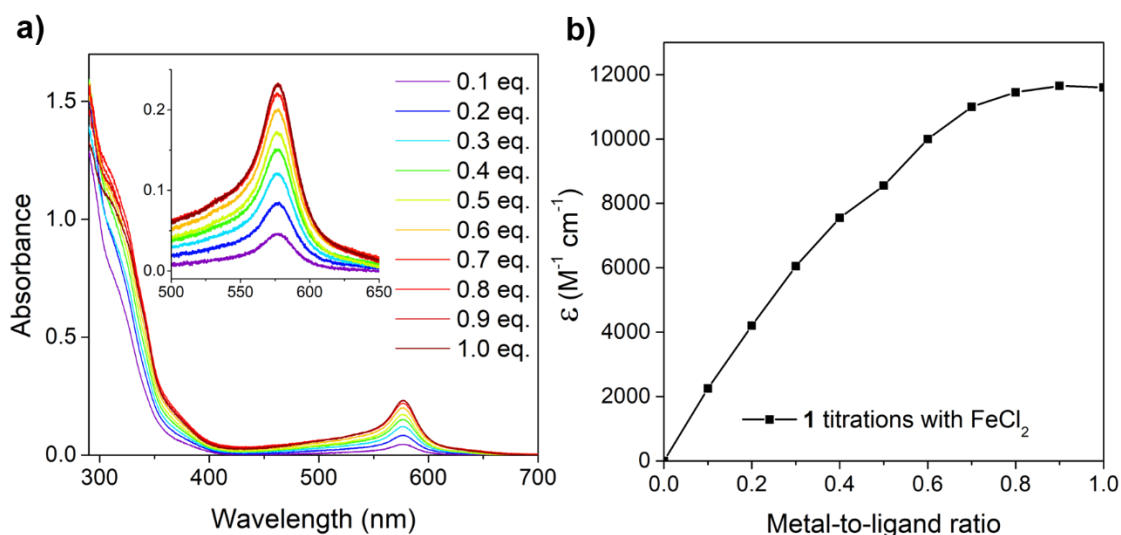


**Figure 71.** a) UV-Vis absorption spectra of **1** titrations in DMF with increasing molar equivalents of  $\text{Fe}^{2+}$ ; b) Titration curve obtained using the maxima of the MLCT band at 577 nm.

#### 4. Multifunctionality of asymmetric hybrid POM (1)

considering that all terpyridine sites can reach saturation at 1 equivalent on forming monomeric POM(*TPY*-Fe<sup>II</sup>) complexes. However, saturation of the *TPY* sites possibly occurs via the formation of a mixture of dimer and monomer complexes up to 1 equivalent, and the slight deviation observed at 0.5 molar equivalents could be an effect of this.

##### 4.2.2.2 Preparation and characterisation of monomeric complex Fe-2

The asymmetric hybrid POM **1** was reacted carefully with 1 molar equivalent of FeCl<sub>2</sub> with the aim of isolating the monomeric POM(*TPY*-Fe<sup>II</sup>) species for comparative studies with **Fe-1** (Fig.72). After stirring **1** with 1 molar equivalent of FeCl<sub>2</sub> overnight at RT, the product, K<sub>3</sub>(C<sub>2</sub>H<sub>8</sub>N)<sub>3</sub>[P<sub>2</sub>W<sub>17</sub>O<sub>57</sub>{FeCl<sub>2</sub>(H<sub>2</sub>O)(PO<sub>3</sub>C<sub>21</sub>H<sub>14</sub>N<sub>3</sub>)(PO<sub>4</sub>C<sub>24</sub>H<sub>41</sub>)}] (**Fe-2**), was isolated by removal of the solvent *in vacuo* and was characterised once adequately dried.

NMR experiments of the isolated solid showed peaks with identical <sup>1</sup>H and <sup>31</sup>P shifts to the dimer, **Fe-1**, but the <sup>1</sup>H signals appeared much broader (Fig.78). This could be indicative of smaller crystal field splitting caused by additional coordinated ligands with a greater weak field/high spin effect relative to terpyridine, such as chloride ions or aqua ligands, that results in a Fe<sup>II</sup> centre that is more paramagnetic in nature.<sup>[22]</sup>

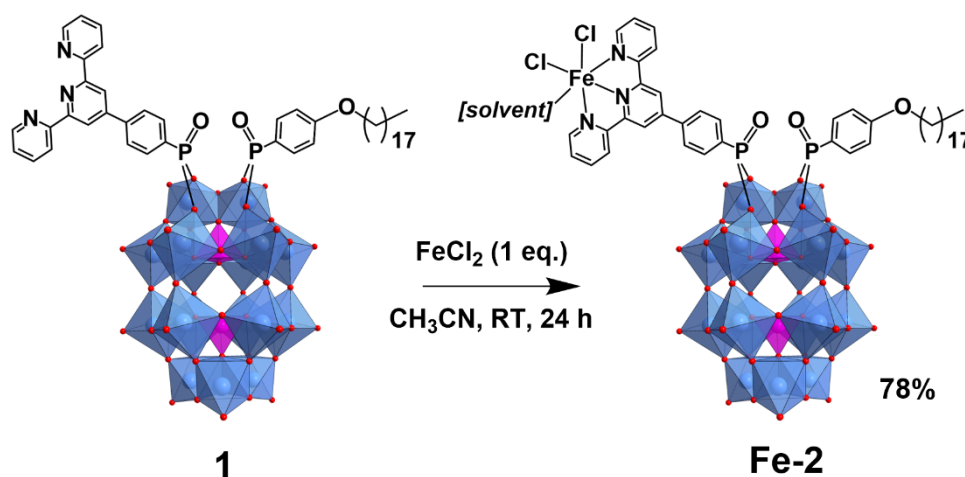


**Figure 72.** Coordination of 1 equivalent of Fe(II) to **1** to prepare the monomeric complex **Fe-2**.

Additional ligand assignments are tentative.

#### 4. Multifunctionality of asymmetric hybrid POM (1)

Alternatively, it could be attributed to tumbling effects, which would again be suggestive of a different structure to that of the dimer complex due to different aggregation behaviour.

Only one signal was observed in ESI-MS analysis that could be assigned to a monomeric POM hybrid complex involving one  $\text{Fe}^{2+}$  ion-  $\text{H}[\text{Fe}\{\text{P}_2\text{W}_{17}\text{O}_{57}(\text{PO}_3\text{C}_{21}\text{H}_{14}\text{N}_3)(\text{PO}_4\text{C}_{24}\text{H}_{41})\}]^{3-}$ , however, no other ligands are included in the complex and other assignable peaks were attributed to POM hybrid species without Fe-coordination (Fig.73, Table 12). This could suggest a lower stability in the hybrid structure in comparison to the dimeric hybrid complex **Fe-1**, which is as expected with the more labile coordination environment in the monomeric complex. Moreover, the remaining assignments could be made to the dimeric structure, but is not surprising considering that the high energies involved in ESI-MS often lead to in-source fragmentation or rearrangement.<sup>[23]</sup>

ICP-OES experiments ran to analyse the Fe-content gave results agreeable (within approx. 6%) with the calculated concentration, assuming a molecular formula of

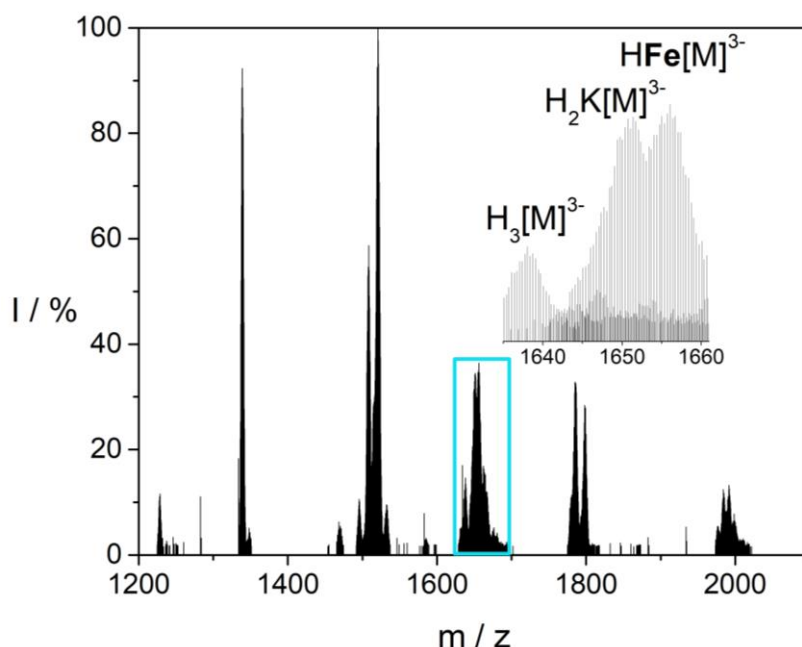


**Figure 73.** Negative mode ESI mass spectrum of **Fe-2** in acetonitrile.  $[\text{M}] = [\text{P}_2\text{W}_{17}\text{O}_{57}\{(\text{PO}_3\text{C}_{21}\text{H}_{14}\text{N}_3)(\text{PO}_4\text{C}_{24}\text{H}_{41})\}]^{6-}$ .

#### 4. Multifunctionality of asymmetric hybrid POM (1)

| Assignment  | z  | m/z (obs.) | m/z (calc.) |
|---|----|------------|-------------|
| $\text{H}_3[\text{P}_2\text{W}_{17}\text{O}_{57}\{(\text{PO}_3\text{C}_{21}\text{H}_{14}\text{N}_3)(\text{PO}_4\text{C}_{24}\text{H}_{41})\}]$                              | 3- | 1638.0758  | 1638.0672   |
| $\text{H}_2\text{K}[\text{P}_2\text{W}_{17}\text{O}_{57}\{(\text{PO}_3\text{C}_{21}\text{H}_{14}\text{N}_3)(\text{PO}_4\text{C}_{24}\text{H}_{41})\}]$                      | 3- | 1650.7275  | 1650.7191   |
| $\text{HFe}[\text{P}_2\text{W}_{17}\text{O}_{57}\{(\text{PO}_3\text{C}_{21}\text{H}_{14}\text{N}_3)(\text{PO}_4\text{C}_{24}\text{H}_{41})\}]$                              | 3- | 1656.0494  | 1656.0405   |
| $\text{H}_5\text{Fe}[\{\text{P}_2\text{W}_{17}\text{O}_{57}(\text{PO}_3\text{C}_{21}\text{H}_{14}\text{N}_3)(\text{PO}_4\text{C}_{24}\text{H}_{41})\}_2]$ (dimer)           | 5- | 1976.6775  | 1976.6663   |
| $\text{H}_4\text{KFe}[\{\text{P}_2\text{W}_{17}\text{O}_{57}(\text{PO}_3\text{C}_{21}\text{H}_{14}\text{N}_3)(\text{PO}_4\text{C}_{24}\text{H}_{41})\}_2]$ (dimer)          | 5- | 1984.2653  | 1984.2574   |
| $\text{H}_3\text{K}_2\text{Fe}[\{\text{P}_2\text{W}_{17}\text{O}_{57}(\text{PO}_3\text{C}_{21}\text{H}_{14}\text{N}_3)(\text{PO}_4\text{C}_{24}\text{H}_{41})\}_2]$ (dimer) | 5- | 1991.8537  | 1991.8485   |

**Table 12.** Selected ESI-MS peak assignments for **Fe-2**.

$\text{K}_3(\text{C}_2\text{H}_8\text{N})_3[\text{P}_2\text{W}_{17}\text{O}_{57}\{\text{FeCl}_2(\text{H}_2\text{O})(\text{PO}_3\text{C}_{21}\text{H}_{14}\text{N}_3)(\text{PO}_4\text{C}_{24}\text{H}_{41})\}]$  that is tentatively assigned by  $^1\text{H}$  NMR, CHN and TGA analysis. Results for **Fe-1** gave an Fe concentration approximately 30% higher than that calculated, but it was notably still 1.6x lower than the Fe content observed for **Fe-2**, highly supportive of dimeric and monomeric structures, respectively.

A comparison of UV-Vis absorption spectra of **Fe-1** and **Fe-2** in DMF taken at the same concentration (10  $\mu\text{M}$ , prepared according to the determined MW of **Fe-1** and the tentative MW of **Fe-2**) supports the successful isolation of the monomer, with the Fe-TPY MLCT peak showing roughly half the absorbance than in **Fe-2** as expected due to the single TPY ligand (Fig.74a). Moreover, the high energy LC  $\pi$ - $\pi^*$  and POM LMCT bands were also of approximately half intensity in **Fe-2**, further supportive of the mono-TPY complex and of a single POM anion per molecule versus the two in the dimer.

CV studies in DMF revealed a less reversible  $\text{Fe}^{2+/3+}$  redox couple than that seen in **Fe-1**, as well as reduced reversibility in the POM redox processes (Fig.74b, Table.13). This is possibly indicative of lower stability in the monomer form, in agreement with the ESI-MS results. Additional processes between -0.2 and -0.5 V (vs.  $\text{Fc}/\text{Fc}^+$ ) may be indicative of Fe-based impurities, which may arise from disassembly of the Fe-TPY complex.

#### 4. Multifunctionality of asymmetric hybrid POM (1)

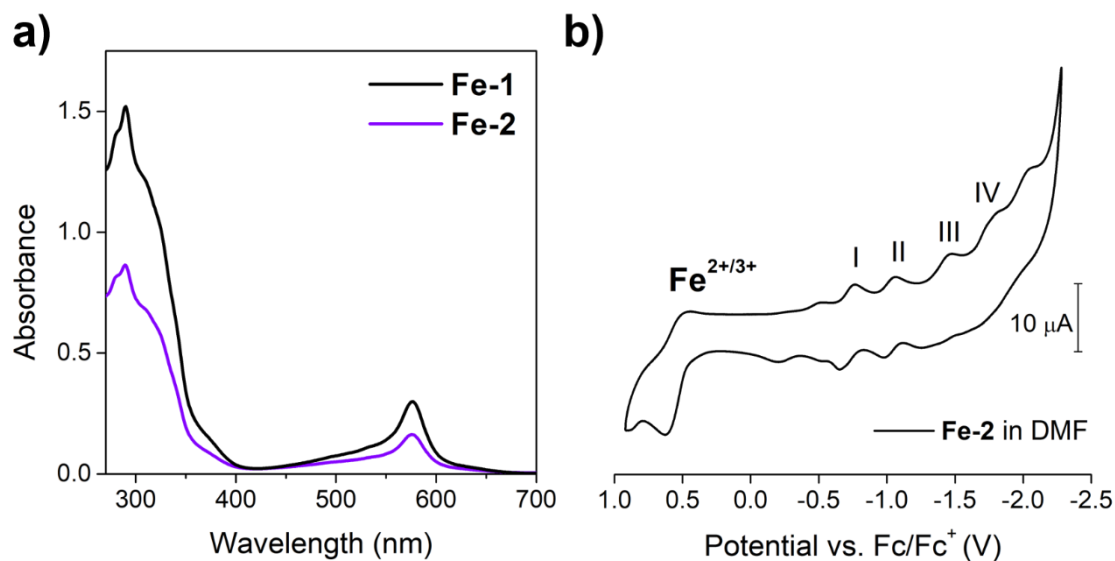


**Figure 74.** a) UV-Vis absorption spectrum of dimeric complex **Fe-1** and monomeric complex **Fe-2** in DMF (both 10  $\mu\text{M}$ ); b) Cyclic voltammogram of **Fe-2** (0.5 mM) in DMF with 0.1M TBAPF<sub>6</sub> as electrolyte at a glassy carbon working electrode. Scan rate: 100  $\text{mVs}^{-1}$ .

| Redox potentials vs. Fc/Fc <sup>+</sup> (V) | Fe <sup>2+/3+</sup> | I             | II            | III    | IV     |
|---|---------------------|---------------|---------------|--------|--------|
| E <sub>red</sub>                            | +0.483              | -0.764        | -1.063        | -1.477 | -1.797 |
| E <sub>ox</sub>                             | +0.627              | -0.652        | -0.982        | -      | -      |
| E <sub>1/2</sub>                            | <b>+0.555</b>       | <b>-0.708</b> | <b>-1.023</b> | -      | -      |

**Table 13.** Redox potentials of **Fe-2** in DMF. The E<sub>1/2</sub> values of processes III and IV could not be determined due to poorly resolved oxidation peaks.

The self-assembly of the monomer complex **Fe-2** was then investigated as was done for **Fe-1**, through DLS, CV and Cryo-TEM experiments. DLS studies indicated aggregates with a D<sub>h</sub> of approx. 6 nm in a 9:1 (v/v) H<sub>2</sub>O-CH<sub>3</sub>CN solvent mixture (Fig.75a). However, cryo-TEM images revealed **Fe-2** aggregates to be much more variable in size and shape to those of **Fe-1**. In some areas much larger aggregates are seen (Fig.75b,c), whilst in others individual POM molecules can be seen, possibly amongst dimeric **Fe-1** structures (Fig.75c,d).

#### 4. Multifunctionality of asymmetric hybrid POM (1)

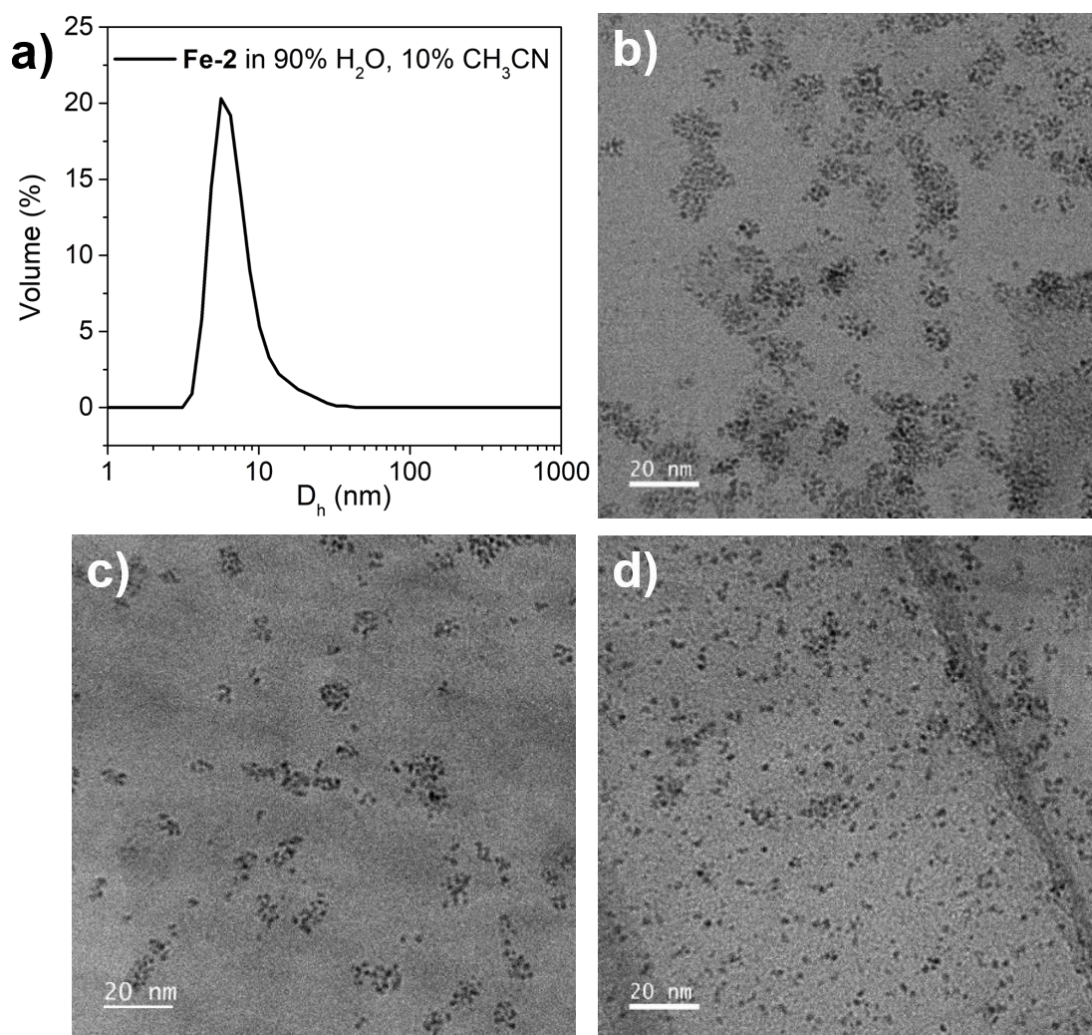


**Figure 75.** a) Particle-size distribution curve determined by DLS of **Fe-2** (1.4 mM) in 90% H<sub>2</sub>O, 10% CH<sub>3</sub>CN, D<sub>h</sub> maxima at 5.6 nm; **b-d)** Cryo-TEM images of **Fe-2** in 90% H<sub>2</sub>O, 10% CH<sub>3</sub>CN (1.4mM). Aggregates of much more varied sizes are visible than for the dimer, including areas of individual POMs.

Notably, the aggregates again do not appear hollow and resemble in areas the nanoparticle-like assemblies observed by Izzet *et al.* formed by the hierarchical aggregation of the terpyridine-terminated organosilyl Dawson hybrid [P<sub>2</sub>W<sub>17</sub>O<sub>61</sub>{O(Si-C<sub>29</sub>H<sub>18</sub>N<sub>3</sub>)<sub>2</sub>}] upon Fe<sup>2+</sup> complexation.<sup>[21]</sup> In their study, the assembly of discrete molecular triangles *ca.* 7 nm in diameter is first observed on complexation with Fe<sup>2+</sup> in DMSO, in which three Dawson clusters are linked by three Fe<sup>II</sup>-bis-terpyridine complexes. Then, on addition of CH<sub>3</sub>CN, the formation of much denser aggregates is



#### 4. Multifunctionality of asymmetric hybrid POM (1)

---

observed which is also shown to be reversible depending on solvent composition. The tight aggregation into dense nanoparticles is proposed to be a result of the strong electrostatic interactions between the coordination oligomers due to the regularly alternating positive and negative charges held by the anionic POMs and cationic metal linkers. Comparable aggregation that is possible with **Fe-2** (and to a similar degree, **Fe-1**) with the anionic POM and cationic  $\text{Fe}^{2+}$  units, may give rise to the variably sized aggregates observed by TEM imaging (Fig.75b-d). However, there is likely a more complex balance between: the dissociating ability of the solvent mixture, the arrangement of the hydrophobic  $C_{18}$  and hydrophilic POM( $\text{TPY-Fe}^{2+}$ ) moieties, and the electrostatic charge interactions.

The redox properties of the **Fe-2** aggregates unfortunately could not be studied due to phase separation when using a 9:1 (v/v) 0.1M  $\text{H}_2\text{SO}_4\text{-CH}_3\text{CN}$  mixture. Assuming a different, more labile ligand environment around the Fe-centre compared to in **Fe-1**, the solubility of **Fe-2** aggregates in an ionic solution can be expected to be different.

### 4.3 Conclusions

The multifunctionality of the new asymmetric Dawson hybrid system **1** has been explored, driven by the nature of the distinct appended organophosphoryl groups. The orthogonal and complementary functions of the aliphatic chain ligand  $C_{18}$  (facilitating solvent-dependent self-assembly) and the chelating group  $\text{TPY}$  (allowing transition metal-binding and also influencing supramolecular interactions) allow the performance of the hybrid system to be tuned through careful postfunctionalisation and the formation of unique redox-active soft nanostructures (Fig.76).

Postfunctionalisation by metal-binding at the chelating group was investigated by the coordination of  $\text{Fe(II)}$  to isolate a dimeric POM( $\text{TPY-Fe}^{\text{II}}\text{-TPY}$ )POM complex, and using stoichiometry, a tentatively assigned monomeric POM( $\text{TPY-Fe}^{\text{II}}$ ) complex was investigated in comparison. With combined metal functionalisation and self-assembling behaviour in such systems, this work demonstrates potential as a modular

## 4. Multifunctionality of asymmetric hybrid POM (1)

---

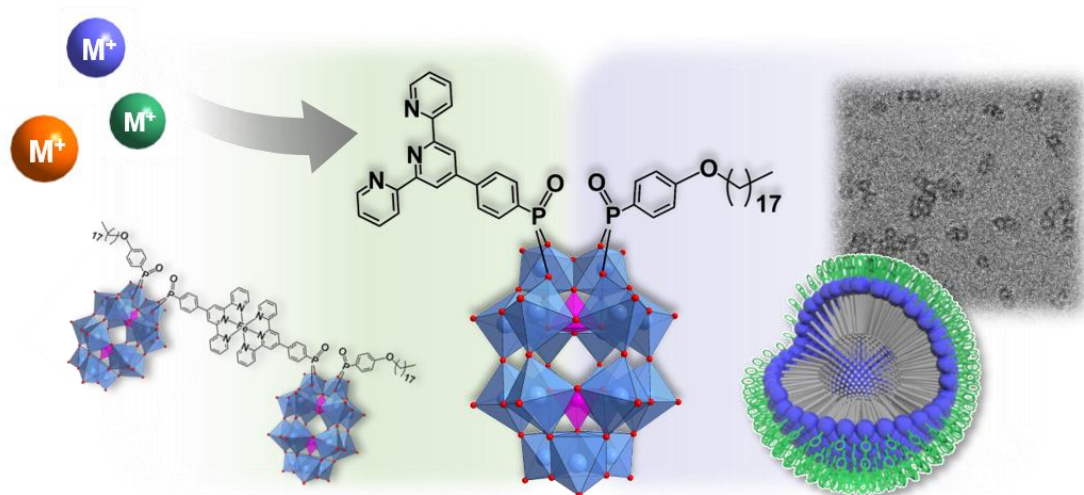


**Figure 76.** The multifunctionality of the asymmetric hybrid POM system, **1**.

design approach to prepare new nanomaterials with controllable architectures and incorporated transition-metal reactivity.

The hybrid POM systems, including the dimeric Fe(II) coordination complex, additionally demonstrate contrasting redox behaviour in the supramolecular state, which can be dynamically reverted to the molecular redox behaviour, offering interesting potential for the development of nanomaterials with applications as responsive or switchable electrochemical devices.

The scope of transition metal functionalisation and the properties of the new metal-functionalised systems will be explored in the following chapter.

## 4.4 Experimental details

### 4.4.1 Methods

Methods used are as outlined in Section 3.7, unless specified below.

DPV measurements were performed on a CHI1140c workstation.

#### 4. Multifunctionality of asymmetric hybrid POM (1)

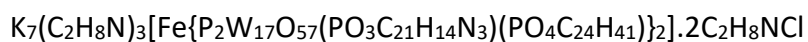
---

Cryo-TEM analysis was run by Dr Julie Watts at the Nanoscale and Microscale Research Centre (University of Nottingham) on a JEOL 2100 Plus operating at 200 kV. Samples were deposited (3  $\mu\text{L}$ ) onto a graphene oxide / holey carbon copper grid, held in tweezers (25  $^{\circ}\text{C}$ , 80% humidity), and blotted (1.5 s), before plunging into liquid ethane (-172  $^{\circ}\text{C}$ ) to vitrify using a Gatan CP3 cryoplunge. The samples were maintained under liquid nitrogen (-196  $^{\circ}\text{C}$ ) during transfer (Gatan 926 cryo sample holder) to the TEM, with the temperature held around -176  $^{\circ}\text{C}$  throughout imaging with a Gatan (Smartset model 900) cold stage controller. Images were recorded (Gatan Ultrascan 100XP camera), with a nominal underfocus value of 3-5  $\mu\text{m}$  and a 60  $\mu\text{m}$  objective aperture to enhance phase contrast.

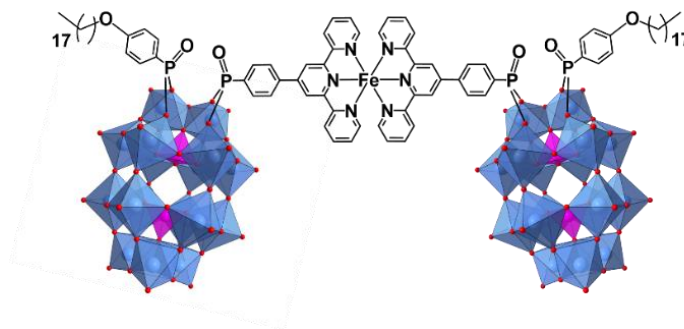
The Fe content determination was performed through analysis of the samples by Inductively Coupled Plasma Optical Emission Spectrometry (ICP-OES) on a Perkin Elmer Optima 2000 DV ICP-OES. The samples were prepared by digestion of  $\sim 5$  mg of dry compound in 2.86 mL conc  $\text{HNO}_3$  (Fisher Primar Plus<sup>TM</sup> >68%) under microwave conditions (135 $^{\circ}\text{C}$  for 2 mins). The digestion mixtures were then diluted to 100 mL with Milli-Q water to obtain solutions with a final acid concentration of 2% (v/v) from which samples were taken for analysis. Calibration curves were prepared using solutions of Fe concentrations of 0.1, 0.2, 0.3, 0.4, 0.5, 0.7 and 1.0 ppm prepared by dilution of the ICP Fe standard solution (Sigma Aldrich ICP TraceCERT<sup>®</sup>, 1000  $\mu\text{g}/\text{mL}$  Fe in 2%  $\text{HNO}_3$ ) with Milli-Q water.

#### 4.4.2 Syntheses

##### 4.4.2.1 $[\text{Fe}\{\text{P}_2\text{W}_{17}\text{O}_{57}(\text{TPY})(\text{C}_{18})\}_2]$ (Fe-1)



#### 4. Multifunctionality of asymmetric hybrid POM (1)

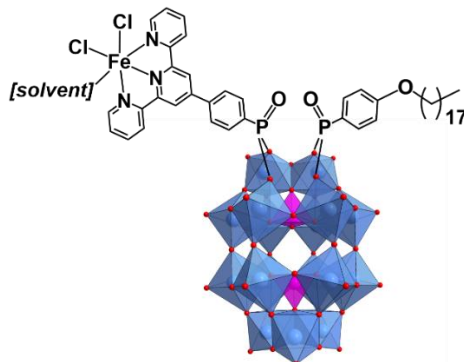
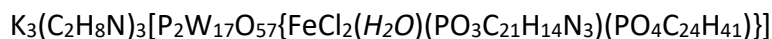


$\text{FeCl}_2$  (2.47 mg, 0.0194 mmol) and **1** (200 mg, 0.0376 mmol) were dissolved in  $\text{CH}_3\text{CN}$  (5 mL) and stirred under argon at RT for 16 h. The solvent was removed in vacuo to leave **Fe-1** as a dark purple solid that was washed with ether and dried in air with gentle heating (140 mg, 71%).

**$^1\text{H}$  NMR** (500 MHz,  $\text{DMSO-d}_6$ )  $\delta$ =9.78 (s, 4H), 9.16-9.05 (d,  $J$ =8.2 Hz, 4H; Ar-H), 8.78-8.64 (m, 4H; Ar-H), 8.44-8.34 (m, 4H; Ar-H), 8.31-8.14 (br, 6H;  $\text{NH}_2(\text{CH}_3)_2^+$ ), 8.06-8.03 (m, 4H; Ar-H), 7.97-7.90 (m, 4H; Ar-H), 7.37-7.17 (m, 8H; Ar-H), 7.06-7.00 (m, 4H; Ar-H), 4.05 (t, 4H; O- $\text{CH}_2$ -), 2.55 (t, 18H;  $\text{NH}_2(\text{CH}_3)_2^+$ ), 1.79-1.72 (m, 4H;  $\text{CH}_2$ ), 1.48-1.10 (m, 60H;  $-\text{CH}_2-$ ), 0.86 (t, 6H;  $-\text{CH}_3$ ) ppm;  **$^{31}\text{P}$  NMR** (202 MHz,  $\text{DMSO-d}_6$ )  $\delta$ = 16.92, 13.15, -11.29, -12.92 ppm; **IR** (ATR): 473 (s), 523 (s), 568 (s), 726 (br, vs), 905 (s), 953 (s), 1050 (m), 1085 (s), 1136 (m), 1253 (w), 1295 (w), 1463 (m), 1504 (w), 1599 (m), 2848 (m), 2918 (m)  $\text{cm}^{-1}$ ; **Elemental Analysis** calc (%) for  $\text{K}_7\text{P}_8\text{W}_{34}\text{O}_{128}\text{C}_{100}\text{H}_{150}\text{N}_{11}\text{Cl}_2\text{Fe}$ : C 11.49, H 1.45, N 1.47, found: C 11.41, H 1.41, N 1.33; **TGA Analysis**: Step transition (205.3 1 to 361.0°C) wt. loss = 3.046 % = loss of 3 DMA + 2 DMA.Cl (calc = 2.941 %); +  $\text{C}_{18}$  (cleaved at phosphonate linker unit) **ICP-OES**: 0.696% Fe (0.348 ppm), calc for  $\text{K}_7\text{P}_8\text{W}_{34}\text{O}_{128}\text{C}_{100}\text{H}_{150}\text{N}_{11}\text{Cl}_2\text{Fe}$  = 0.534 % Fe (0.266 ppm); **UV/Vis (DMF)**:  $\lambda_{\text{max}}$  ( $\epsilon$ ,  $\text{mol}^{-1}\text{Lcm}^{-1}$ ) = 282 (142,000), 290 (152,000), 576 (29,900) nm.

#### 4. Multifunctionality of asymmetric hybrid POM (1)

##### 4.4.2.2 $[P_2W_{17}O_{57}\{(Fe-TPY)(C_{18})\}]$ (Fe-2)



$FeCl_2$  (1.84 mg, 0.0145 mmol) and **1** (75 mg, 0.0145 mmol) were dissolved in  $CH_3CN$  (2mL) and stirred under argon at RT for 24 h. The solvent was removed in vacuo to leave a dark purple solid that was washed with ether and dried in air with gentle heating (60 mg, 78%).

$^1H$  NMR (400 MHz,  $DMSO-d_6$ )  $\delta$ = 9.78 (s, br), 8.70 (m, br), 8.37 (m, br), 8.04 (m, br), 7.31 (m, br), 7.22 (m, br), 7.03 (s, br), 4.06 (m, br), 1.75 (m, br), 1.48-1.17 (m, br), 0.86 (m, br) ppm;  $^{31}P$  NMR (162 MHz,  $DMSO-d_6$ )  $\delta$ = 16.92, 13.15, -11.29, -12.92 ppm; IR (ATR): 471 (s), 527 (s), 566 (s), 729 (br, vs), 908 (s), 955 (s), 1050 (m), 1087 (s), 1136 (m), 1253 (w), 1295 (w), 1465 (m), 1504 (w), 1599 (m), 2850 (m), 2920 (m)  $cm^{-1}$ ; **Elemental Analysis** calc (%) for  $K_3P_4W_{17}O_{65}C_{51}H_{81}N_6FeCl_2$ : C 11.53, H 1.54, N 1.58, found: C 11.65, H 1.53, N 1.60; **TGA Analysis**: Step transition (217.9 to 429.7°C) wt. loss = 2.568 % = loss of 3 DMA +  $1H_2O$  (calc = 2.943 %); **ICP-OES**: 1.108 % Fe (0.555 ppm), calc for  $K_3P_4W_{17}O_{65}C_{51}H_{81}N_6FeCl_2$  = 1.051 % Fe (0.512 ppm); **UV/Vis (DMF)**:  $\lambda_{max}$  ( $\epsilon$ ,  $mol^{-1}Lcm^{-1}$ ) = 282 (86,350), 289 (82,000), 576 (16,240) nm.

#### 4. Multifunctionality of asymmetric hybrid POM (1)

---

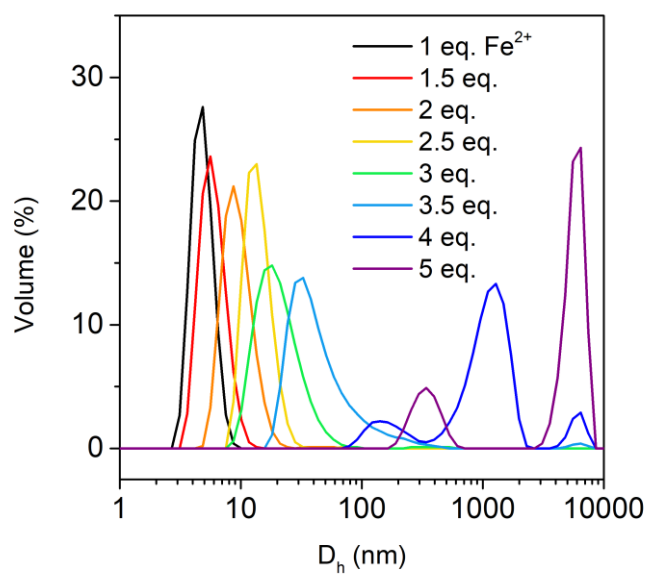


**Figure 77.** Particle-size distribution curves determined by DLS of a solution of **3** (1.4 mM) in 90% H<sub>2</sub>O, 10% DMF after the stepwise addition of 1 to 5 molar equivalents FeCl<sub>2</sub>.

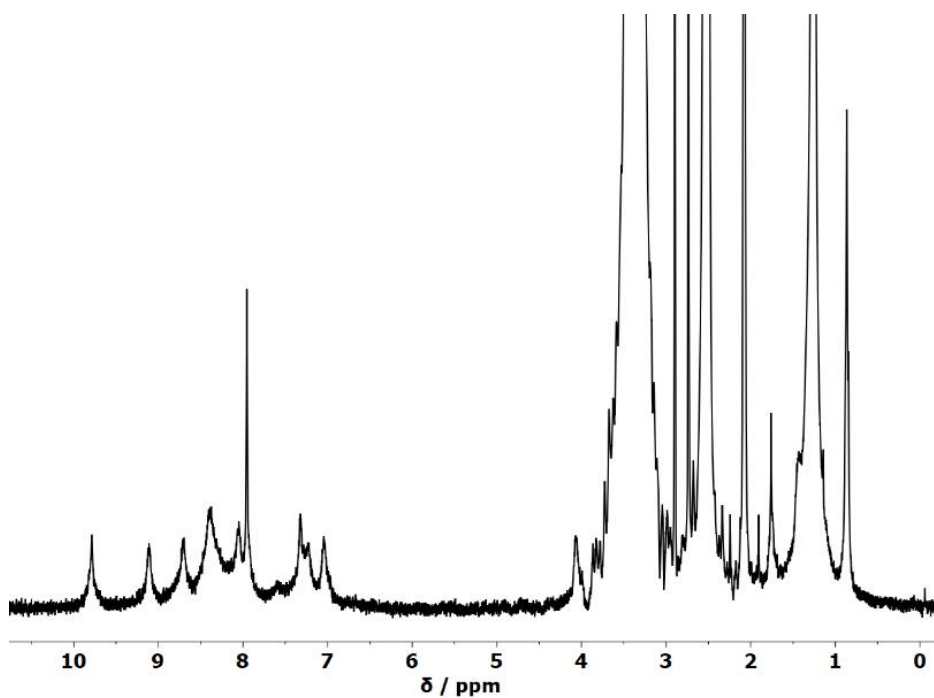


**Figure 78.** <sup>1</sup>H NMR spectra of Fe-2 in DMSO-d<sub>6</sub>.

## 4.5 References

- [1] M. P. Foster, C. A. McElroy, C. D. Amero, Solution NMR of large molecules and assemblies, *Biochemistry*, 2007, **46**, 331-340.
- [2] S. Amin, J. M. Cameron, J. A. Watts, D. A. Walsh, V. Sans, G. N. Newton, Effects of chain length on the size, stability, and electronic structure of redox-active organic–inorganic hybrid polyoxometalate micelles, *Mol. Syst. Des. Eng.*, 2019, **4**, 995-999.
- [3] A. Misra, K. Kozma, C. Streb, M. Nyman, Beyond Charge Balance: Counter-Cations in Polyoxometalate Chemistry, *Angew. Chem. Int. Ed.*, 2020, **59**, 596-612.
- [4] P. Yin, C. P. Pradeep, B. Zhang, F.-Y. Li, C. Lydon, M. H. Rosnes, D. Li, E. Bitterlich, L. Xu, L. Cronin, T. Liu, Controllable Self-Assembly of Organic–Inorganic Amphiphiles Containing Dawson Polyoxometalate Clusters, *Chem. Eur. J.*, 2012, **18**, 8157-8162.
- [5] K. Kastner, A. J. Kibler, E. Karjalainen, J. A. Fernandes, V. Sans, G. N. Newton, Redox-active organic-inorganic hybrid polyoxometalate micelles, *J. Mater. Chem. A*, 2017, **5**, 11577-11581.
- [6] E. Hampson, J. M. Cameron, S. Amin, J. Kyo, J. A. Watts, H. Oshio, G. N. Newton, Asymmetric Hybrid Polyoxometalates: A Platform for Multifunctional Redox-Active Nanomaterials, *Angew. Chem. Int. Ed.*, 2019, **58**, 18281-18285.
- [7] I. Persson, Solvation and complex formation in strongly solvating solvents, *Pure Appl. Chem.*, 1986, **58**, 1153-1161.
- [8] A. Winter, U. S. Schubert, Metal-Terpyridine Complexes in Catalytic Application – A Spotlight on the Last Decade, *ChemCatChem*, 2020, **12**, 2890-2941.
- [9] J. Limburg, J. S. Vrettos, L. M. Liable-Sands, A. L. Rheingold, R. H. Crabtree, G. W. Brudvig, A Functional Model for O-O Bond Formation by the O<sub>2</sub>-Evolving Complex in Photosystem II, *Science*, 1999, **283**, 1524.
- [10] J. J. Leung, J. Warnan, K. H. Ly, N. Heidary, D. H. Nam, M. F. Kuehnel, E. Reisner, Solar-driven reduction of aqueous CO<sub>2</sub> with a cobalt bis(terpyridine)-based photocathode, *Nature Catalysis*, 2019, **2**, 354-365.
- [11] S. Chakraborty, G. R. Newkome, Terpyridine-based metallosupramolecular constructs: tailored monomers to precise 2D-motifs and 3D-metallocages, *Chem. Soc. Rev.*, 2018, **47**, 3991-4016.
- [12] P. Liu, G. Shi, X. Chen, Terpyridine-Containing  $\pi$ -Conjugated Polymers for Light-Emitting and Photovoltaic Materials, *Front. Chem.*, 2020, **8**:592055.
- [13] D. Liu, H. Liu, B. Song, M. Chen, J. Huang, J. Wang, X. Yang, W. Sun, X. Li, P. Wang, Terpyridine-based metallo-organic cages and supramolecular gelation by coordination-driven self-assembly and host–guest interaction, *Dalton Trans.*, 2018, **47**, 14227-14232.
- [14] V. Duffort, R. Thouvenot, C. Afonso, G. Izzet, A. Proust, Straightforward synthesis of new polyoxometalate-based hybrids exemplified by the covalent bonding of a polypyridyl ligand, *Chem. Commun.*, 2009, 6062-6064.

#### 4. Multifunctionality of asymmetric hybrid POM (1)

---

- [15] M.-P. Santoni, A. K. Pal, G. S. Hanan, A. Proust, B. Hasenknopf, Discrete Covalent Organic–Inorganic Hybrids: Terpyridine Functionalized Polyoxometalates Obtained by a Modular Strategy and Their Metal Complexation, *Inorg. Chem.*, 2011, **50**, 6737-6745.
- [16] M. Piot, B. Abécassis, D. Brouri, C. Troufflard, A. Proust, G. Izzet, Control of the hierarchical self-assembly of polyoxometalate-based metallomacrocycles by redox trigger and solvent composition, *Proc. Nat. Acad. Sci.*, 2018, **115**, 8895-8900.
- [17] J. Kang, B. Xu, Z. Peng, X. Zhu, Y. Wei, D. R. Powell, Molecular and Polymeric Hybrids Based on Covalently Linked Polyoxometalates and Transition-Metal Complexes, *Angew. Chem. Int. Ed.*, 2005, **44**, 6902-6905.
- [18] U. S. Schubert, C. Eschbaumer, P. Andres, H. Hofmeier, C. H. Weidl, E. Herdtweck, E. Dulkeith, A. Morteani, N. E. Hecker, J. Feldmann, 2,2':6',2''-Terpyridine metal complexes as building blocks for extended functional metallo-supramolecular assemblies and polymers, *Synth. Met.*, 2001, **121**, 1249-1252.
- [19] A. J. Kibler, G. N. Newton, Tuning the electronic structure of organic–inorganic hybrid polyoxometalates: The crucial role of the covalent linkage, *Polyhedron*, 2018, **154**, 1-20.
- [20] P. S. Braterman, J. I. Song, R. D. Peacock, Electronic absorption spectra of the iron(II) complexes of 2,2'-bipyridine, 2,2'-bipyrimidine, 1,10-phenanthroline, and 2,2':6',2''-terpyridine and their reduction products, *Inorg. Chem.*, 1992, **31**, 555-559.
- [21] G. Izzet, B. Abécassis, D. Brouri, M. Piot, B. Matt, S. A. Serapian, C. Bo, A. Proust, Hierarchical Self-Assembly of Polyoxometalate-Based Hybrids Driven by Metal Coordination and Electrostatic Interactions: From Discrete Supramolecular Species to Dense Monodisperse Nanoparticles, *J. Am. Chem. Soc.*, 2016, **138**, 5093-5099.
- [22] S. Shankar, M. Peters, K. Steinborn, B. Krahwinkel, F. D. Sönnichsen, D. Grote, W. Sander, T. Lohmiller, O. Rüdiger, R. Herges, Light-controlled switching of the spin state of iron(III), *Nat. Commun.*, 2018, **9**, 4750.
- [23] J. S. McIndoe, K. L. Vikse, Assigning the ESI mass spectra of organometallic and coordination compounds, *J. Mass Spectrom.*, 2019, **54**, 466-479



## 5 Transition metal- functionalisation of asymmetric hybrid POMs

Covalent hybrid POMs which are connected to transition metal coordination complexes have emerged as a new class of multicomponent hybrid system which include the collective and complementary properties of the organometallic and inorganic components in a single molecule.<sup>[1]</sup> Moreover, coordination complexes can be effective in directing the self-assembly of functional supramolecular arrays.<sup>[2]</sup> Hybrid materials based on such metal-functionalised hybrid POMs display promise in bringing new advances to the applications of POMs in areas such as catalysis, magnetism, and material science.

Ruthenium polypyridyl complexes are one of the most extensively studied classes of transition metal complexes because of their unique and tuneable photophysical, photochemical and electrochemical properties, and derivatives have been developed over the years in numerous reports on their photosensitising,<sup>[3]</sup> catalytic,<sup>[4]</sup> and biological applications.<sup>[5]</sup> The tris(2,2'-bipyridine (bpy)) derivative of ruthenium(II),  $[\text{Ru}(\text{bpy})_3]^{2+}$  (Fig.79), is the most well-known, recognised for its intense photoluminescence in solution at room temperature.<sup>[6]</sup> Bis(2,2';6',2''-terpyridine

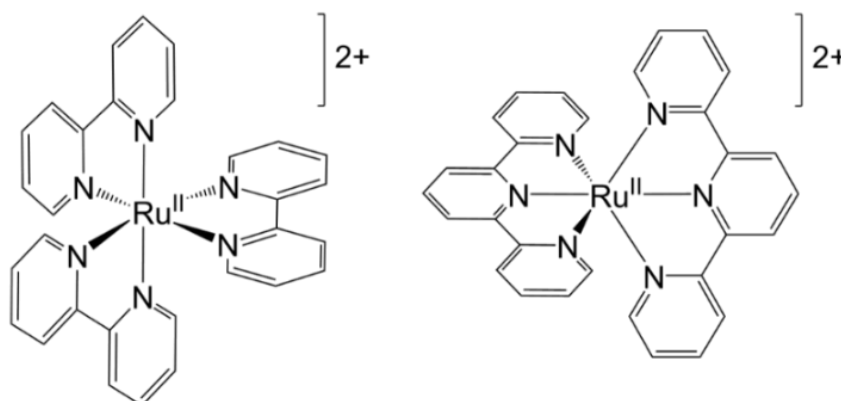


**Figure 79.** Tris(2,2'-bipyridine)ruthenium(II),  $[\text{Ru}(\text{bpy})_3]^{2+}$ , and bis(2,2';6',2''-terpyridine)ruthenium(II),  $[\text{Ru}(\text{tpy})_2]^{2+}$ , complexes.

(tpy)) derivatives also attract significant attention because of the linear directionality and stable connectivity in {tpy-Ru-tpy} complexes (Fig.79), making them useful building blocks in photoactive metallosupramolecular assemblies.<sup>[3, 7]</sup>

Ruthenium polypyridyl complexes based on terpyridine and bipyridine ligands have been shown to be particularly promising as photocatalysts in CO<sub>2</sub> reduction<sup>[8]</sup> and in light-driven water oxidation.<sup>[9]</sup> Similarly well-recognised for their photocatalytic activity, Pt<sup>II</sup>-terpyridine complexes draw attention as hydrogen-evolution photocatalysts.<sup>[10]</sup> Additionally, their rich luminescent properties and planarity render them effective metallointercalators, useful as biomolecular probes and cytotoxic agents.<sup>[11]</sup>

In consideration of such complexes, their combination with the amphiphilic structure of the asymmetric hybrid POM, **1**, could be used to prepare new highly photo- and redox-active soft nanomaterials for applications as advanced catalysts, nanoreactors, or phototherapeutic agents.<sup>[12-14]</sup> In this chapter, the covalent incorporation of transition metal complexes into asymmetric hybrid POM structures will be explored. First, a postfunctionalisation approach is presented, in which a Pt(II) ion is coordinated to the available chelating site on the *TPY* moiety on the asymmetric hybrid POM **1**. In the second section, a different synthetic approach is described in which a {Ru<sup>II</sup>(bpy)(tpy)}-derived complex is prepared as an organophosphonate ligand that can be grafted directly onto a lacunary Dawson anion a new one-pot hybridisation reaction. An investigation of the electro- and photo-chemical properties of the new asymmetric hybrid POMs functionalised with Pt(II) and Ru(II) complexes is discussed, including studies into their solvent-dependent self-assembly, as derivatives of the amphiphilic asymmetric hybrid POM **1**.

### **5.1 Postfunctionalisation of an asymmetric hybrid POM by Pt<sup>II</sup> coordination**

This section covers the work recently published in the article: “Transition metal decorated soft nanomaterials through modular self-assembly of an asymmetric

hybrid polyoxometalate”, E. Hampson, J. M. Cameron, J. A. Watts, G. N. Newton, *Chem. Commun.*, **2020**, 56, 8237-8240.

### 5.1.1 Synthesis of $[P_2W_{17}O_{57}\{(Pt-TPY)(C_{18})\}]$ (Pt-1)

Earlier reported procedures for the coordination of Pt(II) to terpyridine involve refluxing the terpyridine-based ligand with a chloroplatinate (II) salt or with the complex  $[Pt(DMSO)_2Cl_2]$  often for long periods of time (up to several days). However, this often results in poor yields due to the additional formation of anionic platinum complexes causing precipitation of double salts, or disproportionation to Pt(0).<sup>[15-17]</sup> Several attempts at coordination of  $Pt^{2+}$  to the terpyridine site of the *TPY* moiety on the asymmetric hybrid **1** were made initially using  $K_2PtCl_4$ . However, this always resulted in very poor conversion, evidenced by  $^1H$  and  $^{31}P$  NMR, even after refluxing for several days.

Higher yields are reported for more recently adopted methods involving the complex  $[Pt(COD)Cl_2]$  (COD= cycloocta- 1,5-diene), due to the strong *trans*-labilising effect of the *cis*-orientated coordinated diolefin on the halide ligands.<sup>[18]</sup> More facile exchange for the terpyridine is made possible in cationic halogen-free COD complexes, such as  $[PtCOD(acetone)_2][BF_4]_2$ .<sup>[19]</sup> The dihalide complex is first treated with a silver salt, such as silver tetrafluoroborate ( $AgBF_4$ ), to result in the precipitation of the silver halide, followed by the coordination of the terpyridine to the  $Pt^{2+}$  centre in the more labile solvent complex. This method is also reported using the precursor complex  $[Pt(PhCN)_2Cl_2]$ .<sup>[20]</sup> Equimolar silver salt can either be used to remove one chloro ligand from the dichloro- precursor to isolate the  $\{Pt(terpy)Cl\}$  complex, or, by using two molar equivalents both halide ligands can be exchanged.<sup>[21]</sup>

## 5. Transition metal- functionalisation of asymmetric hybrid POMs

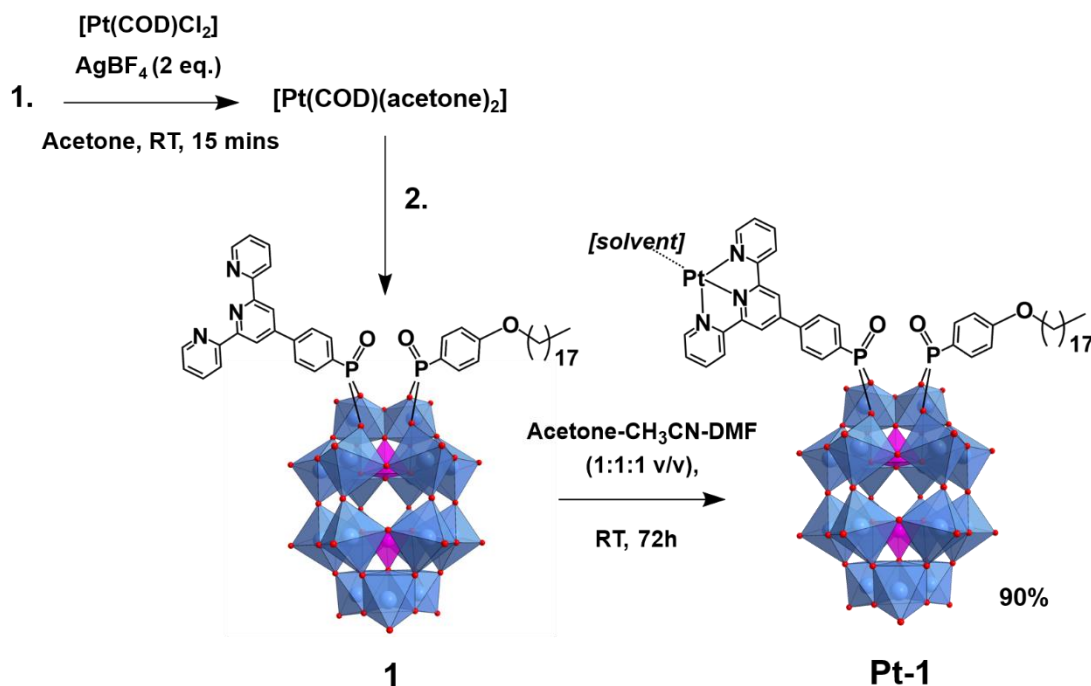


**Figure 80.** Preparation of the Pt(II)-functionalised asymmetric hybrid, **Pt-1**.

Adopting this method here, the Pt(II) complex  $[\text{Pt(COD)Cl}_2]$  was first stirred briefly with two molar equivalents of  $\text{AgBF}_4$  in acetone to labilise the Pt(II) complex (Fig.80). The resultant  $\text{AgCl}$  precipitate was removed by centrifugation and the Pt-containing solution was added to a solution of the asymmetric hybrid **1** in  $\text{DMF-CH}_3\text{CN}$  (1:1 v/v) and stirred for *ca.* three days at RT. This resulted in an orange-yellow coloured reaction mixture, characteristic of many  $\{\text{Pt(tpy)L}\}$  complexes,<sup>[22]</sup> which was then centrifuged to remove any insoluble material, before the solvent was removed *in vacuo*. The final product,  $\text{K}(\text{C}_2\text{H}_8\text{N})_3[\text{P}_2\text{W}_{17}\text{O}_{57}\{(\text{PO}_3\text{C}_{21}\text{H}_{14}\text{N}_3\text{Pt}(\text{sol}v.))(\text{PO}_4\text{C}_{24}\text{H}_{41})\}].\text{DMF}$  (**Pt-1**), was obtained by precipitation from minimal DMF using an excess of diethyl ether. The composition and purity of **Pt-1** was then confirmed by  $^1\text{H}$ ,  $^{31}\text{P}$  NMR and FTIR spectroscopies, ESI-MS and elemental (CHN) analysis.

### 5.1.2 Characterisation of Pt-1

The  $^1\text{H}$  and  $^{31}\text{P}$  NMR spectra of **Pt-1** confirmed the formation of a single new species. Aromatic *TPY* peaks in the  $^1\text{H}$  NMR appeared downfield shifted from in **1**, suggesting

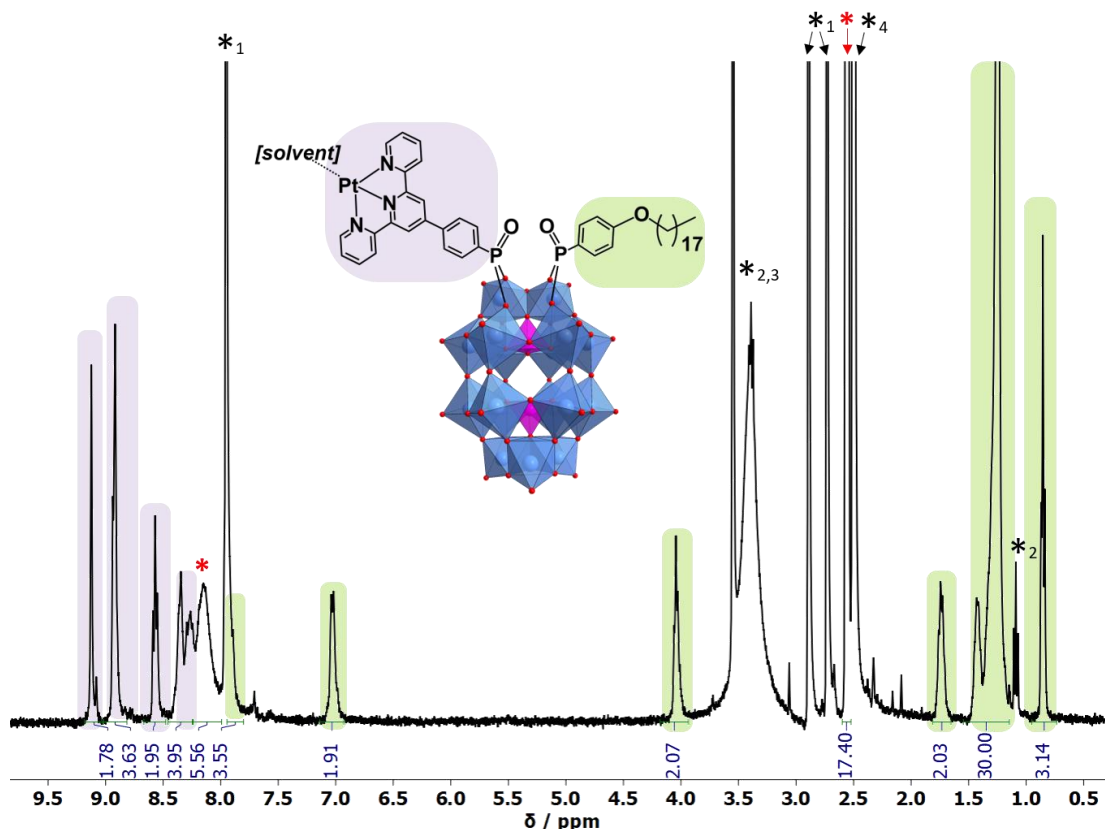


**Figure 81.**  $^1\text{H}$  NMR of **Pt-1** in  $\text{DMSO-d}_6$  showing the assignment of peaks to each ligand: green =  $\text{C}_{18}$ , purple =  $\text{Pt-TPY}$ . Red asterisks indicate DMA cation signals, and black asterisks indicate solvent impurities: 1= DMF, 2= diethyl ether, 3=  $\text{H}_2\text{O}$ , 4= DMSO.

successful coordination of the  $\text{Pt}^{2+}$  ion (Fig.81,82a).<sup>[18]</sup> Signals for both covalently bound ligand groups,  $\text{TPY}$  and  $\text{C}_{18}$ , appear at 12.55 and 17.00 ppm respectively in the  $^{31}\text{P}$  NMR (Fig.82b). Compared to in **1**, the phosphorus nucleus in the  $\text{TPY}$  group is slightly shielded (from 13.40 ppm) due to the effect of the metal ion coordination, and the  $\text{C}_{18}$  phosphorus is very slightly deshielded (from 16.72 ppm). This is again indicative of some electronic communication between the phosphonate linker groups that is possibly mediated by the POM core, as was observed for **Fe-1**.

The ESI mass spectrum of **Pt-1** shows two series of peaks for species with 2- and 3- charges (Fig.83). These are assigned as the POM hybrid anion with varying combinations of proton and sodium cations, in which the  $\text{Pt}^{\text{II}}$  centre in most cases is

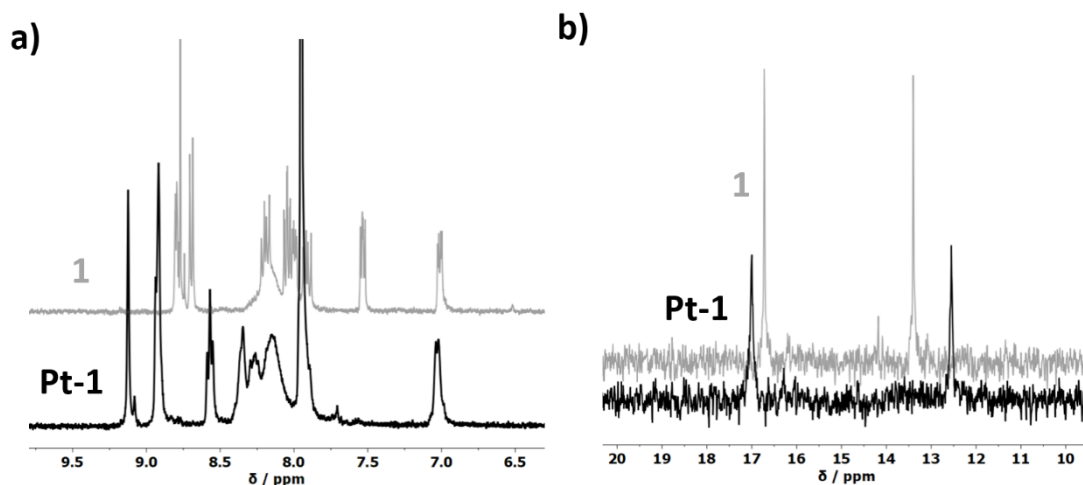


**Figure 82.** Overlaid **a)**  $^1\text{H}$  NMR spectra (focused on the aromatic proton signal region) and **b)**  $^{31}\text{P}$  NMR spectra of **Pt-1** (black) and asymmetrically functionalised precursor **1** (grey) in  $\text{DMSO-d}_6$ . Only the positive chemical shift region for the organophosphonate  $^{31}\text{P}$  nuclei is presented here for simplicity.

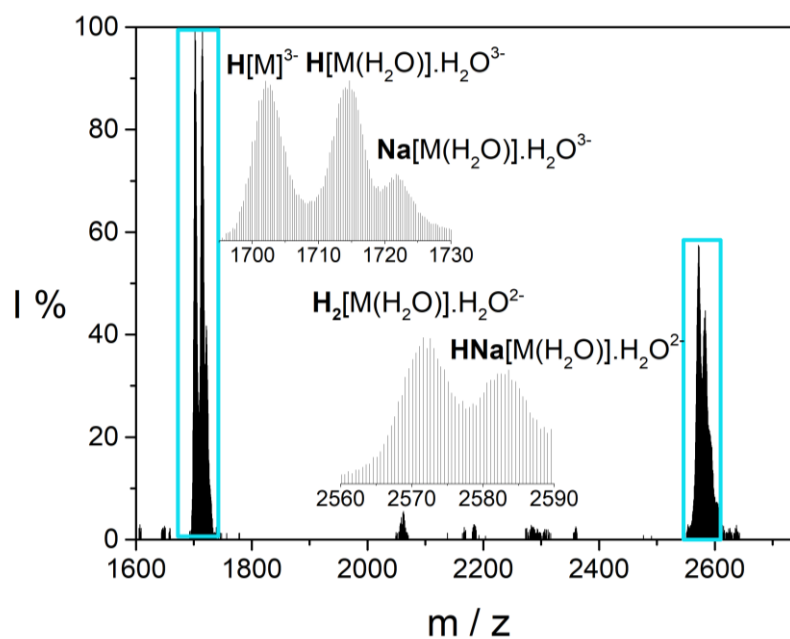


**Figure 83.** Negative mode ESI mass spectrum of **Pt-1** in acetonitrile.  $[\text{M}] = [\text{P}_2\text{W}_{17}\text{O}_{57}\{(\text{PO}_3\text{C}_{21}\text{H}_{14}\text{N}_3\text{Pt})(\text{PO}_4\text{C}_{24}\text{H}_{41})\}]^{4-}$ .

coordinated with a neutral water molecule. The inclusion of a solvating water molecule in addition to the coordinating water in these species gives well-fitted assignments (Table.14). The assignment of the fourth ligand of the Pt centre to a

## 5. Transition metal- functionalisation of asymmetric hybrid POMs

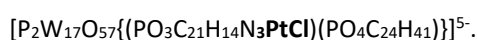
| Assignment   | z  | m/z (obs.) | m/z (calc.) |
|--|----|------------|-------------|
| <b>H</b> [P <sub>2</sub> W <sub>17</sub> O <sub>57</sub> {(PO <sub>3</sub> C <sub>21</sub> H <sub>14</sub> N <sub>3</sub> Pt)(PO <sub>4</sub> C <sub>24</sub> H <sub>41</sub> )}]  | 3- | 1702.3659  | 1702.3570   |
| <b>H</b> [P <sub>2</sub> W <sub>17</sub> O <sub>57</sub> {(PO <sub>3</sub> C <sub>21</sub> H <sub>14</sub> N <sub>3</sub> Pt(H <sub>2</sub> O))(PO <sub>4</sub> C <sub>24</sub> H <sub>41</sub> )}].H <sub>2</sub> O             | 3- | 1714.3491  | 1714.3640   |
| <b>Na</b> [P <sub>2</sub> W <sub>17</sub> O <sub>57</sub> {(PO <sub>3</sub> C <sub>21</sub> H <sub>14</sub> N <sub>3</sub> Pt(H <sub>2</sub> O))(PO <sub>4</sub> C <sub>24</sub> H <sub>41</sub> )}].H <sub>2</sub> O            | 3- | 1721.6727  | 1721.6913   |
| <b>H<sub>2</sub></b> [P <sub>2</sub> W <sub>17</sub> O <sub>57</sub> {(PO <sub>3</sub> C <sub>21</sub> H <sub>14</sub> N <sub>3</sub> Pt(H <sub>2</sub> O))(PO <sub>4</sub> C <sub>24</sub> H <sub>41</sub> )}].H <sub>2</sub> O | 2- | 2572.0956  | 2572.0499   |
| <b>HNa</b> [P <sub>2</sub> W <sub>17</sub> O <sub>57</sub> {(PO <sub>3</sub> C <sub>21</sub> H <sub>14</sub> N <sub>3</sub> Pt(H <sub>2</sub> O))(PO <sub>4</sub> C <sub>24</sub> H <sub>41</sub> )}].H <sub>2</sub> O           | 2- | 2583.0737  | 2583.0409   |

**Table 14.** Selected ESI-MS peak assignments for **Pt-1**.

chloride was initially considered before a re-evaluation of the synthetic method led to the assignment of a labile solvent molecule. As two molar equivalents of AgBF<sub>4</sub> were used in synthesis, it can be assumed that two molar equivalents of AgCl were removed on precipitation, and, therefore, the assignment of a chloride is highly unlikely. Several peaks were initially assigned to the hybrid anion with a {Pt-(TPY)Cl} centre (now possessing an overall 5- charge) with proton and/or sodium cations, which can be seen to give comparably very close fits (Table.15). With the free exchange of ions and solvent under the mass spectrometer conditions, the various possible assignments are not definitive and cannot confirm the exact structure of the hybrid complex in the solid state, but, nevertheless, support the successful coordination of a Pt<sup>2+</sup> ion to the POM hybrid complex.

| Assignment  | z  | m/z (obs.) | m/z (calc.) |
|---|----|------------|-------------|
| <b>H<sub>2</sub></b> [P <sub>2</sub> W <sub>17</sub> O <sub>57</sub> {(PO <sub>3</sub> C <sub>21</sub> H <sub>14</sub> N <sub>3</sub> PtCl)(PO <sub>4</sub> C <sub>24</sub> H <sub>41</sub> )}]   | 3- | 1714.3491  | 1714.3492   |
| <b>HNa</b> [P <sub>2</sub> W <sub>17</sub> O <sub>57</sub> {(PO <sub>3</sub> C <sub>21</sub> H <sub>14</sub> N <sub>3</sub> PtCl)(PO <sub>4</sub> C <sub>24</sub> H <sub>41</sub> )}]             | 3- | 1721.6727  | 1721.6765   |
| <b>H<sub>3</sub></b> [P <sub>2</sub> W <sub>17</sub> O <sub>57</sub> {(PO <sub>3</sub> C <sub>21</sub> H <sub>14</sub> N <sub>3</sub> PtCl)(PO <sub>4</sub> C <sub>24</sub> H <sub>41</sub> )}]   | 2- | 2572.0956  | 2572.0277   |
| <b>H<sub>2</sub>Na</b> [P <sub>2</sub> W <sub>17</sub> O <sub>57</sub> {(PO <sub>3</sub> C <sub>21</sub> H <sub>14</sub> N <sub>3</sub> PtCl)(PO <sub>4</sub> C <sub>24</sub> H <sub>41</sub> )}] | 2- | 2583.0737  | 2583.0187   |

**Table 15.** Alternative *m/z* assignments for **Pt-1** considering a chloride ligand and anionic formula of



## 5. Transition metal- functionalisation of asymmetric hybrid POMs

Considering the reduced overall negative charge of the Pt-coordinated hybrid from 6- in **1** to 4- due to the neutral ligand environment around the Pt<sup>2+</sup> ion, three of the counter-cations were assigned as DMA cations as observed in the <sup>1</sup>H NMR (Fig.81, peaks at 2.55 and 8.22-8.02 ppm) and the fourth to a potassium ion. Two DMF molecules were considered in the molecular formula of **Pt-1** in the solid state in accordance with CHN analysis and TGA.

IR spectroscopy confirmed structural features of the asymmetric hybrid POM precursor **1** are retained in **Pt-1** (Fig.84). A more prominent peak observed at 1651 cm<sup>-1</sup> may be evident of coordinated DMF in the solid state, characteristic of a carbonyl (C=O) stretch that is downshifted by *ca.* 20 cm<sup>-1</sup> from free DMF.<sup>[23]</sup>

The UV-Vis spectrum of **Pt-1** in DMF showed bands characteristic of {Pt(tpy)L} complexes (Fig.85). Intraligand (IL) Pt-tpy  $\pi$ - $\pi^*$  absorption features of the metal-coordinated ligand Pt-TPY were seen from *ca.* 285-350 nm in the region which overlap LMCT POM (O-W) bands. MLCT Pt-tpy (d- $\pi^*$ ) bands were also seen from 380-440 nm.<sup>[22, 24]</sup> The Pt(tpy) absorption features are analogous to those observed for the Pt(II)-coordinated phosphonate ester of TPY, Pt-PO(OEt)<sub>2</sub>TPY (Fig.85), which was

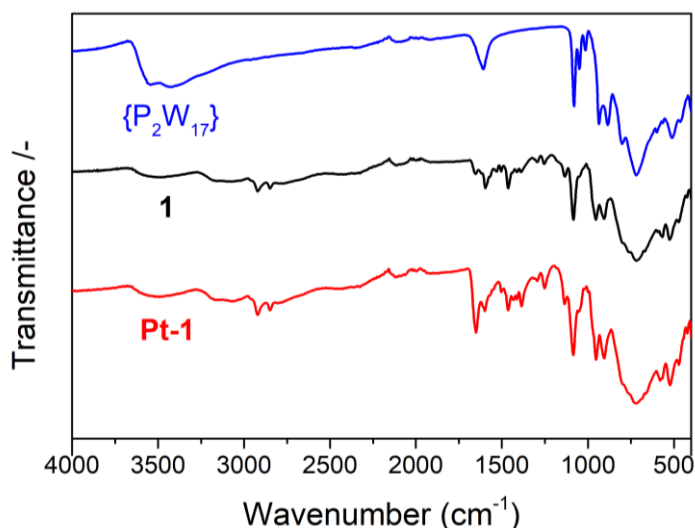


**Figure 84.** Stacked IR (ATR) spectra of **Pt-1** (red) asymmetrically functionalised precursor, **1** (black), and lacunary Dawson K<sub>10</sub>-[P<sub>2</sub>W<sub>17</sub>O<sub>61</sub>] {P<sub>2</sub>W<sub>17</sub>} (blue).



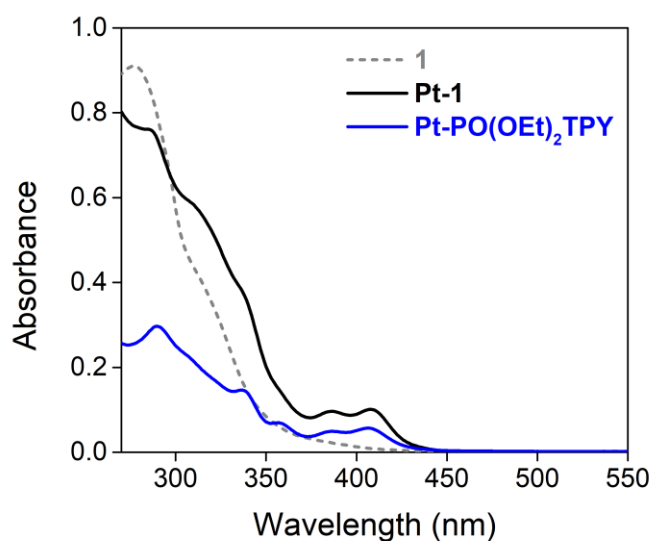


**Figure 85.** Absorption spectra of **Pt-1** (black), asymmetric hybrid precursor **1** (grey dashed) and Pt(II)-coordinated phosphonate ester, Pt-PO(OEt)<sub>2</sub>TPY, (blue) in DMF (all 10  $\mu$ M).

prepared for comparison (see 5.4.2), confirming the assignment of the new features to the Pt-TPY complex.

The redox-activity of **Pt-1** was first studied in the exploration of its multifunctionality. Cyclic voltammetry experiments were conducted on a 0.5 mM solution of **Pt-1** in DMF with 0.1 M TBAPF<sub>6</sub> as the electrolyte. In the potential range of +1.0 to -2.25 V (vs. Fc/Fc<sup>+</sup>) five quasi-reversible redox processes were observed from -0.5 to -2.25 V (Fig.86). Processes I, II, IV and V are attributed to W<sup>VI/V</sup> redox couples centred on the POM core and are found to be very slightly negatively shifted relative to those observed in **1**. This indicates some (though very weak) influence on the electronic structure of the POM core by formation of the new Pt-TPY complex. Process III is assigned to a TPY/TPY<sup>-</sup> redox process and has shifted positively due to stabilisation of the TPY radical anion by metal incorporation.<sup>[25-26]</sup> An additional process, an irreversible oxidation, was observed at approximately +0.5 V (Fig.86, Table.16). This could be assigned to the oxidation of Pt<sup>2+</sup> to Pt<sup>3+</sup>, as has been observed for some similar Pt(tpy) complexes in the literature.<sup>[27-29]</sup> Notably, however, the oxidation only appeared once the potential was taken more negative than *ca.* -1.2 V vs. Ag/Ag<sup>+</sup> (or

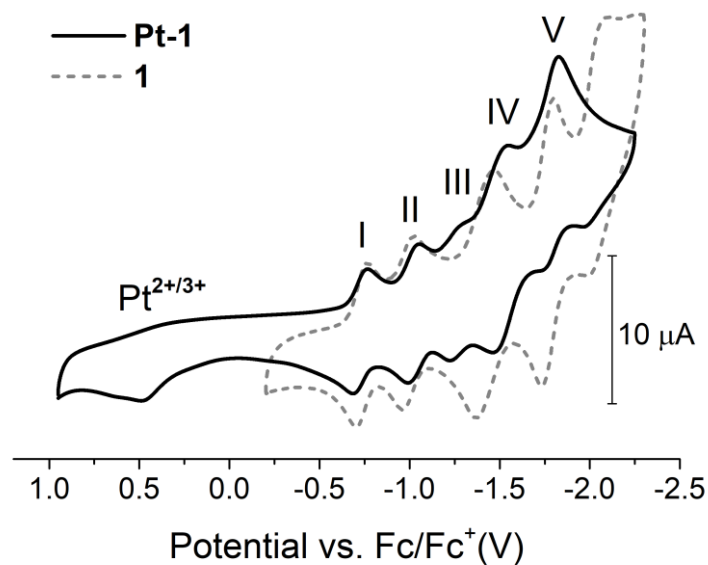


**Figure 86.** Cyclic voltammograms of **Pt-1** (black) and **1** (grey dashed) (both 0.5 mM) in DMF, with 0.1M TBAPF<sub>6</sub> as electrolyte at a glassy carbon working electrode. Scan rate: 100 mVs<sup>-1</sup>.

| Redox potentials vs. Fc/Fc <sup>+</sup> (V) | Pt <sup>2+/3+</sup> | I             | II            | III           | IV            | V             |
|---|---------------------|---------------|---------------|---------------|---------------|---------------|
| E <sub>red</sub>                            | -                   | -0.764        | -1.050        | -1.295        | -1.541        | -1.826        |
| E <sub>ox</sub>                             | <b>+0.476</b>       | -0.688        | -0.998        | -1.227        | -1.475        | -1.737        |
| E <sub>1/2</sub>                            | -                   | <b>-0.726</b> | <b>-1.024</b> | <b>-1.261</b> | <b>-1.508</b> | <b>-1.782</b> |

**Table 16.** Redox potentials of **Pt-1** in DMF.

*ca.* -1.8 V vs. Fc/Fc<sup>+</sup>) on sequential scanning (Fig.87), which could be suggestive that the process arises from a coupling of redox events. For example, in an electrochemical study on the compound [Pt(tpy)Cl]PF<sub>6</sub>, the final irreversible reduction process observed was proposed to be coupled to Cl<sup>-</sup> loss from the triply reduced complex.<sup>[26]</sup>

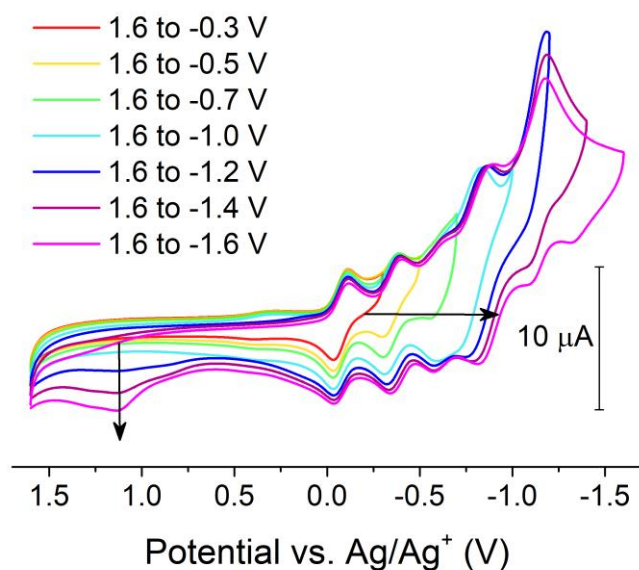


**Figure 87.** Sequential cyclic voltammograms of **Pt-1** (0.5 mM) in DMF on increasing the potential window, starting from +1.6 to -0.3 V (vs. Ag/Ag<sup>+</sup>) (red line) and scanning to more negative potentials from +1.6 V down to -1.6 V (magenta line). Scan rate: 100 mVs<sup>-1</sup>, with 0.1M TBAPF<sub>6</sub> as electrolyte and at a glass carbon working electrode.

### 5.1.3 Solvent-dependent self-assembly of Pt-1

The solvent-dependent self-assembly of **Pt-1** was then studied by dissolving it in a 9:1 (v/v) water–DMF mixture (again, first dissolving in DMF to which was then added water) to prepare a 1.4 mM solution as was carried out for the precursor hybrid POM **1**. DLS experiments indicated the formation of assemblies with a hydrodynamic diameter of approximately 6 nm (Fig.88). Cryo-TEM analysis of the DLS solution when deposited and frozen on a graphene-oxide and holey carbon-supported Cu grid showed spherical structures in good agreement, with diameters of  $6.7 \pm 0.7$  nm (Fig.89a). Interestingly, there are ‘worm-like’ aggregates that are similar in appearance to aggregates reported previously by Piot *et al.*, however, in the case of **Pt-1**, each micellar structure in the “worm” is still clearly visible.<sup>[30]</sup> The spherical assemblies formed by **Pt-1** also differ significantly from the randomly shaped aggregates of the dimeric **Fe-1** derived from **1**. This must be because the micelle-favouring ‘head–tail’ polarity of **1** is retained upon Pt(II) coordination, whereas

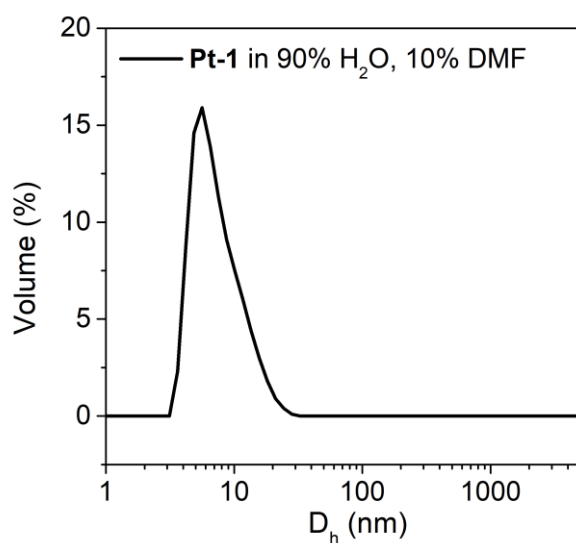


**Figure 88.** Particle-size distribution curves determined by DLS of **Pt-1** (0.7mM) in 90% H<sub>2</sub>O, 10% DMF- D<sub>h</sub> maxima at 5.6 nm (black).

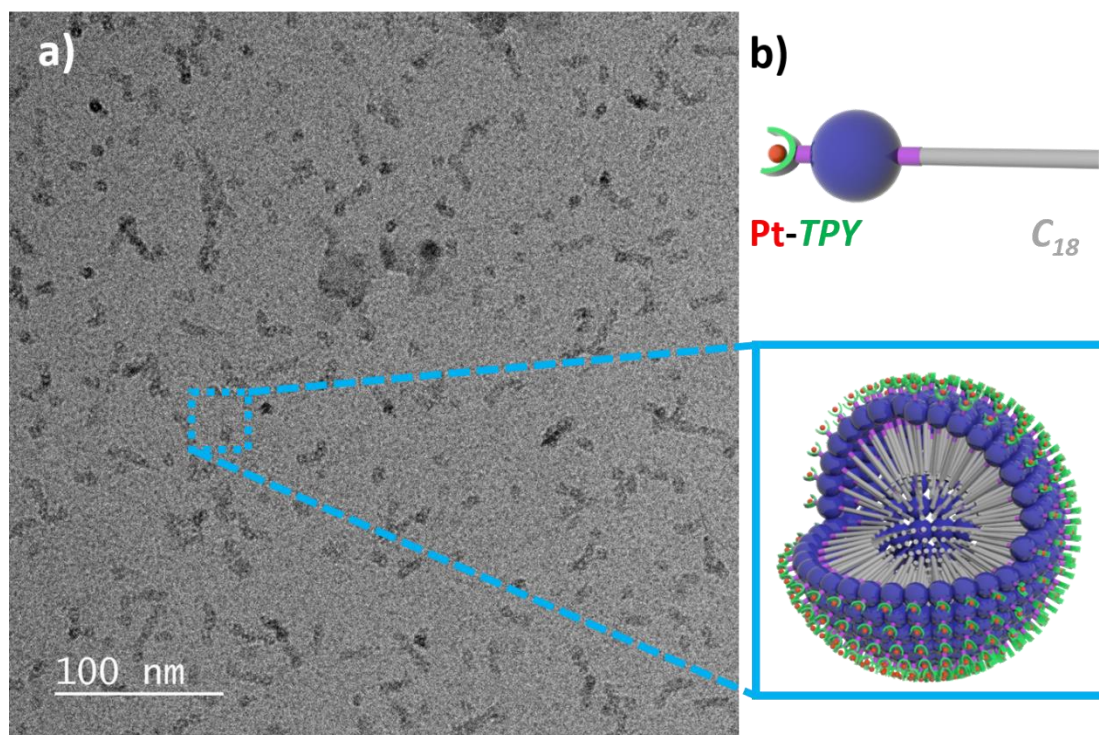


**Figure 89.** a) Cryo-TEM imaging of micellar assemblies of **Pt-1** formed in 1.4 mM water–DMF (9:1 v/v) solution; b) the proposed structure of the micellar assemblies.

formation of the dimeric Fe(II) complex leads to molecules of ill-defined polarity with a reduced driving force to form regular assemblies.

## 5. Transition metal- functionalisation of asymmetric hybrid POMs

Importantly, the structures of the assemblies formed by **Pt-1** constitute a new, entirely unique class of micelles that are essentially surface-decorated (Fig.89b). This surface-decoration is logical as the Pt-coordinated *TPY* sites are likely to be directed outwards from the hydrophobic core (comprised of the interior-facing hydrophobic  $C_{18}$  chains) as a result of the high angle (approx.  $160^\circ$ )<sup>[31]</sup> between the two distinct arylphosphonate ligands.

CV experiments were then conducted on **Pt-1** in a 90% aqueous electrolyte solution to probe its electrochemistry in its supramolecular state. **Pt-1** was found to be insoluble in a  $H_2SO_4$ -DMF mixture as used for **1** and **Fe-1**, and a 9:1 v/v  $H_3PO_4$  (0.1 M)-DMF mixture was instead suitable. CV experiments showed features resemblant of the supramolecular electrochemistry of **1** and **Fe-1**: just two redox processes were observed in the range from +0.5 to -0.5 V (vs. Ag/AgCl) instead of the expected three (Fig.90a). However, beyond the 3<sup>rd</sup> cycle the features of the 2<sup>nd</sup> redox process rapidly became undiscernible beneath the increasing cathodic current and by the 17<sup>th</sup> cycle this current had grown by *ca.* 100  $\mu A$  (Fig.90b). On addition of the same volume of DMF to the electrolyte solution, the cathodic current had returned to the lower intensities observed in the initial three cycles and two redox processes were

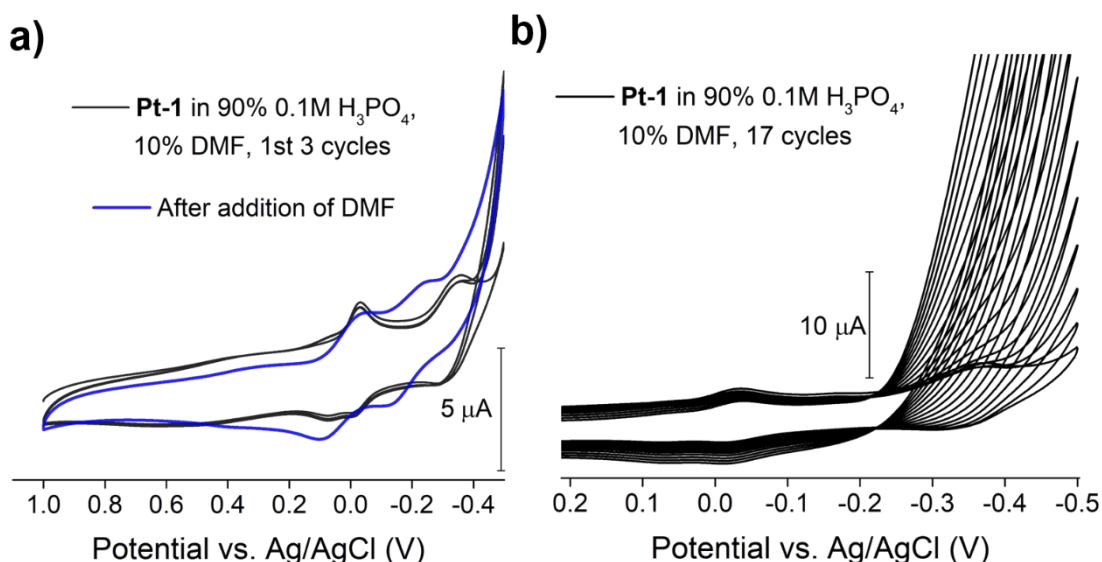


**Figure 90.** a) Overlaid cyclic voltammograms of **Pt-1** (1.4 mM) in 90%  $H_3PO_4$  (0.1 M) 10% DMF for the first 3 cycles (black), and after the addition of the same volume of DMF ( $c_{new} = 0.7$  mM) (blue); b) **Pt-1** (1.4 mM) in 90%  $H_3PO_4$  (0.1 M) 10% DMF over 17 cycles. Scan rate:  $100\text{ mVs}^{-1}$ .

## 5. Transition metal- functionalisation of asymmetric hybrid POMs

discernible again. This suggests disassembly of the micelles into molecular hybrid species in the new mixed solvent. As was observed for the assemblies of **1**, a positive shift in the first redox process was observed which cannot be attributed simply to solvent effects. It appears that this is a result of its separation into the two more closely positioned processes observed in the 50% DMF mixture which had previously been merged. The third redox process expected in this potential window in the DMF mixture is likely swamped by the high current at negative potentials.

**Pt-1** displayed similarly contrasting electrochemistry behaviour in the supramolecular state to the molecular, as observed for the other hybrid POMs discussed previously, but clearly behaves differently at reducing potentials in acidic electrolyte. CV experiments were conducted on **Pt-1** in a reversed composition solvent mixture: 9:1 v/v DMF–H<sub>2</sub>SO<sub>4</sub> (0.1 M) to investigate this further. The POM was dissolved first in DMF with 0.1M TBAPF<sub>6</sub> as electrolyte and to this was added a small volume of 0.1M H<sub>2</sub>SO<sub>4</sub>. Three POM redox processes were seen from +0.5 to -0.5 V (vs. Ag/AgCl) which confirmed that **Pt-1** was in the molecular state, and were stable for many cycles

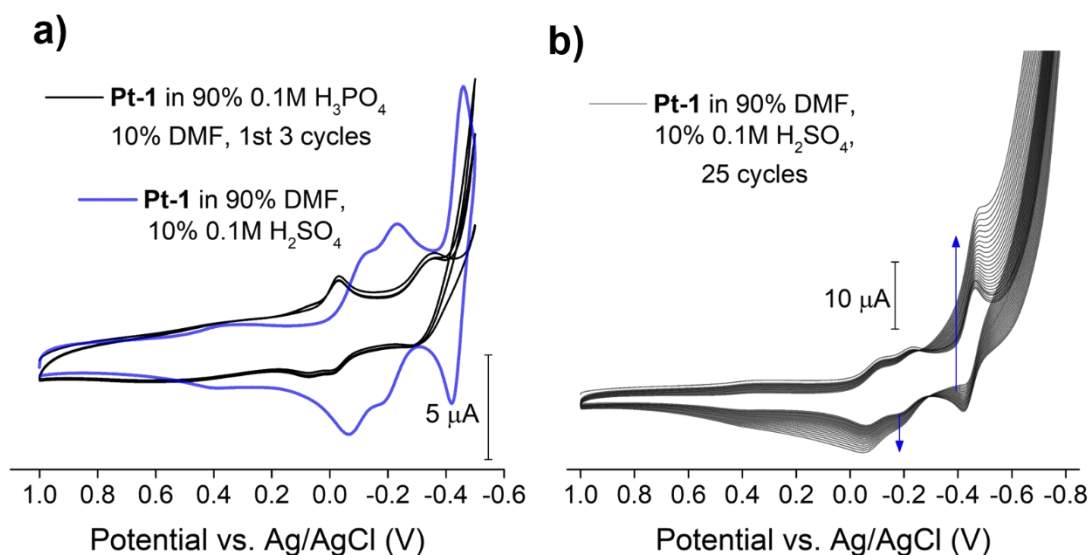


**Figure 91.** a) Overlaid cyclic voltammograms of **Pt-1** (*assemblies*) (1.4 mM) in 90% H<sub>3</sub>PO<sub>4</sub> (0.1 M), 10% DMF (black) and **Pt-1** (*molecular*) (0.5 mM) in 90% DMF, 10% H<sub>2</sub>SO<sub>4</sub> (0.1 M) (blue); b) **Pt-1** in 90% DMF, 10% H<sub>2</sub>SO<sub>4</sub> (0.1 M) scanned to -0.8 V (vs. Ag/AgCl) over 25 cycles, arrows show direction of current growth on cycling. Scan rate: 100 mVs<sup>-1</sup>.

## 5. Transition metal- functionalisation of asymmetric hybrid POMs

---

(Fig.91a). However, once the potential was scanned to -0.8 V, rapidly increasing current was observed over the third reduction process with cycling (Fig.91b), just as was seen in the 90% acid CV experiments.

The high cathodic currents observed in these acidic CV experiments for **Pt-1** in both its molecular and supramolecular forms resemble catalytic currents generated as a result of the hydrogen evolution reaction (HER).<sup>[32]</sup> Even after rinsing the glassy carbon working electrode, high cathodic currents were still observed in fresh electrolyte solution (9:1 v/v 0.1 M H<sub>3</sub>PO<sub>4</sub>-DMF), suggesting deposition of an electrocatalytic species on the electrode surface. Interestingly, the HER electrocatalytic activity of POM-modified electrodes reported in several studies<sup>[33-34]</sup> has now been shown to be due to an activation of the working electrode surface by both the POM and traces of dissolved Pt originating from the counter electrode, as they are co-deposited.<sup>[35-38]</sup> Further electrochemical studies should, therefore, avoid the use of a Pt counter electrode to rule out any catalytic activity due to dissolved Pt that is not derived from the hybrid POM Pt complex. The fact that high cathodic currents were not observed in the acidic CV studies for the other hybrid POMs in this work imply that the effect originated from the presence of the coordinated Pt, but whether the active Pt species was still intact in the *TPY* complex attached to the POM is unclear. Colloidal metal is typically the active catalytic species in the HER, which can be formed by dissociation from the metal complex during the reaction.<sup>[39-40]</sup>

Future studies would focus on the mechanism of the apparent hydrogen evolution, identifying any electrode deposition and the specific nature of the active Pt-containing species through studies using techniques such as SEM and XPS. Investigation of the photo- and electrocatalytic activity of the micellar assemblies of **1** which are effectively “surface-decorated” by Pt(II) active sites is of particular interest, as it can provide insight into how the morphology of the hybrid POM material can be used to tune the activity of the appended transition metal complex.

## 5.2 Preparation of a Ru<sup>II</sup>-functionalised asymmetric hybrid POM

Ruthenium polypyridyl complexes have been combined with POMs in numerous studies, but most often as photoactive cations. Reports of covalently bonded ruthenium complexes in hybrid POMs are fewer,<sup>[41-42]</sup> due to the synthetic challenge in achieving a suitable covalent linkage. In addition to increasing structural stability, covalent interactions enable greater control in the configuration of the hybrid system and tuneability in its electronic structure, which are particularly important in the design of effective charge-transfer materials. The covalent incorporation of a Ru(II) polypyridyl complex into **1** is described in this section.

### 5.2.1 Synthesis of asymmetric hybrid POM [P<sub>2</sub>W<sub>17</sub>O<sub>57</sub>{(Ru<sup>II</sup>TPY)(C<sub>18</sub>)}] (Ru-1)

A postfunctionalisation approach involving the coordination of a Ru(II) centre directly to the tpy site on the TPY ligand group on the asymmetric hybrid **1** was initially considered. Ru(II)-bis(tpy) complexes are typically prepared by the stepwise coordination of two terpyridine ligands to the Ru centre, requiring the reduction of Ru(III) to Ru(II) before the second terpyridine coordination.<sup>[43]</sup> However, the use of a reducing agent in the following step would likely result instead in the reduction of the POM hybrid. Additionally, the reaction of Ru(III) chloride with terpyridine is typically in methanolic or ethanolic solution, in which POM hybrids are highly insoluble. The use of equimolar silver tetrafluoroborate in acetone to dechlorinate the ruthenium trichloride and activate it towards terpyridine coordination, as used for the coordination of Pt(II) to **1** in the preparation of **Pt-1**, could be an alternative method.<sup>[44]</sup> The preparation of the bis(tpy) hybrid complexes, POM(TPY)-Ru<sup>II</sup>(tpy) and POM(TPY)-Ru<sup>II</sup>-(TPY)POM (the latter being a dimeric complex analogous to **Fe-1**), via this postfunctionalisation approach, however, was not considered further in this work. Instead, the design of a phosphonic acid incorporating a heteroleptic {Ru<sup>II</sup>(tpy)(bpy)L} complex was considered, which could be covalently attached to a POM cluster in a one-pot hybridisation reaction, as in the preparation of the hybrid **1**.



## 5. Transition metal- functionalisation of asymmetric hybrid POMs

Suitably, a Ru(II) complex derivative of the ligand **TPY**, **RuTPY**, was designed and prepared.

### 5.2.1.1 Synthesis of RuTPY ligand

The ligand complex, **RuTPY**, was prepared according to the scheme in Fig.92. First, ruthenium (III) chloride was reacted with the substituted-terpyridine phosphonate ester  $\text{PO}(\text{OEt})_2\text{TPY}$  to prepare the ruthenium trichloride complex  $\text{Ru}^{\text{III}}\text{-PO}(\text{OEt})_2\text{TPY}$ . The  $\text{Ru}^{\text{III}}$  centre was then coordinated to 4,4'-dimethyl 2,2'-bipyridine (dmbpy) under reductive conditions using a procedure adapted from literature.<sup>[45]</sup> Finally, the

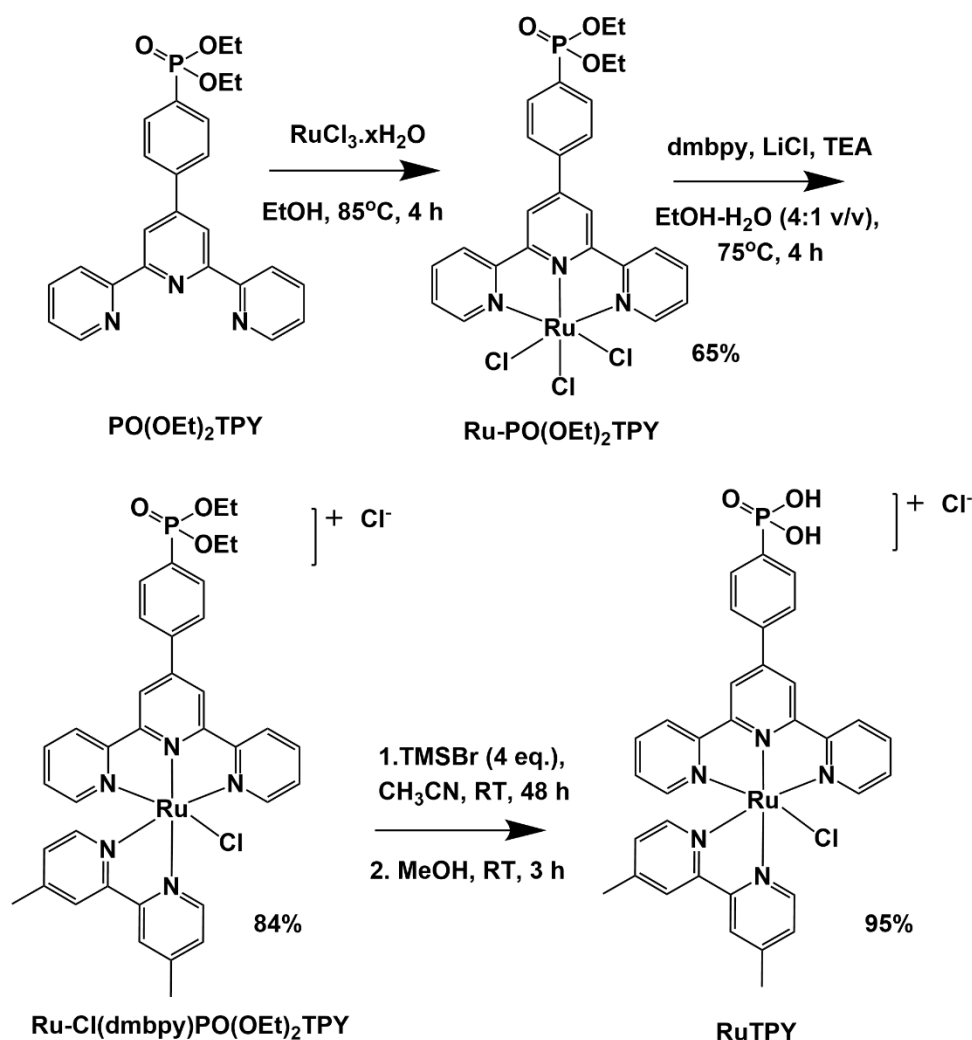


Figure 92. Synthesis of the **RuTPY** ligand.

## 5. Transition metal- functionalisation of asymmetric hybrid POMs

phosphonate ester Ru-Cl(dmbpy)PO(OEt)<sub>2</sub>TPY was hydrolysed via protection with TMSBr, using a similar procedure as used for **TPY**, to prepare the phosphonic acid ligand **RuTPY**.

### 5.2.1.2 One-pot synthesis and purification of Ru-1

The asymmetric POM hybrid  $K_2(C_2H_8N)_3[P_2W_{17}O_{57}\{(PO_3C_{21}H_{14}N_3Ru(C_{12}H_{12}N_2)Cl)\}(PO_4C_{24}H_{41})\}]$ , **Ru-1**, was prepared in a one-pot hybridisation reaction using the same conditions as for the asymmetric POM hybrid **1**; one equivalent of each of  $\{P_2W_{17}\}$ , and phosphonic acids **C<sub>18</sub>** and **RuTPY** in a DMF-CH<sub>3</sub>CN (1:1 v/v) mixture were refluxed overnight in an acid-catalysed condensation reaction (Fig.93). The crude mixture consisted of: the desired

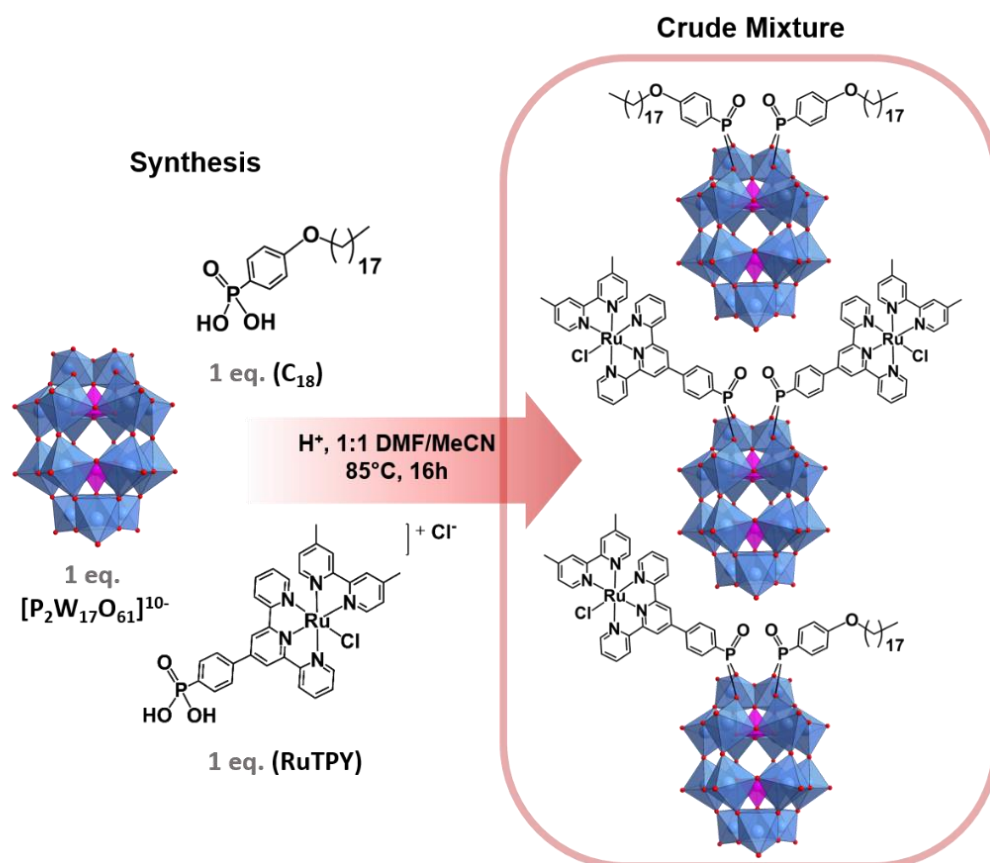


**Figure 93.** One pot synthesis of the asymmetric hybrid-POM, **Ru-1**, and the crude mixture including the symmetric hybrid side-products, **Ru-2** and **3**.

## 5. Transition metal- functionalisation of asymmetric hybrid POMs

asymmetric hybrid, **Ru-1**, the symmetric bis-Ru hybrid, **Ru-2**, and the symmetric  $C_{18}$  hybrid, **3**.

The asymmetric product **Ru-1** was isolated by consecutive solvent extractions, involving precipitations with ether and dissolution in acetone and acetonitrile (Fig.94) as described in more detail in 5.4.2.4. As found for the crude mixture of hybrid products in the preparation of **1**, the addition of excess ether easily precipitated both the Ru-containing hybrids, whilst **3** was left in solution, indicated clearly by the yellow colour of the supernatant above the dark red Ru-containing solids (Fig.95). The solid mixture of **Ru-1** and **Ru-2** was then thoroughly sonicated in acetone to dissolve only the asymmetric hybrid **Ru-1**. Acetonitrile was initially used in this step as used in the

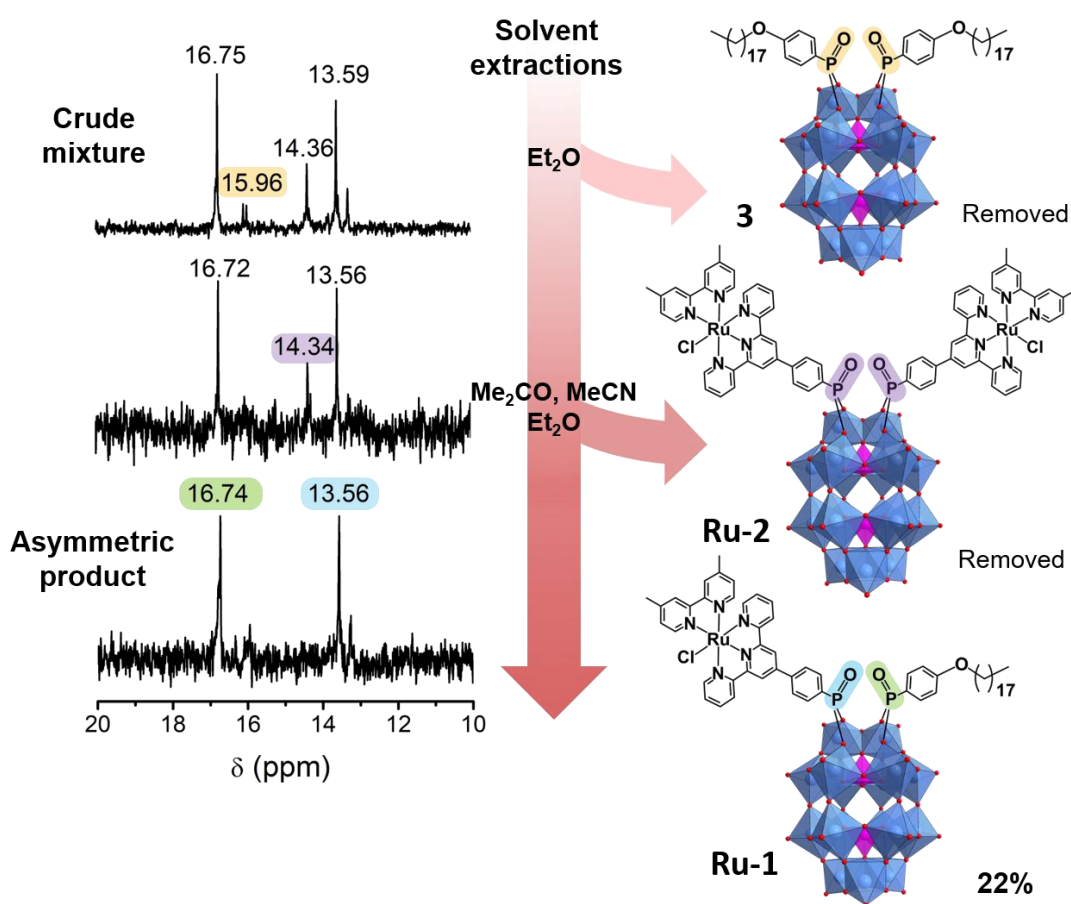


**Figure 94.** Illustration of the purification process of asymmetric hybrid **Ru-1** from the crude mixture. Positive chemical shift region of the  $^{31}\text{P}$  NMR of the reaction mixture in  $\text{DMSO-d}_6$  is shown on the left, taken after each purification step (top: crude; middle **Ru-1** + **Ru-2**; bottom: **Ru-1** only).



**Figure 95.** Photos of the crude mixture in the preparation of **Ru-1** before (left) and after (right) centrifugation following the addition of excess ether, showing the yellow supernatant containing primarily symmetric hybrid POM **3**.

preparation of **1**, but **Ru-2** was found to be slightly soluble in it as indicated by  $^{31}\text{P}$  NMR. The acetone solution was centrifuged to separate the insoluble solid, which was then sonicated in acetone before centrifugation again several more times to ensure the dissolution of all **Ru-1**. The decanted acetone fractions were combined and the solvent was removed *in vacuo* to isolate a solid, which was re-dissolved in minimum acetonitrile and re-precipitated with excess ether to allow any remaining **3** to be removed in the supernatant. The solvent extraction steps were repeated as necessary, starting from the dissolution in acetone step if remaining **Ru-2** was indicated by  $^{31}\text{P}$  NMR, or, if only **3** was remaining, only the dissolution in minimum acetonitrile and re-precipitation with ether steps were repeated.

### 5.2.2 Characterisation of Ru-1

After sufficient purification **Ru-1** was characterised by  $^1\text{H}$  and  $^{31}\text{P}$  NMR, ESI-MS, IR, CHN analysis and TGA. The  $^1\text{H}$  and  $^{31}\text{P}$  NMR spectra of **Ru-1** confirmed a single species. Aromatic peaks in the  $^1\text{H}$  NMR appear downfield shifted from those in **RuTPY**, suggesting successful covalent attachment of the complex, and signals for  $C_{18}$  and **RuTPY** were present in a 1:1 ratio (Fig.96). Signals for both covalently bound ligand

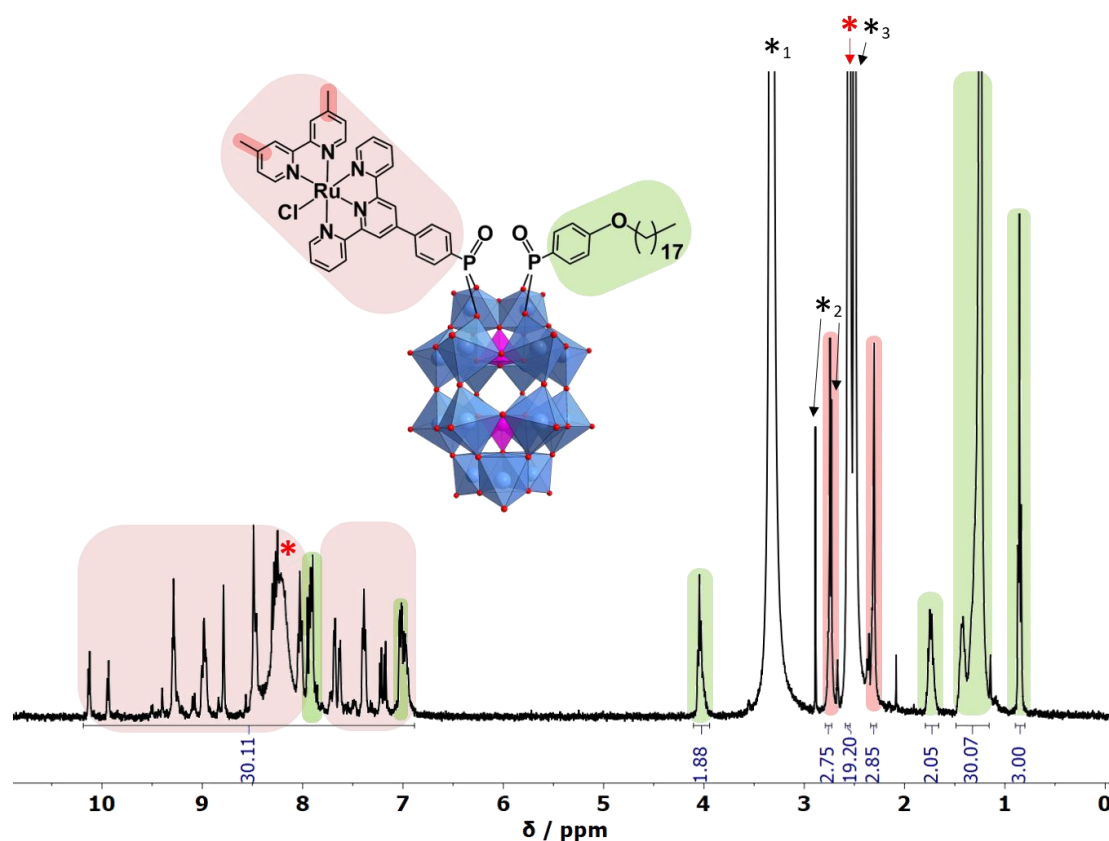


**Figure 96.**  $^1\text{H}$  NMR of **Ru-1** in  $\text{DMSO-d}_6$  showing the assignment of peaks to each ligand: green =  $\text{C}_{18}$ , red =  $\text{RuTPY}$ . Red asterisks indicate DMA cation signals, and black asterisks indicate solvent impurities: 1=  $\text{H}_2\text{O}$ , 2=  $\text{DMF}$ , 3=  $\text{DMSO}$ .

groups,  $\text{RuTPY}$  and  $\text{C}_{18}$ , appear at 13.56 and 16.72 ppm respectively in the  $^{31}\text{P}$  NMR which are not shifted from the signals of  $\text{TPY}$  and  $\text{C}_{18}$  in **1**, indicating no significant electronic influence of the  $\text{Ru}^{2+}$  centre.

The ESI mass spectrum of **Ru-1** confirms the structure of the hybrid POM anion with an overall charge of 5-, due to the 1+ charge of the attached  $\{\text{Ru}^{\text{II}}(\text{dmbpy})\text{Cl}(\text{TPY})\}$  complex. Two peak series for anions with 2- and 3- charges fit closely to assignments as  $[\text{P}_2\text{W}_{17}\text{O}_{57}\{\{\text{RuTPY}\}(\text{C}_{18})\}]^{5-}$  with varying combinations of proton and sodium cations, as commonly seen associated with the other POM hybrids analysed in this work (Fig.97, Table 17).

For comparative studies with **Ru-1**, the symmetric bis(ruthenium) hybrid complex, **Ru-2**,  $[\text{P}_2\text{W}_{17}\text{O}_{57}\{\{\text{RuTPY}\}_2\}]$  a side-product in the one-pot synthesis of **Ru-1**, was

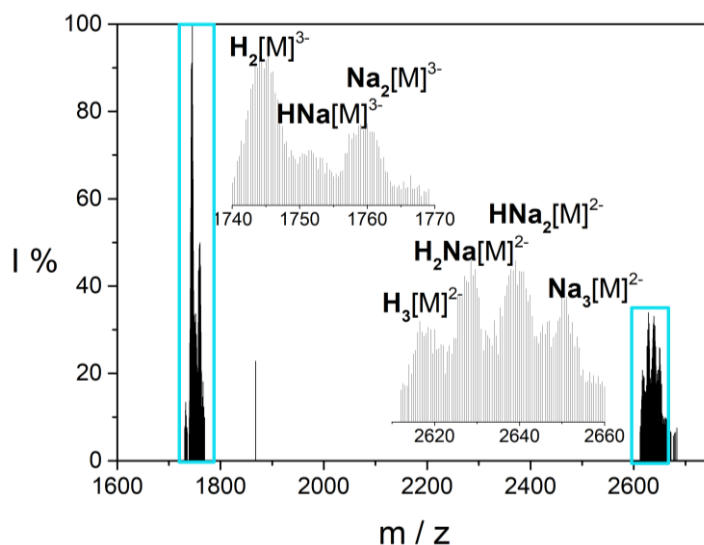


**Figure 97.** Negative mode ESI mass spectrum of **Ru-1** in acetonitrile. [M] =  $[P_2W_{17}O_{57}\{(PO_3C_{21}H_{14}N_3Ru(C_{12}H_{12}N_2)Cl)(PO_4C_{24}H_{41})\}]^{5-}$ .

| Assignment  | z  | m/z (obs.) | m/z (calc.) |
|---|----|------------|-------------|
| $H_2[P_2W_{17}O_{57}\{(PO_3C_{33}H_{26}N_5RuCl)(PO_4C_{24}H_{41})\}]$   | 3- | 1744.7253  | 1744.7226   |
| $HNa[P_2W_{17}O_{57}\{(PO_3C_{33}H_{26}N_5RuCl)(PO_4C_{24}H_{41})\}]$   | 3- | 1752.0547  | 1752.0499   |
| $Na_2[P_2W_{17}O_{57}\{(PO_3C_{33}H_{26}N_5RuCl)(PO_4C_{24}H_{41})\}]$  | 3- | 1759.3756  | 1759.3772   |
| $H_3[P_2W_{17}O_{57}\{(PO_3C_{33}H_{26}N_5RuCl)(PO_4C_{24}H_{41})\}]$   | 2- | 2617.5283  | 2617.5881   |
| $H_2Na[P_2W_{17}O_{57}\{(PO_3C_{33}H_{26}N_5RuCl)(PO_4C_{24}H_{41})\}]$ | 2- | 2628.5323  | 2628.5790   |
| $HNa_2[P_2W_{17}O_{57}\{(PO_3C_{33}H_{26}N_5RuCl)(PO_4C_{24}H_{41})\}]$ | 2- | 2639.5212  | 2639.5700   |
| $Na_3[P_2W_{17}O_{57}\{(PO_3C_{33}H_{26}N_5RuCl)(PO_4C_{24}H_{41})\}]$  | 2- | 2650.4963  | 2650.5610   |

**Table 17.** Selected ESI-MS peak assignments for **Ru-1**.

synthesised exclusively in a separate reaction to ensure high purity.  $K_{10}[P_2W_{17}O_{61}]$  and two molar equivalents of **RuTPY** were reacted in an acid-catalysed condensation in DMF. The hybrid POM product was isolated from solution by precipitation with ether and was characterised once adequately dried by NMR, ESI-MS, IR, elemental (CHN) analysis and TGA (details in 5.4.2.5).

The UV-Vis absorption spectra of **RuTPY**, **Ru-1** and **Ru-2** showed bands characteristic of  $\{Ru^{II}(bpy)(tpy)\}$  complexes, with absorptions assigned to IL tpy and bpy  $\pi-\pi^*$  transitions in the UV region (<350 nm) and a broad  $^1MLCT$   $d\pi-\pi^*$  band centred at *ca.*

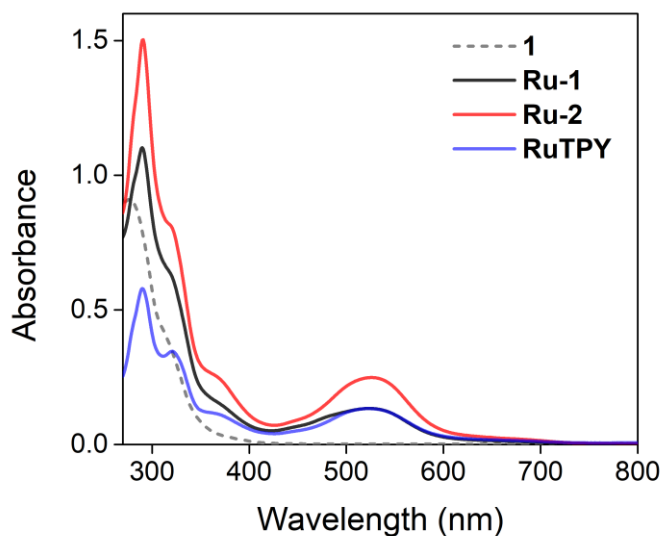


**Figure 98.** Absorption spectra of: **Ru-1** (black), **Ru-2** (red), **1** (grey dashed) and **RuTPY** (blue) in DMF (all 10  $\mu\text{M}$ ).

525 nm (Fig.98).<sup>[43, 46]</sup> As can be expected, the absorbance of the MLCT band is roughly twice as intense in the bis(*RuTPY*) hybrid, **Ru-2**, than in **Ru-1**.

Cyclic voltammetry experiments were conducted on a solution of **Ru-1** in DMF with 0.1 M TBAPF<sub>6</sub> as the electrolyte to study its redox activity. In the potential range of +0.7 to -2.3 V (vs. Fc/Fc<sup>+</sup>) five quasi-reversible POM redox processes were observed from -0.5 to -2.25 V as well as a Ru<sup>2+/3+</sup> process at approximately +0.34 V (Fig.99a, Table.18). The potentials of the POM redox processes were slightly negatively shifted from those in **1** (processes I and II by 45 mV and 54 mV respectively) indicating the cluster is only very weakly influenced electronically by the Ru<sup>2+</sup> complex.

Weak electronic communication between the Dawson anion and appended *RuTPY* can also be deduced from the comparable  $E_{1/2}$  values for the Ru<sup>2+/3+</sup> redox process in **Ru-1** and the free complex **RuTPY**, in which it was observed at +0.32 V vs. Fc/Fc<sup>+</sup> in both (Fig.99b). This process was also observed at the same potential in the bis(ruthenium) hybrid **Ru-2**, but notably alongside a second process, which could be

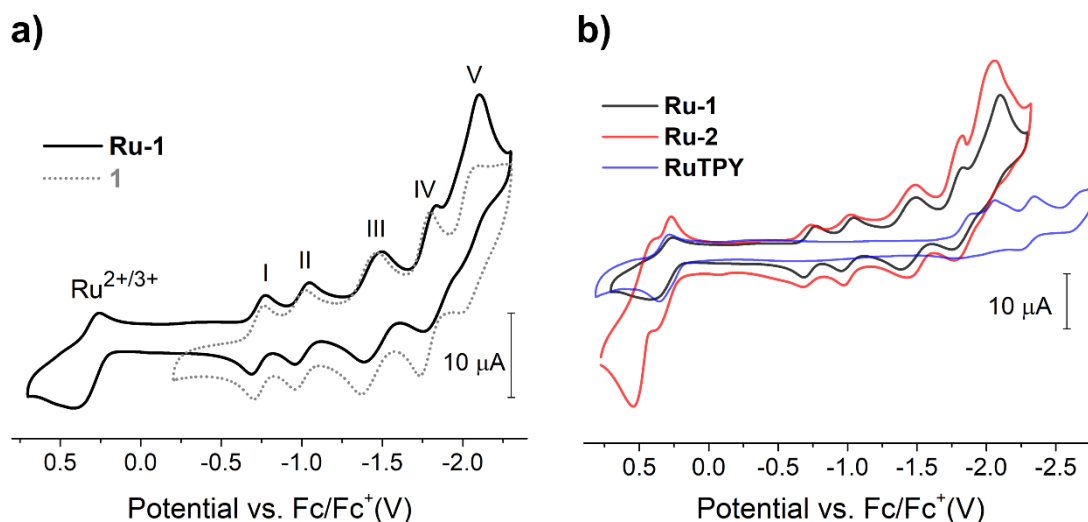


**Figure 99.** a) Overlaid cyclic voltammograms of **Ru-1** and **1**; b) **Ru-1**, **Ru-2** and **RuTPY** (all 0.5 mM) in DMF, with 0.1M TBAPF<sub>6</sub> as electrolyte. Scan rate: 100 mVs<sup>-1</sup>.

| Redox potentials vs. Fc/Fc <sup>+</sup> (V) | Ru <sup>2+/3+</sup> | I             | II            | III           | IV            | V      |
|---|---------------------|---------------|---------------|---------------|---------------|--------|
| E <sub>red</sub>                            | +0.264              | -0.774        | -1.043        | -1.486        | -1.832        | -2.101 |
| E <sub>ox</sub>                             | +0.407              | -0.689        | -0.959        | -1.395        | -1.760        | -      |
| E <sub>1/2</sub>                            | <b>+0.336</b>       | <b>-0.732</b> | <b>-1.001</b> | <b>-1.441</b> | <b>-1.796</b> | -      |

**Table 18.** Redox potentials of **Ru-1** in DMF.

indicative of electronic communication between the two Ru<sup>2+</sup> centres, or, of a Ru-based impurity (Fig.99b).

### 5.2.3 Multifunctionality of Ru-1

#### 5.2.3.1 Solvent-dependent self-assembly of Ru-1

The solvent-dependent self-assembly of **Ru-1** into micelles like those formed by **Pt-1** is expected due to its similar amphiphilic structure: the C<sub>18</sub> group as the hydrophobic tail and the POM core and *RuTPY* group as the polar head-group. This was investigated similarly by dissolving it in a 9:1 (v/v) water–DMF mixture to prepare a 1.4 mM solution. DLS experiments indicated the formation of assemblies with a hydrodynamic diameter of approximately 6 nm (Fig.100). Cryo-TEM analysis of the solution when



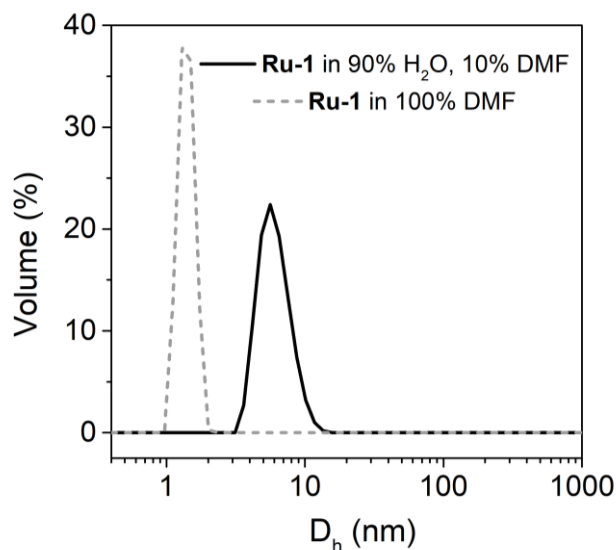


**Figure 100.** Particle-size distribution curve determined by DLS of: **Ru-1** (1.4 mM) in 90% H<sub>2</sub>O, 10% DMF- $D_h$  maximum at 5.6 nm (black) and in 100% DMF,  $D_h$  maximum at 1.3 nm (grey dashed) (suggesting discrete molecular species only under these conditions).

deposited and frozen on a graphene-oxide and holey carbon-supported Cu grid showed spherical structures in good agreement, with diameters of *ca.* 6.7 nm resembling the micelles formed by **1** and **Pt-1**, and with impressively high monodispersity (Fig.101).

The electrochemical behaviour of the assemblies formed by **Ru-1** was then studied. As found for **Pt-1**, the 0.1 M H<sub>2</sub>SO<sub>4</sub>-DMF (9:1, v/v) solvent mixture was not compatible with **Ru-1**, resulting in precipitation on the addition of acid to the DMF fraction, and a 0.1 M H<sub>3</sub>PO<sub>4</sub>-DMF (9:1, v/v) mixture was instead used. DLS measurements confirmed that nanoscale assemblies are formed in this mixture with a  $D_h$  of 10 nm (Fig.102). Two Dawson-based redox processes were observed from -0.5 to 0.5 V (vs. Ag/AgCl) as was seen for **1**, which are a result of the coalescing of the first two of the three redox processes in this potential window (Fig.103a). Additionally, as was observed for the Fe<sup>2+/3+</sup> redox process in **Fe-1**, the Ru<sup>2+/3+</sup> redox process appeared to be indiscernible in the CV. Further confirming this, DPV experiments performed on the solution showed no clear peak observed at positive potentials indicative of the Ru<sup>2+/3+</sup> process (Fig.103b). However, upon the addition of the same volume of DMF to the CV solution,

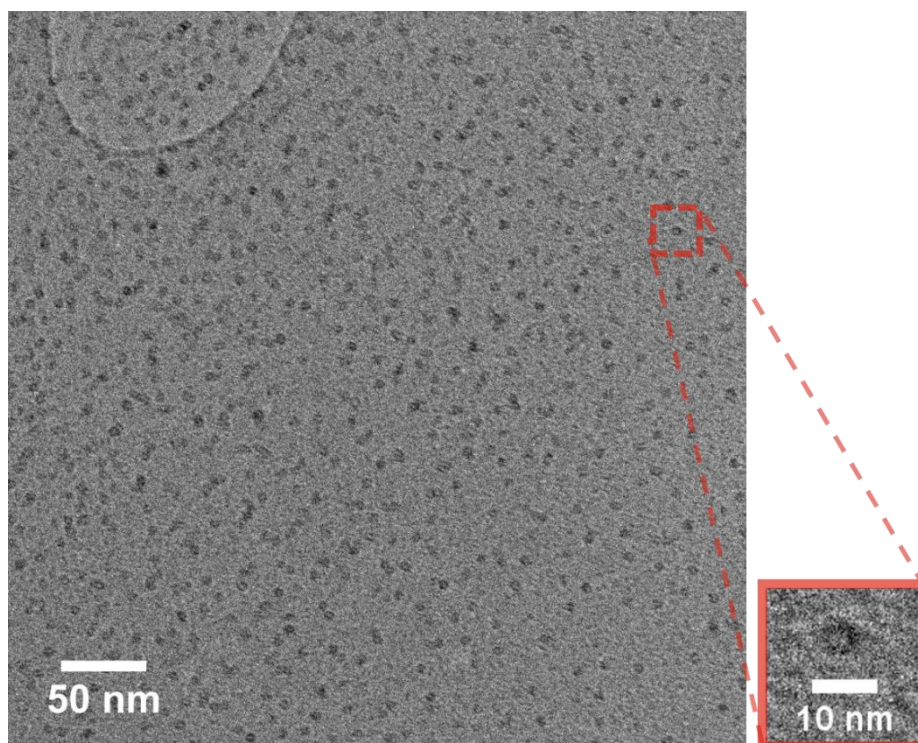


**Figure 101.** Cryo-TEM imaging of micellar assemblies of **Ru-1** formed in 1.4 mM water–DMF (9:1 v/v) solution.

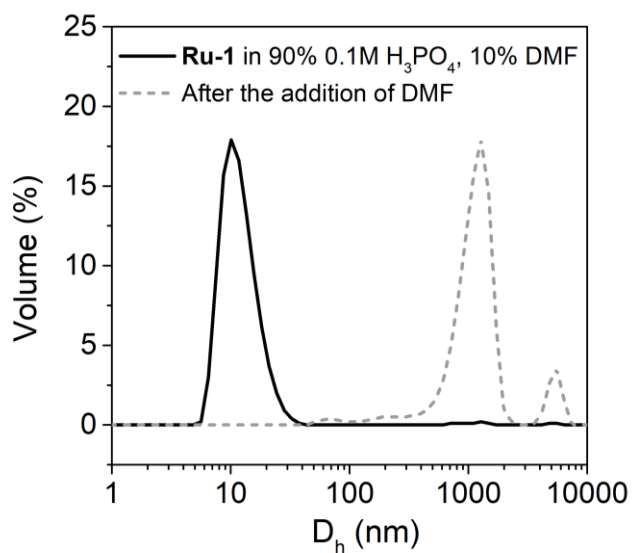


**Figure 102.** Particle-size distribution curve determined by DLS of: **Ru-1** (1.4 mM) in 90%  $\text{H}_3\text{PO}_4$  (0.1M), 10% DMF,  $D_h$  maxima at 10.1 nm (black), and the solution of **Ru-1** after the addition of the same volume of DMF ( $c_{\text{new}} = 0.7$  mM),  $D_h$  maxima at 1280 nm (grey dashed).

the molecular redox behaviour of **Ru-1** is recovered and the reversible  $\text{Ru}^{2+/3+}$  process

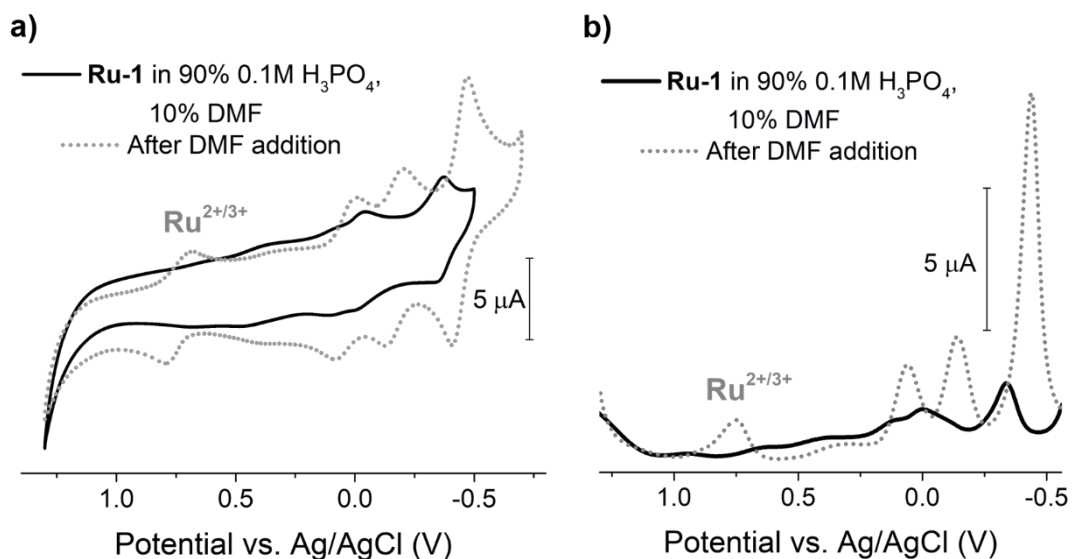


**Figure 103.** a) Overlaid cyclic voltammograms and b) differential pulse voltammograms of **Ru-1** (1.4 mM) in 90% 0.1M H<sub>3</sub>PO<sub>4</sub>, 10% DMF before (black) and after the addition of the same volume of DMF ( $c_{\text{new}} = 0.7$  mM) (dashed). Scan rate: 100 mVs<sup>-1</sup>.

became clearly visible in both DPV and CV scans (Fig.103a,b).

As observed for **Fe-1**, the peak currents were seen to increase after the addition of DMF due to the change from slow diffusing supramolecular aggregates to fast-diffusing molecular species, and this was again more prominent for the redox couple of the coordinated transition metal. This similarly suggests that the *RuTPY* complex in the assembly is hindered in some way from the electrode supramolecularly. The *RuTPY* sites could be orientated so that they are largely in the same plane as the POM clusters in the micelles, rather than protruding outwards into solution. In this case, the POM clusters could primarily serve as the “head” groups and may be more easily reduced with better contact with the electrode, whereas the Ru<sup>II</sup> sites may only be reduced through an indirect electrical contact.

### 5.2.3.2 Photochemistry

#### 5.2.3.2.1 Photoluminescence

The photoluminescence of the Ru hybrid POM complexes at room temperature was then investigated. Intense emission by  $[\text{Ru}(\text{bpy})_3]^{2+}$  complexes is typically observed in the 500-600 nm range due to radiative relaxation of the  $^3\text{MLCT}$  excited state. In comparison,  $[\text{Ru}(\text{tpy})_2]^{2+}$  complexes typically display much weaker emission due to internal conversion from the  $^3\text{MLCT}$  state to a nearby triplet metal-centred ( $^3\text{MC}$ ) state, which then leads to non-radiative decay to the ground state.<sup>[3]</sup> Heteroleptic ruthenium complexes with both tpy and bpy ligands, however, can exhibit emission that is still weaker than the strongly emissive tris(bpy) derivative but stronger than those of bis(tpy).<sup>[12, 47]</sup> Although they are not as effective photosensitisers as tris(bpy)-based Ru complexes, they can be used as catalysts or co-catalysts in photocatalytic systems for the oxidation of water or organic substrates due to their ability to facilitate charge transfer or to undergo photoinduced ligand substitution.<sup>[48-50]</sup> The heteroleptic phosphonate ligand **RuTPY** was expected to display at least weak

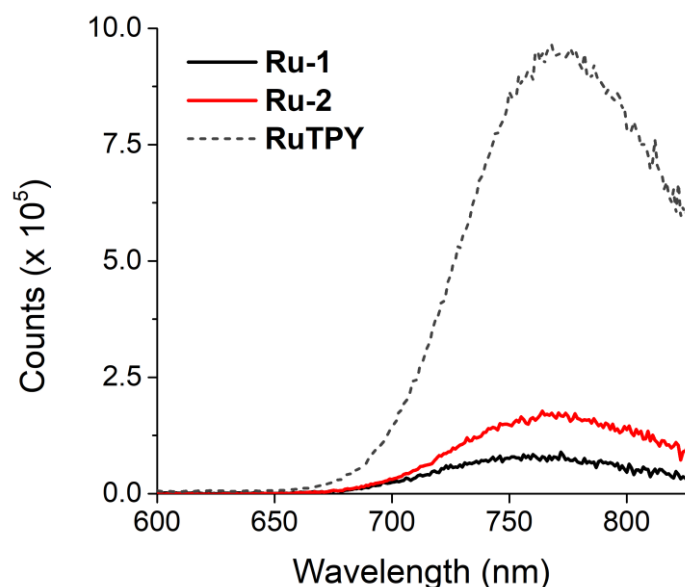


**Figure 104.** Overlaid emission spectra of POM hybrids **Ru-1** (solid black) and **Ru-2** (red) and ligand **RuTPY** (dashed) obtained using an excitation wavelength of 500 nm in DMF (all 10  $\mu\text{M}$ ).

photoluminescence. On excitation of the dominant  $^1\text{MLCT}$  transition using a wavelength of 500 nm at RT, a broad emission peak is observed for **RuTPY** centred at *ca.* 775 nm (Fig.104).

The emission intensities of the hybrids **Ru-1** and **Ru-2** at the same concentration were comparatively much lower, indicating a quenching effect of the POM core. By comparing the area under the emission peaks, the emission intensity of the dinuclear symmetric hybrid **Ru-2** is determined to be approximately double ( $= 2.016 \times$ ) that of the mono-nuclear asymmetric hybrid **Ru-1**. This is expected, as **Ru-2** displays twice the intensity in absorbance corresponding to the  $^1\text{MLCT}$  transition at 525 nm than the mono-nuclear asymmetric hybrid **Ru-1**.

Luminescence is possibly quenched by rapid intramolecular electron transfer from the Ru-MLCT excited state to the POM core in a charge-separated state, before back-transfer (or charge-regeneration) from the POM to the metal complex, such as that observed in a  $\text{Re}^{\text{I}}(\text{bpy})$  functionalised Dawson-type hybrid reported by Hasenknopf *et al.*<sup>[51]</sup> An energy level diagram which can rationalise the thermodynamic driving force can be constructed from the potentials of relevant redox processes and wavelengths of observed radiative bands. HOMO and LUMO energies can be approximated from the oxidation and reduction potentials (vs.  $\text{Fc}/\text{Fc}^+$ ) as shown in the equations:

$$E_{\text{HOMO}} (\text{eV}) = -5.1 - E_{\text{ox}}$$

$$E_{\text{LUMO}} (\text{eV}) = -5.1 - E_{\text{red}}$$

in which potentials are related to the energy level of ferrocene/ferrocenium below vacuum on the Fermi Scale (5.1 eV).<sup>[52]</sup> The wavelengths of absorption and emission of the  $^1\text{MLCT}$  and  $^3\text{MLCT}$  excited states can then be converted to eV according to:

$$E_g (\text{eV}) = \frac{1240}{\lambda}$$

Considering the *RuTPY* complex and Dawson anion in **Ru-1** to be separate molecules, the HOMO energy is approximated from the  $E_{1/2}$  of the  $\text{Ru}^{2+/3+}$  process in *RuTPY* and the energy of the LUMO, *RuTPY*\*  $^1\text{MLCT}$ , can be estimated by considering the energy gap,  $E_g$ , that is taken from the wavelength of the Ru  $^1\text{MLCT}$  absorption (Fig.105). The

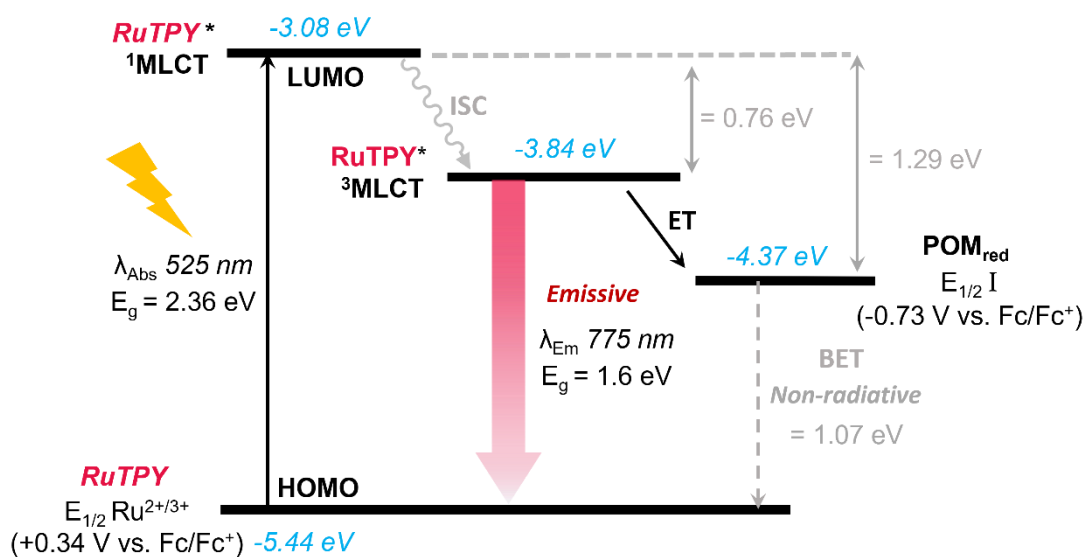


**Figure 105.** Energy level diagram for Ru-1, approximated from redox potentials (vs. Fc/Fc<sup>+</sup>) and wavelengths of absorbance and emission.

LUMO of the POM, estimated from the first POM-based redox process  $E_{1/2}$ , is found to be lower in energy than the  $^3\text{MLCT}$  state by approximately 0.5 eV, which is a sufficient driving force for electron transfer (ET) from the radiative  $^3\text{MLCT}$  state to the POM. This can explain the observed quenching in emission in the Ru hybrid POMs because of the resulting non-radiative back-electron-transfer (BET) from the reduced POM to the ground state.

### 5.2.3.2.2 Spectroelectrochemistry

Spectroelectrochemistry experiments were then conducted to study the photoredox properties of the hybrid POM complexes. UV-Vis absorption spectra were recorded after every 2 min whilst potentials were applied to solutions of the hybrids in DMF with 0.1 M TBAPF<sub>6</sub> as electrolyte.

First, the non-Ru -complexed asymmetric hybrid POM **1** was studied. During bulk electrolysis at the 1<sup>st</sup>, 2<sup>nd</sup> and then 3<sup>rd</sup> POM-based reduction potentials (-0.39, -0.70 and -1.13 V vs. SCE, respectively), three new bands at *ca.* 830, 675 and 665 nm, respectively, are seen to grow sequentially (Fig.106). These are assigned to the characteristic IVCT or d-d transitions that occur between reduced  $d^1$  W centres and  $d^0$

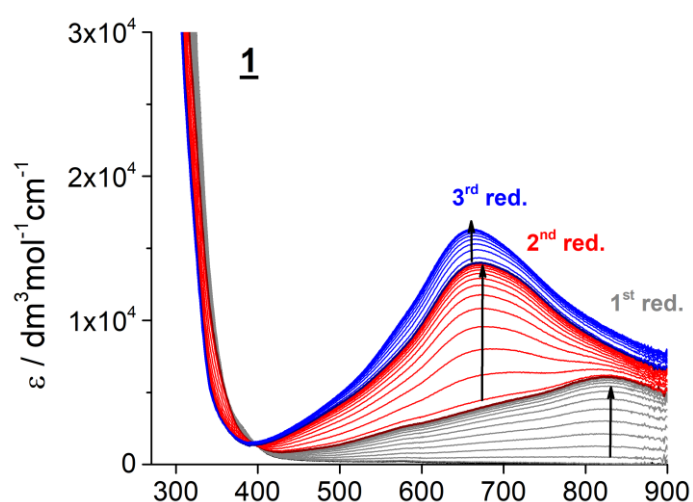


**Figure 106.** Absorption spectra of **1** in DMF during electrolysis at the 1<sup>st</sup>, 2<sup>nd</sup> and 3<sup>rd</sup> POM-based reduction potentials. Data is shown at 2 min intervals.

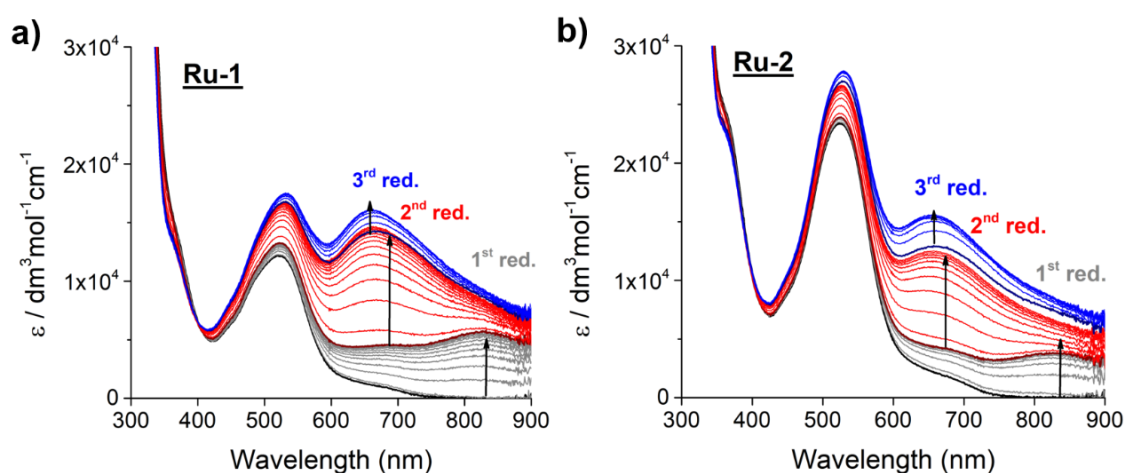


**Figure 107.** Absorption spectra of **a) Ru-1** and; **b) Ru-2** in DMF during electrolysis at the 1<sup>st</sup>, 2<sup>nd</sup> and 3<sup>rd</sup> POM-based reduction potentials. Data is shown at 2 min intervals.

W centres in the POM cluster.<sup>[53]</sup> The fourth POM reduction proved to be difficult to probe by spectroscopy so was not studied in the following experiments on the Ru-complexed hybrid POMs.

The POM-based reductions in **Ru-1** and **Ru-2** were probed similarly by bulk electrolysis at the first three reduction potentials. In both hybrid POMs, the sequential growth of the three bands seen in **1** were also observed (Fig.107a,b). The Ru<sup>2+/3+</sup> oxidation

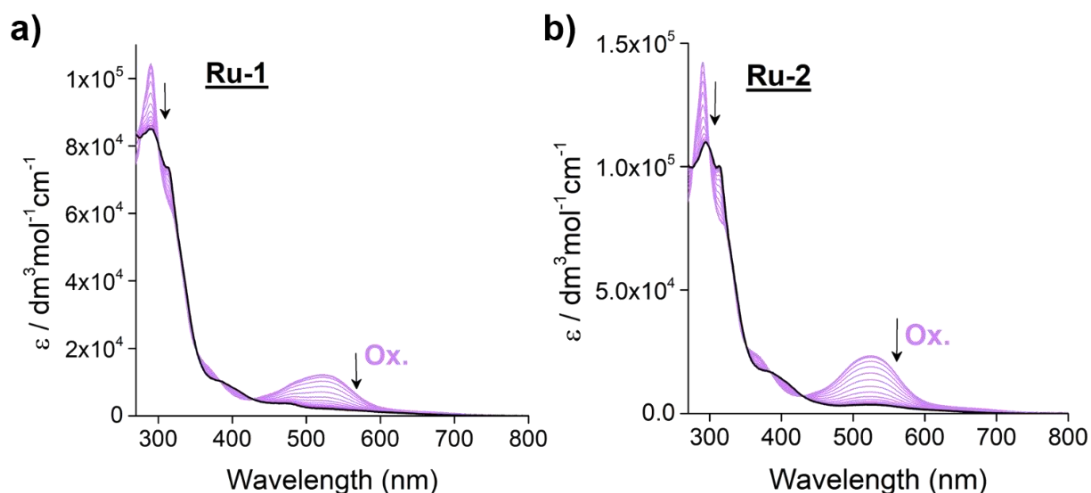


**Figure 108.** Absorption spectra of **a) Ru-1** and **b) Ru-2** in DMF during electrolysis at the Ru-based oxidation potential. Data is shown at 2 min intervals.

processes in **Ru-1** and **Ru-2** were then investigated by bulk electrolysis of the solutions at *ca.* +0.90 vs. SCE, which resulted in a decrease in intensity of the <sup>1</sup>MLCT band at 525 nm in both, as well as a decrease in the IL  $\pi$ - $\pi^*$  band at 290 nm and emergence of a new shoulder at 310 nm (Fig.108). The results of these experiments confirm the successful combining of the redox- and photo-active Dawson POM and *RuTPY* components in the Ru<sup>II</sup>-functionalised hybrid POMs.

An additional oxidative process is observed in the CV of **Ru-2** which may be suggestive of communication between the two *RuTPY* units. However, the full reduction in the MLCT band in **Ru-2** that is approximately twice the intensity in **Ru-1** suggests that both Ru centres are oxidised at the first potential. Additionally, the positions of the new bands in both hybrids after oxidation are the same, suggesting no mixed valence species in **Ru-2**.

### 5.2.3.2.3 Photoreduction studies

The photoredox activity of the hybrids and visible-light sensitisation of the appended Ru<sup>II</sup> complexes was further investigated by charge photoaccumulation studies. Photoreduction of the hybrid POMs was monitored by UV-Vis absorption



## 5. Transition metal- functionalisation of asymmetric hybrid POMs

spectroscopy as their reduced forms can be identified by the emergence of intense IVCT and d-d transitions, as previously probed by spectroelectrochemical analysis.

In charge photo-accumulation studies, a sacrificial electron donor is often necessary to rapidly quench the charge-separated state and reduce charge recombination.<sup>[51]</sup> The ground state of the photosensitiser can then be regenerated, and consecutive photo-induced processes are made possible. In these experiments, triethylamine (TEA) is included in large excess (800 eq.) as a stronger sacrificial electron donor than the solvent (DMF). The solutions were prepared with dry and degassed DMF in the absence of oxygen to prevent the re-oxidation of the reduced species generated throughout the experiments. A 455 nm cut-off filter was used in front of a Hg-Xe lamp to investigate exclusively the photoexcitation of the MLCT transition centred on the *RuTPY* complex unit. After continuous irradiation for 22 h, the generation of the  $1e^-$  reduced species was observed in both Ru hybrids by the emergence of the new band at 828 nm, suggesting the successful visible-light sensitisation of the *RuTPY* unit and intramolecular electron transfer to the POM (Fig.109a). The band intensity was

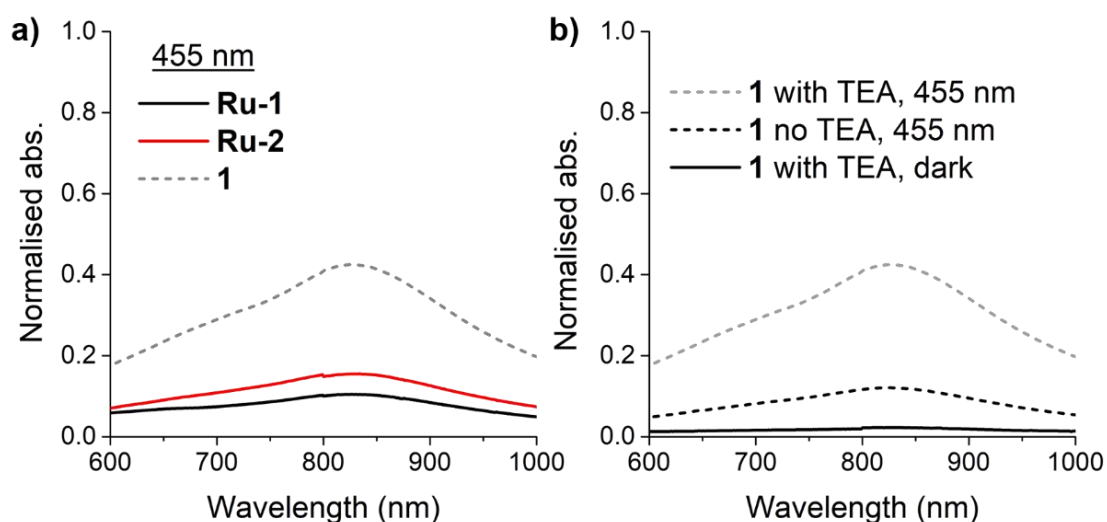


**Figure 109.** Absorbance spectra focused on the  $1e^-$  reduction band of: **a)** Ru-1, Ru-2 and 1 after irradiation (>455 nm) for 22 h (all 100  $\mu$ M in DMF with TEA); **b)** 1 after 22h irradiation (>455 nm) with and without TEA and after 22 h in the dark with TEA (all 100  $\mu$ M in DMF). All normalised by subtraction of the absorbance spectra before each experiment.

## 5. Transition metal- functionalisation of asymmetric hybrid POMs

---

approximately 1.5x higher in the symmetric hybrid **Ru-2** than in **Ru-1**, as could be expected with an extra Ru<sup>II</sup> complex.

Surprisingly, however, the non-complexed asymmetric hybrid **1** was also reduced by >455 nm light, displaying an absorbance band even more intense than that of both the Ru-containing hybrids (Fig.109a). The electron-donor role of TEA was then investigated to further understand this. An identical solution of **1** was left in complete darkness over the same period of time, after which the generation of the 1e<sup>-</sup> reduced species was not observed, confirming that electron-donation by TEA (or DMF) only occurs after photoreduction of the POM (Fig.109b). Another solution of **1** was irradiated in the absence of TEA. After 22 h, the 1e<sup>-</sup> reduction band emerged, although to a much lower intensity than in the experiment with TEA (Fig.109b), reaffirming that TEA is a stronger sacrificial electron-donor than DMF. Interestingly, **1** can undergo comparable photoreduction with only DMF to that of the Ru-complexed hybrids in combination with an additional electron donor, suggesting that electron transfer is influenced by the Ru complexes such that charge accumulation on the POM is significantly hindered.

Photoreduction experiments were then conducted using a 395 nm cut-off filter, to investigate the rates of reduction in the three hybrids more closely. A two-step 2e<sup>-</sup> reduction was observed for the asymmetric hybrids **1** and **Ru-1**. For **1**, the peak maximum for the first 1e<sup>-</sup> reduction was reached after *ca.* 30 min ( $\tau = 300$  s), after which the 2e<sup>-</sup> reduction began to occur, characterised by a shoulder centred at *ca.* 680 nm (Fig.110,111a). This reduction was slower (exponential decay  $\tau = 2275$  s, Fig.111b) and appeared to reach saturation after a total of 4 h irradiation time. A blue colour change in the solution was observed indicative of the reduced POM species, which became darker after the 2<sup>nd</sup> reduction (Fig.112).

In comparison, the 1e<sup>-</sup> reduction in **Ru-1** was slower ( $\tau = 698$  s), reaching saturation after approximately 1 h (Fig.113a,111a). On the other hand, the 2e<sup>-</sup> reduction appeared to occur at a comparable rate ( $\tau = 2450$  s) to in **1**, saturating after 5 h (Fig.111b). A corresponding change in colour of the solution from red to purple was observed due to the blue tinge of the reduced species (Fig.112). Only the 1e<sup>-</sup> reduction

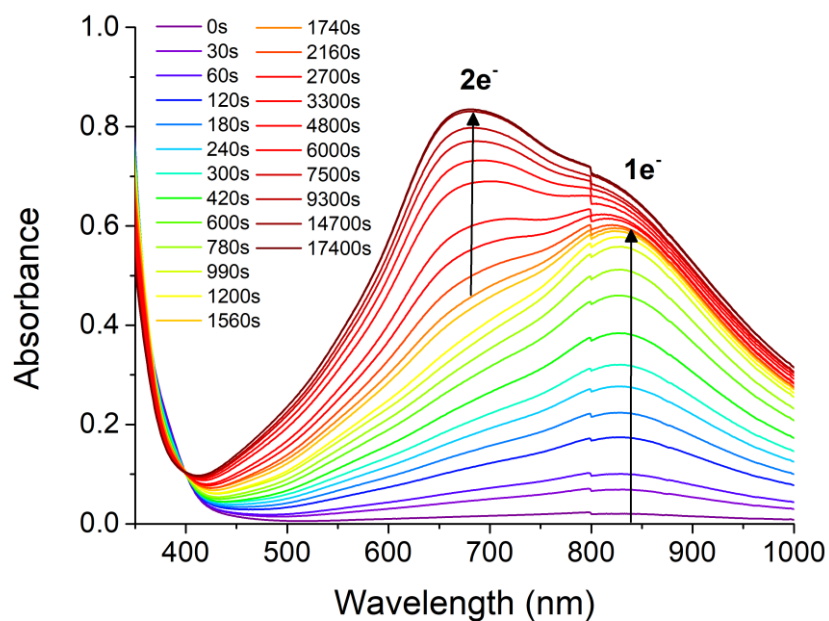


**Figure 110.** Absorbance spectra during the photoreduction experiment of **1** (100  $\mu\text{M}$  in DMF) using a 395 nm cut-off filter.

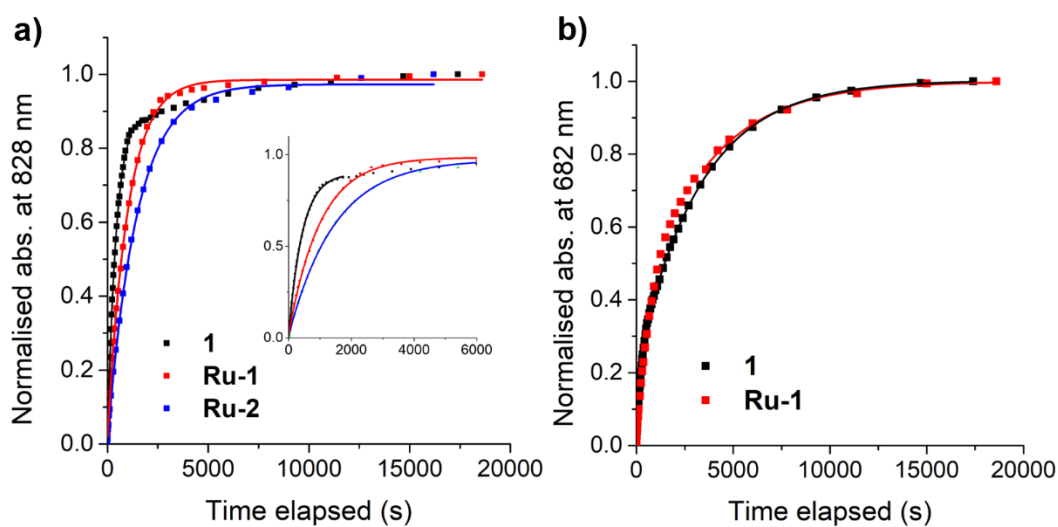


**Figure 111.** Rate plots and exponential decay fitting of: **a)** the increase in the band at 828 nm for the  $1e^-$  reduction in **1**, **Ru-1** and **Ru-2**, fit until band saturation at 1740 s for **1** and for the full timescale for **Ru-1** and **Ru-2**); **b)** the increase in the band at 682 nm for the  $2e^-$  reduction in **1** and **Ru-1**, fit from the band onsets at 1200 s for **1** and 3600 s for **Ru-1**.

was observable in a similar timescale for **Ru-2**, which saturated after 4.5 h at the

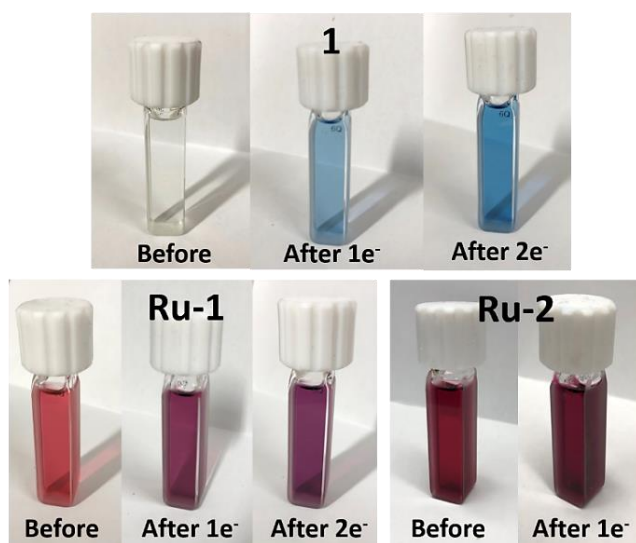


**Figure 112.** Photos showing the changes in colour of the solution of **1**, **Ru-1** and **Ru-2** after photoreduction with  $>395$  nm light.

slowest rate in comparison to the other hybrids ( $\tau = 1015$  s, Fig.113b,111a).

The unexpected reverse trend in the ease of photoreduction with  $>395$  nm light with increasing numbers of Ru complex units provides interesting information on the charge transfer processes in these hybrid POM systems. In the case of  $>395$  nm irradiation, the Dawson POM and Ru chromophore can both be photoexcited, and if they occur on the same timescale then there could be competing processes. For example, the excited electron centred on the POM (LMCT) could compete with the sacrificial electron donor, TEA, in quenching the hole generated on the excited Ru complex. The quenching of two Ru excited states in the **Ru-2** by the photoexcited electrons of the POM cluster will slow charge accumulation on the cluster more so than in **Ru-1** and could explain its slower  $1e^-$  reduction and inaccessible  $2e^-$  reduction. The use of a highly monochromatic light source would be ideal in future studies to prevent both excitations taking place simultaneously.

From the  $>455$  nm irradiation experiments, it is obvious that the hybrid POMs can be photoreduced to some extent without the combination of a photosensitising unit or additional electron donor. Several studies by Hill *et al.* have reported the enhancement of the visible light absorption of POMs in certain organic solvents,

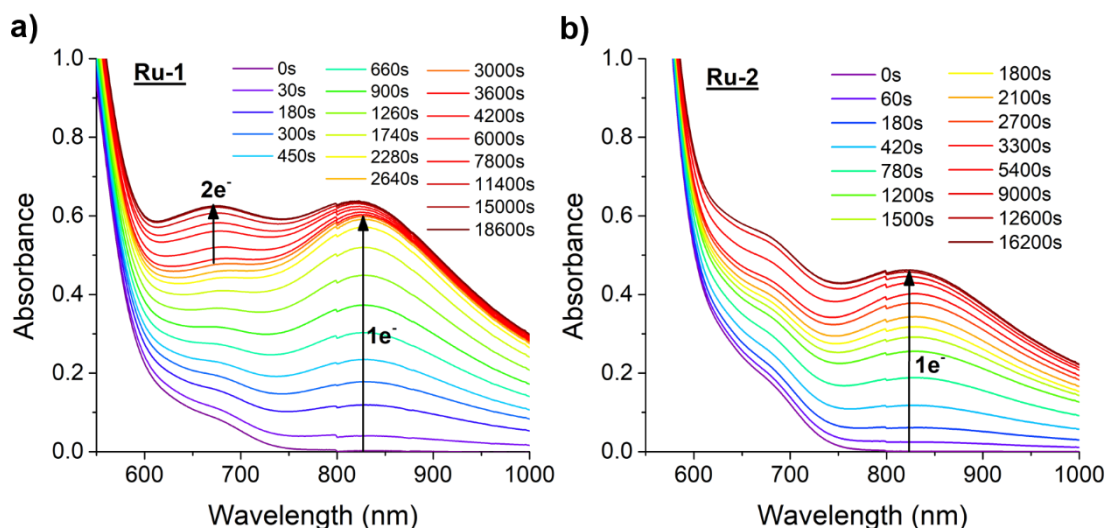


**Figure 113.** Absorbance spectra during the photoreduction experiments using a 395 nm cut-off filter of: a) **Ru-1** and b) **Ru-2**. Both 100  $\mu\text{M}$  in DMF.

including DMA and DMF, with the observed shifting of the low energy absorption tail towards visible wavelengths. This is attributed to charge transfer transitions involving complex weak intermolecular interactions between the donor solvent molecules and acceptor POM anions.<sup>[55-56]</sup> The low energy absorption in **1** does appear to tail to 500 nm ( $\epsilon = \text{ca. } 150 \text{ M}^{-1}\text{cm}^{-1}$  at 455 nm), but the enhanced visible light sensitisation in the Ru<sup>II</sup>-functionalised hybrid POMs does not increase the POM photoreduction, indicating charge-recombination must be significantly accelerated. Further investigation will use transient spectroscopic techniques to elucidate the photophysical processes in these systems, which can give useful insight into how the molecular design can be tailored in order to optimise electronic structure.

### 5.3 Conclusions

Transition metal functionality has been incorporated into the asymmetric hybrid POM **1** successfully via two different synthetic routes. The postfunctionalisation of **1** at the chelation site on the appended *TPY* unit was demonstrated by the coordination of a platinum(II) centre. The synthetic strategy demonstrates to be a straightforward and

broadly applicable approach, displaying potential in the preparation of new soft nanomaterials that are surface-functionalised with transition metal active sites.

A new one-pot hybridisation method has also been devised by which a preformed photosensitising Ru<sup>II</sup> complex has been directly covalently attached to a Dawson POM to isolate a new asymmetric hybrid POM derivative of **1**. The redox-active and photo-active units have been successfully combined in the asymmetric hybrid system, as demonstrated by photoluminescence and spectroelectrochemical characterisation and charge-accumulation studies, however, it displays a non-optimised electronic structure with quenched emission and rapid charge-recombination. Nevertheless, the new Ru<sup>II</sup>-functionalised asymmetric hybrid POM, with its solvent-dependent self-assembling behaviour, could be a promising model system in the development of new photocatalytic POM-based nanomaterials.

Future studies should investigate how the photophysical and photo- and electro-chemical properties of transition metal functionalised asymmetric hybrid POMs such as **Pt-1** and **Ru-1** are translated from their molecular structures into their supramolecular assemblies. This will give valuable insight into how such multicomponent hybrid POM systems can be fine-tuned through their molecular design in their development as new nanomaterials for photo- and electro-catalytic applications.

## 5.4 Experimental details

### 5.4.1 Methods

Methods used are as described in Section 3.7, unless specified below.

DPV measurements were performed on a CHI1140c workstation.

Cryo-TEM analysis was run by Dr. Julie Watts at the Nanoscale and Microscale Research Centre (University of Nottingham). Samples were vitrified using a Gatan CP3 cryoplunge and imaged with a JEOL 2100 Plus TEM operating at 200 kV. Samples (3  $\mu$ L) were deposited onto a graphene oxide / holey carbon copper 300 mesh grid, in a controlled environment (20°C, 78% humidity) and blotted (1.5 s), before plunging

## 5. Transition metal- functionalisation of asymmetric hybrid POMs

---

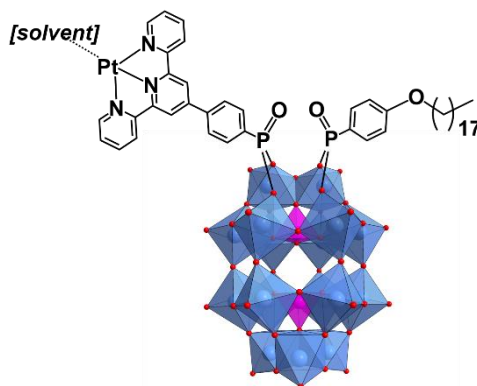
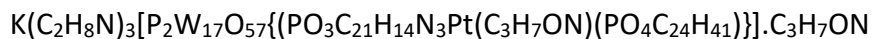
into liquid ethane (-172°C). The sample was maintained under liquid nitrogen (-196°C) during transfer (Gatan 926 cryo sample holder) to the TEM, with the temperature held around -176°C throughout imaging (Gatan Smartset model 900 cold stage controller). Images were recorded using a Gatan Ultrascan 100XP camera, with a nominal underfocus value of 3-6  $\mu\text{m}$  and a 60  $\mu\text{m}$  objective aperture to enhance phase contrast. Sizes were measured using ImageJ 2.0.0 64-bit software.

Fluorescence emission spectra were obtained on an Edinburgh Instruments FLS980 spectrometer at room temperature. Excitation and emission bandwidths were set to 5 nm and 3 scans were taken for each sample. The spectra were corrected by subtraction of the solvent emission spectra taken with the same settings. Emission intensities were determined using the Integration gadget tool on OriginPro 9.0.

Photoreduction experiments were conducted using a 500 W mercury-xenon lamp (operating at 200 W) in a dark enclosure. Solutions of hybrid POM (25 mL, 100  $\mu\text{M}$ ) were prepared under an inert, dry atmosphere using dry, degassed DMF with 800 eq. dry and degassed TEA (279  $\mu\text{L}$ ) added. Screw cap quartz cuvettes filled with the solution were placed in front of the lamp lens with a 395 or 455 nm filter applied and were left to be irradiated for 22 h. Half-lives of exponential decay ( $\tau$ ) were determined using the exponential decay fitting tool (ExpDec1 function) on OriginPro 9.0.

Spectroelectrochemistry experiments were performed by Dr. Stephen Davies. An optically transparent quartz electrochemical cell with a 0.5 mm path length was used for a three-electrode configuration: a Pt/Rh gauze working electrode, Pt wire counter electrode and saturated calomel reference electrode (SCE). The potential at the working electrode was controlled with an AutoLab PGSTAT20 potentiostat and spectra were recorded every two minutes using a Perkin Elmer Lambda 16 spectrophotometer. Analyte concentrations used were 0.62, 0.20, 0.21 mM for **1**, **Ru-1** and **Ru-2**, respectively, in DMF containing TBAPF<sub>6</sub> (0.1 M) as supporting electrolyte. Potentials were held at: **1**: -0.39, -0.70, -1.13 and -1.42 V; **Ru-1**: +0.95, -0.40, -0.73, and -1.12 V; **Ru-2**: +0.90, -0.36, -0.68, and -1.12 V (vs. SCE).

## 5.4.2 Syntheses

5.4.2.1  $[P_2W_{17}O_{57}\{(Pt^{II}-TPY)(C_{18})\}] - (Pt-1)$ :

Pt(COD)Cl<sub>2</sub> (30.5 mg, 0.0814 mmol) and AgBF<sub>4</sub> (31.7 mg, 0.163 mmol) were dissolved in acetone (14 mL) and stirred at room temperature for 15 mins. The white precipitate was removed by centrifugation before the colourless filtrate was added to a solution of **1** (400 mg, 0.0775 mmol) in CH<sub>3</sub>CN-DMF (1:1 v/v, 14 mL) and stirred for 72 h at room temperature. The yellow-orange solution was then centrifuged to remove any insoluble material before the solvent was decanted and then removed *in vacuo*. The remaining yellow-green solid was then sonicated in ether and the suspension was centrifuged. The solvent was then decanted and the retained solid was allowed to dry in air before it was re-dissolved in minimum DMF. An excess of ether was then added to cause precipitation and the cloudy mixture was centrifuged before the supernatant was decanted to leave a green solid. The process of sonicating the solid in ether, centrifuging and decanting the solvent was then repeated a few times (as necessary, checking purity by NMR) in order to wash the solid product before it was finally dried in air with gentle heating (393 mg, 90%).

<sup>1</sup>H NMR (DMSO-d<sub>6</sub>, 400.1 MHz) δ= 9.12 (m, 2H; Ar-H), 8.93 (m, 4H; Ar-H), 8.57 (t, 2H; Ar-H, *J* = 7.8 Hz), 8.42- 8.22 (m, 4H; Ar-H), 8.22-8.02 (br, 6H; NH<sub>2</sub>(CH<sub>3</sub>)<sub>2</sub><sup>+</sup>), 7.95 (s, 2H; HCON(CH<sub>3</sub>)<sub>2</sub>), 7.94-7.87 (m, 4H; Ar-H), 7.03 (d, 2H; Ar-H, *J* = 8.7 Hz), 4.03 (t, 2H; O-CH<sub>2</sub>-, *J* = 6.1 Hz), 2.89 (s, 6H; HCON(CH<sub>3</sub>)<sub>2</sub>), 2.73 (s, 6H; HCON(CH<sub>3</sub>)<sub>2</sub>), 2.56 (t, 18H; NH<sub>2</sub>(CH<sub>3</sub>)<sub>2</sub><sup>+</sup>, *J* = 5.5 Hz), 1.73 (m, 2H; CH<sub>2</sub>-CH<sub>3</sub>), 1.47-1.18 (m, 30H; -CH<sub>2</sub>-), 0.85 (t, 3H; -CH<sub>3</sub>, *J* = 6.6 Hz) ppm; <sup>31</sup>P NMR (DMSO-d<sub>6</sub>, 162 MHz) δ= 17.00, 12.55, -11.32, -12.93



## 5. Transition metal- functionalisation of asymmetric hybrid POMs

---

ppm; **IR** (ATR): 471 (s), 523 (s), 580 (s), 727 (br, vs), 906 (s), 953 (s), 1085 (s), 1136 (w), 1251 (w), 1295 (w), 1385 (m), 1412-1432 (w), 1463 (m), 1504 (w), 1601 (m), 1651 (s), 2850 (m), 2920 (m)  $\text{cm}^{-1}$ ; **Elemental Analysis** calc (%) for  $\text{KP}_4\text{W}_{17}\text{O}_{66}\text{C}_{57}\text{H}_{93}\text{N}_8\text{Pt}$ : C 12.62, H 1.73, N 2.06, found: C 12.50, H 1.79, N 2.11; **TGA Analysis**: Weight change from 105.1 to 399.6°C = 5.071% = 3  $\text{C}_2\text{H}_8\text{N}^+$  (DMA<sup>+</sup>) + 2 DMF (calc = 5.220%); **UV/Vis (DMF)**:  $\lambda_{\text{max}}$  ( $\epsilon$ ,  $\text{mol}^{-1}\text{Lcm}^{-1}$ ) = 285 (76,120), 386 (9640), 408 (10,110) nm.

### 5.4.2.2 Pt-PO(OEt)<sub>2</sub>TPY

To a solution of PO(OEt)<sub>2</sub>TPY (35 mg, 0.0768 mmol) dissolved in acetone (4 mL) was added a suspension of Pt(COD)Cl<sub>2</sub> (28.8 mg, 0.0770 mmol) in H<sub>2</sub>O (2.5 mL) followed by a solution of AgBF<sub>4</sub> (15 mg, 0.0771 mmol) dissolved in H<sub>2</sub>O (2 mL) with stirring to form a yellow solution. The mixture was stirred at RT for 5 days and was orange-red mixture on completion. The mixture was centrifuged to collect a bright orange solid that was washed with H<sub>2</sub>O and ether, and finally dried in air with gentle heating (45 mg, 77%).

<sup>1</sup>H NMR (400 MHz, DMSO-*d*<sub>6</sub>)  $\delta$  9.06 (s, 2H, *H*<sub>3'</sub>), 9.00 – 8.97 (dd, *J* = 5.7, 1.1 Hz, 2H, *H*<sub>3</sub>), 8.88 – 8.84 (dd, *J* = 7.9, 1.2 Hz, 2H, *H*<sub>6</sub>), 8.60-8.56 (td, *J* = 7.9, 1.5 Hz, 2H, *H*<sub>4</sub>), 8.32 (m, 2H, *H*<sub>2</sub>), 8.04 – 7.97 (m, 4H, *H*<sub>3''</sub>, *H*<sub>5</sub>), 4.10 (m, 4H), 1.28 (t, *J* = 7.0 Hz, 6H); <sup>31</sup>P NMR (DMSO-*d*<sub>6</sub>, 162 MHz)  $\delta$  = 16.61 ppm; **ESI MS**- 676.0867<sup>+</sup> (Calc for  $\text{PO}_3\text{C}_{25}\text{H}_{24}\text{N}_3\text{PtCl}^+$ : 676.0883).

### 5.4.2.3 RuTPY

Synthesis of Ru-PO(OEt)<sub>2</sub>TPY

RuCl<sub>3</sub> (0.273 g, 1.32 mmol) and PO(OEt)<sub>2</sub>TPY (0.5 g, 1.32 mmol) were dissolved in ethanol (150 mL) and heated at reflux (85°C) whilst stirring for 3.5 h. The mixture was allowed to cool to room temperature before it was centrifuged. The dark red supernatant was decanted, and the brown solid left was washed with ethanol by sonication, centrifugation and decanting the solvent from the solid. This process was repeated three times, by which time the solvent was very pale in colour. The solid was then allowed to dry in air before being washed with ether, and finally dried under vacuum to yield Ru-PO(OEt)<sub>2</sub>TPY as a red-brown solid (0.562 g, 65%).

## 5. Transition metal- functionalisation of asymmetric hybrid POMs

**<sup>1</sup>H NMR** (400 MHz, CDCl<sub>3</sub>) δ=9.74 (dd, *J*=12.6, 6.9 Hz, 2H; Ar-H), 6.94 (s, br, 2H; Ar-H), 4.09-3.71 (m, 4H; -OCH<sub>2</sub>-), 1.12 (t, *J*=7.1 Hz, 6H; -CH<sub>3</sub>), -0.12 (s, br, 2H; Ar-H), -2.95 (s, br, 2H, Ar-H) ppm (additional -δ peaks could not be seen in this spectral window)<sup>[57]</sup>;

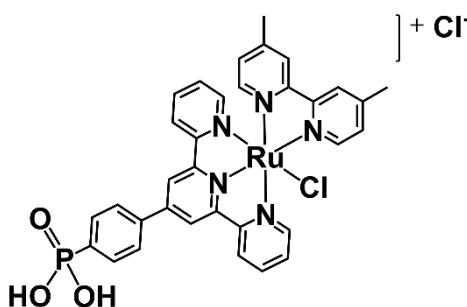
**<sup>31</sup>P NMR** (162 MHz, CDCl<sub>3</sub>) δ= -10.99 ppm.

### Synthesis of Ru-Cl(dmbpy)PO(OEt)<sub>2</sub>TPY

Ru-PO(OEt)<sub>2</sub>TPY (2.07 g, 3.17 mmol), 4,4'-dimethyl 2,2'-dipyridyl (0.698 g, 3.79 mmol) and LiCl (0.401 g, 9.46 mmol) were suspended in ethanol-H<sub>2</sub>O (4:1 v/v, 190 mL) and triethylamine (1.06 mL, 7.61 mmol) was added to the mixture whilst stirring. The mixture was heated at reflux (90°C) whilst stirring for 4 h. The mixture was filtered hot and then the solvent was removed in vacuo. The brown solid left was washed with HCl (2 M) by sonication, centrifugation and decanting the orange-brown supernatant from the solid. This process was repeated three times, by which time the solvent was very pale in colour. The solid was then washed in the same way with ether three times, before drying under vacuum to yield Ru-Cl(dmbpy)PO(OEt)<sub>2</sub>TPY as a dark brown-red solid (2.14 g, 84%).

**<sup>1</sup>H NMR** (400 MHz, DMSO-d<sub>6</sub>) δ=9.92 (d, *J*=5.8 Hz, 1H; Ar-H), 9.22 (s, 2H; Ar-H), 8.93 (d, *J*=8.1 Hz, 2H; Ar-H), 8.81 (s, 1H; Ar-H), 8.52 (s, 1H; Ar-H), 8.46 (dd, *J*=8.3, 3.5 Hz, 2H; Ar-H), 8.05-7.98 (m, 4H; Ar-H), 7.94 (d, *J*=6.0 Hz, 1H; Ar-H), 7.65 (d, *J*=5.6 Hz, 2H; Ar-H), 7.41 (ddd, *J*= 7.1, 5.6, 1.3 Hz, 2H; Ar-H), 7.18 (d, *J*=5.9 Hz, 1H; Ar-H), 6.90 (d, *J*= 6.0 Hz, 1H; Ar-H), 4.17-4.07 (m, 4H; -OCH<sub>2</sub>-), 2.75 (s, 3H; bpy-CH<sub>3</sub>), 2.31 (s, 3H; bpy-CH<sub>3</sub>), 1.31 (t, *J*=7.1 Hz, 6H; CH<sub>3</sub>) ppm; **<sup>31</sup>P NMR** (162 MHz, DMSO-d<sub>6</sub>) δ= 17.21 ppm; **MS (ESI)** *m/z* [*M*]<sup>+</sup> calc for [C<sub>37</sub>H<sub>36</sub>N<sub>5</sub>O<sub>3</sub>P<sub>1</sub>Ru<sub>1</sub>Cl<sub>1</sub>]<sup>+</sup>: 766.1289, found: 766.1260, calc for [C<sub>37</sub>H<sub>36</sub>N<sub>5</sub>O<sub>3</sub>P<sub>1</sub>Ru<sub>1</sub>]<sup>2+</sup>: 365.5799, found: 365.5692.

### Synthesis of RuTPY



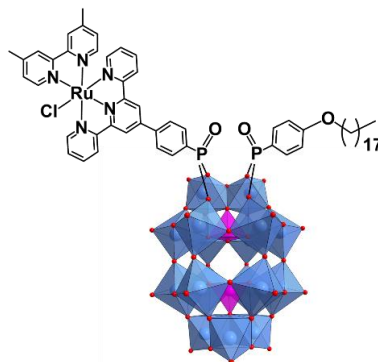
## 5. Transition metal- functionalisation of asymmetric hybrid POMs

Bromotrimethylsilane (2.69 mL, 19.6 mmol) was added to Ru-Cl(dmbpy)PO(OEt)<sub>2</sub>TPY (3.57 g, 4.66 mmol) whilst stirring in dry acetonitrile (150 mL) under argon and the mixture was kept stirring at RT for 40 h. Methanol (150 mL) was then added to the solution and it was kept stirring at room temperature in air for an additional 3 h. The solvent was removed in vacuo, and the solid left was suspended in methanol (~60 mL) before centrifuging. The dark red-brown supernatant was decanted from the solid, which was then washed with ether several times by repeating the process of: sonication, centrifugation, then decanting the solvent from the solid, until the solvent was colourless. Finally, the solid was left to dry in air with gentle heating to yield **RuTPY** as a dark red solid (3.13 g, 95%).

<sup>1</sup>H NMR (400 MHz, DMSO-d<sub>6</sub>) δ 9.91 (d, *J* = 5.8 Hz, 1H; Ar-H), 9.20 (s, 2H; Ar-H), 8.93 (d, *J* = 8.1 Hz, 2H; Ar-H), 8.80 (s, 1H; Ar-H), 8.52 (s, 1H; Ar-H), 8.41 (td, *J* = 9.0, 8.4, 3.0 Hz, 2H; Ar-H), 8.05-7.89 (m, 5H; Ar-H), 7.64 (d, *J* = 5.6 Hz, 2H; Ar-H), 7.41 (t, *J* = 6.6 Hz, 2H; Ar-H), 7.19 (t, *J* = 5.8 Hz, 1H; Ar-H), 6.90 (d, *J* = 6.3 Hz, 1H; Ar-H), 2.75 (s, 3H; bpy-CH<sub>3</sub>), 2.31 (s, 3H; bpy-CH<sub>3</sub>) ppm; <sup>31</sup>P NMR (162 MHz, DMSO-d<sub>6</sub>) δ = 11.89 ppm; **MS (ESI)** *m/z* [*M*]<sup>+</sup> calc for [C<sub>33</sub>H<sub>28</sub>N<sub>5</sub>O<sub>3</sub>P<sub>1</sub>Ru<sub>1</sub>Cl<sub>1</sub>]<sup>+</sup>: 710.0662, found: 710.0652; **IR (ATR)**: 827 (s), 919 (s), 987(s), 1132 (m), 1206 (m), 1241 (w), 1354 (w), 1395 (w), 1426 (w), 1476 (m), 1605(m), 2914 (w), 3060 (w) cm<sup>-1</sup>; **UV/Vis (DMF)**: λ<sub>max</sub> (ε, mol<sup>-1</sup>Lcm<sup>-1</sup>) = 290 (57,000), 321 (34,600), 367 (11,400), 524 (13,300) nm.

### 5.4.2.4 [P<sub>2</sub>W<sub>17</sub>O<sub>57</sub>{(RuTPY)(C<sub>18</sub>)}] – (Ru-1)

K<sub>2</sub>(C<sub>2</sub>H<sub>8</sub>N)<sub>3</sub>[P<sub>2</sub>W<sub>17</sub>O<sub>57</sub>{(PO<sub>3</sub>C<sub>21</sub>H<sub>14</sub>N<sub>3</sub>Ru(C<sub>12</sub>H<sub>12</sub>N<sub>2</sub>)Cl)(PO<sub>4</sub>C<sub>24</sub>H<sub>41</sub>)}



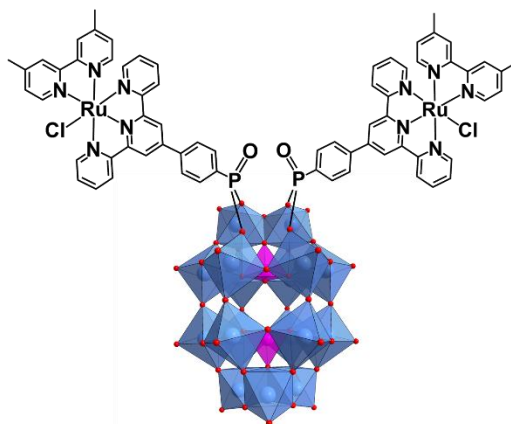
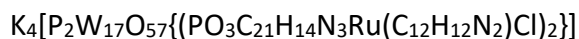
K<sub>10</sub>-[P<sub>2</sub>W<sub>17</sub>O<sub>61</sub>] (2 g, 0.439 mmol), **RuTPY** (0.327 g, 0.438 mmol), **C<sub>18</sub>** (0.187g, 0.438 mmol), and KCl (0.65 g, 8.72 mmol) were suspended in a DMF-CH<sub>3</sub>CN mixture (40 mL,

## 5. Transition metal- functionalisation of asymmetric hybrid POMs

---

1:1 v/v) and stirred. 12 M HCl (366  $\mu$ L, 4.38 mmol) was added dropwise to the solution whilst stirring, and the mixture was heated to 85°C for 19 h. The mixture was allowed to cool to room temperature before filtering. An excess of ether was added (~100 mL) to give a red-purple (maroon) milky solution, which was centrifuged to give a maroon precipitate and a yellow-orange supernatant. The solvent was decanted and the process of sonicating the precipitate in ether, centrifuging and decanting was repeated until the precipitate resembled a free-flowing powder. The solid was then sonicated in acetone (~35 mL) and centrifuged to separate an insoluble dark maroon solid. The maroon supernatant was decanted and the washing process of sonicating the solid in acetone (~35 mL) and centrifuging was repeated three more times. The supernatant solutions were combined, and the solvent was removed *in vacuo*. The solid obtained was suspended in CH<sub>3</sub>CN (~5 mL) and an excess of ether was added (30 mL). The solution was centrifuged to collect a dark maroon solid, and this was sonicated in ether and dried in air with gentle heating. The process of: re-dissolving this solid in acetone and centrifuging to remove any insoluble **Ru-2** before removing the acetone *in vacuo*, followed by dissolution of the obtained solid in CH<sub>3</sub>CN and re-precipitation of **Ru-1** from the solution with ether, was repeated until no **Ru-2** or **3** was visible in the <sup>31</sup>P and <sup>1</sup>H NMR. **Ru-1** was yielded as a dark maroon solid (520 mg, 22%).

<sup>1</sup>H NMR (400 MHz, DMSO-d<sub>6</sub>)  $\delta$  10.14-6.95 (m, 24H; Ar-H), 8.20 (br, 6H; NH<sub>2</sub>(CH<sub>3</sub>)<sub>2</sub><sup>+</sup>), 4.05 (t, 2H; O-CH<sub>2</sub>-, *J* = 6.9 Hz), 2.74 (s, 3H; bpy-CH<sub>3</sub>), 2.56 (s, br, 18H; NH<sub>2</sub>(CH<sub>3</sub>)<sub>2</sub><sup>+</sup>), 2.32 (s, 3H; bpy-CH<sub>3</sub>), 1.79-1.66 (m, 2H; O-CH<sub>2</sub>-CH<sub>2</sub>-), 1.49-1.15 (m, 30H; -CH<sub>2</sub>-), 0.86 (t, 3H; -CH<sub>3</sub>, *J* = 6.9 Hz) ppm; <sup>31</sup>P NMR (162 MHz, DMSO-d<sub>6</sub>)  $\delta$  = 16.72, 13.56, -11.31, -12.94 ppm; ; IR (ATR): 422 (s), 471 (s), 523 (s), 568 (s), 580 (s), 726 (br, vs), 908 (s), 955 (s), 1087 (s), 1136 (w), 1253 (w), 1297 (w), 1410 (w), 1426 (w), 1463 (m), 1504 (w), 1597 (m), 2848 (m), 2918 (m) cm<sup>-1</sup>; TGA Analysis: Step transition (249.8 to 350.2°C) wt loss of 2.818 = loss of 3 DMA (calc = 2.538 %); Elemental Analysis calc (%) for K<sub>2</sub>P<sub>4</sub>W<sub>17</sub>O<sub>64</sub>C<sub>63</sub>H<sub>91</sub>N<sub>8</sub>RuCl: C 13.89, H 1.68, N 2.06, found: C 13.74, H 1.83, N 2.22; UV/Vis (DMF): .  $\lambda_{\max}$  ( $\epsilon$ , mol<sup>-1</sup>Lcm<sup>-1</sup>) = 290 (110,200), 316 (65,200), 366 (16,000), 524 (13,400) nm.

5.4.2.5  $[P_2W_{17}O_{57}\{(RuTPY)_2\}] - (Ru-2)$ 

$K_{10}[P_2W_{17}O_{61}]$  (0.25 g, 0.055 mmol), **RuTPY** (82 mg, 0.110 mmol), and KCl (82 mg, 10.1 mmol) were suspended in DMF (10 mL) and stirred. 12 M HCl (46  $\mu$ L, 0.552 mmol) was added dropwise to the solution whilst stirring, and the mixture was heated to 85°C for 19 h. The mixture was allowed to cool to RT before filtering. An excess of ether was added (~30 mL) to result in a red-purple (maroon) milky solution, which was centrifuged to give a maroon precipitate. The supernatant was decanted and the process of: sonicating the solid in ether, centrifuging and then decanting the supernatant was repeated until the precipitate resembled a free-flowing powder. The solid was dried in air with gentle heating and finally under vacuum. **Ru-2** was yielded as a dark maroon solid (256 mg, 81%).

$^1H$  NMR (400 MHz, DMSO- $d_6$ )  $\delta$  9.98-9.88 (m, 2H; Ar-H), 9.35-9.13 (m, 4H; Ar-H), 9.04-8.90 (m, 4H; Ar-H), 8.79 (s, 2H; Ar-H), 8.53-8.20 (m, 10H; Ar-H), 8.07-7.97 (m, 4H; Ar-H), 7.94-7.87 (m, 2H; Ar-H), 7.71-7.58 (m, 4H; Ar-H), 7.44-7.33 (m, 4H; Ar-H), 7.27-7.16 (m, 2H; Ar-H), 7.02-6.88 (m, 2H; Ar-H), 2.75 (s, 6H; bpy- $CH_3$ ), 2.31 (s, 6H; bpy- $CH_3$ ) ppm;  $^{31}P$  NMR (162 MHz, DMSO- $d_6$ )  $\delta$  = 14.35, -11.25, -12.88 ppm; IR (ATR): 422 (s), 471 (s), 521 (s), 567 (s), 587 (s), 722 (br, vs), 906 (s), 953 (s), 1085 (s), 1136 (w), 1251 (w), 1385 (m), 1410 (w), 1432 (w), 1463 (m), 1618 (m), 2927 (w)  $cm^{-1}$ ; TGA Analysis: Weight change from 117.3 to 360.8 = 0.389% = 0 DMA or DMF; Elemental Analysis calc (%) for  $K_4P_4W_{17}O_{63}C_{66}H_{52}N_{10}Ru_2Cl_2$ : C 13.98, H 0.92, N 2.47, found: C 13.45, H 1.33, N 2.40; UV/Vis (DMF): .  $\lambda_{max}$  ( $\epsilon$ ,  $mol^{-1}Lcm^{-1}$ ) = 291 (150,300), 318 (81,800), 366 (25,400), 525 (24,800) nm.

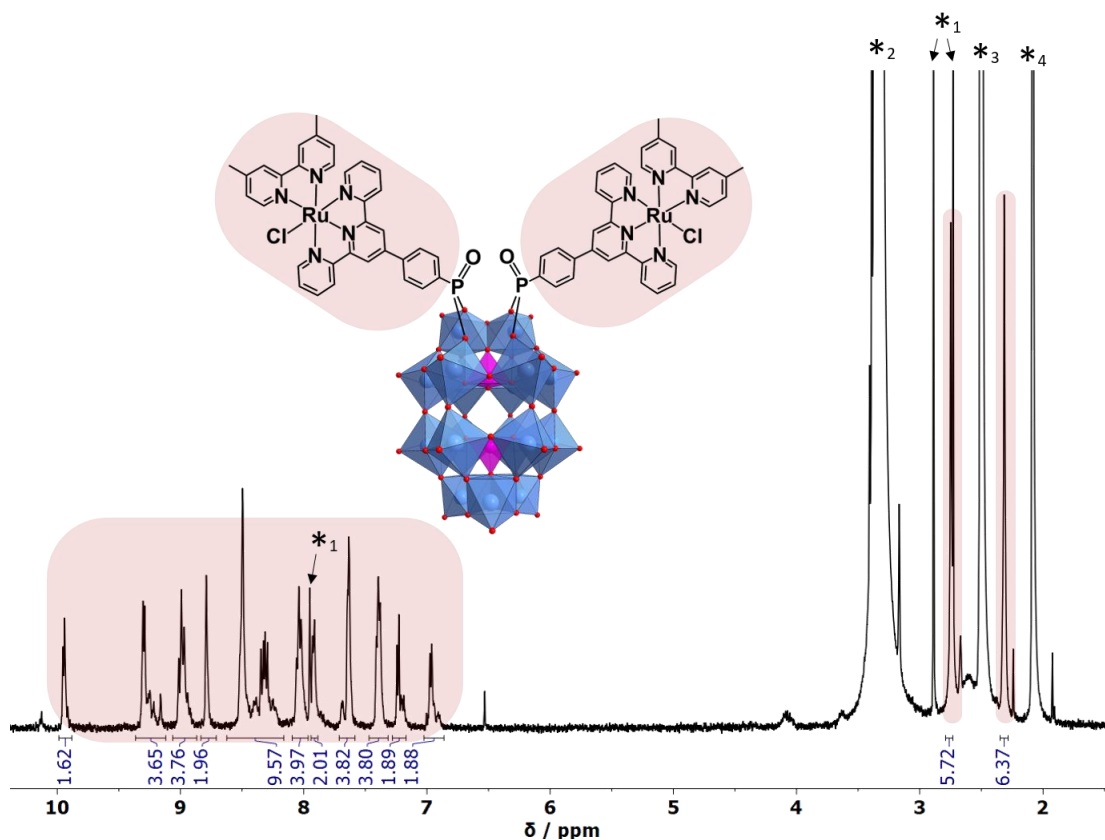


**Figure 114.**  $^1\text{H}$  NMR of **Ru-2** in  $\text{DMSO-d}_6$ . Black asterisks indicate solvent impurities: 1= DMF, 2=  $\text{H}_2\text{O}$ , 3= DMSO, 4 = acetone.

| Assignment   | z  | m/z (obs.) | m/z (calc.) |
|--|----|------------|-------------|
| $\text{H}[\text{P}_2\text{W}_{17}\text{O}_{57}\{(\text{PO}_3\text{C}_{33}\text{H}_{26}\text{N}_5\text{RuCl})_2\}]$   | 3- | 1838.2467  | 1838.6223   |
| $\text{H}_2[\text{P}_2\text{W}_{17}\text{O}_{57}\{(\text{PO}_3\text{C}_{33}\text{H}_{26}\text{N}_5\text{RuCl})_2\}]$ | 2- | 2758.0866  | 2757.9335   |
| $\text{HNa}[\text{P}_2\text{W}_{17}\text{O}_{57}\{(\text{PO}_3\text{C}_{33}\text{H}_{26}\text{N}_5\text{RuCl})_2\}]$ | 2- | 2769.0725  | 2768.9245   |

**Table 19.** Selected ESI-MS peak assignments for **Ru-2**.

## 5.5 References

- [1] M.-P. Santoni, G. S. Hanan, B. Hasenknopf, Covalent multi-component systems of polyoxometalates and metal complexes: Toward multi-functional organic–inorganic hybrids in molecular and material sciences, *Coord. Chem. Rev.*, 2014, **281**, 64-85.

## 5. Transition metal- functionalisation of asymmetric hybrid POMs

---

- [2] Y. Yan, J. Huang, Hierarchical assemblies of coordination supramolecules, *Coord. Chem. Rev.*, 2010, **254**, 1072-1080.
- [3] J. P. Sauvage, J. P. Collin, J. C. Chambron, S. Guillerez, C. Coudret, V. Balzani, F. Barigelletti, L. De Cola, L. Flamigni, Ruthenium(II) and Osmium(II) Bis(terpyridine) Complexes in Covalently-Linked Multicomponent Systems: Synthesis, Electrochemical Behavior, Absorption Spectra, and Photochemical and Photophysical Properties, *Chem. Rev.*, 1994, **94**, 993-1019.
- [4] A. Winter, U. S. Schubert, Metal-Terpyridine Complexes in Catalytic Application – A Spotlight on the Last Decade, *ChemCatChem*, 2020, **12**, 2890-2941.
- [5] M. R. Gill, J. A. Thomas, Ruthenium(ii) polypyridyl complexes and DNA—from structural probes to cellular imaging and therapeutics, *Chem. Soc. Rev.*, 2012, **41**, 3179-3192.
- [6] J. V. Caspar, T. J. Meyer, Photochemistry of tris(2,2'-bipyridine)ruthenium(2+) ion ( $\text{Ru}(\text{bpy})_3^{2+}$ ). Solvent effects, *J. Am. Chem. Soc.*, 1983, **105**, 5583-5590.
- [7] D. Rota Martir, E. Zysman-Colman, Photoactive supramolecular cages incorporating Ru(ii) and Ir(iii) metal complexes, *Chem. Commun.*, 2019, **55**, 139-158.
- [8] Z. Chen, C. Chen, D. R. Weinberg, P. Kang, J. J. Concepcion, D. P. Harrison, M. S. Brookhart, T. J. Meyer, Electrocatalytic reduction of  $\text{CO}_2$  to CO by polypyridyl ruthenium complexes, *Chem. Commun.*, 2011, **47**, 12607-12609.
- [9] N. Kaveevivitchai, R. Chitta, R. Zong, M. El Ojaimi, R. P. Thummel, A Molecular Light-Driven Water Oxidation Catalyst, *J. Am. Chem. Soc.*, 2012, **134**, 10721-10724.
- [10] R. Okazaki, S. Masaoka, K. Sakai, Photo-hydrogen-evolving activity of chloro(terpyridine)platinum(ii): a single-component molecular photocatalyst, *Dalton Trans.*, 2009, 6127-6133.
- [11] D.-L. Ma, T. Y.-T. Shum, F. Zhang, C.-M. Che, M. Yang, Water soluble luminescent platinum terpyridine complexes with glycosylated acetylde and arylacetylde ligands: photoluminescent properties and cytotoxicities, *Chem. Commun.*, 2005, 4675-4677.
- [12] B. Siewert, M. Langerman, Y. Hontani, J. T. M. Kennis, V. H. S. van Rixel, B. Limburg, M. A. Siegler, V. Talens Saez, R. E. Kieltyka, S. Bonnet, Turning on the red phosphorescence of a  $[\text{Ru}(\text{tpy})(\text{bpy})(\text{Cl})]\text{Cl}$  complex by amide substitution: self-aggregation, toxicity, and cellular localization of an emissive ruthenium-based amphiphile, *Chem. Commun.*, 2017, **53**, 11126-11129.
- [13] N. A. Larew, A. R. Van Wassen, K. E. Wetzel, M. M. Machala, S. D. Cummings, Solution luminescence from chloro(2,2':6',2''-terpyridine)platinum(II) chloride in micelles, *Inorganica Chim. Acta*, 2010, **363**, 57-62.
- [14] A. Klaiber, T. Kollek, S. Cardinal, N. Hug, M. Drechsler, S. Polarz, Electron Transfer in Self-Assembled Micelles Built by Conductive Polyoxometalate-Surfactants Showing Battery-Like Behavior, *Adv. Mater. Interfaces*, 2018, **5**, 1701430.
- [15] G. Annibale, M. Brandolisio, B. Pitteri, New routes for the synthesis of chloro(diethylenetriamine) platinum(II) chloride and chloro(2,2' : 6',2''-terpyridine) platinum(II) chloride dihydrate, *Polyhedron*, 1995, **14**, 451-453.
- [16] S. D. Cummings, Platinum complexes of terpyridine: Synthesis, structure and reactivity, *Coord. Chem. Rev.*, 2009, **253**, 449-478.

## 5. Transition metal- functionalisation of asymmetric hybrid POMs

---

- [17] M. Howe-Grant, S. J. Lippard, in *Inorganic Syntheses, Vol. 20*, John Wiley & Sons, **1980**, p. 101.
- [18] I. Eryazici, C. N. Moorefield, G. R. Newkome, Square-Planar Pd(II), Pt(II), and Au(III) Terpyridine Complexes: Their Syntheses, Physical Properties, Supramolecular Constructs, and Biomedical Activities, *Chem. Rev.*, 2008, **108**, 1834-1895.
- [19] Y. Suzuki, T. Yagyu, K. Osakada, Transmetalation of arylpalladium and platinum complexes. Mechanism and factors to control the reaction, *J. Organomet. Chem.*, 2007, **692**, 326-342.
- [20] J. S. Field, R. J. Haines, D. R. McMillin, G. C. Summerton, Tuning solid emission by salts of the [Pt{4'-(*o*-CH<sub>3</sub>-Ph)trpy}Cl]<sup>+</sup> and [Pt{4'-(*o*-CF<sub>3</sub>-Ph)trpy}Cl]<sup>+</sup> luminophores: crystal structures of [Pt{4'-(*o*-CH<sub>3</sub>-Ph)trpy}Cl]A (A = BF<sub>4</sub> or SbF<sub>6</sub>) and [Pt{4'-(*o*-CF<sub>3</sub>-Ph)trpy}Cl]SbF<sub>6</sub> (trpy = 2,2':6',2''-terpyridine), *J. Chem. Soc., Dalton Trans.*, 2002, 1369-1376.
- [21] T. Yutaka, I. Mori, M. Kurihara, J. Mizutani, N. Tamai, T. Kawai, M. Irie, H. Nishihara, Photoluminescence Switching of Azobenzene-Conjugated Pt(II) Terpyridine Complexes by Trans-Cis Photoisomerization, *Inorg. Chem.*, 2002, **41**, 7143-7150.
- [22] J. A. Bailey, M. G. Hill, R. E. Marsh, V. M. Miskowski, W. P. Schaefer, H. B. Gray, Electronic Spectroscopy of Chloro(terpyridine)platinum(II), *Inorg. Chem.*, 1995, **34**, 4591-4599.
- [23] P. Serp, M. Hernandez, B. Richard, P. Kalck, A Facile Route to Carbonylhalogenometal Complexes (M = Rh, Ir, Ru, Pt) by Dimethylformamide Decarbonylation, *Eur. J. Inorg. Chem.*, 2001, **2001**, 2327-2336.
- [24] D. R. McMillin, J. J. Moore, Luminescence that lasts from Pt(trpy)Cl<sup>+</sup> derivatives (trpy=2,2';6',2''-terpyridine), *Coord. Chem. Rev.*, 2002, **229**, 113-121.
- [25] Q.-Z. Yang, L.-Z. Wu, Z.-X. Wu, L.-P. Zhang, C.-H. Tung, Long-Lived Emission from Platinum(II) Terpyridyl Acetylide Complexes, *Inorg. Chem.*, 2002, **41**, 5653-5655.
- [26] M. G. Hill, J. A. Bailey, V. M. Miskowski, H. B. Gray, Spectroelectrochemistry and Dimerization Equilibria of Chloro(terpyridine)platinum(II). Nature of the Reduced Complexes, *Inorg. Chem.*, 1996, **35**, 4585-4590.
- [27] E. Sakuda, A. Funahashi, N. Kitamura, Synthesis and Spectroscopic Properties of Platinum(II) Terpyridine Complexes Having an Arylborane Charge Transfer Unit, *Inorg. Chem.*, 2006, **45**, 10670-10677.
- [28] G.-J. Zhang, X. Gan, Q.-Q. Xu, Y. Chen, X.-J. Zhao, B. Qin, X.-J. Lv, S.-W. Lai, W.-F. Fu, C.-M. Che, Photophysical and electrochemical properties of platinum(ii) complexes bearing a chromophore-acceptor dyad and their photocatalytic hydrogen evolution, *Dalton Trans.*, 2012, **41**, 8421-8429.
- [29] A. Maroń, K. Czerwińska, B. Machura, L. Raposo, C. Roma-Rodrigues, A. R. Fernandes, J. G. Małecki, A. Szłapa-Kula, S. Kula, S. Krompiec, Spectroscopy, electrochemistry and antiproliferative properties of Au(III), Pt(II) and Cu(II) complexes bearing modified 2,2':6',2''-terpyridine ligands, *Dalton Trans.*, 2018, **47**, 6444-6463.
- [30] M. Piot, B. Abécassis, D. Brouri, C. Troufflard, A. Proust, G. Izzet, Control of the hierarchical self-assembly of polyoxometalate-based metallomacrocycles by redox trigger and solvent composition, *Proc. Nat. Acad. Sci.*, 2018, **115**, 8895-8900.



## 5. Transition metal- functionalisation of asymmetric hybrid POMs

---

- [31] J. M. Cameron, S. Fujimoto, K. Kastner, R.-J. Wei, D. Robinson, V. Sans, G. N. Newton, H. H. Oshio, Orbital Engineering: Photoactivation of an Organofunctionalized Polyoxotungstate, *Chem. Eur. J.*, 2017, **23**, 47-50.
- [32] S. Elmas, W. Beelders, S. J. Bradley, R. Kroon, G. Laufersky, M. Andersson, T. Nann, Platinum Terpyridine Metallopolymer Electrode as Cost-Effective Replacement for Bulk Platinum Catalysts in Oxygen Reduction Reaction and Hydrogen Evolution Reaction, *ACS Sustain. Chem. Eng.*, 2017, **5**, 10206-10214.
- [33] B. Keïta, L. Nadjo, New oxometalate-based materials for catalysis and electrocatalysis, *Mater. Chem. Phys.*, 1989, **22**, 77-103.
- [34] B. Keïta, L. Nadjo, Activation of electrode surfaces: Application to the electrocatalysis of the hydrogen evolution reaction, *J. Electroanal. Chem. Interf. Electrochem.*, 1985, **191**, 441-448.
- [35] P. J. Kulesza, W. Lu, L. R. Faulkner, Cathodic fabrication of platinum microparticles via anodic dissolution of a platinum counter-electrode: Electrocatalytic probing and surface analysis of dispersed platinum, *J. Electroanal. Chem.*, 1992, **336**, 35-44.
- [36] M. A. Bird, S. E. Goodwin, D. A. Walsh, Best Practice for Evaluating Electrocatalysts for Hydrogen Economy, *ACS Appl. Mater. Interfaces*, 2020, **12**, 20500-20506.
- [37] R. Chen, C. Yang, W. Cai, H.-Y. Wang, J. Miao, L. Zhang, S. Chen, B. Liu, Use of Platinum as the Counter Electrode to Study the Activity of Nonprecious Metal Catalysts for the Hydrogen Evolution Reaction, *ACS Energy Lett.*, 2017, **2**, 1070-1075.
- [38] C. Zhang, Y. Hong, R. Dai, X. Lin, L.-S. Long, C. Wang, W. Lin, Highly Active Hydrogen Evolution Electrodes via Co-Deposition of Platinum and Polyoxometalates, *ACS Appl. Mater. Interfaces*, 2015, **7**, 11648-11653.
- [39] P. Lei, M. Hedlund, R. Lomoth, H. Rensmo, O. Johansson, L. Hammarström, The Role of Colloid Formation in the Photoinduced H<sub>2</sub> Production with a Ru<sup>II</sup>-Pd<sup>II</sup> Supramolecular Complex: A Study by GC, XPS, and TEM, *J. Am. Chem. Soc.*, 2008, **130**, 26-27.
- [40] P. Du, J. Schneider, P. Jarosz, R. Eisenberg, Photocatalytic Generation of Hydrogen from Water Using a Platinum(II) Terpyridyl Acetylide Chromophore, *J. Am. Chem. Soc.*, 2006, **128**, 7726-7727.
- [41] B. Matt, C. Coudret, C. Viala, D. Jouvenot, F. Loiseau, G. Izzet, A. Proust, Elaboration of Covalently Linked Polyoxometalates with Ruthenium and Pyrene Chromophores and Characteriation of Their Photophysical Properties, *Inorg. Chem.*, 2011, **50**, 7761-7768.
- [42] K. Barthelmes, M. Sittig, A. Winter, U. S. Schubert, Molecular Dyads and Triads Based on Phenothiazine and  $\pi$ -Extended Tetrathiafulvalene Donors, Bis(terpyridine)ruthenium(II) Complexes, and Polyoxometalates, *Eur. J. Inorg. Chem.*, 2017, 3698-3706.
- [43] M. Maestri, N. Armaroli, V. Balzani, E. C. Constable, A. M. W. C. Thompson, Complexes of the Ruthenium(II)-2,2':6',2''-terpyridine Family. Effect of Electron-Accepting and -Donating Substituents on the Photophysical and Electrochemical Properties, *Inorg. Chem.*, 1995, **34**, 2759-2767.

## 5. Transition metal- functionalisation of asymmetric hybrid POMs

---

- [44] M. Beley, J. P. Collin, R. Louis, B. Metz, J. P. Sauvage, 3,3',5,5'-Tetrapyridylbiphenyl, a bis-cyclometalating bridging ligand with a high coupling ability in ruthenium(III), ruthenium(II) mixed valence systems, *J. Am. Chem. Soc.*, 1991, **113**, 8521-8522.
- [45] B. A. Johnson, H. Agarwala, T. A. White, E. Mijangos, S. Maji, S. Ott, Judicious Ligand Design in Ruthenium Polypyridyl CO<sub>2</sub> Reduction Catalysts to Enhance Reactivity by Steric and Electronic Effects, *Chem. Eur. J.*, 2016, **22**, 14870-14880.
- [46] A. Juris, V. Balzani, F. Barigelletti, S. Campagna, P. Belser, A. von Zelewsky, Ru(II) polypyridine complexes: photophysics, photochemistry, electrochemistry, and chemiluminescence, *Coord. Chem. Rev.*, 1988, **84**, 85-277.
- [47] A. T. Vu, D. A. Santos, J. G. Hale, R. N. Garner, Tuning the excited state properties of ruthenium(II) complexes with a 4-substituted pyridine ligand, *Inorganica Chim. Acta*, 2016, **450**, 23-29.
- [48] C. Herrero, A. Quaranta, R.-A. Fallahpour, W. Leibl, A. Aukauloo, Identification of the Different Mechanisms of Activation of a [Ru<sup>II</sup>(tpy)(bpy)(OH<sub>2</sub>)]<sup>2+</sup> Catalyst by Modified Ruthenium Sensitizers in Supramolecular Complexes, *J. Phys. Chem. C*, 2013, **117**, 9605-9612.
- [49] L. Bai, F. Li, Y. Wang, H. Li, X. Jiang, L. Sun, Visible-light-driven selective oxidation of benzyl alcohol and thioanisole by molecular ruthenium catalyst modified hematite, *Chem. Commun.*, 2016, **52**, 9711-9714.
- [50] H. J. Jang, S. L. Hopkins, M. A. Siegler, S. Bonnet, Frontier orbitals of photosubstitutionally active ruthenium complexes: an experimental study of the spectator ligands' electronic properties influence on photoreactivity, *Dalton Trans.*, 2017, **46**, 9969-9980.
- [51] M.-P. Santoni, A. K. Pal, G. S. Hanan, M.-C. Tang, A. Furtos, B. Hasenknopf, A light-harvesting polyoxometalate-polypyridine hybrid induces electron transfer as its Re(i) complex, *Dalton Trans.*, 2014, **43**, 6990-6993.
- [52] C. M. Cardona, W. Lei, A. E. Kaifer, D. Stockdale, G. C. Bazan, Electrochemical Considerations for Determining Absolute Frontier Orbital Energy Levels of Conjugated Polymers for Solar Cell Applications, *Adv. Mater.*, 2011, **23**, 2367-2371.
- [53] E. Papaconstantinou, Photochemistry of polyoxometallates of molybdenum and tungsten and/or vanadium, *Chem. Soc. Rev.*, 1989, **18**, 1-31.
- [54] Y. Pellegrin, F. Odobel, Sacrificial electron donor reagents for solar fuel production, *Comptes Rendus Chimie*, 2017, **20**, 283-295.
- [55] C. L. Hill, D. A. Bouchard, Catalytic photochemical dehydrogenation of organic substrates by polyoxometalates, *J. Am. Chem. Soc.*, 1985, **107**, 5148-5157.
- [56] M. M. Williamson, D. A. Bouchard, C. L. Hill, Characterization of a weak intermolecular photosensitive complex between an organic substrate and a polyoxometalate. Crystal and molecular structure of  $\alpha$ -H<sub>3</sub>PMO<sub>12</sub>O<sub>40</sub>.6DMA.CH<sub>3</sub>CN.0.5H<sub>2</sub>O (DMA = N,N-dimethylacetamide), *Inorg. Chem.*, 1987, **26**, 1436-1441.
- [57] P. A. Benavides, T. A. Matias, K. Araki, Unexpected lability of the [Ru<sup>III</sup>(phtpy)Cl<sub>3</sub>] complex, *Dalton Trans.*, 2017, **46**, 15567-15572.

## 6 Surface-immobilisation of an asymmetric hybrid POM

The immobilisation and patterning of POMs onto surfaces can be used to fabricate functional materials and devices for applications including in catalysis, electronics and sensors.<sup>[1-4]</sup>

As charged structures, POMs are commonly immobilised onto surfaces by adsorption methods or by deposition after entrapment within polymeric or gel matrices,<sup>[5]</sup> approaches which are often based on electrostatic interactions or ill-defined chemisorption. The covalent grafting of POMs onto surfaces through hybrid structures can allow much greater control of the molecular organisation of the material and its stability, although is less well-reported in comparison due to the challenging synthesis of hybrid structures with suitable remote functionalities. Their covalent grafting onto planar surfaces is then achievable either directly through the reactive functionality or via coupling to reactive groups of molecules in a preformed self-assembled monolayer on the surface (SAM).<sup>[2, 6]</sup>

The covalent immobilisation of hybrid POMs onto conductive materials and electrode surfaces is a promising method to improve their electrochemical stability and tune their electronic properties, whilst configuring them into high surface-area materials. This can ultimately aid in their application in electro- or photo-catalysis,<sup>[7]</sup> as well as in various electronic devices, such as photovoltaics and sensors.<sup>[8]</sup> Many examples of hybrid POMs grafted to silicon and conductive carbon materials have been reported, with the motivation of developing molecular electronic and memory devices, including those based on the redox-active Keggin cluster.<sup>[9-12]</sup> The terminal diazonium functionality of an organogermanyl Keggin POM synthesised by Rinfrey *et al.*,  $[PW_{11}O_{39}\{Ge(C_6H_4)CC(C_6H_4)N_2^+\}]$ , was shown to enable its covalent anchoring by electrochemical reduction onto glassy carbon<sup>[2]</sup> and silicon surfaces,<sup>[13]</sup> preparing electroactive monolayers of POMs. The grafting of an organotin molybdate derivative onto graphene was also demonstrated, and interestingly was shown to have a doping

## 6. Surface-immobilisation of an asymmetric hybrid POM

effect on the graphene substrate.<sup>[14]</sup> Gold surfaces have also been covalently modified by hybrid POMs, a notable example of which is the nanostructuring of an organosiloxane functionalised Keggin,  $[PW_{11}O_{39}\{O(SiC_6H_4NH_2)_2\}]$ , reported by Mercier *et al.* which was shown to prepare sensing layers. The first terminal amine group on the siloxane linker was used to couple the hybrid POM to a SAM of mercapto-undecanoic acid on a gold surface, whilst the second free amine could act as a biorecognition site for a specific protein.<sup>[4]</sup> In a following study, the postfunctionalisation of the hybrid POM SAM by the covalent bonding of the free amine moiety to a pyrene molecule was used to prepare a new sensing layer comprised of a now asymmetrically functionalised hybrid POM (Fig.115). This nanostructured gold material then demonstrated enhanced analytical performance as a biosensor for small molecules via interactions at the pyrene site.<sup>[15]</sup>

The work in this chapter looks at the introduction of further functionality into the base asymmetric hybrid Dawson structure investigated in this thesis that allows its immobilisation onto surfaces. Whilst the previous chapter explored the introduction of transition metal functionality at the chelating *TPY* unit, this chapter will look at the addition of a terminal functional group on the aliphatic  $C_n$  chain moiety. This will

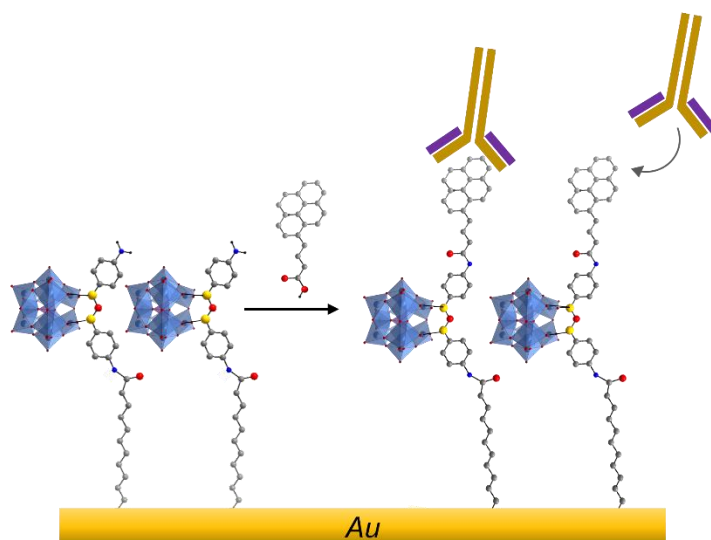


**Figure 115.** Preparation of an asymmetric hybrid POM- modified gold surface which displays biosensing activity, reported by Mercier *et al.* Adapted from reference 15.

increase the complexity of the asymmetric hybrid POM as a versatile postfunctionalisation platform as various modifications at a terminal reactive group can allow the covalent attachment of organic molecules, in addition to enabling the hybrid molecule to be grafted onto surfaces or nanomaterials. Importantly, immobilisation can be used to improve its employability as a material for application, through its heterogenisation and by further modulation of its electronic properties. As a hybrid POM based on the Dawson cluster with rich redox- and photo-chemistry, and with its the capability to incorporate organometallic functionality, this investigation will be particularly valuable for its development as a tailored electro- and/or photo-catalytic material.

The preparation of a new asymmetric hybrid POM with an appended thiol-terminated alkyl chain group is first described in this chapter. Following this, its use in covalent grafting the asymmetric hybrid directly to gold surfaces and nanoparticles is investigated, and the characterisation of the hybrid POM-modified materials is discussed.

### 6.1 One-pot synthesis of asymmetric hybrid POM

#### $[P_2W_{17}O_{57}\{(TPY)(C_{11}SH)\}]$ (4)

Alkylthiolates are common spacer groups in immobilised substrates on gold surfaces due to the tuneable length and orientation of the alkyl chain unit and the strength of the Au-S bond.<sup>[16]</sup> With the intention to introduce further functionality into an asymmetric hybrid POM which enables its nanostructuration onto gold, an asymmetric hybrid derivative of **1** with an alkylthiol moiety was synthesised. A suitable phenylphosphonic acid incorporating an aliphatic C<sub>11</sub> chain terminated in a thiol group, **C<sub>11</sub>SH**, was used, which had been synthesised and supplied by Dr Carmen Martin-Gandul (Fig.116).<sup>[17]</sup>

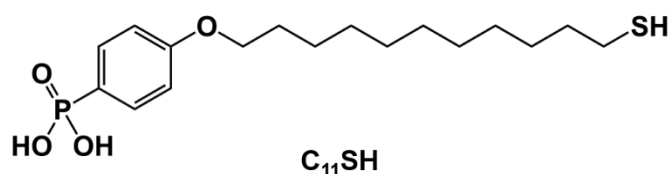


**Figure 116.** Structure of the thiol-terminated alkyl chain phosphonate ligand,  $C_{11}SH$ .

$C_{11}SH$  was reacted in a one-pot synthesis with **TPY** and the potassium salt of the Dawson anion  $\{P_2W_{17}\}$  using the same reaction conditions as for **1** (Fig.117).  $^{31}P$  NMR confirmed a crude mixture of three hybrid POM products: the desired asymmetric hybrid,  $K_5(C_2H_8N)[P_2W_{17}O_{57}\{(PO_3C_{21}H_{14}N_3)(PO_3C_{17}H_{26}SH)\}]$  (**4**), the symmetric  $C_{11}SH$  hybrid (**SymC<sub>11</sub>SH**) and symmetric **TPY** hybrid **2** (Fig.118). The same purification procedure of successive solvent extractions used in the preparation of **1** was carried

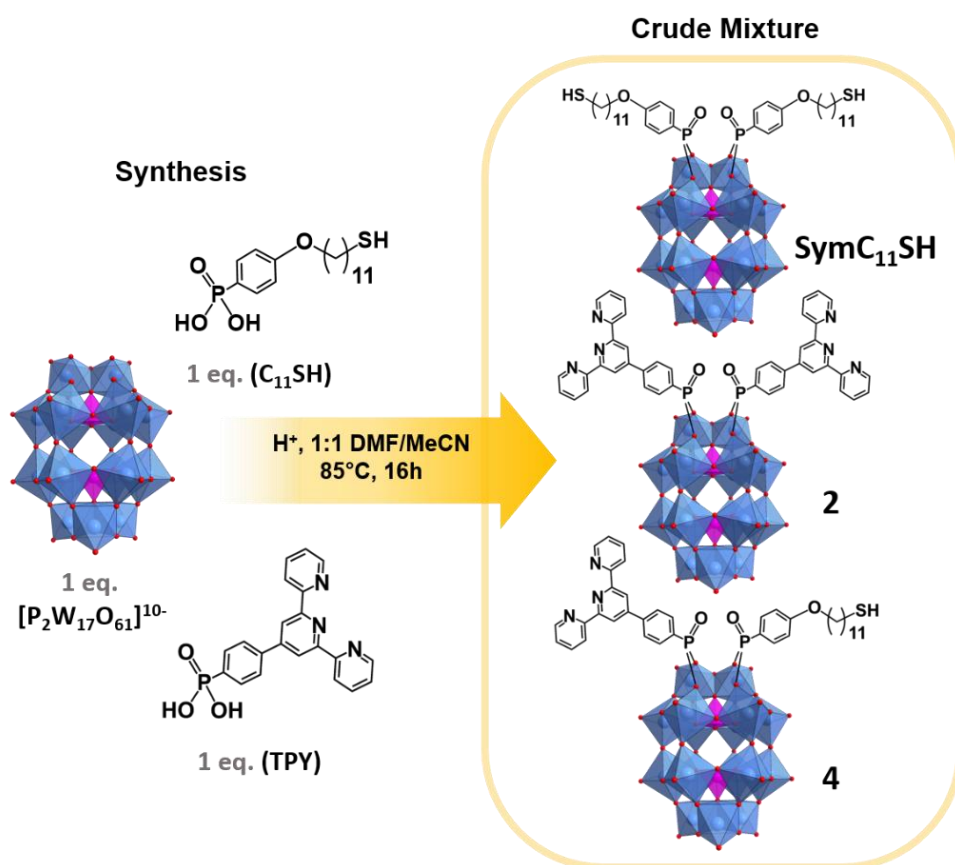


**Figure 117.** One pot synthesis of the asymmetric hybrid POM, **4**, and the crude mixture including the symmetric hybrid side-products, **2** and **SymC<sub>11</sub>SH**.

## 6. Surface-immobilisation of an asymmetric hybrid POM

out (discussed in 6.4.2.2), assuming similar differences in solubility in the hybrid products in this mixture and assessing purity by  $^{31}\text{P}$  NMR (Fig.118). **SymC<sub>11</sub>SH** could be removed in the same way as the symmetric *C<sub>18</sub>* hybrid **3** (Note: **SymC<sub>11</sub>SH** was not isolated or synthesised exclusively for full characterisation). After the addition of excess ether to the reaction mixture, **SymC<sub>11</sub>SH** remains soluble in the ether solvent mixture whilst the other hybrids are precipitated. **2** could then be separated from **4** through washes with acetonitrile, in which **4** is soluble and **2** is insoluble. The separation of the symmetric side products from **4** proved to be slightly less straightforward than in the purification of **1**, requiring more cycles of solvent extractions, but a high purity asymmetric product in good yield was again achievable with multiple batches (~20 %).

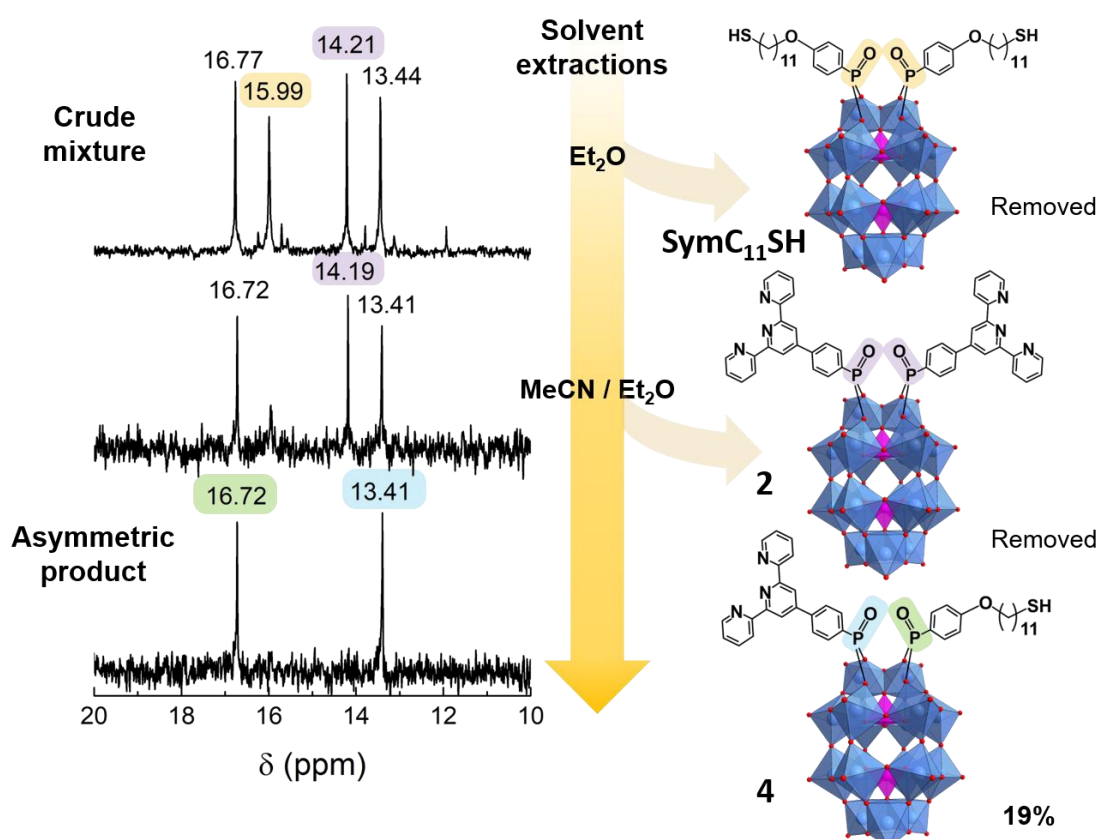


**Figure 118.** Illustration of the purification process of asymmetric hybrid **4** from the crude mixture.  $^{31}\text{P}$  NMR of the reaction mixture in  $\text{DMSO-d}_6$  is shown on the left, taken after each purification step (top: crude; middle **4** + **2**; bottom: **4** only). Chemical shifts corresponding to each product are colour coded as shown (only the positive chemical shift region for the organophosphonate  $^{31}\text{P}$  nuclei is presented for simplicity).

6.1.1 Characterisation of **4**

After sufficient purification, **4** was characterised by  $^1\text{H}$  and  $^{31}\text{P}$  NMR, ESI-MS, IR, CHN analysis and TGA. The asymmetric structure of **4**,  $\text{K}_5(\text{C}_2\text{H}_8\text{N})[\text{P}_2\text{W}_{17}\text{O}_{57}\{(\text{PO}_3\text{C}_{21}\text{H}_{14}\text{N}_3)(\text{PO}_3\text{C}_{17}\text{H}_{26}\text{SH})\}]$ , was confirmed by  $^1\text{H}$  and  $^{31}\text{P}$  NMR. Aliphatic proton signals integrating to total the 22 protons in the  $\text{C}_{11}\text{SH}$  ligand and aromatic proton signals totalling to 18 confirm the presence of both ligands in a 1:1 stoichiometric ratio (Fig.119). The two  $^{31}\text{P}$  signals for the covalently-bound ligands, *TPY* and  $\text{C}_{11}\text{SH}$ , appear at 13.41 and 16.72 ppm respectively, and again are slightly shifted relative to their chemical shifts in the respective symmetric hybrids, as was observed for **1**.

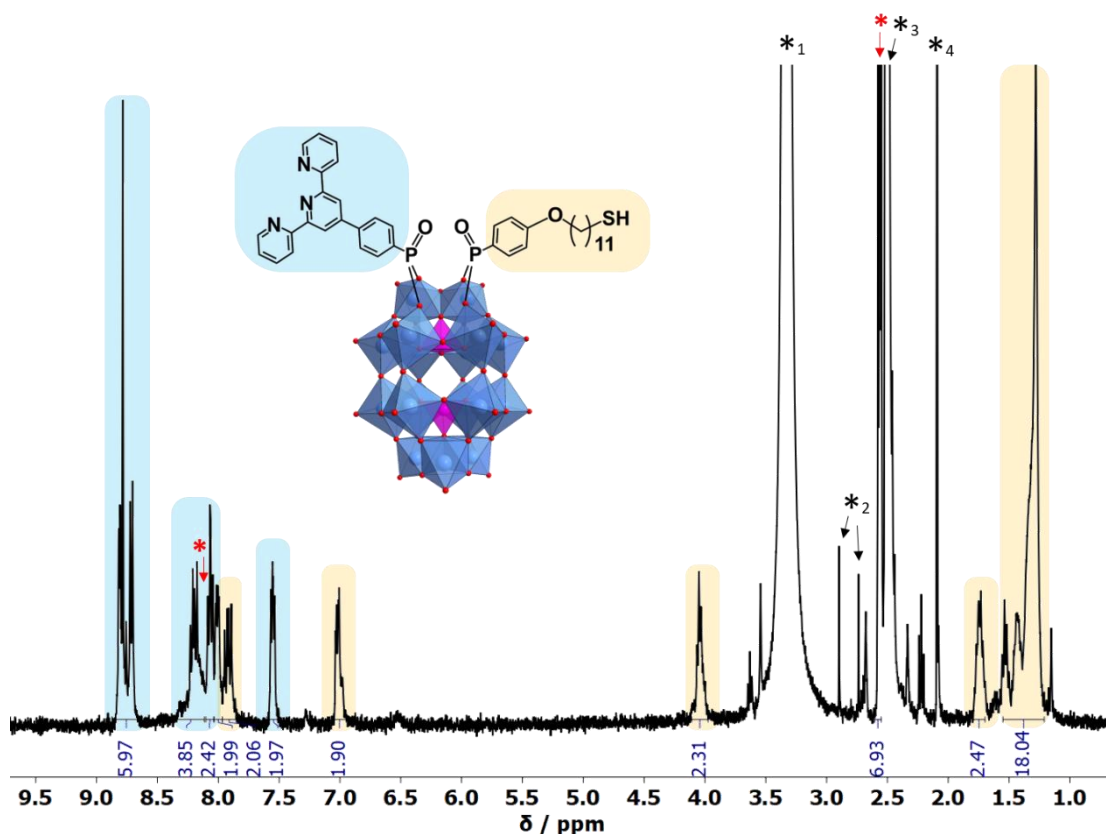


**Figure 119.**  $^1\text{H}$  NMR of **4** in  $\text{DMSO-d}_6$  showing the assignment of signals to each ligand: yellow =  $\text{C}_{11}\text{SH}$ , blue = *TPY*. Red asterisks indicate DMA cation signals, and black asterisks indicate solvent impurities:

1=  $\text{H}_2\text{O}$ , 2= DMF, 3= DMSO, 4 =  $\text{CH}_3\text{CN}$ .



## 6. Surface-immobilisation of an asymmetric hybrid POM

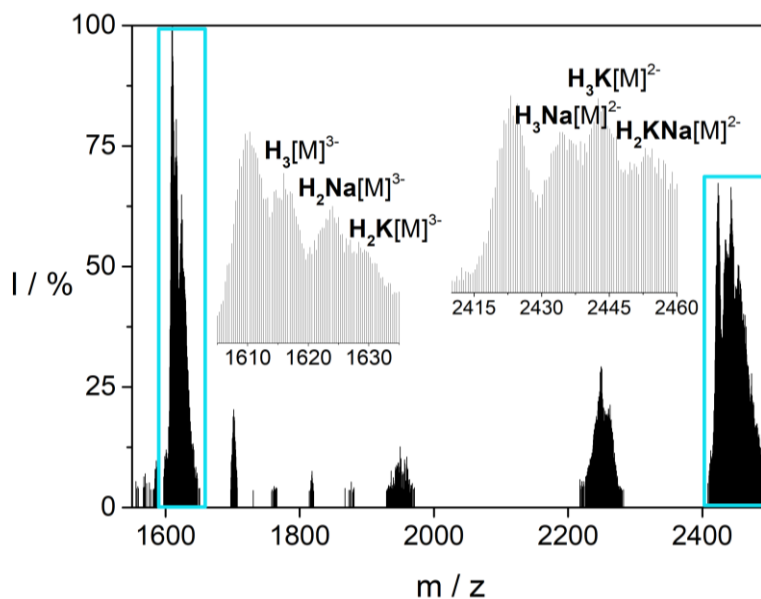


**Figure 120.** Negative mode ESI mass spectrum of **4** in acetonitrile. [M] =  $[P_2W_{17}O_{57}\{(PO_3C_{21}H_{14}N_3)(PO_4C_{17}H_{26}SH)\}]^{6-}$ .

| Assignment   | z  | m/z (obs.) | m/z (calc.) |
|--|----|------------|-------------|
| $H_3[P_2W_{17}O_{57}\{(PO_3C_{21}H_{14}N_3)(PO_4C_{17}H_{26}SH)\}]$    | 3- | 1615.9616  | 1615.9964   |
| $H_2Na[P_2W_{17}O_{57}\{(PO_3C_{21}H_{14}N_3)(PO_4C_{17}H_{26}SH)\}]$  | 3- | 1623.2820  | 1623.3237   |
| $H_2K[P_2W_{17}O_{57}\{(PO_3C_{21}H_{14}N_3)(PO_4C_{17}H_{26}SH)\}]$   | 3- | 1628.5929  | 1628.6483   |
| $H_3Na[P_2W_{17}O_{57}\{(PO_3C_{21}H_{14}N_3)(PO_4C_{17}H_{26}SH)\}]$  | 2- | 2435.6213  | 2435.4894   |
| $H_3K[P_2W_{17}O_{57}\{(PO_3C_{21}H_{14}N_3)(PO_4C_{17}H_{26}SH)\}]$   | 2- | 2443.5988  | 2443.4764   |
| $H_2KNa[P_2W_{17}O_{57}\{(PO_3C_{21}H_{14}N_3)(PO_4C_{17}H_{26}SH)\}]$ | 2- | 2454.5525  | 2454.4674   |

**Table 20.** Selected ESI-MS assignments for **4**.

ESI-MS further confirmed the asymmetric structure, with two series of broad peaks assignable to the complete anionic structure of **4**,  $[P_2W_{17}O_{57}\{(TPY)(C_{11}SH)]^{6-}$ , with 2- and 3- total charges (Fig.120, Table.20). As seen for the other hybrid POMs in this work, the anions were with varying combinations of proton, sodium and potassium cations.

The molecular electrochemistry of **4** was studied by cyclic voltammetry in DMF. Its redox profile closely resembled that of **1**, with four quasi-reversible processes

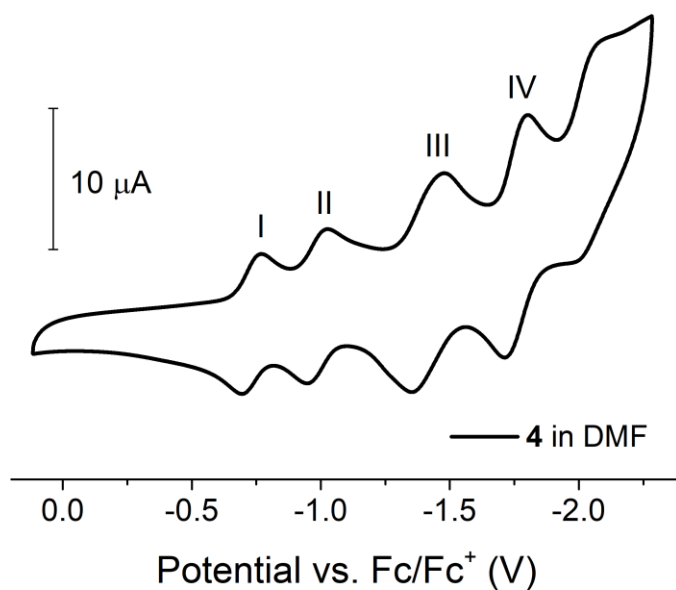


**Figure 121.** Cyclic voltammogram of **4** (0.5 mM) in DMF with 0.1M TBAPF<sub>6</sub> as electrolyte at a glassy carbon working electrode. Scan rate: 100 mVs<sup>-1</sup>.

| Redox potentials vs. Fc/Fc <sup>+</sup> (V) | I             | II            | III           | IV            |
|---|---------------|---------------|---------------|---------------|
| E <sub>red</sub>                            | -0.765        | -1.018        | -1.447        | -1.789        |
| E <sub>ox</sub>                             | -0.689        | -0.946        | -1.336        | -1.695        |
| E <sub>1/2</sub>                            | <b>-0.727</b> | <b>-0.982</b> | <b>-1.392</b> | <b>-1.742</b> |
| ΔE <sub>p</sub>                             | <b>0.076</b>  | <b>0.072</b>  | <b>0.111</b>  | <b>0.094</b>  |

**Table 21.** Redox potentials of **4** in DMF.

observed between  $-0.5$  to  $-2.0$  V vs. Fc/Fc<sup>+</sup> at very similar potentials (Fig.121, Table.21).

### 6.1.2 Self-assembly of **4**

The aliphatic C<sub>11</sub>SH ligand in **4** is expected to impart amphiphilic character on the hybrid as was observed in the other asymmetric C<sub>18</sub> hybrid POMs in this work and its solvent-dependent self-assembly was investigated. **4** was first dissolved in DMF and to it was added water to prepare a 1.4 mM 9:1 (v/v) DMF-H<sub>2</sub>O solution. DLS measurements of the solution confirmed the presence of particles with a

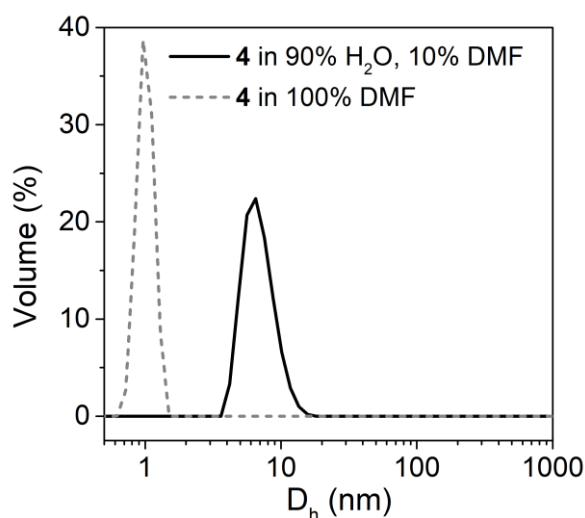


**Figure 122.** Particle-size distribution curve determined by DLS of: **4** (1.4 mM) in a H<sub>2</sub>O-DMF (9:1 v/v) solution- D<sub>h</sub> maximum at 6.5 nm, and **4** (1.4mM) in 100% DMF (grey dashed), D<sub>h</sub> maximum at 1 nm (suggesting discrete molecular species only under these conditions).

hydrodynamic diameter of 6.5 nm comparable to those formed by **1**, suggesting similar micellar assemblies (Fig.122).

The electrochemical behaviour of the **4** nanoassemblies was then studied by cyclic voltammetry in a 9:1 (v/v) 0.1 M H<sub>3</sub>PO<sub>4</sub>-DMF solvent mixture (Fig.123a). DLS measurements of the solution indicated the presence of assemblies slightly larger than those observed in the H<sub>2</sub>O-DMF mixture, with a peak D<sub>h</sub> of 21 nm (Fig.123b). This was similarly observed in the electrolyte solution of **1** (see 4.1.1) and is likely an effect of the high ionic concentration on the assembly size and/or aggregation. Interestingly, the features in the CV do not appear as distinct from the molecular CV in DMF as in the equivalent electrochemical studies for **1**. In comparison to **1**, the first two redox processes in the range from +0.5 to -0.5 V (vs. Ag/Ag<sup>+</sup>) appear to have coalesced to a lesser extent, with both reduction peaks still distinguishable (Fig.123a). On addition of DMF, the three redox processes in this window then become more distinct, as was observed in the equivalent experiment for **1**.

The shorter chain length in the C<sub>11</sub>SH ligand likely influences the assembly of **4** into micellar structures differently to C<sub>18</sub> in **1**. Amin *et al.* recently reported the effect of

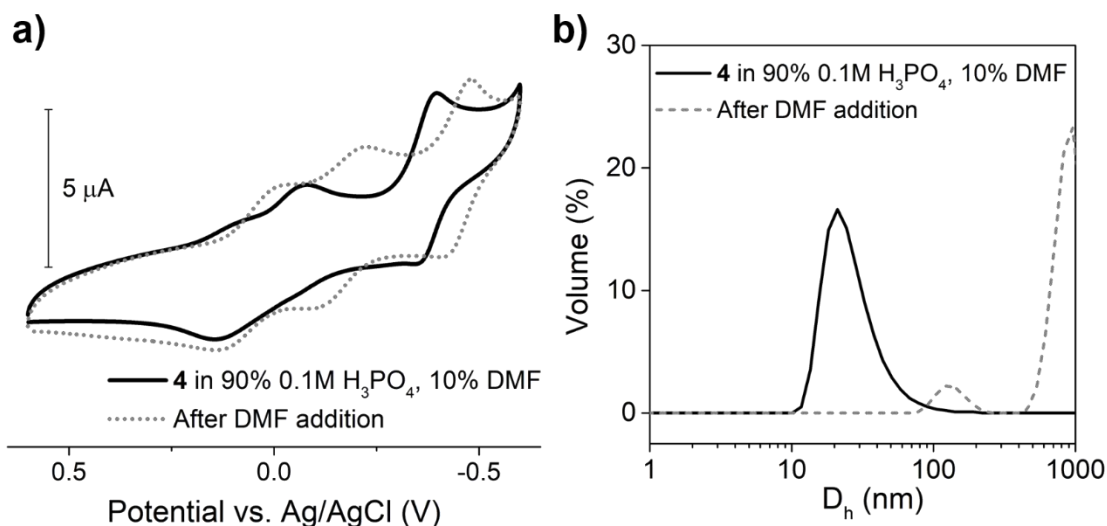


**Figure 123.** a) Comparison of the cyclic voltammograms of **4** (1.4 mM) in 90%  $\text{H}_3\text{PO}_4$  (0.1 M) 10% DMF (black) and after the addition of the same volume of DMF ( $c_{\text{new}} = 0.7$  mM) (grey dotted). Scan rate:  $100 \text{ mVs}^{-1}$ ; b) Particle-size distribution curves determined by DLS of the CV solution of **4** before (black),  $D_h$  maxima at 21.0 nm, and after (grey dashed) the addition of the same volume of DMF,  $D_h$  maxima at 122 nm and 955 nm.

chain length in a series of surfactant symmetric hybrid POMs,  $\text{K}_6[\text{P}_2\text{W}_{17}\text{O}_{57}\{(\text{PO}_3\text{C}_6\text{H}_4\text{O}(\text{C}_n\text{H}_{2n+1}))_2\}]$  ( $n = 10, 12, 14, 16, 18$  and  $20$ ), on the stability and electrochemistry of their supramolecular assemblies.<sup>[18]</sup> The hybrid POMs with ligand chain lengths of  $n \leq 14$  displayed redox behaviour in aqueous electrolyte that was more typical of the molecular species, with the separation between the first two redox processes becoming more apparent with decreasing chain length. This was attributed to a higher concentration of free molecular species in solution due to the reduced stability of the micelles. This may be an effect of the high angle (*ca.*  $160^\circ$ ) between the two chain ligands that restricts their flexibility in ‘bending’ inwardly in micelles more so in the shorter chain species. However, this is not relevant in the asymmetric amphiphilic hybrid POMs, and it could instead be due to effects of steric hindrance between the outward facing *TPY* groups which would be increased with shorter chain lengths.

## 6.2 Surface-immobilisation of **4**

### 6.2.1 Surface-confined electrochemistry of **4**

The immobilisation of **4** on gold was investigated by probing its surface-confined electrochemistry by CV experiments at a gold electrode. A monolayer of **4** was fabricated by immersing a clean gold disk electrode in a stirred solution of **4** in DMF for 24 h. The electrode was first thoroughly rinsed with DMF to ensure the removal of any non-covalently grafted hybrid POM before it was then placed in fresh electrolyte (0.1 M TBAPF<sub>6</sub> in DMF) solution for CV experiments. Three reversible redox processes were observed from +0.5 to -1.0 V (vs. Ag/Ag<sup>+</sup>) indicative of the presence of **4** (Fig.124a), and the redox profile did not change after numerous cycles, suggesting the successful covalent grafting of a stable layer of **4** onto the electrode surface. In comparison, CV experiments of **1** using a gold electrode after the same preparation procedure showed no clear, surface-confined POM redox processes (Fig.124b), and

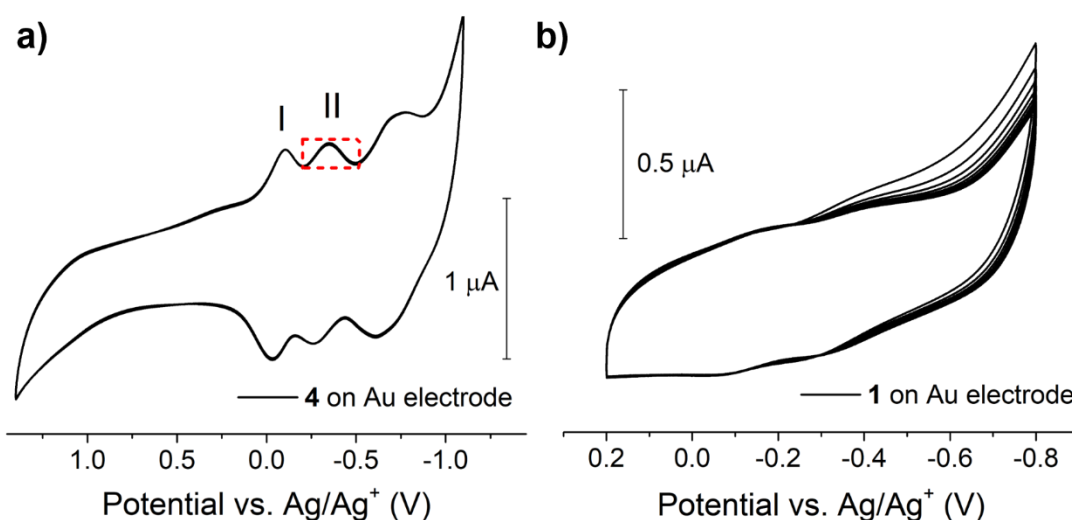


**Figure 124.** Cyclic voltammograms of: **a)** **4** fabricated as a layer on a gold disk electrode, reduction peak used for surface coverage calculations is highlighted in the red box; **b)** **1** using a gold disk electrode over 10 cycles. Both in DMF with 0.1M TBAPF<sub>6</sub> as electrolyte. Scan rate 100 mVs<sup>-1</sup>.

## 6. Surface-immobilisation of an asymmetric hybrid POM

very subtle features ambiguously visible amongst the background current were shown to be unstable with cycling, suggestive of only weakly bound species, if present at all.

The peaks in the CV of surface-bound **4** appear more Gaussian-like in shape in comparison to the peaks observed in the solution CV of **4** using a carbon electrode. This Gaussian shape is typical for a diffusion-controlled solution phase CV and is particularly prominent for the 2<sup>nd</sup> reduction process (Fig.125a). For a surface-confined redox process in an adsorbate layer, the faradaic current,  $i_p$ , should also be directly proportional to the scan rate,  $v$ , as described by the equation:

$$i_p = \frac{n^2 F^2}{4RT} v A \Gamma = (9.39 \times 10^5) n^2 v A \Gamma$$

where  $A$  is the area of the electrode,  $\Gamma$  is the surface coverage of adsorbate, and  $n$  is the number of electrons involved in the redox process.<sup>[19-20]</sup> The linear fits of the peak currents for the reduction and oxidation peaks for the first two redox processes

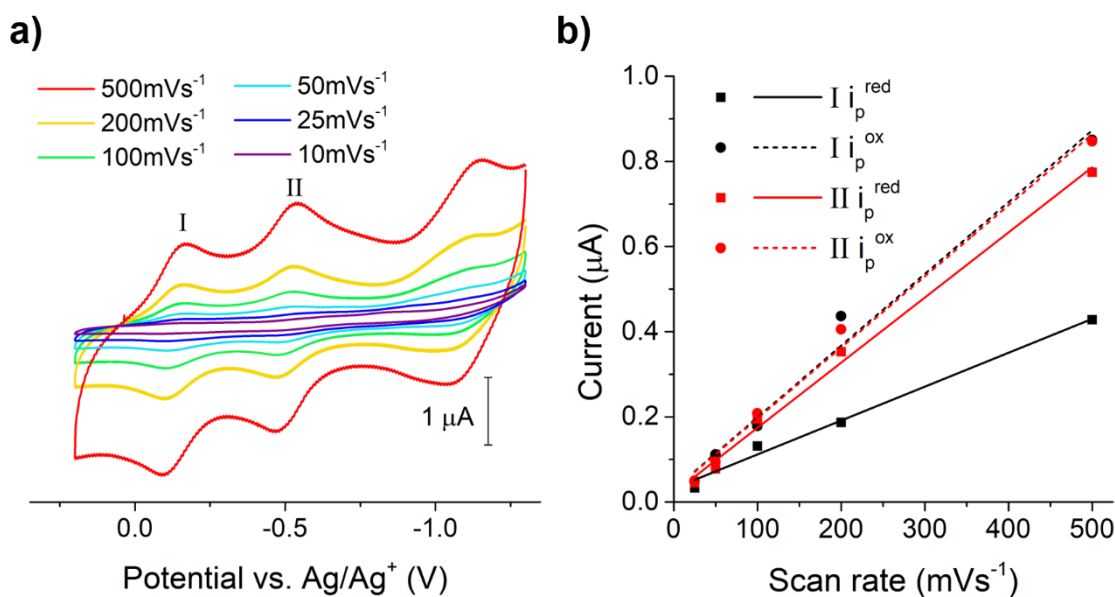


**Figure 125.** a) Cyclic voltammograms of **4** on a Au working electrode at different scan rates in DMF with 0.1M TBAPF<sub>6</sub> as electrolyte; b) Plots of peak current vs. scan rate for the reduction and oxidation peaks of the first two redox processes of **4** showing the linear fits.

## 6. Surface-immobilisation of an asymmetric hybrid POM

plotted against different scan rates are well-fitted, particularly for process II ( $R^2=0.9931$  ( $i_p^{\text{red}}$ ),  $0.9906$  ( $i_p^{\text{ox}}$ )) (Fig.125a,b).

Additionally, for an ideal reversible surface-confined electron transfer process the expected peak-to-peak separation,  $\Delta E_p$ , should be zero. However, even at low scan rates peak separations of 39 and 56 mV are observed for redox processes I and II respectively, suggesting that the rate of electron transfer between the POM and electrode is limited somewhat (Table.22). Experimental surface-confined systems are seldom ideal, but this could be largely attributed to the long distance between the redox-active POM cluster and the electrode, assuming the hybrid POMs in the monolayer are arranged with the  $C_{11}SH$  linkers fully extended.

The surface coverage,  $\Gamma$ , of **4** can be estimated from the charge passed,  $Q$ , which is determined by finding the area under the background-subtracted peak, according to the equation:<sup>[19-20]</sup>

$$\Gamma = Q/nFA$$

By integration of the most Gaussian-like peak, for the 1-electron reduction of process II, a surface coverage of  $6.64 \times 10^{-11} \text{ mol}^{-1}\text{cm}^2$ , or  $4 \times 10^{13} \text{ molecules}^{-1}\text{cm}^2$ , for **4** can be

| Scan rate<br>(mVs <sup>-1</sup> ) | Potential vs. Ag/Ag <sup>+</sup> (V) |                 |                 |                  |                 |                 |
|-----------------------------------|--------------------------------------|-----------------|-----------------|------------------|-----------------|-----------------|
|                                   | I                                    |                 |                 | II               |                 |                 |
|                                   | E <sub>red</sub>                     | E <sub>ox</sub> | ΔE <sub>p</sub> | E <sub>red</sub> | E <sub>ox</sub> | ΔE <sub>p</sub> |
| 500                               | -0.175                               | -0.089          | <b>0.086</b>    | -0.544           | -0.469          | <b>0.075</b>    |
| 200                               | -0.162                               | -0.100          | <b>0.062</b>    | -0.530           | -0.468          | <b>0.062</b>    |
| 100                               | -0.142                               | -0.101          | <b>0.041</b>    | -0.529           | -0.474          | <b>0.055</b>    |
| 50                                | -0.142                               | -0.102          | <b>0.040</b>    | -0.529           | -0.474          | <b>0.055</b>    |
| 25                                | -0.148                               | -0.109          | <b>0.039</b>    | -0.551           | -0.495          | <b>0.056</b>    |
| 10                                | -0.152                               | -0.089          | <b>0.063</b>    | -                | -               | -               |

**Table 22.** Peak potentials for the first and second redox processes of **4** on a Au electrode at different scan rates as seen in Fig.125a.

## 6. Surface-immobilisation of an asymmetric hybrid POM

---

estimated, which closely fits the typical adsorbate coverage for monolayers.<sup>[19]</sup> This corresponds to an area of approximately 2.5 nm<sup>2</sup> per molecule, which suggests reasonably tight packing of the POMs in the monolayer (the Dawson anion is approximately 1 nm in size). The hybrid POMs can, therefore, be expected to be arranged with the *C<sub>11</sub>SH* spacer chains extended outwards at a low tilt angle, or near perpendicular, from the electrode surface. This could explain the observed non-zero  $\Delta E_p$  values because of the slowed electron transfer across the distance that is the length of *C<sub>11</sub>SH* (~17 Å, determined by 3D modelling). The rate of electron transfer between redox-active centres and gold connected by alkylthiols has been shown to depend on the distance between them, often decreasing with increasing alkane length. For example, rate constants were shown to vary from 10<sup>2</sup> s<sup>-1</sup> to 10<sup>6</sup> s<sup>-1</sup> for alkyl chains that are 5-13 methylene units long between a ferrocene centre and gold electrode.<sup>[21]</sup> Furthermore, in a similar POM hybrid system reported by Yaqub *et al.*, slower electron transfer was observed for a Keggin grafted to a gold electrode by a longer thioacetyl-terminated alkyl linker than for its shorter analogue.<sup>[22]</sup> However, the limitations in electron transfer in **4**-modified gold surfaces will be much more complex, considering additional factors such as the dynamics of the reorganisation of solvent and counter-cations in the monolayer.<sup>[20]</sup>

This dense patterning of covalently bound hybrid Dawson POMs on a conductive surface is promising as a material for electronic devices,<sup>[23]</sup> and with the free *TPY* functionalities at the surface, the material could also be effective as a sensor for metallic ions. Additionally, potential effects of surface-confinement could have implications on the electro- and/or photo-catalytic activity of the hybrid POM, particularly in consideration of grafted derivatives of the asymmetric hybrid structure in which a photosensitising or catalytic organometallic complex is appended, such as in the structures of **Pt-1** or **Ru-1** discussed in Chapter 5.

Future investigation will look at the tuning of the electronic properties of the hybrid POM SAM through the precise molecular design of the linker functionality, for example, by the introduction of conjugation to increase electrical conductivity between the Dawson anion and gold surface. Further analysis would focus on imaging a monolayer of **4** on Au, using techniques such as STM, AFM, and ellipsometry, to



understand how **4** is arranged on the surface, as well as probing the surface interactions by spectroscopies such as XPS and Raman. Comparative studies on the micellar assemblies of **4** would also be interesting, to see how the different surface interactions of the molecular and supramolecular forms of **4** on gold affect its surface patterning and redox behaviour.

### 6.2.2 Surface modification of gold nanoparticles by **4**

Gold nanoparticles (AuNPs) offer another interesting scaffold for the nanostructuring of hybrid POMs. They make versatile components of hybrid materials with their unique optoelectronic properties and tuneability by their size, shape, and rich surface functionalisation chemistry.<sup>[24]</sup> Detectable changes in their characteristic surface plasmon resonance (SPR) absorption, conductivity and redox activity render them particularly effective as materials in sensor applications.<sup>[25]</sup>

POMs have been used to stabilise and functionalise AuNPs in many studies, displaying promise in new photo- and electrocatalysis, sensing, and biomedical applications.<sup>[26]</sup> Notably, POM-AuNP composite systems in which hybrid POMs are directly attached as capping agents to AuNPs are much less explored than electrostatic POM-AuNP systems. Understanding the stability and emergent properties of these capped systems is valuable in the preparation of tailored POM-based nanomaterials, and just a few studies have started to explore this.

Polartz *et al.* recently reported the impressive enhancement in catalytic activity of a hybrid Keggin after its direct attachment to AuNPs via thiol-terminated siloxane ligands.<sup>[27]</sup> This was attributed to synergistic coupling between the AuNP SPR and the catalytic activity of the Keggin cluster, because of an increase in catalytic activity that was observed with shorter lengths of alkylthiol linker and specific green light irradiation. Additionally, our research group recently reported the preparation of highly stable hybrid POM capped AuNPs, in which symmetric  $C_{11}SH$  hybrid POMs are directly attached via terminating thiol groups on the organophosphonate ligands. The POM-NP composite demonstrated to be an effective photochemically active material,

## 6. Surface-immobilisation of an asymmetric hybrid POM

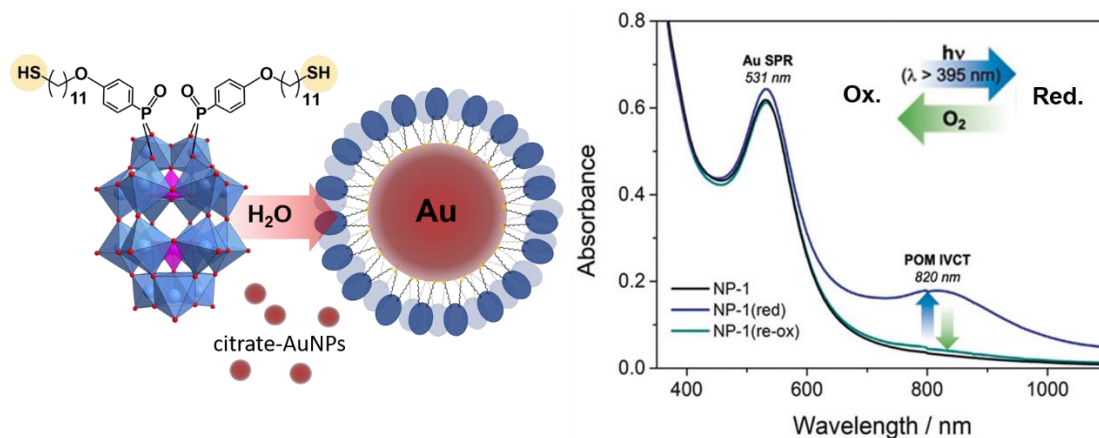


**Figure 126.** Left: Preparation of AuNPs stabilised by a symmetric thiol-terminated POM hybrid; right: UV-Vis absorption spectra of the hybrid NPs before and after photoreduction of the capping POMs with visible light (>395 nm), and after re-oxidation, showing recovery of the native state. Adapted from reference 17.

displaying reversible photoreduction under visible light irradiation (>395nm) whilst retaining excellent stability, which could be promising for photocatalytic applications (Fig.126).<sup>[17]</sup>

As highly versatile platforms, asymmetric hybrid POMs could be especially effective in tailoring properties and synergistic interactions in these hybrid systems. The asymmetric hybrid POM **4** is enabled to assemble on the surface of AuNPs, but with its single grafting moiety, C<sub>11</sub>SH, the arrangement and orientations of the POMs in the monolayer will be different to in the previously reported symmetric hybrid systems. Importantly, unique tuneability is available through both surface-grafted and non-grafted organic moieties in the hybrid POM-NP material, as the second, free appended organic group on **4** offers additional opportunity in tuning the structure and function of the hybrid POM SAM. These design features could have interesting implications on the stability of the composite material and in the tuning of its electronic and optical properties, such as the electrical conductivity in the hybrid POM SAM and the gold SPR.

The preparation of **4**-stabilised AuNP composites has been briefly investigated, by adapting slightly the procedure reported by Martin *et al.*<sup>[17]</sup> A solution of 10 nm

## 6. Surface-immobilisation of an asymmetric hybrid POM

citrate-stabilised AuNPs in water was added to a concentrated solution of **4** in acetonitrile and stirred at RT for two days (Fig.127). The NPs were then collected by precipitation from an excess of methanol as a dark-red solid and washed before characterisation.

The UV-Vis spectrum of the solid material dissolved in DMF exhibits features that are characteristic of both the AuNPs and **4**: an SPR absorption at 527 nm and an intense absorption centred at *ca.* 275 nm attributed to the LMCT band of the POM anion (Fig.128a). The SPR peak wavelength does not appear shifted from that in the citrate-stabilised precursor AuNPs, unlike for the NPs modified by the reported symmetric  $C_{11}SH$  hybrid POM (+4 nm shift).<sup>[17]</sup> However, the earlier emergence and drastic ascent of the high energy band in comparison to that seen in the AuNP precursor is highly supportive of the presence of POMs, but whether they are covalently bound is not definitive from the spectrum.

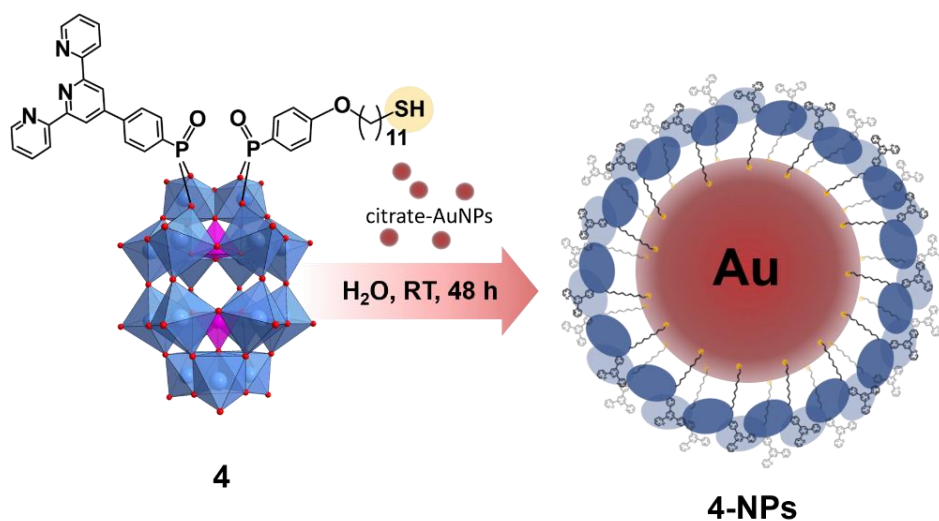


**Figure 127.** Preparation of **4**-modified AuNPs, **4-NPs**.

## 6. Surface-immobilisation of an asymmetric hybrid POM

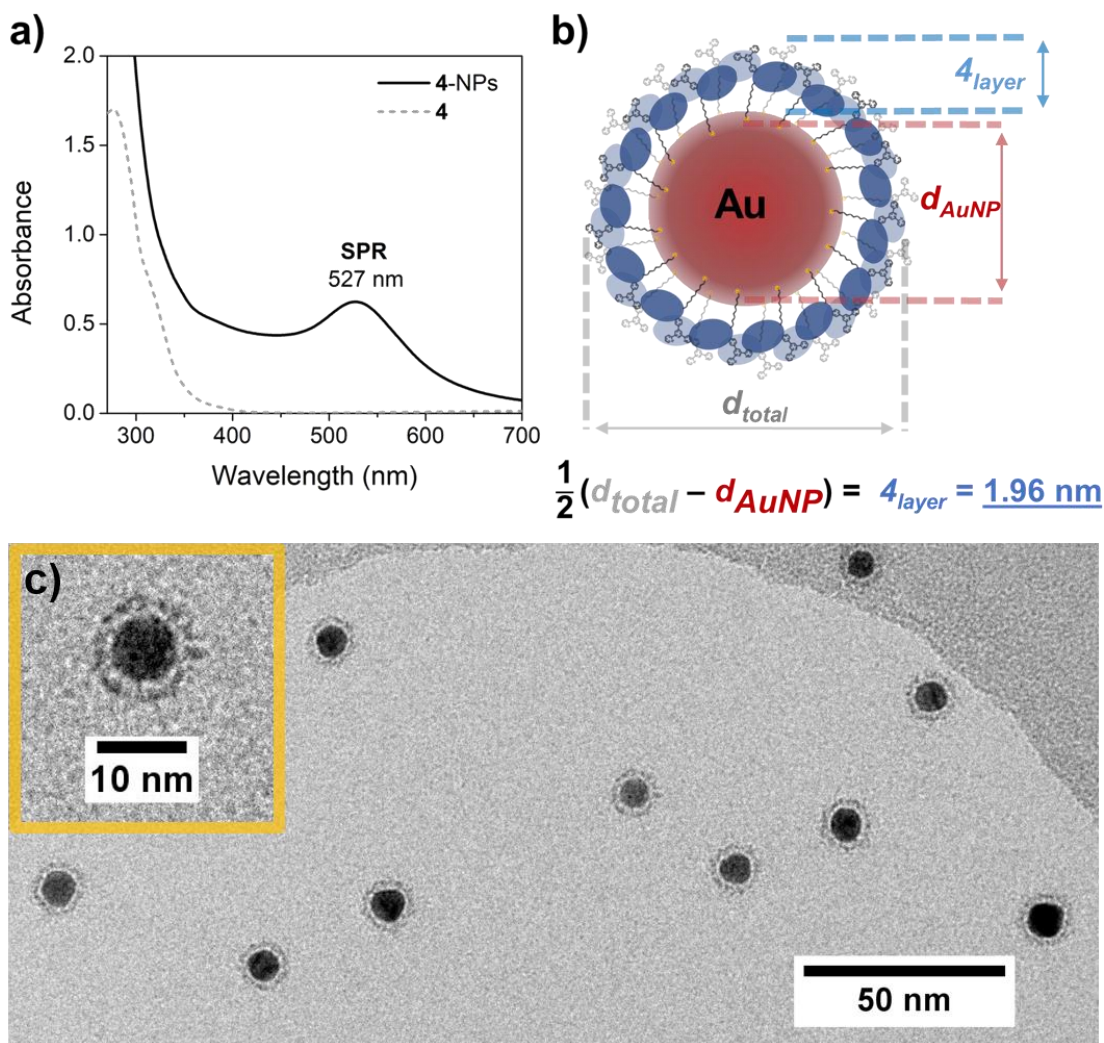


**Figure 128.** a) UV-Vis absorption spectrum of **4** and **4-NPs** in DMF, both 0.5 mg in 5 mL; b) Estimation of the thickness of surface layer of **4** ( $4_{layer}$ ) from the diameter of **4-NPs** ( $d_{total}$ ) and diameter of the AuNP core ( $d_{AuNP}$ ); c) TEM image of **4-NPs** with inset showing a single **4**-modified AuNP.

TEM imaging of the solution, however, strongly supports the attachment of **4** onto the surface of AuNPs. Monodisperse NPs with an average diameter of 8.3 nm could be seen that are surrounded by well-resolved rings, indicative of a surface layer of POMs due to the high contrast of W (Fig.128c). The thickness of this layer of **4** is approximated as 1.96 nm, which fits with the expected size of a molecule of **4** across the length of both ligands (Fig.128b). In agreement, energy-dispersive X-ray (EDX) mapping analysis of the sample showed concentrated regions of W, P and S at the AuNP locations, suggestive of the successful capping of AuNPs by molecules of **4** (Fig.129).

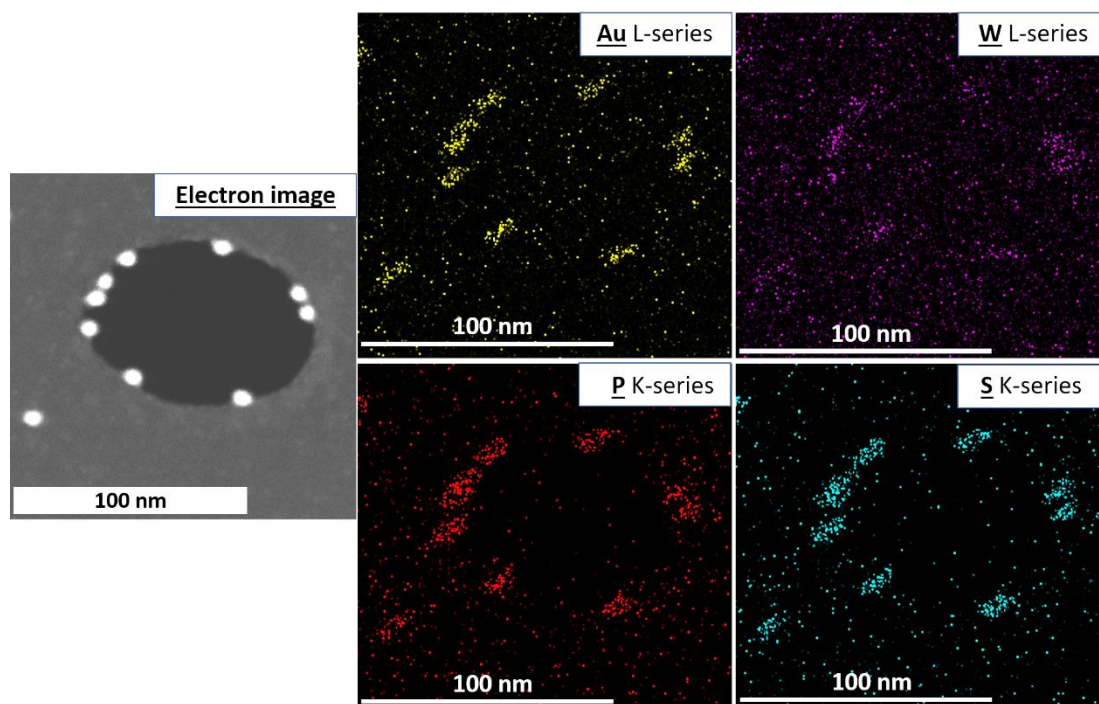
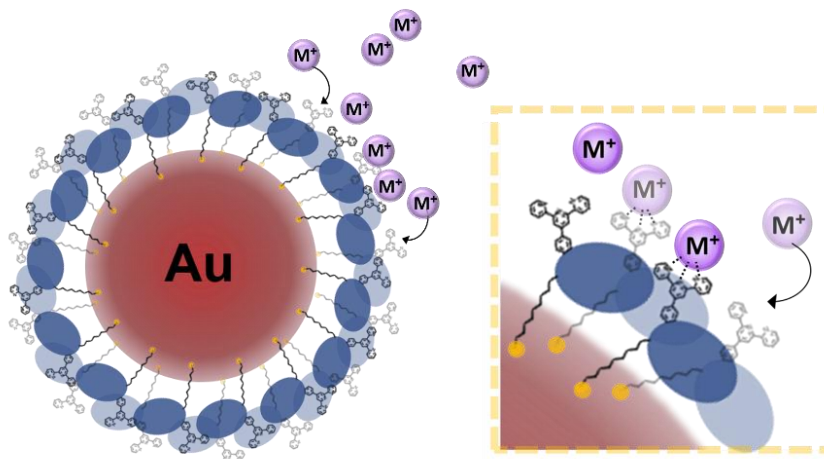


Figure 129. EDX mapping analysis of **4**-NPs.

Crucially, with the unique asymmetric structure of **4**, the *TPY* moiety enables AuNPs modified with a monolayer of **4** to be equipped for chemosensing applications through its capability to bind to metal ions (Fig.130). Furthermore, metal ions complexed in the monolayers protecting the surface of AuNPs can themselves act as additional recognition sites or imaging agents for other molecules, including biomacromolecules such as proteins or DNA.<sup>[28]</sup> For example, the combination of a Ru<sup>II</sup>-polypyridyl complex with AuNPs can be highly sensitive material both as a luminescent probe for DNA binding and as an imaging agent for cellular uptake.<sup>[29]</sup>

Considering this, further studies would investigate the metal-ion sensing of the hybrid material by the addition of various metal cations to a solution of **4**-NPs. The photochemical stability and reactivity of **4**-NPs will also be studied as an interesting comparison to the photochemically-active POM-AuNP systems mentioned above formed from symmetric hybrid POM surfactants. Finally, the capping of AuNPs by a



**Figure 130.** Depiction of the metal-ion sensing by coordination at *TPY* sites of **4**-modified AuNP composites.

derivative of the asymmetric hybrid POM structure in which an organometallic complex is grafted will also be explored, as it could lead to the design of novel, highly complex photocatalytic systems.

### 6.3 Conclusion

The incorporation of additional functionality at the end of the hydrophobic chain moiety in an asymmetric hybrid POM derivative of **1**, has been investigated. A new asymmetric hybrid Dawson with a thiol-terminated alkyl chain ligand has been synthesised by a one-pot procedure as established for the asymmetric hybrid **1**. The amphiphilic hybrid POM displays solvent-dependent self-assembly as observed for the other asymmetric hybrid POM systems in this thesis (in 4.1, 5.1.3 & 5.2.3.1). However, now with an additional functionality on the chain group, a terminal thiol, the covalent immobilisation of the asymmetric hybrid POM onto gold materials in a single step is also enabled.

Its fabrication as a redox-active monolayer onto a surface has been demonstrated through CV experiments on a gold electrode which confirm surface-confined electrochemical behaviour. Additionally, a new composite material comprised of AuNPs surface-modified by the asymmetric hybrid POM, has been prepared and

briefly characterised. The unique surface functionalities of the modified gold materials, with available chelating sites for metal ion coordination on the second ligand, can potentially lead to novel applications for the asymmetric hybrid Dawson POM as an advanced sensing or electro- or photocatalytic material.

This work has further explored how an asymmetrically hybridised POM can be used as a highly versatile platform by which multiple functionalities can be introduced and tailored into a hybrid POM through the molecular design of the individual components. Ultimately, the modular design approach presented demonstrates great potential for the development of new multifunctional molecular systems, nanomaterials and devices based on POMs.

### 6.4 Experimental details

#### 6.4.1 Methods

Methods used are as outlined in Section 3.7, unless specified below.

Electrochemical measurements were performed on CHI600e and CHI450c (CH Instruments) workstations. CV experiments under non-aqueous conditions were performed using a three-electrode arrangement; working electrode (glassy carbon,  $d = 3\text{ mm}$  or gold  $d = 2\text{ mm}$ ), reference electrode (Ag wire) and a counter electrode (Pt wire) in TBAPF<sub>6</sub> (0.1 M) as the supporting electrolyte in dry DMF. Experiments under aqueous conditions were performed using a working electrode (glassy carbon,  $d = 3\text{ mm}$ ), reference electrode (Ag/AgCl) and a counter electrode (Pt wire). For surface-confined electrochemistry experiments, the 2 mm diameter gold disk electrode was prepared by polishing on porous neoprene before immersing in piranha solution (30% H<sub>2</sub>O<sub>2</sub>–conc. H<sub>2</sub>SO<sub>4</sub>, 1:3 v/v) for 10 min. The electrode was rinsed with Milli-Q water before cycling in a 0.1 M HClO<sub>4</sub> solution from -0.1 to 1.1 V for: 10 cycles at 100 mVs<sup>-1</sup>, then 10 cycles at 500 mVs<sup>-1</sup> before another 10 cycles at 100 mVs<sup>-1</sup>. A monolayer of POM was then fabricated by immersing the clean gold electrode in a stirred 1 mM solution of POM in DMF for 24 h. The electrode was then rinsed thoroughly with DMF before it was placed in fresh electrolyte solution (0.1 M TBAPF<sub>6</sub> in DMF) for the CV

## 6. Surface-immobilisation of an asymmetric hybrid POM

experiments. All solutions were purged with nitrogen for 10 mins and kept under a positive pressure of nitrogen for the duration of the experiment.

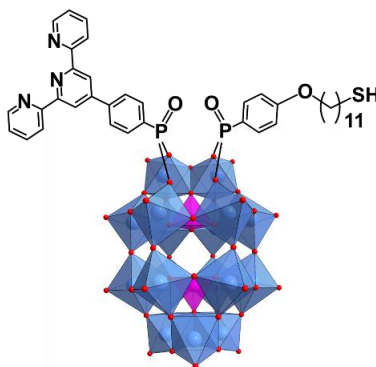
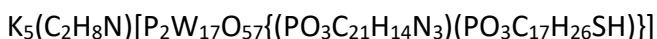
TEM experiments were run by Dr. Michael Fay at the Nanoscale and Microscale Research Centre (University of Nottingham) on a JEOL 2100F operating at 200 kV, equipped with a Gatan Orius camera for imaging and an Oxford Instruments XMax 80 for EDX analysis. Samples (0.5 mg in 5 mL DMF) were dispersed onto graphene oxide on holey carbon film supports (EM Resolutions).

### 6.4.2 Syntheses

#### 6.4.2.1 C<sub>11</sub>SH

C<sub>11</sub>SH was prepared and supplied by Dr Carmen Martin-Gandul.<sup>[17]</sup>

#### 6.4.2.2 [P<sub>2</sub>W<sub>17</sub>O<sub>57</sub>{(TPY)(C<sub>11</sub>SH)}] (4)



K<sub>10</sub>-[P<sub>2</sub>W<sub>17</sub>O<sub>61</sub>] (2 g, 0.439 mmol), TPY (0.171 g, 0.439 mmol), C<sub>11</sub>SH (0.158 g, 0.439 mmol), and KCl (0.65 g, 8.72 mmol) were suspended in DMF (35 mL) and stirred. 12M HCl (256 μL, 3.07 mmol) was added dropwise to the solution whilst stirring, and the mixture was heated to 85°C for 19 h. The mixture was allowed to cool to RT before filtering. An excess of ether was added (75 mL) to give a milky yellow solution, which was centrifuged to give a beige precipitate in a yellow supernatant. The solvent was decanted and the process of sonicating the precipitate in ether, centrifuging and decanting was repeated until the precipitate resembled a free-flowing beige powder. The solid was then sonicated in acetonitrile (10 mL) and centrifuged to separate an



## 6. Surface-immobilisation of an asymmetric hybrid POM

---

insoluble pale green-blue solid. The yellow supernatant was decanted and ether was added (20 mL) to it to precipitate a pale orange-beige solid and leave a pale yellow supernatant. The process of: re-dissolving in acetonitrile and centrifuging to remove any insoluble **2**, followed by re-precipitating **4** from the supernatant with ether, was repeated until no **2** or **SymC<sub>11</sub>SH** was visible in the <sup>31</sup>P and <sup>1</sup>H NMR. The solid was collected by centrifugation, sonicated in ether and centrifuged again. The solvent was decanted and the solid was dried in air with gentle heating to yield **4** as an orange-beige solid (416 mg, 19%).

<sup>1</sup>H NMR (400.1 MHz, DMSO-d<sub>6</sub>) δ = 8.84-8.65 (m, 6H; Ar-H), 8.26-8.16 (m, 2H; Ar-H), 8.16 (br, 2H; NH<sub>2</sub>(CH<sub>3</sub>)<sub>2</sub><sup>+</sup>), 8.08-8.01 (m, 2H; Ar-H), 8.01-7.96 (m, 2H; Ar-H), 7.94-7.97 (m, 2H; Ar-H), 7.56-7.50 (m, 2H; Ar-H), 7.04-6.98 (m, 2H; Ar-H), 4.07-3.97 (m, 2H; O-CH<sub>2</sub>), 2.55 (s, 6H; NH<sub>2</sub>(CH<sub>3</sub>)<sub>2</sub><sup>+</sup>), 1.78-1.67 (m, 2H; CH<sub>2</sub>-SH), 1.66-1.19 (m, 18H; -CH<sub>2</sub>-) ppm; <sup>31</sup>P NMR (162 MHz, DMSO-d<sub>6</sub>) δ = 16.72, 13.41, -11.33, -12.95 ppm; IR (ATR): 424 (s), 471 (s), 527 (s), 568 (s), 578 (s), 595 (s), 729 (br, vs), 764 (br, vs), 908 (s), 953 (s), 1087 (s), 1134 (w), 1253 (w), 1295 (w), 1391 (w), 1414 (w), 1465 (m), 1504 (w), 1531 (w), 1597 (m), 1651 (w), 2852 (m), 2927 (m) cm<sup>-1</sup>; **Elemental Analysis:** calc (%) for K<sub>5</sub>P<sub>4</sub>W<sub>17</sub>O<sub>64</sub>C<sub>40</sub>H<sub>49</sub>N<sub>4</sub>S<sub>1</sub>: C 9.45, H 0.97, N 1.10, found: C 9.47, H 1.21, N 0.78; **TGA Analysis:** Step transition (234.0 to 301.5°C) wt loss of 1.260 % = loss of 1 C<sub>2</sub>H<sub>8</sub>N<sup>+</sup> (DMA<sup>+</sup>) (calc = 0.906 %); **UV/Vis (DMF):** λ<sub>max</sub> (ε, mol<sup>-1</sup>Lcm<sup>-1</sup>) = 276 (88,100), 315 (38,100) nm.

### 6.4.2.3 4-NPs

The procedure reported by Martin *et al.* was adapted for the preparation of **4**-stabilised AuNPs.<sup>[17]</sup> Assuming ~400 POMs are needed per AuNP as determined by Martin *et al.*, **4** was used in approximately 20 times excess of this.

**4** (10 mg, 1.97 μmol) was dissolved in CH<sub>3</sub>CN (2 mL) before a solution of citrate-stabilised AuNPs in water (10 nm, Sigma Aldrich, 25 mL, OD 1, ~6.0<sup>12</sup> particles/mL) was added to it whilst stirring. The solution was stirred at RT in the dark for 2 days. The solution was centrifuged, and the supernatant was decanted from a small amount of insoluble material. The solvent was concentrated by removal in *vacuo* to ~ 1-2 mL,

## 6. Surface-immobilisation of an asymmetric hybrid POM

---

before an excess of MeOH was then added (~40 mL). The solution was centrifuged for 15 mins at 8000 rpm and the supernatant was decanted from a dark red-black precipitate. The precipitate was washed with MeOH-CH<sub>3</sub>CN (1:1 v/v, 3 mL) three times and then once with ether (3 mL), collecting it each time by centrifugation (10 mins at 8000 rpm). Finally, the solid was allowed to dry in air to yield **4-NPs** as a dark red solid (0.5 mg).

## 6.5 References

- [1] A. S. Cherevan, S. P. Nandan, I. Roger, R. Liu, C. Streb, D. Eder, Polyoxometalates on Functional Substrates: Concepts, Synergies, and Future Perspectives, *Adv. Sci.*, 2020, **7**, 1903511.
- [2] C. Rinfray, G. Izzet, J. Pinson, S. Gam Derouich, J.-J. Ganem, C. Combellas, F. Kanoufi, A. Proust, Electrografting of Diazonium-Functionalized Polyoxometalates: Synthesis, Immobilisation and Electron-Transfer Characterisation from Glassy Carbon, *Chem. Eur. J.*, 2013, **19**, 13838-13846.
- [3] R. Solarska, K. Bienkowski, S. Zoladek, A. Majcher, T. Stefaniuk, P. J. Kulesza, J. Augustynski, Enhanced Water Splitting at Thin Film Tungsten Trioxide Photoanodes Bearing Plasmonic Gold-Polyoxometalate Particles, *Angew. Chem. Int. Ed.*, 2014, **53**, 14196-14200.
- [4] D. Mercier, S. Boujday, C. Annabi, R. Villanneau, C.-M. Pradier, A. Proust, Bifunctional Polyoxometalates for Planar Gold Surface Nanostructuring and Protein Immobilization, *J. Phys. Chem. C*, 2012, **116**, 13217-13224.
- [5] M. Ammam, Polyoxometalates: formation, structures, principal properties, main deposition methods and application in sensing, *J. Mater. Chem. A*, 2013, **1**, 6291-6312.
- [6] Y.-F. Song, N. McMillan, D.-L. Long, S. Kane, J. Malm, M. O. Riehle, C. P. Pradeep, N. Gadegaard, L. Cronin, Micropatterned Surfaces with Covalently Grafted Unsymmetrical Polyoxometalate-Hybrid Clusters Lead to Selective Cell Adhesion, *J. Am. Chem. Soc.*, 2009, **131**, 1340-1341.
- [7] I. Ullah, A. Munir, A. Haider, N. Ullah, I. Hussain, Supported polyoxometalates as emerging nanohybrid materials for photochemical and photoelectrochemical water splitting, *Nanophotonics*, 2021.
- [8] S. Herrmann, C. Ritchie, C. Streb, Polyoxometalate - conductive polymer composites for energy conversion, energy storage and nanostructured sensors, *Dalton Trans.*, 2015, **44**, 7092-7104.
- [9] M. Laurans, K. Dalla Francesca, F. Volatron, G. Izzet, D. Guerin, D. Vuillaume, S. Lenfant, A. Proust, Molecular signature of polyoxometalates in electron transport of silicon-based molecular junctions, *Nanoscale*, 2018, **10**, 17156-17165.

## 6. Surface-immobilisation of an asymmetric hybrid POM

---

- [10] M. Laurans, K. Trinh, K. Dalla Francesca, G. Izzet, S. Alves, E. Derat, V. Humblot, O. Pluchery, D. Vuillaume, S. Lenfant, F. Volatron, A. Proust, Covalent Grafting of Polyoxometalate Hybrids onto Flat Silicon/Silicon Oxide: Insights from POMs Layers on Oxides, *ACS Appl. Mater. Interfaces*, 2020, **12**, 48109-48123.
- [11] J. Nicoleta, R. Séverine, D. Guillaume, B. Gérard, C. Lise-Marie, T. René, G. Pierre, P. Anna, Organosilyl/-germyl Polyoxotungstate Hybrids for Covalent Grafting onto Silicon Surfaces: Towards Molecular Memories, *Chem. Eur. J.*, 2010, **16**, 5043-5051.
- [12] M. Lu, W. M. Nolte, T. He, D. A. Corley, J. M. Tour, Direct Covalent Grafting of Polyoxometalates onto Si Surfaces, *Chem. Mater.*, 2009, **21**, 442-446.
- [13] F. Volatron, J.-M. Noël, C. Rinfra, P. Decorse, C. Combellas, F. Kanoufi, A. Proust, Electron transfer properties of a monolayer of hybrid polyoxometalates on silicon, *J. Mater. Chem. C.*, 2015, **3**, 6266-6275.
- [14] L. Huder, C. Rinfra, D. Rouchon, A. Benayad, M. Baraket, G. Izzet, F. Lipp-Bregolin, G. Lapertot, L. Dubois, A. Proust, L. Jansen, F. Duclairoir, Evidence for Charge Transfer at the Interface between Hybrid Phosphomolybdate and Epitaxial Graphene, *Langmuir*, 2016, **32**, 4774-4783.
- [15] D. Mercier, M. Ben Haddada, M. Huebner, D. Knopp, R. Niessner, M. Salmain, A. Proust, S. Boujday, Polyoxometalate nanostructured gold surfaces for sensitive biosensing of benzo[a]pyrene, *Sens. Actuators B: Chem.*, 2015, **209**, 770-774.
- [16] J. C. Love, L. A. Estroff, J. K. Kriebel, R. G. Nuzzo, G. M. Whitesides, Self-Assembled Monolayers of Thiolates on Metals as a Form of Nanotechnology, *Chem. Rev.*, 2005, **105**, 1103-1170.
- [17] C. Martin, K. Kastner, J. M. Cameron, E. Hampson, J. Alves Fernandes, E. K. Gibson, D. A. Walsh, V. Sans, G. N. Newton, Redox-Active Hybrid Polyoxometalate-Stabilised Gold Nanoparticles, *Angew. Chem. Int. Ed.*, 2020, **59**, 14331-14335.
- [18] S. Amin, J. M. Cameron, J. A. Watts, D. A. Walsh, V. Sans, G. N. Newton, Effects of chain length on the size, stability, and electronic structure of redox-active organic-inorganic hybrid polyoxometalate micelles, *Mol. Syst. Des. Eng.*, 2019, **4**, 995-999.
- [19] A. J. Bard, L. R. Faulkner, *Electrochemical Methods: Fundamentals and Applications*, Wiley, New York, **2001**.
- [20] A. L. Eckermann, D. J. Feld, J. A. Shaw, T. J. Meade, Electrochemistry of redox-active self-assembled monolayers, *Coord. Chem. Rev.*, 2010, **254**, 1769-1802.
- [21] D. B. Robinson, C. E. D. Chidsey, Submicrosecond Electron Transfer to Monolayer-Bound Redox Species on Gold Electrodes at Large Overpotentials, *J. Phys. Chem. B*, 2002, **106**, 10706-10713.
- [22] M. Yaqub, J. J. Walsh, T. E. Keyes, A. Proust, C. Rinfra, G. Izzet, T. McCormac, R. J. Forster, Electron Transfer to Covalently Immobilized Keggin Polyoxotungstates on Gold, *Langmuir*, 2014, **30**, 4509-4516.
- [23] C. Busche, L. Vilà-Nadal, J. Yan, H. N. Miras, D.-L. Long, V. P. Georgiev, A. Asenov, R. H. Pedersen, N. Gadegaard, M. M. Mirza, D. J. Paul, J. M. Poblet, L. Cronin, Design and fabrication of memory devices based on nanoscale polyoxometalate clusters, *Nature*, 2014, **515**, 545.

## 6. Surface-immobilisation of an asymmetric hybrid POM

---

- [24] M.-C. Daniel, D. Astruc, Gold Nanoparticles: Assembly, Supramolecular Chemistry, Quantum-Size-Related Properties, and Applications toward Biology, Catalysis, and Nanotechnology, *Chem. Rev.*, 2004, **104**, 293-346.
- [25] H. Jans, Q. Huo, Gold nanoparticle-enabled biological and chemical detection and analysis, *Chem. Soc. Rev.*, 2012, **41**, 2849-2866.
- [26] U. Jameel, M. Zhu, X. Chen, Z. Tong, *Recent progress of synthesis and applications in polyoxometalate and nanogold hybrid materials, Vol. 51*, **2015**.
- [27] S. Sutter, B. Trepka, S. Siroky, K. Hagedorn, S. Theiß, P. Baum, S. Polarz, Light-Triggered Boost of Activity of Catalytic Bola-Type Surfactants by a Plasmonic Metal–Support Interaction Effect, *ACS Appl. Mater. Interfaces*, 2019, **11**, 15936-15944.
- [28] C. Pezzato, S. Maiti, J. L. Y. Chen, A. Cazzolaro, C. Gobbo, L. J. Prins, Monolayer protected gold nanoparticles with metal-ion binding sites: functional systems for chemosensing applications, *Chem. Commun.*, 2015, **51**, 9922-9931.
- [29] N. S. Murray, S. P. Jarvis, T. Gunnlaugsson, Luminescent self-assembly formation on a gold surface observed by reversible ‘off–on’ switching of Eu(iii) emission, *Chem. Commun.*, 2009, 4959-4961.

## 7 Summary and outlook

### 7.1 Comparison of key data

The asymmetric hybrid POMs: **1**, **2**, **3**, **4**, and transition metal-coordinated asymmetric hybrid POMs **Fe-1**, **Fe-2**, **Pt-1**, **Ru-1** and **Ru-2** have been characterised in terms of their structure and their properties. A brief comparison of key data for these asymmetric hybrid POMs and free organophosphonate ligands of focus in this thesis is given herein,  $^{31}\text{P}$  chemical shifts ( $\delta$ ) for  $C_{18}$ ,  $C_{11}\text{SH}$  and  $\text{TPY}$ /metal-coordinated  $\text{TPY}$  derivative ligands;  $E_{1/2}$  of the 1<sup>st</sup> POM redox process, I; and the sizes ( $D_h$ ) of the supramolecular assemblies as measured by DLS (Table.23).

Comparison of the  $^{31}\text{P}$  chemical shifts ( $\delta$ ) of the organophosphonate ligands covalently grafted in the hybrid POMs can indicate the degree of electron-withdrawing or electron-donating effects of the ligands in each hybrid. The  $^{31}\text{P}$   $\delta$  of the  $\text{TPY}$  phosphorus in the asymmetric hybrid POM **1** is more shielded (-0.8 ppm) than in the symmetric  $\text{TPY}$  hybrid POM, **2**, indicating a shielding effect of the  $C_{18}$  ligand across the POM core. Correspondingly, the  $^{31}\text{P}$   $\delta$  of the  $C_{18}$  phosphorus in **1** is deshielded in comparison to in the symmetric  $C_{18}$  hybrid POM, **3**. The  $^{31}\text{P}$   $\delta$  values of the  $\text{TPY}$  and  $C_{11}\text{SH}$  ligands in **4** are the same as for the analogous ligands in **1**, indicating no significant electronic effect of the different carbon chain length and terminating thiol group on the phosphorus centre.

The coordination of a transition metal to the chelating  $\text{TPY}$  ligand can be seen to influence the  $^{31}\text{P}$   $\delta$  of  $\text{TPY}$ , as well as the  $C_{18}$  in most cases. The coordination of Fe(II) in the hybrids **Fe-1** and **Fe-2** can be seen to result in a slight shielding (-0.25 ppm) of the  $\text{TPY}$  phosphorus. Similarly, the coordination of Pt(II) in **Pt-1** results in a shielding effect, although more pronounced (-0.85 ppm). The  $C_{18}$  phosphorus centres in these hybrids are consequently slightly deshielded (+0.20 (Fe), +0.28 (Pt) ppm), indicating a small extent of electronic communication between the transition metal,  $\text{TPY}$  phosphorus and  $C_{18}$  phosphorus, mediated across the POM cluster. Interestingly, the

## 7. Summary and outlook

|   | $C_{18}$ ligand $^{31}\text{P}$ $\delta$<br>(ppm, in DMSO- $d_6$ ) | $TPY$ -based ligand $^{31}\text{P}$ $\delta$<br>(ppm, in DMSO- $d_6$ ) | $E_{1/2}$ POM I<br>(V vs. $\text{Fc}/\text{Fc}^+$ ) | Assembly $D_h$ in 9:1 (v/v) $\text{H}_2\text{O}$ - $\text{CH}_3\text{CN}/\text{DMF}$ (nm) |
|---|--|--|---|---|
| <b>Hybrid POMs</b>  |  |  |   |   |
| <b>1</b> ,<br>[ $\text{P}_2\text{W}_{17}\text{O}_{57}\{(\text{TPY})(\text{C}_{18})\}$ ]               | 16.72  | 13.40  | -0.733  | 6.5   |
| <b>2</b> ,<br>[ $\text{P}_2\text{W}_{17}\text{O}_{57}\{(\text{TPY})_2\}$ ]                            | ---  | 14.20  | -0.728  | ---   |
| <b>3</b> ,<br>[ $\text{P}_2\text{W}_{17}\text{O}_{57}\{(\text{C}_{18})_2\}$ ]                         | 16.04  | ---  | -0.754  | 4.8   |
| <b>Fe-1</b> ,<br>[ $\text{Fe}\{\text{P}_2\text{W}_{17}\text{O}_{57}(\text{TPY})(\text{C}_{18})\}_2$ ] | 16.92  | 13.15  | -0.757  | 4.2   |
| <b>Fe-2</b> ,<br>[ $\text{P}_2\text{W}_{17}\text{O}_{57}(\text{Fe-TPY})(\text{C}_{18})\}$ ]           | 16.92  | 13.15  | -0.708  | 5.6   |
| <b>Pt-1</b> ,<br>[ $\text{P}_2\text{W}_{17}\text{O}_{57}\{(\text{Pt-TPY})(\text{C}_{18})\}$ ]         | 17.00  | 12.55  | -0.726  | 5.6   |
| <b>Ru-1</b> ,<br>[ $\text{P}_2\text{W}_{17}\text{O}_{57}\{(\text{RuTPY})(\text{C}_{18})\}$ ]          | 16.72  | ( $\text{RuTPY}$ )<br>13.56  | -0.732  | 5.6   |
| <b>Ru-2</b> ,<br>[ $\text{P}_2\text{W}_{17}\text{O}_{57}\{(\text{RuTPY})_2\}$ ]                       | ---  | ( $\text{RuTPY}$ )<br>14.35  | -0.709  | ---   |
| <b>4</b> ,<br>[ $\text{P}_2\text{W}_{17}\text{O}_{57}\{(\text{TPY})(\text{C}_{11}\text{SH})\}$ ]      | ( $\text{C}_{11}\text{SH}$ )<br>16.72                              | 13.41  | -0.727  | 6.5   |
| <b>Organophosphonate ligands</b>  |  |  |   |   |
| <b><math>\text{C}_{11}\text{SH}</math></b>  | ( $\text{C}_{11}\text{SH}$ )<br>13.40                              | ---  | ---   | ---   |
| <b><math>\text{TPY}</math></b>  | ---  | 11.95  | ---   | ---   |
| <b><math>\text{RuTPY}</math></b>  | ---  | 11.89  | ---   | ---   |

**Table 23.** Comparison of data for the hybrid POMs and free organophosphonate ligands of focus in this thesis:  $^{31}\text{P}$  chemical shifts ( $\delta$ ) for  $C_{18}$ ,  $C_{11}\text{SH}$  and  $TPY$ /metal-coordinated  $TPY$  derivative ligands;  $E_{1/2}$  of the 1<sup>st</sup> POM redox process, I; and the sizes ( $D_h$ ) of the supramolecular assemblies measured by DLS.  $^{31}\text{P}$  data for  $\text{C}_{18}$  is not included due to insolubility in DMSO- $d_6$ .

effect of Ru(II) coordination to  $TPY$  in the  $\text{RuTPY}$  ligand grafted in both **Ru-1** and **Ru-2** on the  $^{31}\text{P}$   $\delta$  is marginal, as the  $TPY$  phosphorus centres are only slightly deshielded by

## 7. Summary and outlook

---

*ca.* 0.15 ppm from in their respective hybrid POMs **1** and **2**, and the  $C_{18}$  phosphorus in **Ru-1** is not shifted from in **1**.

A comparison of the  $E_{1/2}$  potentials of the first POM-based redox process in each of the hybrid POMs can also give an indication of the extent of electronic communication between the ligands and POM cluster and the effect of transition metal coordination at the *TPY* moieties. It is interesting to note that potentials do not differ significantly or show a clear trend. The  $E_{1/2}$  potentials of the POM-based redox process I in **1** and **4** are comparable, in line with their analogous  $^{31}\text{P}$   $\delta$  values, as can be expected with their similar ligand environments. However, the  $E_{1/2}$  of process I in **2** is also comparable to in **1**, despite the different ligands, shifted more positively by only 5 mV. The  $E_{1/2}$  of process I in the other symmetric hybrid POM, **3**, is shifted more negative by 21 mV, in line with the slightly more electron-donating nature of  $C_{18}$  in comparison to *TPY*.

The effect of transition metal coordination to *TPY* in the hybrid POMs on the  $E_{1/2}$  of the first POM-based redox process is less clear. The coordination of Pt(II) to **1** does not significantly affect  $E_{1/2}$  (I), despite the shielding by *ca.* 1 ppm observed for the *TPY* phosphorus and slight deshielding of the  $C_{18}$  in the  $^{31}\text{P}$  NMR suggesting that the electron density on the POM could be affected by the metal complex. Similarly,  $E_{1/2}$  (I) in **Ru-1** does not differ from in **1**. The more positive charge of the transition metal functionalised hybrid POMs could be expected to cause the POM to be more easily reduced, resulting in a more positive  $E_{1/2}$  (I). This appears to be the case for the symmetric *RuTPY* hybrid, **Ru-2**, and the monomer Fe(II) complex **Fe-2**, which have slightly positively shifted potentials (*ca.* 20 mV) relative to the respective hybrid POMs **2** and **1**. However, the opposite is observed for the dimer Fe(II) complex, **Fe-1**, in which  $E_{1/2}$  (I) is negatively shifted by *ca.* 20 mV. The remote metal complex and the POM cluster perhaps behave as if electrochemically isolated somewhat, so that the reduced charge of the transition metal functionalised hybrid POMs does not have a significant effect on the reducibility of the POM.

Interestingly, the peak  $D_h$  values as measured by DLS of the supramolecular assemblies formed by the hybrid POMs in a 9:1 (v/v)  $\text{H}_2\text{O}-\text{CH}_3\text{CN}/\text{DMF}$  mixture are all

very similar, differing only by *ca.* 2 nm. Notably, the lowest  $D_h$ , 4.2 nm, is observed for **Fe-1**, which has a much less pronounced amphiphilic structure compared to the other hybrid POMs. The aggregates as observed by cryo-TEM also do not resemble spheres, making the average  $D_h$  determined by DLS less reliable.

### 7.2 Final conclusions and outlook

The key goals of this research were to develop synthetic strategies to prepare and isolate new asymmetrically bi-organofunctionalised hybrid POMs, and to probe their functional characteristics that are derived from their structures and properties. This work has demonstrated that the preparation of asymmetrically functionalised hybrid POMs is certainly accessible and brings exciting opportunities to the development of multifunctional hybrid POMs. As the asymmetric hybrid POM systems synthesised are based on the highly redox-active Dawson anion, for which stable, covalent asymmetric hybridisation had not yet been established, these studies are particularly impactful in the development of new redox- and photo-active multifunctional hybrid materials.

Through the development of a new straightforward and inexpensive one-pot synthetic approach, the preparation of a new family of asymmetric hybrid Dawson systems has been successfully achieved. The use of distinct organophosphonate functionalising groups has been shown to enable “bench-top” purification of the asymmetric products, by employing the different solubilities that are imparted to the symmetric and asymmetric hybrid POM products in the crude reaction mixture. Fundamentally, the designs of the distinct organic components can be used to introduce, combine, and tailor multiple functional characteristics in the hybrid POM, and this was demonstrated through the characterisation of the unique structure and properties of the new asymmetric hybrid POM, **1**.



## 7. Summary and outlook

In light of this, **1** can effectively be seen as a versatile molecular platform, as modified structures of the asymmetric hybrid POM can be designed and built in a modular fashion, either through its postfunctionalisation or by a similar one-pot methodology combining alternative ligands. The platform structure comprises centrally a Dawson anion, intrinsically rich in redox- and photo-activity, to which two organophosphonate components are covalently appended (Fig.131). The modification of the appended functions in the structure has been explored in this work in the preparation of several asymmetric hybrid POM derivatives of **1**, and their characterisation has given valuable insight into the implications of molecular design on the properties of the hybrid material. The aliphatic chain moiety has been shown to enable the solvent-dependent self-assembly of the hybrid POMs into redox-active soft nanoassemblies, offering exciting opportunities for the development of the family of asymmetric hybrid POMs as nanomaterials with controllable morphologies and electrochemical behaviours. By appending a thiol-terminated derivative of the chain ligand to the Dawson POM, the capacity for assembly of the material was extended to enable its immobilisation onto material surfaces. The second function, by bearing a chelating site, opens diverse opportunity for incorporating transition metal activity into the hybrid material, demonstrated by both the direct coordination of metal ions to the appended ligand, and by the grafting of a preformed organometallic function in an alternative one-pot

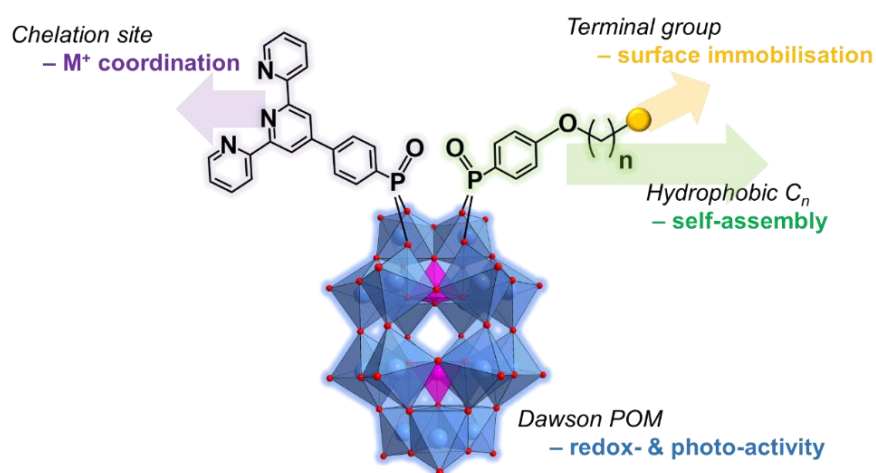


**Figure 131.** The structural components of the asymmetric hybrid POM investigated in this work.

## 7. Summary and outlook

---

methodology. It has been shown that these modifiable functionalities allow the tuning and synergistic coupling of many characteristics of the material, including morphology, redox behaviour, and visible-light photoactivation.

With the vast design opportunities available in organic chemistry, in theory, almost any kind of organic or organometallic function could be grafted to the POM covalently by an appropriate organic linker. Using the approach developed in this work, combinations of more complex functions could be explored, for example, instead of an aliphatic chain moiety, a peptide or biomolecule could be incorporated along with a photoactive function, creating opportunity for the design of new phototherapeutic or luminescent tagging agents. Alternatively, a complex catalytic triad system could be designed, in which two different catalytic or photosensitising substrates are appended to the POM core, which could pave the way for new multicomponent molecular and supramolecular catalysts that are capable of efficient multi-electron processes. In line with this concept, a derivative of the asymmetric hybrid modified-gold nanoparticle composite prepared and briefly investigated in this work, in which an organic or organometallic photoactive unit is appended to the POM, holds great potential.

The family of asymmetric hybrid POMs synthesised in this work represent a new type of hybrid material in which synergistic properties and function can be derived from the asymmetric structure. Ultimately, this work has demonstrated the enormous scope of opportunity that is available via the asymmetric hybridisation of POMs for the design of new, multifunctional hybrid materials, with a range of potentially novel applications as redox-, photo-, and catalytically active nanomaterials.